


Doctoral Dissertation
Doctoral Program in Chemical Engineering (32nd Cycle)

Fe-N-C non-noble catalysts for applications in Fuel Cells and Metal Air Batteries

Lorenzo Pezzolato
* * * * * *

Supervisor
Prof. Stefania Specchia

Doctoral Examination Committee:
Prof. Barbara Mecheri, Referee, Università degli Studi di Roma Tor Vergata
Dr. Stefania Siracusano, Referee, Consiglio Nazionale delle Ricerche
Dr. Cinthia Alegre Gresa, Referee, Consejo Superior de Investigaciones Cientìficas, Zaragoza (Spain)
Prof. Carlotta Francia, Referee, Politecnico di Torino
Prof. Bojoi Iustin Radu, Referee, Politecnico di Torino

Politecnico di Torino
January 20, 2020

I hereby declare that, the contents and organisation of this dissertation constitute my own original work and does not compromise in any way the rights of third parties, including those relating to the security of personal data.

Lorenzo Pezzolato
Turin, January 20, 2020

Summary

In this work of thesis, two non noble metal (NNM) catalysts active toward oxygen reduction reaction (ORR) were synthesized, optimized, characterized and finally tested in Direct Ethanol Fuel Cell (DEFC) and Metal Air Battery (MAB).

The catalysts were designed combining carbonaceous materials with iron and nitrogen precursors. The first catalyst, named Z/F 2HT, was obtained mixing the metal organic frameworks Basolite z1200 (Zif-8) with Fe-Phthalocyanine. The synthesis was performed using an autoclave step followed by two heat treatment (HT) at high temperature with intermediary acid leaching. The synthesis optimization was carried out following both the *design of experiment* method and the *one factor at one time* approach. The second catalyst, named V/F BM, was obtained mixing different amount of Vulcan XC 72 with Fe-Phthalocyanine using the mechanochemical synthesis through ball milling (BM) process. The synthesis optimization was carried out following the *one factor at one time approach.* Several heat treatments were evaluated as well.

Different electrochemical, chemical and surface analyses were carried out in order to investigate the properties and the difference between the two catalysts obtained after their synthesis processes. Specifically, the catalysts were analysed in RDE and RRDE configurations, in alkaline medium, in terms of stair case voltammetry, cyclic voltammetry, Tafel analysis, short load cycle durability test, ethanol tolerance, Koutecky Levich analysis, and H_2O_2 production as electrochemical evaluation. BET, SEM, XPS, and %Fe with ICP analysis as chemical physical analyses. A Pt/C commercial catalyst was used as a reference in the RDE/RRDE analyses. Since the characterization showed good results (half wave potential Z/F 2HT: 0.87V, V/F BM: 1,01 V, Pt/C: 1.01 V), the catalysts were further tested in electrochemical devices. The V/F BM catalyst showed better performance compared to the Z/F 2HT catalyst in terms of electrochemical

activity and was studied for both DEFC and MAB applications. The Z/F 2HT material was tested only in MAB.

Pt/C and MnO_2/C were used respectively as DEFC and MAB commercial catalyst references. The experiments carried out in DEFC were promising: V/F BM reached 70 mW cm^{-2} as maximum power density and 53 mW mg_{Pt}^{-1} as mass specific power density. These values have the same order of magnitude of the best non noble metal catalysts reported in literature for DEFC. Concerning the durability, further improvement are required with the aim to understand if the performance loss are caused by the device or the catalyst. The application of the two catalysts in MAB demonstrated a different behaviour from the laboratory predictions. At lower discharge current density (1.6 mA cm^{-2}) the Z/F 2HT showed better results both in terms of durability and capacitance. At higher discharge current density (3.2 mA cm^{-2}) V/F BM catalyst showed the best performance. Both the Z/F 2HT and V/F BM catalysts showed closer but still lower electrochemical performance compared to the commercial MnO_2/C reference catalyst.

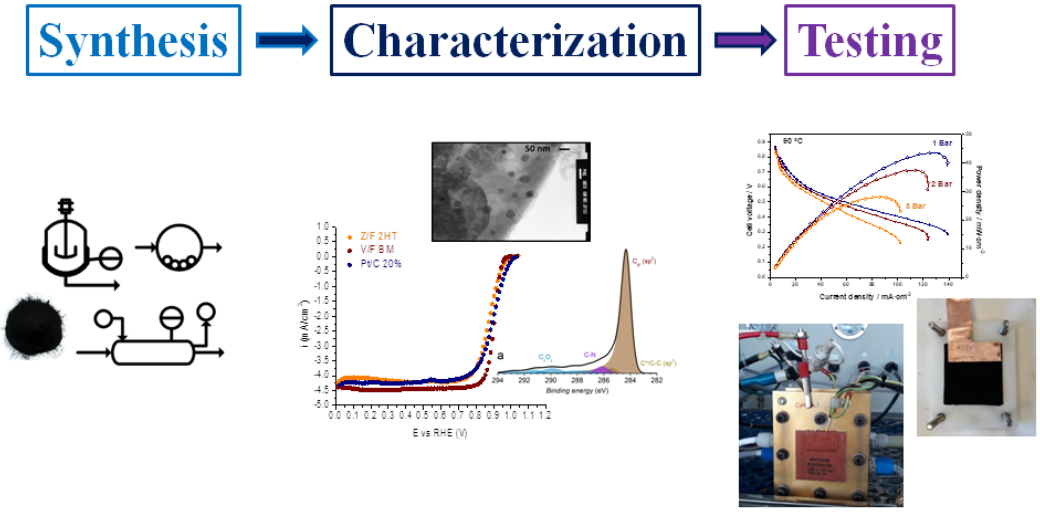

Graphical abstract

Acknowledgment

I would like to express acknowledge to:

- Professor Stefania Specchia, for the support provided during this thesis work.
- Professor Pilar Ocon, Daniel Guillermo, Oxel, Laura end Kerly from the Universidad Autonoma de Madrid for their kindness support and shared experience during my special permanence in Madrid.
- Kyoto Institute of technology for the TEM analysis
- University of California – Irvine for the XPS analysis
- Instituto de Catàlisis Petroleoquimica (ICP) de Madrid for the BET analysis.
- My colleagues Carmen, Alessandro, Luigi and Stefano for the time spent together.

- Last but not least I would like to express my sincere gratitude to my beloved Sara

Contents

List of Tables

List of Figures

Chapter 1

Introduction

1.1 Introduction to the project

Global warming, mainly due to a continuous increase in the concentration of greenhouse gases in the atmosphere is the major environmental problem observed since the 19th century. The increase in greenhouse gas emissions, mainly carbon dioxide, is due to the use of fossil fuels as a source of electricity. To reduce emissions more attention is oriented to the production of energy from renewable sources. To solve this unpleasant situation, the development and commercialization of efficient electrochemical converters fed with hydrogen or renewable biofuel is a big challenge. A further challenge is the importance of solving the problem of energy storage through the development of low-cost battery device with high performance and long durability. Among several electrochemical converter, fuel cells (FC) are energy system that can solve the first challenge and metal-air battery (MAB) the second one (**Figure 1.1 A-B**).

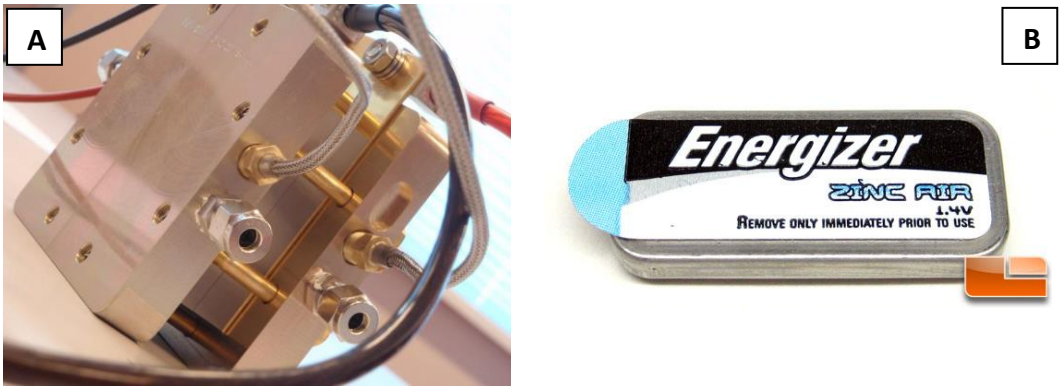

Figure 1.1 A-B. Example of Fuel Cell (A) and Metal Air Battery (B) device.

In a FC, the energy is stored outside the stack while in a MAB is stored inside the battery. Although the final application is different these devices have in common the oxygen reduction reaction (ORR) that takes place to their cathodes. As a consequence, many of the catalysts that accelerate this reaction are similar or identical allowing their development in a single stage.

1.2 Fuel cell introduction

A fuel cell is an energy conversion system which can convert the chemical energy of a fuel and an oxidant into electrical energy through an electrochemical reaction. It differs from the internal combustion engine since there is no thermal cycle. As result, the device shows higher conversion efficiency because it is not limited by the thermodynamics Carnot's theorem. Also, emissions of the main air pollutants such as carbon dioxide (CO_2), nitrogen oxides (NO_x) and sulphur dioxide (SO_2) are reduced. [1]

Like all the electrochemical devices, a single cell consists of two electrodes separated by an electrolyte. On the electrodes surface, catalysts are deposited to accelerate chemical reactions. The reagents, fed to the electrodes, are in contact with both the catalysts and the electrolyte and react in a triphasic region.

At the anode an oxidation reaction takes place. Generally, the fuel is hydrogen but may also consist of natural gas, alcohols or polyols [2]. At the cathode the oxygen reduction reaction takes place since the most common oxidants are pure oxygen or air. The electrons flow into an external circuit from the anode to the cathode while the ions generated from the reactions migrate through the electrolyte keeping closed the electrical circuit. The electrodes requires high catalytic activity, good electrical conductivity and gas permeability. On the contrary, the electrolyte requires high ion conductivity to allow the transport of ions and low electronic conductivity to block the electrons flow. Furthermore it must be impermeable to gases [3].

Several type of fuel cells are classified according to different parameters such as the type of fuel (hydrogen, natural gas, methanol...), the type of electrolyte (solid, liquid, alkaline, acidic...) and the working temperature (high temperature and low temperature) [4]. The five most common typologies of fuel cell are listed below and their property are summarized in **Table 1.1:**

- AFC: Alkaline Fuel Cell
- PEMF: Polymer Electrolyte Membrane Fuel Cell
- PAFC: Phosphoric Acid Fuel Cell
- MCFC: Molten Carbon Fuel Cell
- SOFC: Solid Oxide Fuel Cell

The PEMFC are the most widespread fuel cells in the market. Since they work at temperature below 100 °C, they can be employed for different application providing fast start up and shut down operation as well as ensuring greater simplification of the device. PEMFC are used for mobile and stationary applications. Cars, delivery vehicles, buses, ships, drones are mobile applications while power generators in the domestic and industrial sector are the main stationary application.

Table 1.1. Fuel cell classification and main characteristic.

	Low-temperature fuel cell			**High-temperature fuel cell**	
	AFC	**PEMFC**	**PAFC**	**MCFC**	**SOFC**
Electrolyte	KOH solution in porous matrix	Proton exchange membrane or Anion exchange membrane	Phosphoric acid in porous matrix	Lithium or potassium carbonate in porous matrix	Zirconium stabilized with yttrium
Fuel	Hydrogen	Hydrogen, methanol, ethanol	Hydrogen, natural gas	Hydrogen, natural gas	Hydrogen, natural gas
Operative temperature (°C)	60 - 90	50 - 90	160 - 220	620 - 660	800 - 1000
Electric efficiency (%)	50	40 - 50	40	45 - 55	50 - 60

The PEMFC category is furthermore subdivided in proton exchange membrane (PEM) FC and anion exchange membrane (AEM) FC depending on the type of ion exchanged: H^+ or OH^- respectively. It is fundamental to don't confuse the dualism of the names: proton exchange membrane is a type of "polymer exchange membrane fuel cell" and both are indicated with the PEM acronym. Although several number of challenges have to be overcame, the proton exchange membrane fuel cell fed with hydrogen are the closest to a wide commercialization since they are the most studied and performing devices. Due to this reason, the project of this thesis was focused on the synthesis of catalysts for AEMFC fed with alcohols. Further details will be described below in the following paragraphs.

1.2.1 Direct alcohol fuel cell DAFC and anion exchange membranes AEMs

Direct Alcohol Fuel Cells (DAFCs) were increasingly studied over the past years as valid alternative to PEMFCs. The primary difference of this devices concerns the use of a liquid fuel instead of hydrogen gas. If the cell is fed with methanol the device is called direct methanol fuel cell (DMFC) while if fed with ethanol is called direct ethanol fuel (DEFC) [2]. The commercialization of hydrogen PEMFCs is limited by three problems: production (often connected to fossil fuels), storage and distribution infrastructures. Storage and distribution could be partially resolved through the use of a less dangerous liquid fuel. Alcohol derived fuel as ethanol and methanol possess high volume energy density (24 MJ/l and 15.6 MJ/l respectively), and they can also be produced from renewable sources such as biomass derivatives. To decrease environmental and safety problems, the use of ethanol is preferred to methanol due to his non-toxic behavior [5,6] and was chosen as specific fuel investigated in this thesis. Depending on the type of membrane used, a distinction can be made between proton exchange membranes (PEMs) and alkaline exchange membranes (AEMs) for DEFCs applications. In the following work, the analysis of AEM-DEFCs was considered for a series of advantages that will be described later in this chapter. **Figure 1.2** show the basic scheme of an alkaline DEFCs.

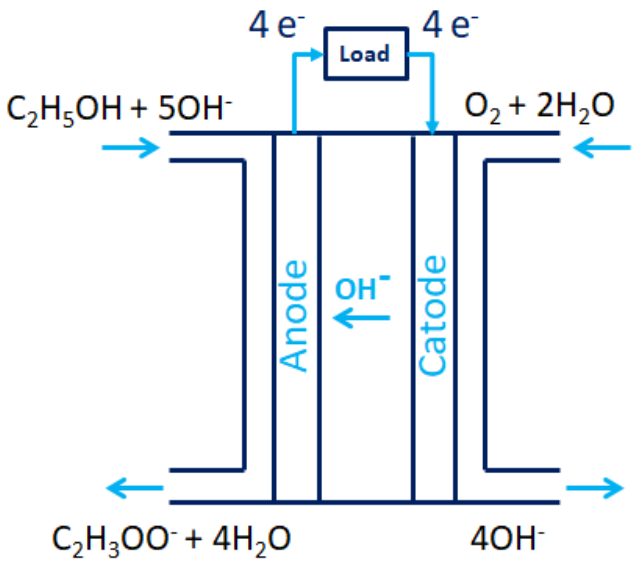

Figure 1.2. Scheme of AEM-DEFC

The fundamental difference of an alkaline membrane lies in its ability to transport negative OH^- ions from the cathode to the anode while acidic membranes transports positive H^+ ions from the anode to the cathode. An alkaline

membrane is generally composed of quaternary ammonium functional positive groups linked to polymeric chains [7]. Through different transport mechanisms the negative hydroxyl ions can switch between the positive functional groups. The mechanism is a combination of different transport phenomena [8] listed below and summarized in **Figure 1.3**:

- surface site hopping on quaternary side chains;
- Grotthuss behavior;
- migration and diffusion due potential and concentration gradients;
- convection due to electrostatic and/or pressure gradients.

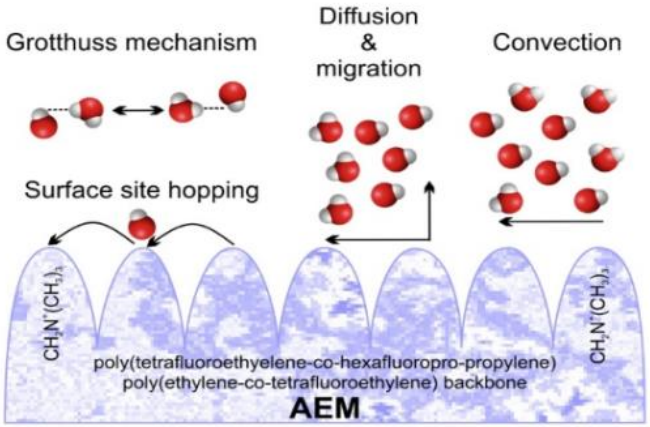

Figure 1.3. The four transport phenomena of H_2O and OH^- in alkaline exchange membranes. Figure modified from [8].

Since the OH^- ion is larger than the simple H^+, the ion conductivity of the alkaline membranes is lower compared to acidic membranes and currently the research is involved in the study of alkaline membranes with high conductivity [9]. As an advantage, the anionic current due to the OH^- transport into the alkaline membrane is opposite respect the H^+ cationic current in acidic membranes, resulting in an overall reduction of fuel crossover caused by the reverse direction of the electro-osmotic drag [10].

1.2.2 DEFCs reaction description

The ORR takes place at the cathode fed with humidified air or pure oxygen. The reaction in alkaline environmental produces OH^- ions that pass through the membrane and reach the anode on the other side (**Equation 1.1**):

$$3O_2 + 6H_2O + 12e^- \rightarrow 12\ OH^- \qquad \text{Equation 1.1}$$

At the anode side the ethanol oxidation reaction (EOR) takes place. Carbon dioxide (CO_2), water (H_2O) and 12 e^- are produced in case of total conversion as described in **Equation 1.2**.

$$CH_3CH_2OH + 12OH^- \rightarrow 2CO_2 + 9H_2O + 12e^- \quad \text{Equation 1.2}$$

The total reaction is gave as **Equation 1.3**:

$$CH_3CH_2OH + 3O_2 \rightarrow 2CO_2 + 3H_2O \quad \text{Equation 1.3}$$

In reality EOR may also proceed through two alternative reactions involving the transfer of 2 or 4 electrons with formation respectively of acetaldehyde (**Equation 1.4**) or acetic acid (**Equation 1.5**) [5].

$$CH_3CH_2OH + 2OH^- \rightarrow CH_3CHO + 2H_2O + 2e^- \quad \text{Equation 1.4}$$

$$CH_3CH_2OH + 4OH^- \rightarrow CH_3COOH + 3H_2O + 4e^- \quad \text{Equation 1.5}$$

Generally, OH^- ions are added to the liquid ethanol solution in the form KOH or NaOH to increase the fuel cell performance and decrease the membrane resistance [11,12]. This improvement is physically described from the presence of $[OH^-]$ in the of EOR kinetic equation.

1.2.3 DEFCs device description

A single alkaline DEFC consists of several components. A typical scheme is shown in **Figure 1.2**. The main components are the AEM, the anodic and cathodic electrodes, two gasket and two bipolar plate. The joint between the membrane and electrodes is called membrane-electrode assembly (MEA) and consists specifically of five elements [13]:

- Anodic gas diffusion layer (AGDL)
- Anodic catalyst layer (ACL)

- Alkaline exchange membrane (AEM)
- Cathodic catalyst layer (CCL)
- Cathodic gas diffusion layer (CGDL)

Different catalyst layer are deposited on the gas diffusion layer (GDL) through brush, manually airbrush or robotic airbrush. The GDLs have high electric conductivity and consist of a series of channels for the transport of reagents and products. They consist of a macroporous layer made of carbon paper (carbon fiber sheets) or carbon cloth (carbon tissue) combined with another microporous layer in contact with the catalytic layer [14]. The AEM is placed between the two GDL keeping in contact with the catalyst layer. The MEA is then covered on both sides by two gaskets that guarantee the sealing of the reagents. Two bipolar plate are placed in contact with the gaskets. They consist of channels that distribute the reagents uniformly to the electrodes and remove the water produced. They are made of graphite plates since the device requires high electrical conductivity. At the extremes of the device, two metal plates are placed to work as current conductors and to allow the clamping through the use of bolts.

Usually, individual cells are combined to form a stack to increase the power production of the electro converting system.

1.2.4 AEM advantages and disadvantages

Among a multitude of benefits, AEMFCs also present a series of drawbacks that the technological development is trying to minimize. With regard to the advantages it is possible to report the following list:

- The alkaline environmental reduces the problem of corrosion inside the device [15]: the durability of the equipment increase and furthermore is possible the use of low-cost materials [16];
- Enhancement of the alcohols oxidation reaction (AOR) and ORR kinetic reactions [15];
- Possibility to use cheap non noble metal catalyst at the cathode keeping the performance comparable with the same electrode loaded with Pt [17];
- A wide variety of cheap polymers are available for the membrane preparation [18];
- Possibility to use different fuels to hydrogen thanks to the membrane low crossover: methanol and ethanol as alcohols, glycerol and ethylene glycol as polyols, ammonia and hydrazine as N-based fuels [2];

With regard to the drawbacks it is possible to affirm the following:

- Low OH^- conductivity due its lower diffusion coefficient [19].

- Carbonation of the membrane when the cathode is fed with air instead of pure oxygen. The CO_2 contained in the air tend to form carbonate in alkaline environmental thus K_2CO_3 precipitate on the catalyst surface blocking its activity [20];
- Introduction of OH^- ions in the fuel solution to increase the AOR kinetic;
- Loss of performance in case of ethanol crossover from the anode side to the cathode side [21]. Although this phenomena is lower compared to the PEMFCs, is to be considered a negative phenomenon because increase the cathode overpotential and thus reduction of the cell efficiency [22]. Furthermore, the simultaneous reduction of oxygen and oxidation of ethanol at the cathode it does not produce external current to the circuit [23]. The crossover phenomena is affected by cell temperature, produced current density, ethanol concentration. In relation to the latter, a diluted ethanol solution (2 M) is fed to the anode [24];
- Water management to avoid flooding at the electrodes keeping in any case the membrane correctly hydrated. Water is produced at the anode and used at the cathode. Is fundamental for the membrane hydration to keep the anionic conductivity. At the same time, if water is not correctly removed, catalyst layer and GDLs are subject to flooding. The fuels flow rates, the design of the bipolar flow channel and the chemical-physical properties of the membrane affect the flooding phenomena [25,26].

1.2.5 DEFCs performance - state of art

The best performance obtained from non noble metal catalysts used in AEM-DEFCs fed with pure oxygen at the cathode side are summarized below. **Figure 1.4** shows the maximum power density available in the literature. Actually, the best activity belongs to the commercial cathodic catalyst developed by Acta (Italy) called Hypermec TM K14 (with Hypermec TM 3020 at the anode side) [27]. This configuration has reached 101 mW cm^{-2} as PPD while Pt/C MEA showed 90 mW cm^{-2} at the same conditions. Bambagioni et al. [28] obtained 73 mW cm^{-2} using the same cathodic catalyst and Pd/C at the anode side. Rauf et al. [29] obtained 58 mW cm^{-2} with Fe nanoparticles encapsulated in bamboo-like carbon matrix. Osmieri et al have achieved 73 mW cm^{-2} [30] and 62 mW cm^{-2} [31] working with two Fe-N-C catalysts synthesised by SSM. In these experiments, Fe was finely dispersed as nanoparticles on mesoporous carbon supports. Osmieri et al. were the only to perform durability analysis with alkaline DEFCs showing a performance reduction of 42% [30] and 64% [31] respectively.

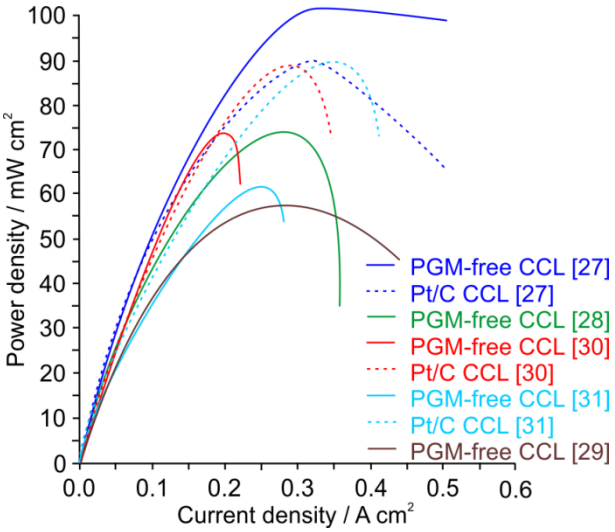

Figure 1.4. Best result of ethanol/oxygen-fed AEM-DEFCs described in the literature. Full curves related to MEA with non noble cathodic catalyst. Dotted curves related to MEAs with commercial Pt/C cathodic catalyst. Figure modified from [2].

Table 1.2 summarizes the catalysts synthesis, the fuel cell set up and the relative results in terms of peak power density (PPD) and specific power density referred to the overall amount of Pt present in the electrochemical devices. It is fundamental to underline that the AEM-FC research is mainly focused to solve problems relative to the electrochemical device like the membrane development [9] and the water management [32]. The ORR activity in alkaline environment is not the real problem since good results have been achieved as will be explained in next paragraphs.

NNM Catalyst cathode	Precursor, heat treatment and template removal	Cathode loading [$mgcm^{-2}$]	Anode catalyst and loading [$mgcm^{-2}$ or $mg_{Pt}\ cm^{-2}$]	AEM type and size	FC test conditions	MEA peak power density [$mWcm^{-2}$]	Mass specific power density [$mWmg_{Pt}^{-1}$]	Pt/C@cathode MEA peak power density [$mWcm^{-2}$]	Ref
Fe-N-C (Bg-CAMFe/ N/C)	benzoguanamine, cyanuric acid, melamine, $FeCl_3$, KJ600 carbon black HT: 1st and 2nd pyrolysis 1h + 3 h @ 800 °C in Ar; Acid leaching between the two pyrolysis with 0.1 M H2SO4 @ 80 °C	2.56	20 wt% Pd/C: 2.56 mgc m^{-2} (0.512 $mg_{Pd}\ cm^{-2}$)	6.25 cm^2 A201 Tokuyama Corporation Japan	80 °C 2 M C_2H_5OH + 1 M KOH: 2 mL min^{-1} O_2: 0.3 $Lmin^{-1}$ (humidified)	58	113 $mWmg_{Pd}^{-1}$	n.a.	[29]
Hypermec TM K14	n.a. (Acta S.p.A.) (FeCo-based)	n.a.	Pd/MWCNT 1 $mg_{Pd}\ cm^{-2}$	5 cm^2 A006 Tokuyama Corporation Japan	80 °C 10 wt.% C_2H_5OH + 2 M KOH: 4 mL min^{-1} O_2: 0.2 L min^{-1} (dry)	73	73 $mWmg_{Pd}^{-1}$	n.a	[28]
Hypermec TM K14	n.a. (Acta S.p.A.) (FeCo-based)	3.5	Hypermec TM 3020 15 mg cm^{-2}	5 cm^2 A006 Tokuyama Corporation Japan No hot pressing	60 °C 10 wt.% C_2H_5OH + 10wt.% KOH: 7 mL min^{-1} O_2: 0.15 $Lmin^{-1}$ (dry), 100 KPa	101	n.a.	90 cathode: 10% Pt/C Johnson Matthey, 3.5 mg cm^{-2}	[27]

Table 1.2. Summary of the best non noble metal catalyst tested in DEFC and described in literature

NNM Catalyst cathode	Precursor, heat treatment (HT) and template removal (TR)	Cathode loading [$mg cm^{-2}$]	Anode catalyst loading [$mg cm^{-2}$ or $mg_{Pt} cm^{-1}$]	AEM type and size	FC test conditions	MEA peak power density [$mW cm^{-2}$]	Mass specific power density [$mW mg_{Pt}^{-1}$]	Pt/C@cathode MEA peak power density [$mW cm^{-2}$]	Ref
Fe-N-C	Poly-pyrrole $C_{10}H_{14}N_2O_8Na_2 \cdot 2H_2O$ (EDTA-2Na), $FeCl_3 \cdot 6H_2O$, C_2H_5OH, NH_3 HT: 1st pyrolysis 1 h @ 800 °C in N_2, 2nd pyrolysis 1 h @ 900 °C in N_2	3.0	PtRu black: 3.0 mg cm^{-2} Johnson Matthey, 60%Pt 30% Ru, 1.8 $mg_{Pt} cm^{-2}$	1 cm^2 AEM Tokuyama	80 °C 2 M C_2H_5OH + 1 M NaOH: 1 mL min^{-1} Dry O_2: 0.1 L min^{-1}	33	18 $mW mg_{Pt}^{-1}$	8 cathode: 20% Pt/C Johnson Matthey, 0.12 mg cm^{-2}	[33]
Fe-N-C	mesoporous carbon, 1,10-phenantroline, $FeCl_3$ HT: 1st and 2nd pyrolysis 3 h @ 830 °C in N_2; TR: between the two pyrolysis with 5 wt.% HF	2.5	45% PtRu/C: 1.33 $mg_{Pt} Cm^{-2}$	4 cm^2 commercial polybenzimidazole (PBI) membrane (Danish Power Systems) doped with 6 M KOH, no hot pressing	90 °C 2 M C_2H_5OH 2 M KOH: 1 mL min^{-1} (0.33 bar,rel) dry O2: 0.2 $L min^{-1}$ 3 bar backpressure	73 (–42% after short durability test, initial activity fully after MEA reactivation)	55 $mW mg_{Pt}^{-1}$	89 cathode: 40% Pt/C Johnson Matthey, 3.5 mg cm^{-2}	[30]
Fe-N-C	Fe(II)-phthalocyanine, SBA-15 silica HT: 1 h pyrolysis @ 800 °C in N_2 (800 mL min^{-1}, 10 °C/min) TR: 5 wt.% HF	2.5	45% PtRu/C: 1.33 $mg_{Pt} Cm^{-2}$	4 cm^2 commercial polybenzimidazole (PBI) membrane (Danish Power Systems) doped with 6 M KOH, no hot pressing	90 °C 2 M C_2H_5OH 2 M KOH: 1 $mL min^{-1}$ (0.33 bar,rel) O2: 0.2 L/min (dry), 3 bar backpressure	62 (–64% after short durability test, –34% after MEA reactivation)	47 $mW mg_{Pt}^{-1}$	89 cathode: 40% Pt/C Johnson Matthey, 3.5 mg cm^{-2}	[31]

Table 1.2. (continued)

1.3 Metal Air Battery short introduction

A MAB is an electrochemical device in which the ORR (discharge process) takes place on the cathode surface with the O_2 present in the air at atmospheric pressure. MAB are promising source of energy since the weight is reduced from the use of O_2 as reactant which is not stored within the stack. This technology offers high space for energy storage, high theoretical energy density (up to 200 Wh kg^{-1}), and low production and disposal costs [34]. In contrast, the main problem is related to the sluggish kinetic of ORR which is the slowest chemical reactions of the battery and limits the voltage output and high current performance. Moreover, if not properly handled it can produce corrosive intermediates that damage the battery and decrease its lifetime. Thus, MAB are still limited in terms of both rate capability and long term durability. The electrodes are separated by a solid or liquid electrolyte which serves also as ion conductor [35]. The device scheme is represented in **Figure 1.5**.

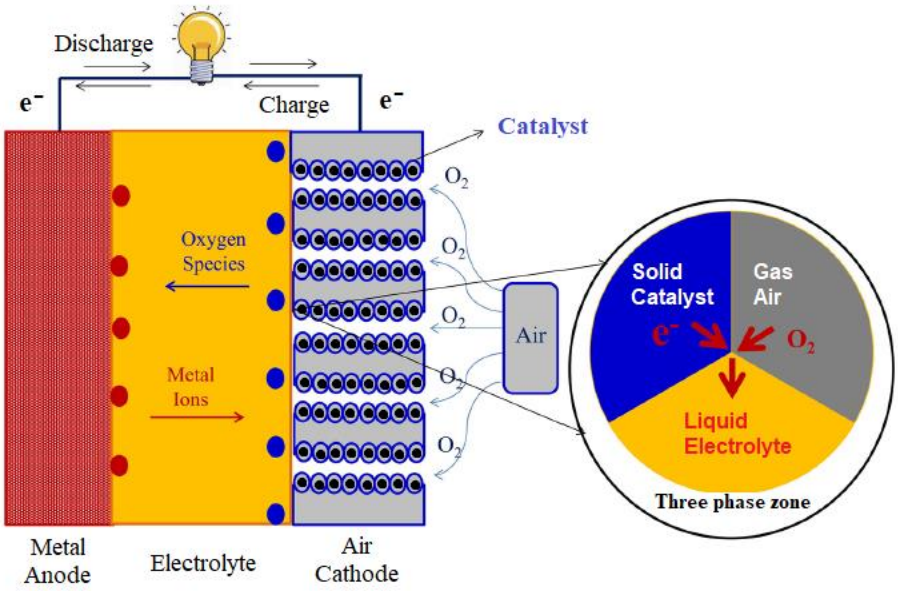

Figure 1.5. Basic metal air battery scheme. Figure modified from [36].

Actually the metals or alloys used for the fabrication of the anodes consists of Li, Ca, Mg, Zn, Al, Fe, Na, K, Sn, Si, Ge [36]. In **Table 1.3** are showed the theoretical specific energy obtainable combining some of these elements with O_2 in MAB [37]. Zn-air, Al-air and Li-air are the most investigated batteries:

- Zinc-air batteries: are non-rechargeable alkaline battery with a specific energy of more than three times higher compared to lead-acid batteries. They are used in hearing aids and other small applications [38]. The possibility of a mechanically recharging through a tank of zinc pellets is under evaluation.

- Aluminum-air batteries: are non-rechargeable alkaline battery, characterized by a higher energy density of about 4000 Wh kg^{-1}, thanks to the greater lightness of aluminum compared to zinc. However, this technology is still under development [38].
- Lithium-air batteries: rechargeable batteries with specific energy of more than 5000 Wh kg^{-1}, thanks to the lightness of lithium. Li-air battery can be fabricated in aqueous or non-aqueous environment, with different constructive solutions to protect lithium from water (risk of explosion).

Table 1.3. Common MAB theoretical specific energy considering non-aqueous electrolytes. [a] Includes the mass of the oxygen that reacts in the cell. Specific energy is higher when oxygen is excluded [37].

Battery	**Theoretical specific energy[a] Wh kg^{-1}**
Li/O_2	5200
Al/O_2	4304
Ca/O_2	2990
Mg/O_2	2789
Na/O_2	1677
Zn/O_2	1090
	Practical specific energy Wh kg^{-1}
Li - ion	265
Pb-acid	30

A wide range of materials could be used for the development of the cathodes. The most performing catalysts are based on noble element such as Pt and Ru. Considering their expensive cost and their non-applicability in primary batteries several studies were carried out on non noble metal catalysts [6-10].

A large variety of precursor were analyzed and combined during the last decades. A common condition of these catalysts is the use of carbon as support to improve electric conductivity and catalytic activity. The carbon matrix is then combined with other carbon-based materials (polymer, nanotube, graphene etc…) or with metal/metal oxides particles [39]. A huge amount of results are present in the literature and it is almost impossible to report all of them. The syntheses processes are the same described for catalysts used for fuel cells application in which for instance solution synthesis, mechanical/ball mill mixing, hydrothermal synthesis, wet impregnation, chemical vapor deposition (CVD) could be combined with thermal processes. The most important catalysts class are listed below:

- *Catalysts obtained combining different carbon*. The composited catalysts show better structural and electrical properties respect single carbon materials.

Porosity, surface area and electronic conductivity are fundamental since directly affect the electron conductivity, the catalytic site distribution and the ionic/electronic transport phenomena. Like for FC cathode applications, the mesoporous structure is to be preferred since it retain electrocatalytic active sites with uniform distribution and shorter the conducting paths of ions and electrons. Combination of carbonaceous materials as carbon nano fiber, quantum dots, carbon nanotube, carbon aerogel and graphene belong to this category [36].

- *Composites of carbon-doped with heteroatom*. This type of materials are made combining carbon supports like carbon fiber, nanotube, carbon aerogel/xerogel and graphene with heteroatoms such as nitrogen (N), boron (B), or phosphorus (P). Generally dicyanamide is used as N source, boric acid as B source and phosphoric acid as P source. Heteroatom(s)-doped carbon composites improves ORR performance by creating more ORR active sites and more conductive pathways. If ordered mesoporous carbon (OMC) is used as carbon support, in alkaline media with a doping level lower than 1%, the ORR activity of this heteroatom increase following the order N-OMC < P-OMC < B-OMC [40].
- *Composites of carbon with oxides*. Metal oxides show promising activities for ORR/OER (oxygen evolution reaction OER) however the performance are limited from their low electrical conductivity, self-passivity and corrosion which decrease the number of active sites [41]. To overcome this issue metal oxide are combined with carbon precursor [42]. Before talking about perovskite and spinel oxides, it is appropriate affirm that simply cobalt, manganese and ruthenium oxides combined with carbon have been used to synthesized bifunctional active catalyst active toward ORR/EOR. Co_3O_4 combined with rGO or with only carbon has showed specific mass capacitance of 14000 and 2000 mAh gr^{-1} respectively (mass calculated based on the mass of carbon) while α-MnO_2 on carbon reaches 2000 mAh gr^{-1} [36]. Perovskite oxides have formula ABO_3 in which A is a rare alkaline earth metal cations and B is a 3d transition metal cation [43]. The peculiarity of these materials resides in their good oxygen mobility and defective structures which affect their electronic and coordination structures. The carbon support improves stability electric conductivity and energy efficiency. The combination of these synergistic effects increase the ORR overall performance. Spinel oxides show generic formula $A_xB_{3-x}O_4$ where A and B may be Mn, Fe, Ni, Co, Cu, Zn, etc. As for the perovskites, Spinel oxides are combined with conducting carbon supports to increase the electron transport phenomena [44].
- *Composites of carbon with nitrides/carbides*. Materials based on nitrides are made combining carbon support with nitrides such as TiN or CN. This strategy improves the battery rechargeability and roundtrip efficiency. In particular when TiN is combined with Vulcan XC-72 through template synthesis, the ORR catalytic activity is enhanced [45]. Graphitic carbon nitride (g-CN) is another nitride under investigation due to its heart abundance even if a good ORR activity has not been reached because of its low electrical conductivity [46]. Carbide materials are obtained combining carbon supports (Ketjenblack EC600 carbon black, nanowire, nanotube…) with tungsten carbide (WC) or boron

carbide (B_4C) through vapor deposition. Also this class, seems to show an improvement in capacity, rechargeability and ORR activity [47].

- Carbon-based binary and ternary composites. These high-performance catalysts are developed combining two or three separate components to improve the final property through the synergistic effects of each material precursor. In carbon-based multi composites, the high surface area and the porous structure come from the carbonaceous support while the electrochemical and physicochemical properties (ORR, conductivity, chemical stability…) derive from the other components. Several combination are described in literature demonstrating the beneficial effects of multi combined precursor in terms of electrocatalytic activity, durability, and MAB performances but, further investigation and improvements are required to achieve the commercialization. To mention a few examples, Lyu et al. [48] combined cobalt acetate and thioacetamide as Co and S precursor to obtain CoS_2 nanoparticles distributed in reduced graphene oxide (rGO). This work aimed to solve the carbon corrosion problems in MABs. Wu et al. [49]combined $NiCo_2S_4$ with *r*GO obtaining ORR activity higher than 20 wt% Pt/C. Regarding the ternary composites materials, usually carbon is combined with an oxide and a third component such as a metal, a second oxide or a polyelectrolyte. Zhai et al. [50], for instance, have synthesized a multi-components catalyst starting by functionalization of CNTs with poly(diallyl dimethylammonium chloride) (PDDA) used as positively charged polyelectrolyte both combined with spinel $CoMn_2O_4$. The final tri-compound, renamed $CoMn_2O_4$/PDDA-CNTs showed ORR current densities higher than Pt/C catalyst in alkaline and neutral conditions.

- *Composites of carbon with noble metals*. Although Pt/carbon composites have been widely used as fuel cell cathodic electrocatalysts showing high ORR performance, is well documented that they are not efficient for EOR. To overcame this problem, different metals such as Ru, Pd, Ir, Au, Co an Zn have been combined to prepare Pt-Alloy/carbon catalysts for metal air battery application [36]. Lu et al. [51] showed that combining Au and Pt as nanoparticles on carbon surface (40 wt % of noble metals) was possible to increase both ORR and EOR activity and obtain 1200 mAh g^{-1} as specific mass capacitance. Su et al. [52] synthesized a similar catalyst combining Co instead of Au with Pt supported by Vulcan XC 72. As result, $PtCo_2$/C catalyst tested in Mg-AB showed higher capacitance (3040 mAh g^{-1}) compared to PtAu/C nanoparticles indicating Co as a more suitable element for MAB. The presence of Co atoms near to Pt atoms increased the electron density on Pt surface leading to an improvement of ORR, OER and battery cyclability. PtZn/carbon aerogel catalyst was synthesized from Zhang et al. [53]. This material showed higher mass specific discharge capacitance (1349.5 mAh g^{-1}) compared to the Pt/carbon aerogel (1113 mAh g^{-1}) PtCo/carbon aerogel (1283 mAh g^{-1}), and Pt/carbon black (997 mAh g^{-1}) resulting promising for MAB applications. Moreover, Ir combined with deoxygenated hierarchical graphene (Ir@DHG), Ru combined with carbonized bacterial cellulose (RU/CBC), Pd with nano carbon fiber (Pd/CNF), and carbon-supported

non-platinum binary metal (Pd3Pb/C PdIr/C) showed promising ORR and EOR activity among the Noble/carbon-based catalysts [36].

- *Composites of carbon with non-noble metals*. This category was voluntarily left as last evaluation since is inherent of this thesis work. Low-cost and more available materials such as transitional metals, carbides nitrides, oxide, conducting polymers, Fe phthalocyanine…etc are replacing noble metals. Furthermore the rapid development of the chemical processes is facilitating the scale-up of this class of materials. About the non noble metal catalysts, different works are reported in literature. Yu et al. [54] demonstrated that Ta combined with vertically aligned carbon nanotubes (VACNTs-Ta) reduce the overpotential and the battery polarization. Moreover, VACNTs-Ta shoved good stability, cycling performances and ORR EOR activity with a mass specific capacity of 4300 mAh g^{-1}. The use of two noble metals usually show better performance compared to the single metal. In fact, transition metal as Fe, Co, Ni, Cu and Mg were combined in carbon composite materials MABs exploiting their synergistic effect. Chen et al. [55] synthesized Co-Cu bimetallic nanoparticles supported on graphene (CoCu/G). The catalyst showed higher mass specific discharge capacitance (14821 mAh g^{-1}) compared to the two separated metallic/carbon catalysts (Co/G and Cu/G). Kwak et al. [56] performed a similar work combining Fe and Co with CNT (FeCo/CNT) for Li-AB applications. The catalyst demonstrated higher capacitance 3600 mAh g^{-1}) than virgin CNTs (1276 mAh g^{-1}) indicating superior ORR/EOR performances. Moreover, the combination of Cu with Fe on Kentjen carbon black significantly increase the number of catalytic sites resulting in improvement of ORR activity [57]. Huang et al. [58] encapsulated Co and Ni nanoparticles in carbon nanofibers (CoNi/CNFs). The encapsulation suppressed the aggregation increasing the number of active site available for ORR and EOR with further improvement of the electrocatalytic activity. Last but not least, ternary and quaternary composites materials like $FeNi_3$@GR@Fe–NiOOH, Co_3O_4/Ni/C, Fe–Fe_3C/CNFs, showed promising ORR and EOR results for MABs applications in terms of capacity, efficiency and cycling stability.

Table 1.4 contains a comparison between a series noble and non noble bifunctional catalysts tested in different MAB configurations. In terms of durability, non noble metals catalysts show higher performance compared to noble metal-based catalysts. This behavior is due to the formation of efficacious nanostructures which interact strongly with the carbon supporting materials.

Table 1.4. Electrochemical properties of bi-functional noble and non-noble metals catalysts tested in MABs [36].

Catalyst	Maximum Capacity [mAh g^{-1}] (Current Density) [a mA g^{-1}] [b mA cm^{-2}]	Potential range [V]	Cycle number (Current Density) [a mA g^{-1}] [b mA cm^{-2}] (Upper-limit Capacity) [mAh g^{-1}]	Electrolyte	MAB type	Ref.
BI-FUNCTIONAL NOBLE METAL CATALYSTS						
40 wt% Pd/C	855 (70a)	2.0–4.3	10 (70a) (–)	1 M $LiPF_6$ in PC	rLAB	[59]
10 wt% Pt/GNS	1200 (70a)	2.0–4.8	20 (100a) (720)	1 M $LiPF_6$ in EC:DMCd (1:1 v/v)	LAB	[60]
20 wt% $Pt_{51}Au_{49}$/C	1329 (0.12b)	2.0–4.5	1 (0.12b) (240)	1 M $LiPF_6$ in EC:DMCd (1:1 v/v)	LOB	[61]
20 wt% $PtCo_2$/C	3040 (100a)	2.0–4.6	5 (100a) (–)	1 M $LiClO_4$ in PC:DMEe (1:2 v/v)	LAB	[52]
Pt/CNTs/Ni	4050 (20a)	2.0–4.2	80 (400a) (1500)	1 M LITFSI in TEGDME	LAB	[62]
BI-FUNCTIONAL NON NOBLE METAL CATALYSTS						
Fe–N/C	731 (100b)	-	-	6 M KOH	ZAB	[63]
CoCu/graphene	14’821 (200a)	2.5–4.5	122 (200a) (1000)	1 M LiTFSI/TEGDME	rLOB	[55]
CoNi/CNFs	8635 (200a)	2.0–4.5	60 (200a) (1000)	0.5 M LiTFSI/TEGDME	rLOB	[58]
FeCo/CNTs	3600 (250a)	2.4–4.5	50 (100a) (1000)	1 M LiTFSI/TEGDME	rLOB	[56]
Fe–Fe_3C/CNFs	6250 (200a)	2.0–4.3	41 (300a) (600)	1 M LiTFSI/TEGDME	rLOB	[64]
Co_3O_4/Ni/C	14’830 (400a)	2.0–4.3	48 (100a) (2000)	0.1 M $LiClO_4$/DME	LOB	[65]
Ta/CNTs	4300 (200a)	2.0–4.5	65 (200a) (1000)	1 M LiTFSI/TEGDME	rLOB	[54]

1.4 ORR Catalysts overview

An electro-catalyst is a material able to increase the electrochemical reaction speed. The catalyst performs its function by decreasing the cell overpotential at high values of exchange current density. It can operate with two different mechanisms:

- increasing the Exchange current density to accelerate the chemical reaction without modifying the reaction mechanism;
- changing the normal reaction mechanism by reducing the charge transfer coefficient [66].

Fundamental requirements in order to be classified as electrocatalyst are high catalytic activity and electronic conductivity [21].

1.4.1 Anodic catalysts for DEFC

The anode catalyst should exhibit high selectivity towards the CO_2 formation. The main difficulty is break the C-C bond in the ethanol molecule. In relation to the used catalyst, the ethanol oxidation reaction can proceed towards the formation of acetaldehyde or acetic acid (**Equations 1.4 - 1.5**) with a subsequent reduction in cell efficiency [5].

The ethanol oxidation reaction (EOR) is a slow kinetic process and noble catalysts are used to overcome this problem. Pt-based catalysts are the most widely used for the EOR catalysis. In this application, Pt is dispersed on a carbonaceous support with high surface area to reduce the overall catalyst loading. The use of a single noble metal catalyst result in high production of acetaldehyde and acetic acid with low CO_2 formation [21,67]. The catalytic activity and the selectivity toward CO_2 formation increased by additing a second noble element in catalyst formulation. In fact, the addition of Ru or Sn (PtRu/C, PtSn/C) results in an overall performance improvement even if the complete ethanol oxidation into CO_2 is not achieved [68–70]. As an alternative, Palladium (Pd) based catalysts have proven to be a good substitute to platinum in terms of activity towards the EOR. Furthermore, studies focused on the synthesis of bimetallic catalysts demonstrated even for the Pd that the presence of a second metal such as Ru (PdRu/C) improves the catalyst activity [71].

1.4.2 Aluminium as anodic catalysts for MAB

The rechargeable Al-air battery are very promising electrochemical devices. The use of Al implies a series of advantages. Is one of the most abundant element (the fourth) and is almost fully recyclable. Compared to Zn, which is another widely used catalyst in MABs, Al is cheaper in terms of weight and produce more ampere-hour. When electrochemical recharging is not possible, the Al anode can be replaced mechanically with a new one [72]. Unfortunately Al shows also some drawbacks. Primarily, Al tends to form an oxide film layer on the surface when it is placed in contact with aqueous solution or air. The presence of the oxide film protects the material from the corrosion but at the same time slows its dissolution and considerably reduce the extractable energy. Apart anode corrosion, aluminium battery suffer from high self-discharge rate and sluggish discharge products [38]. Although Al may seems unattractive as anodic material, the batteries built with this element exhibit good theoretical performance in terms of cell voltage in alkaline electrolyte (2.4 V – **Equation 1.6**) an energy density (8076 Wh/g). The use of gelled electrolytes prepared from KOH/NaOH concentrated solution limit the problems described previously and increase the battery performance. However the Al self corrosion (**Equation 1.7**) cannot be neglected and is fundamental to enhance the aluminium oxidation rate (**Equation 1.8**) to

avoid the auto-consumption of Al through spontaneously generation of H_2. This undesired reaction decrease the coulombic efficiency.

$$4Al + 3O_2 + 6H_2O + 4OH^- \rightarrow 4Al(OH)_4^- \quad \text{Equation 1.6}$$

$$Al + 3H_2O + OH^- \rightarrow Al(OH)_4^- + H_2 \uparrow \quad \text{Equation 1.7}$$

$$Al + 4OH^- \rightarrow Al(OH)_4^- + 3e^- \quad \text{Equation 1.8}$$

$$Al(OH)_4^- \rightarrow Al(OH)_3 + OH^- \quad \text{Equation 1.9}$$

Furthermore, the oxide layer present on the Al surface generates a polarization effect when it is under current load. As a negative result, the effective cell potential decreases compared to the theoretical value. The addition of doping element as Ga, Sn, In or Mg in the aluminum alloys which act as corrosion inhibitors, have shifted the potential into more negative value with further reduction of the for Al dissolution overpotential [73].

1.4.3 Catalysts for ORR

Oxygen reduction reaction (ORR) is one of the most fundamental reaction that takes place in life processes such as biological respiration, in oxygen sensor and electrical converting system like fuel cells and metal-air batteries. To be used in real applications, ORR catalysts require 4 fundamental properties [74]:

- High reactivity of active sites;
- Large density of active sites;
- Efficient transfer of electrons and reagents;
- Good durability in electrochemical devices.

The oxygen reduction reaction that occurs at the cathode shows a sluggish kinetic slower than the oxidation process that occurs at the anode. Due to this problem the cathode require a high amount of catalyst. Nowadays platinum remains the most performing catalyst active toward ORR. However, its hypothetical demand for large-scale application such as the development of electrical vehicles equipped with fuel cell, is not economically sustainable [75,76]. The infographic summarized in **Figure 1.6** shows the low Pt annual production (referred to the years 2016 and 2017), its limited world distribution and the main few companies that manage the business.

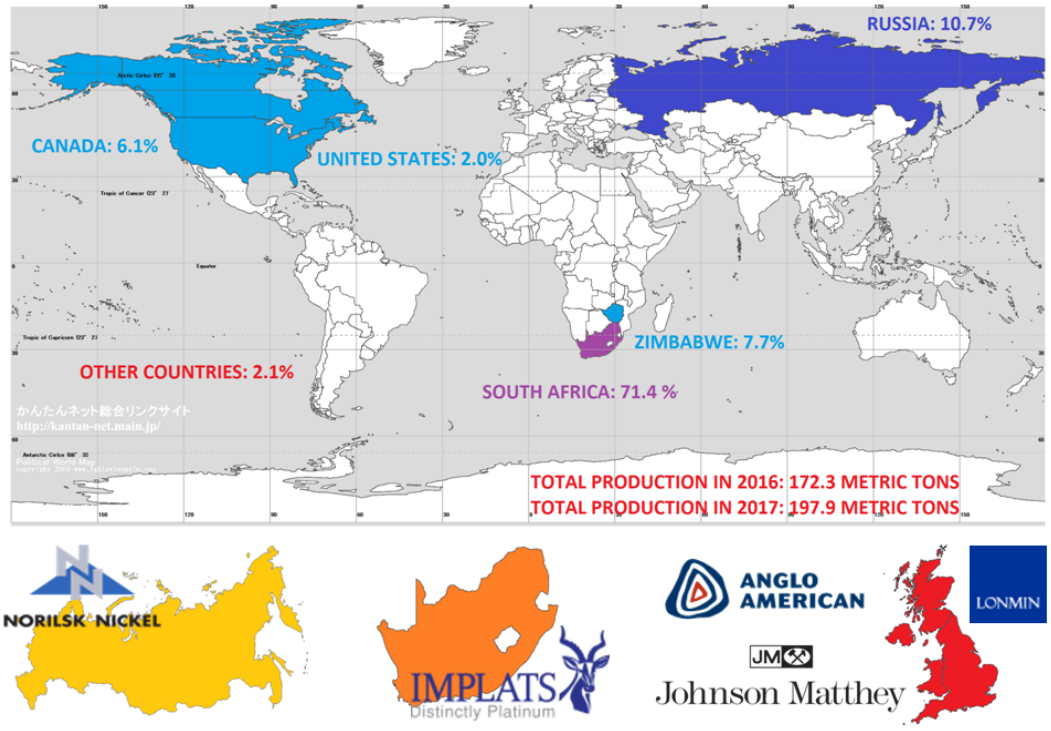

Figure 1.6. Pt infographic – Total production in 2016/2017 – Pt world distribution – Dislocation of the companies that manage the Pt market.

To solve this problem different studies on cheaper and possibly more active alternative materials have been carried out since the 1960s. Two different research direction were carried out: the first one relative the study of catalysts with low platinum metal group (PMG) content [77,78] and the second one focused on the development of non noble metal (NNM) electrocatalysts. To obtain the best future commercialization result, NNM catalyst seem to be the most promising solution [79].

In commercial catalyst, Pt is uniformly dispersed as nanoparticles on carbon support with high surface area. In this configuration the Pt exposed surface is greater respect the unsupported catalyst and lower Pt loading is required [80]. A low PMG loading catalyst can be prepared decreasing the amount of noble metal on the carbon support through the implementation of new synthesis methodologies. The most used carbon supports are carbon black, carbon nanotube, multiwalled carbon nanotube, carbon nanofiber, metal-organic framework, graphene etc. [81–83]. Alternatively, the deposition of a platinum monolayer on metal nanoparticles support [84] or inorganic oxides support such as titanium suboxide [85] may be taken into account. Pt could be replaced by other more expensive noble elements like Pd in very lower concentration because are combined in binary systems with another transition metal (Pd-M with M = Co, Ni, Fe, Cu) dispersed on carbonaceous support [84].

The non noble metal catalysts offer different obvious advantages like low cost, easy processability, high electrical conductivity and surface area [86]. Among the several catalysts evaluated in the last fifty years, two type of materials have proved to be promising in ORR: the MnO_2 [87] based catalysts and the M-N4/C based catalyst obtained from cyclic organic macromolecules doped with nitrogen as precursor [88]. The materials studied in this thesis are part of the last category. The M-N4/C catalysts are made up of a central transition metal coordinated by nitrogen ligands (**Figure 1.7**) [83]. Among the various transition metals (M = Fe, Co, Ni, Cu, Zn), the most active are those based on iron and cobalt supported on carbon particles since their good conductivity facilitate the electrons transfer process in ORR [79,89,90].

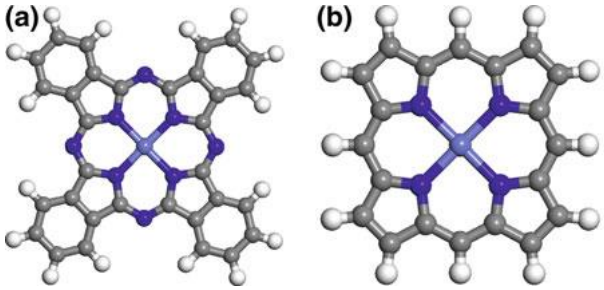

Figure 1.7. Metal phthalocyanine (a) and metal porphyrin (b). M – N - C and H atoms are respectively colored in light blue, dark blue, grey and white. Figure modified from [83]

Among the different available raw materials, Fe(II)-phthalocyanine, Fe(III)-phthalocyanine chloride, Fe(II)-acetate and Fe(II)-chloride combine with phenanthroline, aniline, pyrrole or their polymer are part of the most widely used precursors for the synthesis of the Fe-N-C catalysts [88,91].

To be active toward ORR, is fundamental the formation of a metal–nitrogen ($M–N_X/C$) and metal-carbon (M/C) ensembles through heat treatment under inert atmosphere or ball mill process [74,92]. The Active ensembles is a specific arrangement of surface atoms which promotes the reaction [93]. According to the literature, if iron precursors are used as metal sources, three types of active ensembles are formed during the NNM synthesis: FeN_4/C (**Figure 1.8 A**), FeN_{2+2}/C (**Figure 1.8 B**) and N-FeN_{2+2}/C with a fifth coordinated nitrogen (**Figure 1.8 C**) [79,94,95].

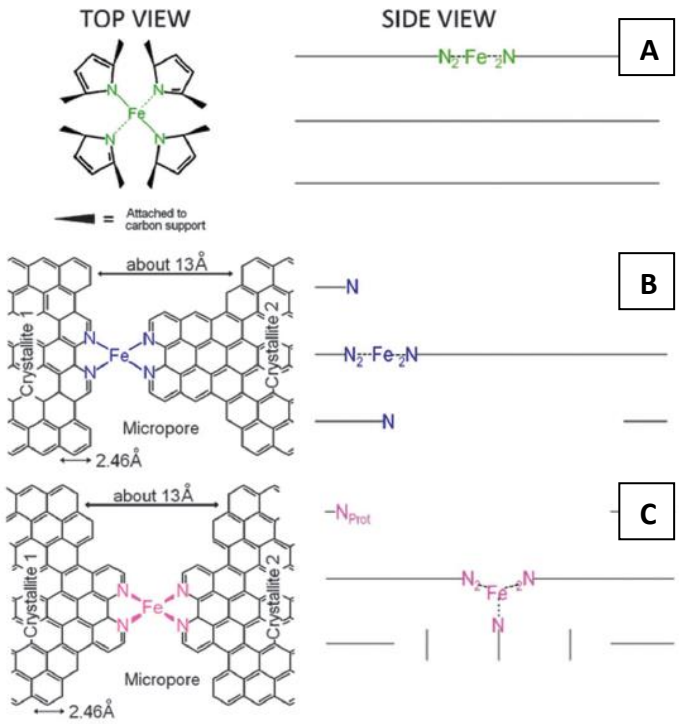

Figure 1.8. Iron active ensembles. A) FeN_4/C B) FeN_{2+2}/C and C) N-FeN_{2+2}/C with a fifth coordinated nitrogen observed using Mossbauer spectroscopy for catalyst prepared through pyrolysis of a mixture consisting of iron acetate and carbon black in ammonia. Figure modified from [83].

The amount of metal added is not related with the catalyst activity because only a relatively small amount of metal atoms are incorporated in the M–N_X/C moieties [95], and the excess remain inactive as metal oxide forms which should be eliminated.

The surface porosity is another property which play a fundamental role in ORR. The direct use of highly microporous carbon support does not increase the activity enough as the micropore formed during pyrolysis processes [96]. Without heat treatments, the low disordered carbon does not favor the anchoring of surface nitrogen. Due to this behavior, only micro and especially the mesopores generated during pyrolyzation may host active ensembles with high efficiency [97].

1.4.4 Type of NNM Synthesis

M-N-C can be synthesises through different methods. In base of the procedure developed in the last decade, it is possible to divide the synthesis methods in five groups as suggested by Osmieri [95]:

- Group 1: catalytic materials derived from the combination of carbonaceous support and nitrogen-containing molecules;

- Group 2: catalytic materials derived from polymerization of nitrogen-containing polymer;
- Group 3: catalytic materials obtained from sacrificial synthesis methods (SSM) with silica template and organic precursors;
- Group 4: catalytic materials obtained from metal-organic frameworks (MOFs);
- Group 5: catalytic materials obtained from MOFs and other additional precursors.

Since this division is not a universally standard, groups 4 and 5 will be described combined because they both refer to the MOF category.

Group 1

In this type of synthesis, carbon, nitrogen and metal derive from different precursor. The metal is introduced through the use of inorganic salts such as chlorides, acetates, sulphates and nitrates. The use of a salt precursor rather than another one may affect the final catalyst performance [83-85]. The carbon-based materials play a fundamental role as high surface and high conductive support. In generally carbon black, carbon nanonetwork, nanotube, mesoporous carbon and graphene are used for this application as previously described. The Nitrogen molecules could be introduced through a variety of precursors. Among them, the most investigated N-containing molecules were those able to form solution complex with metal ions like 1,10-phenanthroline, 2,20-bipyridine, 2,4,6-tris(2-pyridyl)-1,3,5-triazine (TPTZ), 2,3,5,6-tetra(2-pyridyl)pyrazine (TPPZ), as well as cyanamide [78], and dicyandiamide, hexamethylene diamine, and urea [95]. Metallic N-containing macrocyclic like phthalocyanine and porphyrins are often used as described in **Paragraph 1.4.3**. In some experiments, NH_3 was used as direct gaseous source of nitrogen [98] or combined with other N-precursors [77,99].

Regarding the processes, a generic synthesis scheme is showed in **Figure 1.9**. The precursor are mixed by impregnation, mechanical mixing in mortar or through ball mill. The mixture is then thermally treated in pyrolysis furnace which is the fundamental step since it provides the required energy to incorporate N and M atoms in the carbonaceous matrix. To form active and stable ORR active sites, temperature comprised between 700 and 1100 °C [100] are recommended depending on the starting precursors. Usually, perform two heat treatment on the catalyst mixture increase the overall activity performance [101,102]. Acid leaching treatment are sometimes performed between the two pyrolysis or at the end of the last heat treatment to remove metallic oxide not embedded in the carbonaceous matrix [95].

Group 2

In this methodology part of the carbon and nitrogen atoms may come from polymer. Several carbon supports described previously for the catalysts belonged to group 1 may be used in addition to the polymer macromolecules. Among different studies, macromolecules as polyaniline (PANI), polypyrrole (PPY), polythiophene [103] and polyphenylenediamine [104], have proven to be the best solution for synthesis of M-N-C catalysts thanks to their excellent characteristics in terms of electronic conductivity low cost and redox properties [105].

Generally the mixing of the precursor is carried out in solution and the polymerization began by addition of a polymerizing agent which is usually an oxidant such as $(NH_4)_2S_2O_8$, $FeCl_3$, H_2O_2. The chain propagation occurs by radical mechanism. The general process consist of the same steps described for group 1 and **Figure 1.9** (considering N containing polymers) is also valid for describe the method to obtain this class of materials. An alternative to the classic process was proposed by Liu et al. [106] producing nanofiber covered by polyacrylonitrile in dimethylformamide using electrospinning. The nanofiber were then impregnated with metal salts and thermally treated under NH_3 atmosphere. The use of NH_3 as gaseous N-precursor or adding other solid/liquid N-precursor always results in an improvement of the catalyst activity. Regarding the type of metal used in the formulation of the catalyst, iron and cobalt have always proved to be the most promising. Oh and Kim [107] compared this two metals using PPY and ethylenediamine as N precursor. It was discovered that the presence of Fe improves durability thanks to the formation of graphitic-N groups which are more stable in the acidic medium respect to other types of N-bonding. On the other hand, Co showed an improvement of the ORR activity increasing the overall N content of the catalyst. Other studies present in literature demonstrate that a combination of the two metals further increase the catalyst performance [108].

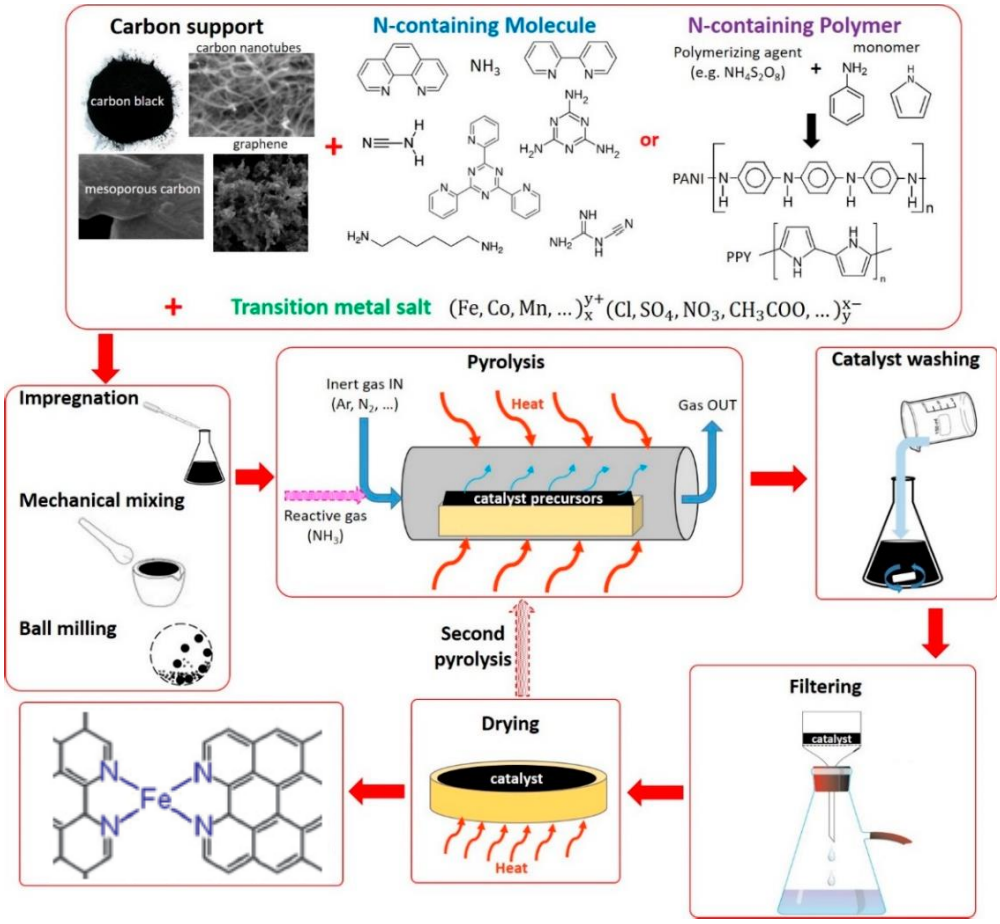

Figure 1.9. Synthesis scheme relative to the materials belonging to groups 1 and 2. Figure modified from [95].

Group 3

In this type of synthesis the idea is to use a hard template agent like porous silica to negatively replicate its structure after its incorporation in the mixed catalysts precursors. Generally the mixing is carried out through standard methods such as wet impregnation [31], evaporation [109] ball milling [110] or polymerization around the template support [111]. The process is fulfilled after a heat treatment at high temperature followed by acid leaching with diluted HF solution (5-10 %). The heat treatment is performed at high temperature and inert atmosphere like in the methods described in group 1 and 2 to form the M–N_X/C active sites. A final acid leaching is mandatory to remove the template. Although HF is a strong and dangerous acid, it allows the effective removal of silica preserving the M-N-C catalyst. **Figure 1.10** represents this process method. As N-containing precursor, a wide range of molecules can be used like for the other methods describe previously (N- containing polymers, organic molecules and metallic macrocyclic compounds).

The hard template method may be used with carbonaceous support combined with metal salts and nitrogen precursor or directly without carbon support since the silica could provides the required porous final structure. Furthermore, the porosity of the final catalyst can be controlled using directly different porous silica or varying some process parameters during its preparation phase (temperature, reaction time, surfactant type and concentration).

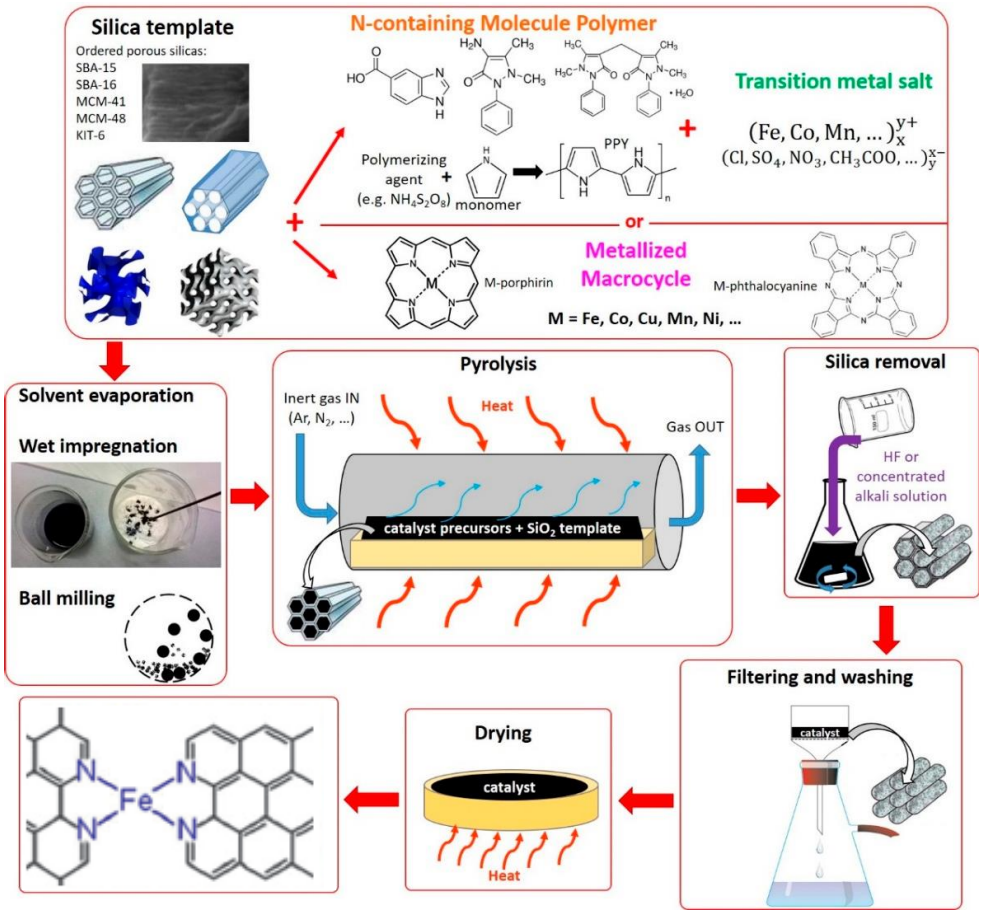

Figure 1.10. Synthesis scheme relative to the materials belonging to groups 3 obtained through sacrificial synthesis methods. Figure modified from [95].

Groups 4 and 5

The metal-organic frameworks (MOFs) are defined crystal structure with high volume and surface area due to the presence of micropores [112]. They have different applications in gas storage, energy storage, catalyst synthesis and drug delivery. They are synthesised dissolving metal-containing unit (e.g. Zn, Fe, Co chloride) with organic linker (e.g., methylimidazole, triazolate, and tetrazolate) which arrange themselves in ordered framework during the synthesis growth phase. Water, ethanol, methanol, and dimetilformammide may be used as

solvent. The type of solvent and its chemical properties affect the MOFs synthesis.

The use of MOFs for the preparation of electrocatalysts active toward ORR is very recent. The intensive research in MOFs for ORR started at the Argonne National Laboratory in 2010 when Liu et al. [113,114] synthesised a cobalt zeolitic imidazolate framework (ZIF) derived carbon catalyst through an easy and cheap synthesis process fulfilling the ORR requirements. From that moment this type of MOFs became the most studied for the synthesis of M-N-C electrocatalysts. In these years, among different metal and ligand precursor combination, only MOFs derived catalysts containing Fe or Co have shoved high ORR activity due to the formation of FeNx and CoNx active ensembles sites [115]. Furthermore, the incorporation of both metals to produce a bimetal Co-Fe MOF showed better performance respect MOFs containing only one metal. If the MOFs is directly used as M-N-C catalyst as describe until now, their synthesis belong to the group 4. Otherwise, if the MOFs is combine with other N or M containing precursor or other carbon support, their synthesis belong to the group 5. In fact, MOFs may be used as support materials as described above for group 1 and 2 since they possess a highly porous structure. M-containing and N-containing precursor mixture combined with MOFs provide the formation of catalysts with high surface area after heat treatment [116,117] enhancing the accommodation of active ensemble sites and improving the mass transfer. Generally, ZIF-8 is preferred as MOF, because Zn provides high surface area and increase the microporosity, due to its sublimation during the heat treatment processes [86]. Fe and Co are usually introduced with metal salts precursors. The combination is carried out trough ball mill, electrospinning deposition, hydrothermal synthesis or synthesis in liquid solution. Then the process may continue following heat treatment and acid leaching as showed for the materials belonging to the group 1 and 2. These synthesis methods are showed in **Figure 1.11.**

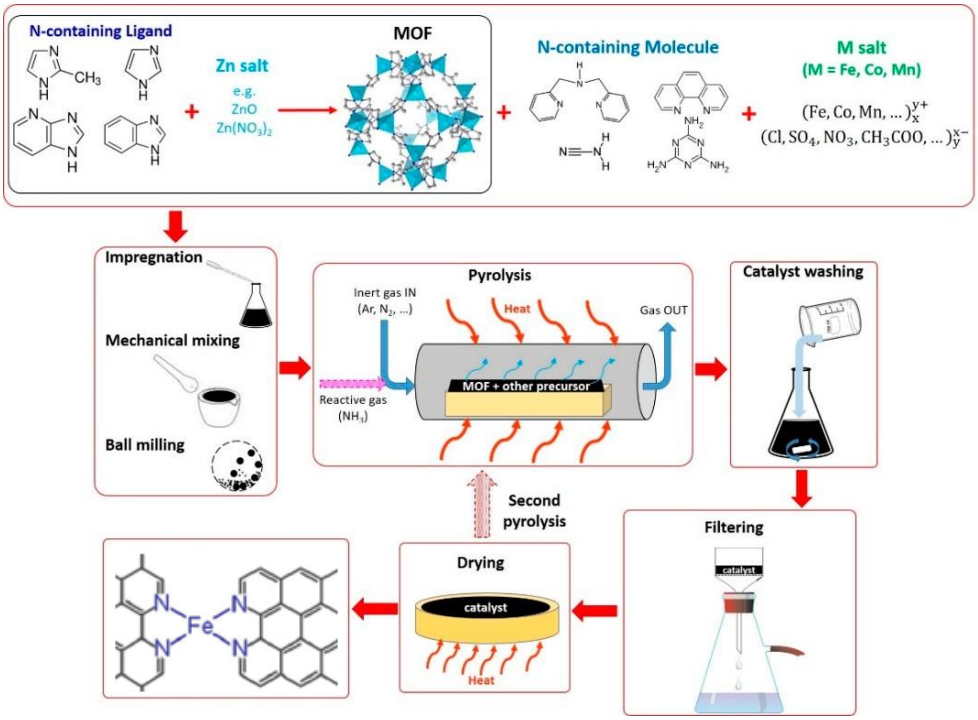

Figure 1.11. Synthesis scheme relative to the materials belonging to groups 4 and 5. Figure modified from [95].

1.4.5 Catalysts for ORR studied in this thesis

This thesis was focalized in the study and optimization of two synthesis regarding the combination of Fe(III)-phthalocyanine-chloride with Basolite 1200 (Zif-8) as organic framework support and Fe(II)-phthalocyanine with Vulcan XC 72 as carbon black support. The first material was prepared through hydrothermal synthesis followed by pyrolysis processes with intermediary acid leaching. The second material was obtained through mechanochemical mixing in ball mill. The molecular structures of the catalyst precursor are showed in **Figure 1.12**. Compared to what was described above, the synthesis refer to group 5 and group 1 respectively.

In this project Fe was preferred to Co since the Fe-phthalocyanine precursor is less toxic. **Table 1.5** summarizes the best result of catalysts obtained combining iron with MOF and tested in alkaline conditions. These values present in literature refer to December 2017 [86].

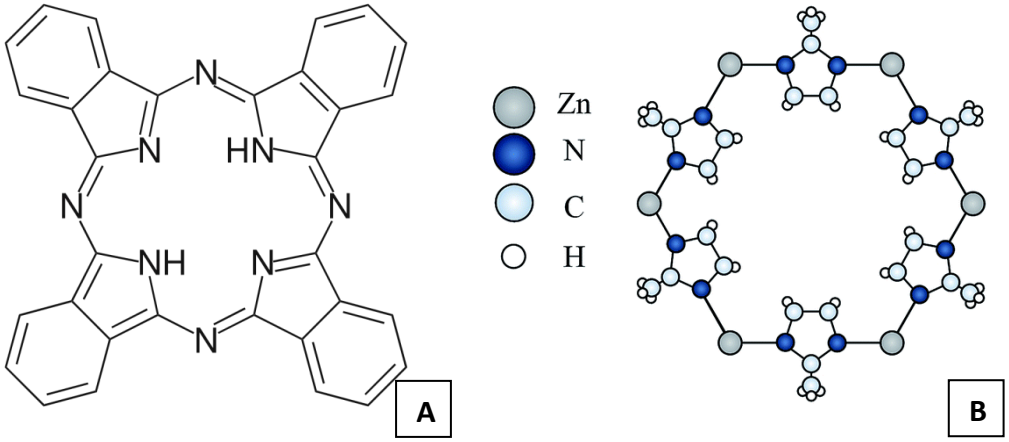

Figure 1.12. A) Phthalocyanine macromolecule structure. B) Basolite 1200 (Zif-8) macromolecule structure

The experiments performed in this thesis were focused on the synthesis optimization of a catalyst based on a combination of Zif-8 with iron phthalocyanine. The goal was to increase the overall performance of the final catalyst considering the minimum economical efforts in terms of process operation. A combination of experiments performed following the design of experiment procedure combined with activity (RDE) and surface analysis (XPS and BET) were carried out to determine the best process parameters.

Metal phthalocyanine are molecular complex structurally related to the family of the porphyrin complex present in nature as part of enzyme involved in the management of oxygen (oxidation, reduction and transport) and destruction of peroxides [118]. These macromolecular structure are used for different technological application including nonlinear optical design, semiconductor, information storage devices, liquid crystal and of course in industrial catalysis [119–122].

In the catalysis field are used in different oxidation and reduction processes. About the oxidation processes, the phthalocyanine complexes are used in the oxidation of alkanes aliphatic and aromatic C−H bonds, methane, olefins, phenols, alcohols and sulfur compounds. Regarding the reduction process these macromolecules could be used for example to reduce nitrite and nitrate but the most important application is surely the ORR. In fact, metal macrocycles such as Fe- and Co-based materials are the major exponents as non noble metal catalyst for ORR in PEMFC [77,79], AAEMFC [123,124] and Li-air battery [125].

Metals	MOFs	Other precursor	1st heat treatment	Acid-leaching	2nd heat treatment	Electrolyte and rpm	Onset potentials vs RHE	Half wave potentials vs RHE	Ref.
Fe, Zn	Zif-8	Iron acetate(II) and 1,10-phenanthroline	1050 °C, Ar	-	1050 °C, NH3	0.1 M KOH, 1600 rpm	1.03 V	0.87 V	[126]
Fe, Zn	Fe-Zif-7	-	1000 °C, N_2	yes	-	0.1 M KOH, 1600 rpm	1.04 V	0.87 V	[127]
Fe	IRMOF-3	-	800 °C, Ar	-	-	0.1 M KOH, 1600 rpm	0.93 V	0.78 V	[128]
Fe	Mil-100	5-aminotetrazole	800 °C, Ar	Yes	-	0.1 M KOH, 1600 rpm	0.92 V	0.77 V	[129]
Fe	Mil-88B-NH	-	900 °C, Ar	-	-	0.1 M KOH, 1600 rpm	1.03 V	0.92 V	[130]
Fe, Zn	Zif-8	Dicyandiamide	900 °C, N_2	Yes	700 °C, N_2	0.1 M KOH, 1600 rpm	0.82 V	0.78 V	[131]
Fe, Co	Co(PTP)	Iron acetate(II) and Dicyandiamide	1000 °C, N_2	yes	1000 °C N_2	0.1 M KOH, 900 rpm	1.02 V	0.88 V	[132]

Table 1.5. Summary of synthesis and ORR activity of Fe-MOFs catalyst in alkaline electrolytes [86]

Among different process combinations involving liquid-phase synthesis, heat treatments, sacrificial synthesis and impregnation, it is possible to affirm that studies related to the mixing at the solid-state level of Vulcan with iron phthalocyanine through ball mill are recently and very limited. Vulcan carbon is a carbon black powder with high conductivity and surface area ranging from 200 up to more than 600 $m^2\ g^{-1}$. It is widely used in the development of ORR catalyst including those based on precious metals like Pt/C. This catalyst support is very cheap since is often generated as a waste product from other chemical processes. Zhang et al. [133] demonstrated in 2015 an high ORR activity of this mixture without performing a ratio optimization between the raw materials and obtaining at the end some only some mg of catalyst. Furthermore, any fuel cell or metal-air battery test has not been made since the author focalized his efforts in the study of high active polymerized phthalocyanine [134]. With the combination of Fe-phthalocyanine with carbon black E600 they obtained more than 40 A g^{-1} as mass activity at 0.9 V and 0.91 V as half-wave potential through RDE analysis in alkaline solution.

According with this introduction, the work of this thesis was oriented in the study of the catalyst mixture composition followed by ink optimization, testing in ethanol fuel cell and metal-air battery. Several studies have been carried out combining different heat treatment after the ball mill process. Moreover, all the experiments were performed paying attention to the reproducibility of the tests and evaluating the final amount of the produced catalyst.

1.5 Fundamental mechanistic understanding of ORR

The ORR electrochemical mechanism on noble and non noble catalysts in acidic or alkaline environmental is still under investigation. Although different solutions have been described for Pt-based noble catalysts, enormous efforts to describe the ORR mechanism on non-noble catalysts were made. Actually, the chemical processes on non noble catalysts is still partially unknown. Below are summarized the ORR fundamental mechanisms present in literature. The oxygen reduction can follow two different pathway: the 4 e^- pathway and the undesired 2 e^- pathway. With the 4 e^- pathway water and hydroxide ion are respectively formed in acidic and alkaline solution. The 2 e^- pathway involves the transfer of two electrons, in which oxygen is first reduced in hydrogen peroxide in acidic solution (**Equation 1.11 – 1.12**) or hydro-peroxide ion in alkaline solution (**Equation 1.14 – 1.15**) [135].

Reaction in acidic environmental

$$O_2 + 4H^+ + 4e^- \leftrightarrow 2H_2O \qquad \text{Equation 1.10}$$

$$O_2 + 2H^+ + 2e^- \leftrightarrow H_2O_2 \qquad \text{Equation 1.11}$$

$$H_2O_2 + 2H^+ + 2e^- \leftrightarrow 2H_2O$$ Equation 1.12

Reaction in alkaline environmental

$$O_2 + 2H_2O + 4e^- \leftrightarrow 4OH^-$$ Equation 1.13

$$O_2 + H_2O + 2e^- \leftrightarrow HO_2^- + OH^-$$ Equation 1.14

$$HO_2^- + H_2O + 2e^- \leftrightarrow 3OH^-$$ Equation 1.15

In the specific case of Pt, which is the most noble metal studied for ORR applications, the reaction mechanism is divided in well known elementary steps. Considering M as the active Pt site on the catalyst surface, the following mechanism is suggested for ORR in alkaline media [136]:

$$M + O_2 \leftrightarrow MO_2$$ Equation 1.16

$$MO_2 + e^- \leftrightarrow MO_2^-$$ Equation 1.17

$$MO_2^- + H_2O \leftrightarrow MO_2H + OH^-$$ Equation 1.18

$$MO_2H + e^- \leftrightarrow MO + OH^- \text{ or } MO_2H + e^- \leftrightarrow MOOH^-$$ Equation 1.19

In acidic media equations 13-14 are replaced with Equation 1.20:

$$MO_2 + H_3O^+ + e^- \leftrightarrow MO_2H + H_2O$$ Equation 1.20

With idea to investigate more in depth, further studied were made to understand the highest activity of platinum and non noble metal in alkaline solution respect acidic solution. Although the detailed process description is not part of this context, it is fundamental to understand what is shown in **Figure 1.13** to capture the essential acidic/alkaline behavior. The picture shows the schematic formation of a double layer structure in contact with the surface of Pt-catalyst. The double-layer can be divided in two parts. The first plane, very close to the electrode, is called inner Helmholtz plane (IHP). The second plane, farther from

the surface, is called outer Helmholtz plane (OHP). During ORR, the processes in the Inner sphere (inset a) involve molecular O_2 chemisorptions on oxide-free Pt active site followed from 4 e^-/4H^+ transfer. This behavior is common in acidic and alkaline solutions. In the outer sphere (inset b) there are molecular O_2 solvated inside several water clusters. In alkaline condition, the hydroxyl ions adsorbed on the Pt surface could interact with the water clusters through hydrogen bond. This type of interaction is weaker respect the strongest chemisorption between Pt and O_2. As consequence, the water clusters are stabilized and more electrons are transferred to the O_2 molecules placed in the second outer plane. In acidic condition this behavior does not occur since hydroxyl ions are not present and as a result, ORR kinetics is not enhanced like in alkaline medium [137].

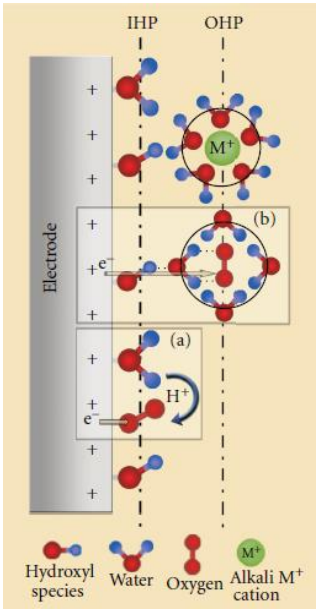

Figure 1.13. Electric double-layer structure during ORR in alkaline media. Insets (a) indicate Inner Helmholtz plane (IHP) while Insets (b) indicate outer Helmholtz plane (OHP). Figure modified from [137].

About the non noble metal catalyst, different structure and chemical reorganization take place during the pyrolysis and ball mill processes. At the end, the catalyst is composed by a complex mixture containing nitrogen-doped species surrounded by graphitic and amorphous carbon in presence of metal oxides, sulfides and carbides [102,138]. Due to this heterogeneous structure, it is difficult to identify the real active site structure/s [83,139]. Also, also the surrounding carbon structure around the M-N-C site seems to participate in the ORR through electron induction or geometric effect [140,141]. Some studies published in literature assert that the metal is not part of the catalytic center, although transition metals result useful in the formation of active nitrogen/carbon groups [93,142]. Other research streams consider the metal ions (such as $Fe^{2+/3+}$ showed in **Figure 1.14**) as a strong contributor to the active site [74,143,144]. Recently, modeling

simulation, are supporting the FeN_4 ensembles into carbon plane as the active site which adsorb and dissociate the O=O bond during ORR [35,36]. Furthermore the N_4 coordination provide a relative stable structure which is not easily removed or destroyed after acid leaching treatment or during ORR activity analysis.

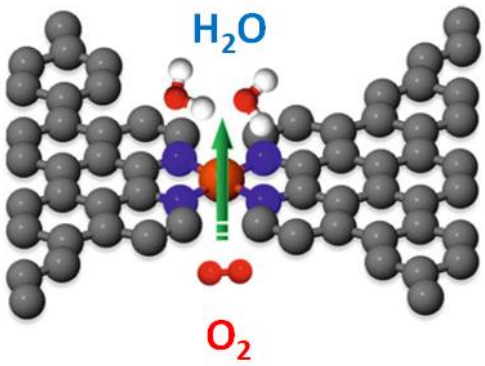

Figure 1.14. Most proposed catalytic site for ORR in FeN_4/C non noble catalysts family. Figure modified from [83,145].

As previously described for Pt catalysts, also the non noble metal catalysts show higher performances in alkaline media. Mukerjee and Ramaswamy [137] proposed a catalytic cycle regarding the mechanism of ORR on pyrolyzed Fe porphyrin macrocycles in alkaline solution (**Figure 1.15**) useful to describe a theoretical reaction pathway for the FeN_4/C catalysts family.

Although this mechanism is not confirmed, Mukerjee and Ramaswamy [137] demonstrated through ORR polarizations curve analysis that the Fe^{2+}/Fe^{3+} couple of the transition metal show higher redox potential in alkaline media. Furthermore they showed that the peroxide intermediate on the active site is more stable respect the same in acidic conditions and this behavior involves in an efficient 4 e^- pathway ORR reaction.

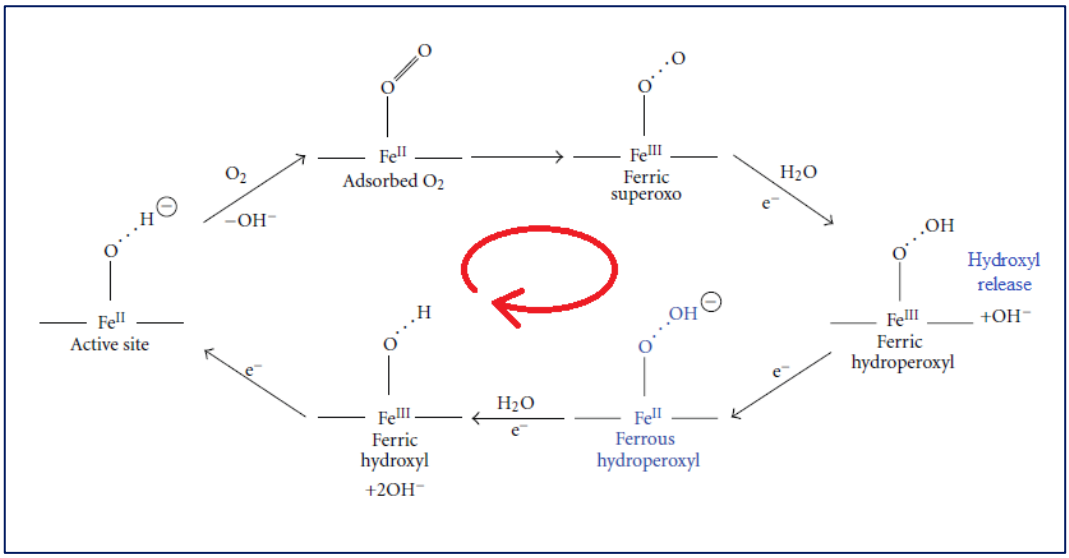

Figure 1.15. Catalytic cycle of ORR mechanism on pyrolyzed Fe porphyrin macrocycles in alkaline solution. Nitrogen atoms in FeN_4/C square planar position were omitted from the author for clarity. Figure modified from [137].

1.5.1 ORR testing

The rotating disk electrode (RDE) and the rotating ring disk electrode (RRDE) are the most important electrochemical techniques use to measure the ORR activity and the H_2O_2 production. For this application, a three electrodes cell is adopted as configuration with a rotating disk electrode [147] used as working electrode in which the catalyst is deposited (**Figure 1.16**). The potential between the working electrode (WE) and a reference electrode (RE) is swept linearly in time while the current at working electrode is measured. The reference electrode is used to measure and control the potential applied to the working electrode, since its potential remains constant within the electrochemical cell. The counter electrode (CE) is used to close the circuit inside the cell, it ensures the transport of the current generated to the working electrode.

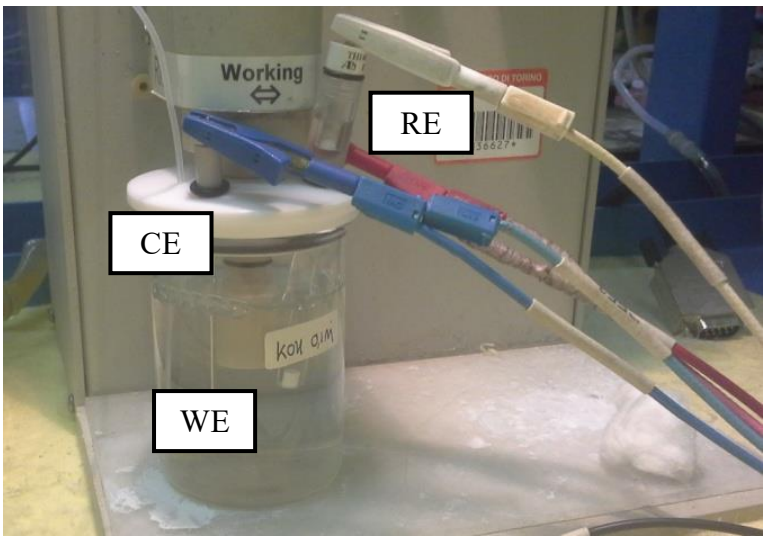

Figure 1.16. Three electrodes cell

RDE is a type of working electrode that rotates within the electrolytic solution. It is used for electrochemical measurements in three-electrode systems. Generally, the equipment consists of a glassy carbon electrode disk inserted into a cylindrical sheath of insulating material (such as Teflon). Moreover, when a Pt ring is present around the central electrode disk and works as secondary electrode, the equipment is called RRDE. The electrode rotates around its axis through an electric motor with a specific angular speed (ω) that can be varied as desired (**Figure 1.17-A**). When an electrochemical reaction in heterogeneous phase occurs between a solid surface and an adjacent solution phase, an electronic transfer takes place. In general, the mass transport becomes the dominant step in dilute solution since the reaction requires the supply of reactant and the removal of products [147]. In electrochemistry, three different mass transport process occur:

- Diffusion due to a difference in the concentration gradient;
- Convection due to external mechanical energy like the RDE rotation;
- Migration due to a potential gradient coming from only the charged species [148].

The disc through the rotation attracts the fluid to the surface, dragging the solution radially from the center to the outside with a movement of the solution perpendicular to the electrode. With this define regime, the mass transport of the species is almost totally due to convection [149,150] and it is possible to describe the concentration profile with mathematical equation useful in laboratory experiments. According to the Nernst diffusion layer model (**Figure 1.17-B**), the mass transport of the reagents close to the electrode at distance δ, take place only by diffusion mechanism. In this conditions, the current density can be determined because the electrochemical reaction is kinetically controlled by mass transport.

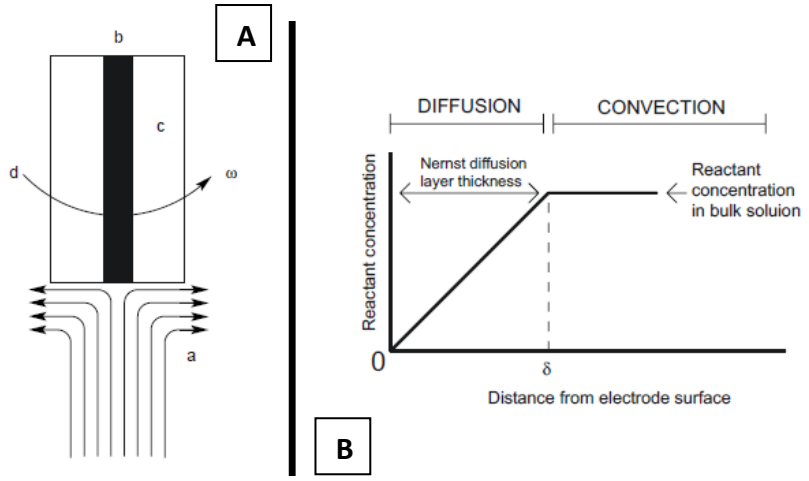

Figure 1.17. A) Solution movement caused by rotation of an RDE. a: flow of electrolyte solution; b: Glassy carbon electrode; c: RDE body; d: direction of electrode rotation. B) Representation of the Nernst diffusion layer profile model. Figure modified from [147]

The surface concentration of the reactive species is zero and the maximum limit current that could be developed is described by the Levich equation (**Equation 1.21**) [151]:

$$i_l = 0.62 \cdot n \cdot F \cdot A \cdot D_O^{2/3} \cdot \omega^{1/2} \cdot \nu^{-1/6} \cdot C_0 \qquad \text{Equation 1.21}$$

Where 0.62 is a constant valid using rad s^{-1} as rotation speed, n is the number of electrons involved in the reaction, F is the Faraday constant (96485 C mol^{-1}), A is the electrode area D_0 is the species diffusion coefficient (1.90×10^{-5} cm^2 s^{-1} for the oxygen), ω is the electrode rotation speed ν is the cinematic viscosity of the solution (0.0109 cm^2 s^{-1} for KOH 0.1 M solution) and C_0 is the reagent bulk concentration (1.20×10^{-6} mol cm^{-3} for oxygen saturated solution) [152,153].

From the **Equation 1.21** is it possible to determine the number of the electron involved in the electrochemical reaction from the slope of the line obtained plotting i_L^{-1} versus $\omega^{-1/2}$ (**Equation 1.22**):

$$n = \frac{1}{slope * 0{,}62 * F \cdot A \cdot C \cdot D^{2/3} \cdot \upsilon^{-1/6}} \qquad \text{Equation 1.22}$$

In a real system, the overall current measured at the electrode results from a combination of two components: the limit current i_L already described above and the kinetic current i_k due to the electrons charge transfer at the electrode. The total current is thus described from the Koutecky-Levich equation (**Equation 1.23**) [152]:

$$\frac{1}{i} = \frac{1}{i_k} + \frac{1}{i_l}$$ Equation 1.23

From this equation, plotting i^{-1} versus $\omega^{-1/2}$ allows to determine n from the slope and i_k from the intercept of the line. The selectivity of the reaction could be evaluated through the H_2O_2 (%) analysis. This parameter could be determined using the RRDE equipment and setting the ring potential for H_2O_2 oxidation to ca 1.2 – 1.4 vs RHE [154] [83]. The H_2O_2 (%) is obtained from **Equation 1.24**:

$$H_2O_2(\%) = 200 \cdot \frac{i_R/N}{(i_R/N)+i}$$ Equation 1.24

Where i and i_R are the current density measured respectively at the disk and at the ring. N is the ring collection efficiency and depend on the type of RRDE working electrode. From the previous equation, it is possible to determine directly the real number of electrons involved in ORR per O_2 molecule through **Equation 1.25**:

$$n = 4 - (\%H_2O_2)/50\%$$ Equation 1.25

1.5.2 Cyclic voltammetry

Cyclic voltammetry (CV) is an electrochemical technique commonly used to study the oxidation and reduction reactions of molecular species present in solution and in contact with the working electrode [155]. CV is also use to investigate the electron transfer-initiated chemical reactions and evaluate the capacitance of supercapacitors materials [156]. The analysis consists in the measurement of the current (y-axis) flowing between the working electrode and the counter electrode as a result of an applied potential (x-axis) that varies linearly over time driven by the scan rate (ν). The curves showed in **Figure 1.18** as

example are called voltammograms or cyclic voltammograms. Following the IUPAC convention, when the high potential is on the right of the x-axis, the lower curve, called forward scan, is related to the reduction of the electrochemical processes and the upper curve, called backward scan, is related to the oxidation processes. The potential is scanned in the direction indicated from the arrow. From the starting potential E1 to the switching potential E2 the potential is swept negatively. In the reverse scan direction from E2 back to E1 the potential is swept positively [157,158].

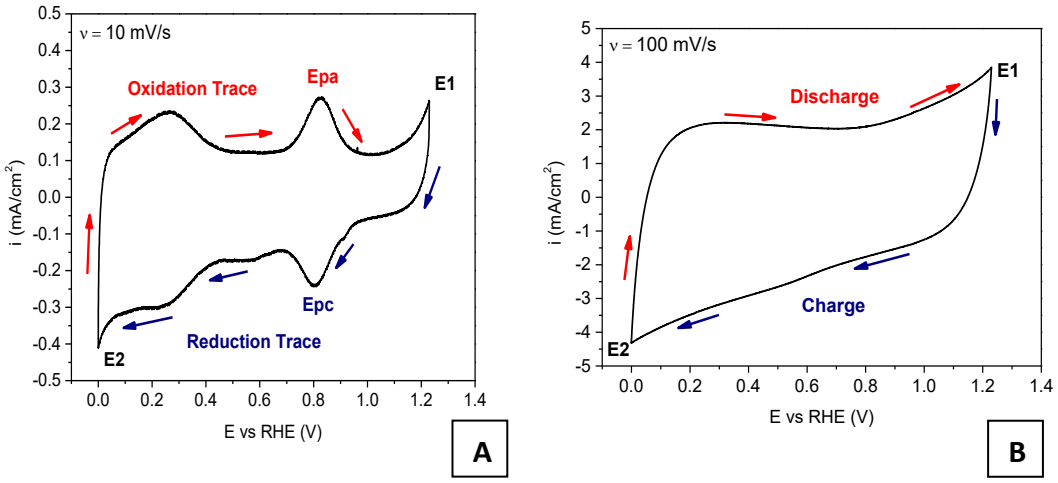

Figure 1.18. Examples of cyclic voltammograms. A) With well defined redox peaks. B) With capacitive behavior.

When reaction peaks are present and well defined, is it possible to calculate the reaction formal potential through the use of **Equation 1.26**:

$$E_0' = \frac{E_{pa}+E_{pc}}{2} \qquad \text{Equation 1.26}$$

Furthermore, if reactive peaks are not present and capacitance analysis are required, the area underlying the reduction trace is called charge capacitance while the higher area under the oxidation trace is called discharge capacitance. Considering the electrode area indicated as A, their specific values can be calculated through the use of the following **Equation 1.27**:

$$C_s(Fcm^{-2}) = \frac{1}{\nu\cdot(E_1-E_2)\cdot A}\int_{E_2}^{E_1} IdV \qquad \text{Equation 1.27}$$

1.5.3 Linear sweep and stair case voltammetry

The electroactivity of catalysts active toward ORR at laboratory scale is determined through a linear sweep voltammetry (LSV) or stair case voltammetry (SCV) in aqueous oxygen-saturated solution. The solution is kept under stirring by the rotating disk to facilitate the transport of oxygen from the bulk to the surface of the catalyst. LSV is a common measure used for the study of electrochemical systems especially when the reaction is irreversible or the cyclic voltammetry cannot provide much information [155].

The stair case voltammetry is a powerful derivation of the linear sweep voltammetry. In SCV, the potential is swept in a series of stair steps (**Figure 1.19 A**) and the current is measured at the end of each potential change (**Figure 1.19 B**) [150].

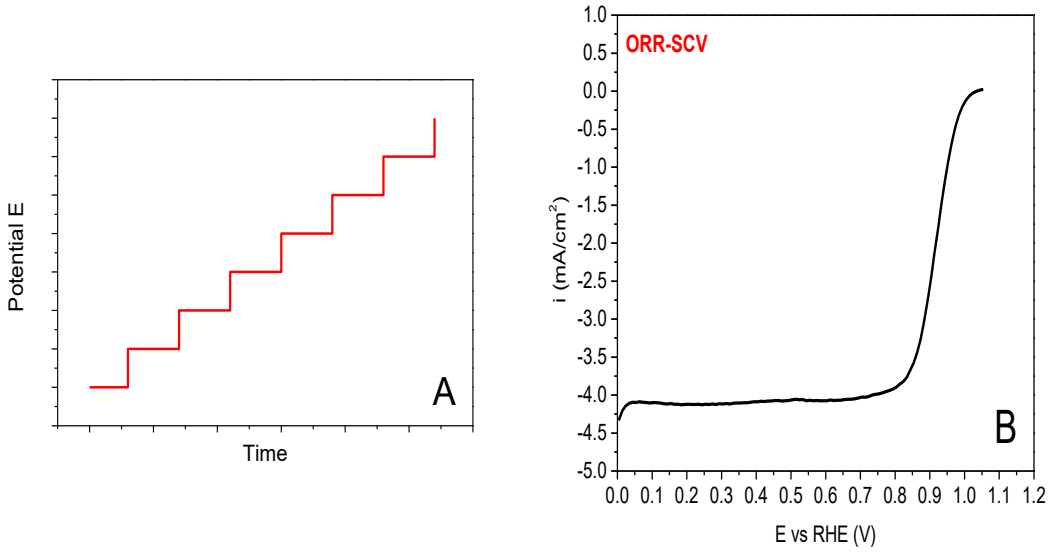

Figure 1.19. A) Stair step scan. B) ORR polarization curve resulting from SCV

When a LSV experiments is carried out, the faradic current due to the electrochemical reaction measured at the working electrode is negatively affected by the capacitive current (**Equation 1.28**). Capacitive current is due to the formation of a double electric layer with charge separation in the electrode-solution interface. This separation is caused by the negative or positive electrode state of charge, which attracts opposite ions close to itself. In LSV experiment the elimination of the capacitive current requires the subtraction of the LSV measured in deoxygenated electrolyte from the LSV obtained in oxygen saturated electrolyte [83].

$$i = i_f - i_c = n \cdot F \cdot A \cdot c \cdot \sqrt{\frac{D}{\pi \cdot t}} - C \cdot \frac{dE}{dt}$$ Equation 1.28

Where c is the oxygen concentration and C is the capacitance of the medium, n is the number of electron exchanged in the electrochemical process, A is the electrode area and D the oxygen diffusion coefficient. The time is indicated with t and the electric field with dE/dt. In SCV configuration the contribution to the current signal from the capacitive current is reduced and the current signal from the faradic current obtained from the chemical reaction is enhanced. In fact, waiting some seconds at constant potential, the dE/dt contribution of the **Equation 1.28** is reduced close to zero.

1.5.4 Theoretical background, thermodynamics and kinetic

Considering a complete reduction reaction from oxygen to water, the ORR thermodynamic electrode potential at standard conditions is 1.23 V in acidic aqueous solution (pH 1) and 0.40 V in alkaline aqueous solution (pH 14). The basic mechanism is a 4-electron reduction pathway but may involve in different intermediates depending on the quality of the catalyst and the type of the electrolyte. **Table 1.6** show the different reactions held in acidic or alkaline solution.

Table 1.6. Thermodynamic electrode potential of ORR referred to the pH of the Electrolyte

Electrolyte	pH	ORR reactions	Thermodynamic electrode potential (V)
Acidic solution	1	$O_2 + 4H^+ + 4e^- \rightarrow 2H_2O$	1.23
Alkaline solution	14	$O_2 + 2H_2O + 4e^- \rightarrow 4OH^-$	0.40

Since the application vary from fuel cell to metal-air battery, the reaction take place in different favorable pH conditions. Based on the pH of the solution, it is essential to define the potential range in which the catalyst active toward ORR are analyzed through linear sweep voltammetry. Generally, the analysis is carried out in a range comprised between 0 V and 1.23 V vs RHE. With the intention of obtain a more refined result, it is appropriate to restrict the range starting from 0.05 V and finishing at 1.2 V or, if is possible, at 0 V referred to the open circuit potential (E_{ocv}) to avoid hydrogen evolution reaction at 0 V and oxygen evolution reaction at potential close to 1.23V. The instrumental range values are determinate through the applications of the Nernst equations (**Equation 1.29**) considering the pH of the electrolyte and the type of the reference electrode used in the electrochemical cell to carry out the experiment [150]

$$E_{lower/upper} = E - 0.059*pH - E^{0}_{ref}$$ Equation 1.29

For instance, using $Ag/AgCl_{sat}$ as reference (E°=0.197V vs RHE) in a solution at pH 13 the lower and upper limit become respectively –0.914 V (considering E = 0.05 V) and 0.236 V (considering E = 1.2 V). **Figure 1.20** show a typical sigmoidal ORR polarization curve. There are three specific regions divided depending on the kinetically determining step. At high potential the reaction is under faradic control, the current density is low and the kinetic mainly depends on the electrons charge transfer. This step may be interpreted as the activation process of the reaction. At lower potentials the reaction is under mass transport control: the electrons are available, but the oxygen has reached its maximum concentration determined from the Henry law and depending from the physical condition of the system (type of solvent, oxygen partial pressure, etc.). In this step, since the oxygen concentration is constant, the current density reaches therefore a maximum constant value called diffusion limit current (i_L). In the middle of the polarization curve the process is controlled partially from the electron charge transfer and partially from the oxygen diffusion. In this step slight potential variations lead to wide current improvements [155,159,160].

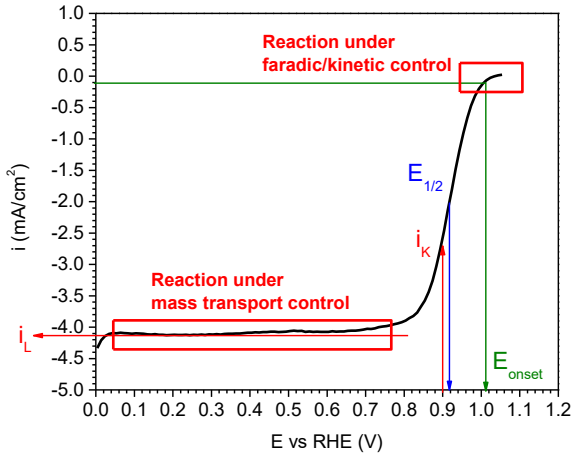

Figure 1.20. ORR polarization curve

From the polarization curve is possible derive all the parameters that could describe the catalyst performance at the laboratory scale. Concerning the graph shown in **Figure 1.20**, i_k (mA cm^{-2}) is the corrected kinetic current density, $E_{1/2}$ (V) is the half-wave potential and E_{onset} (V) is the onset potential. The kinetic current density is a measure of the electrochemical activity toward the oxygen reduction

reaction: higher is the kinetic current density, higher are the performance of the catalyst. In generally is evaluated at 0.9 V vs RHE to be closer to the kinetic region [147]. i_k is determined by subtracting the limiting current contribution from the total current i measured by the instrument through the application of the Koutecky-Levich equation (**Equation 1.30 and 1.31**) [151]:

$$\frac{1}{i} = \frac{1}{i_k} + \frac{1}{i_l} \qquad \text{Equation 1.30}$$

$$i_k = \frac{-i_l \cdot i}{i_l - i} \qquad \text{Equation 1.31}$$

i_k could be converted in the weight specific current i_m dividing it by the catalyst loading L (g cm^{-2}) deposited on the electrode surface (**Equation 1.32**):

$$i_m = \frac{i_{k(0.9V)}}{L} \qquad \text{Equation 1.32}$$

The onset potential is the potential for which the reaction products are formed [161]. For conventions is the potential evaluates at a current density of 0.1 mA cm^{-2}. The more the onset potential is shifted away from the thermodynamic potential and the higher is the overpotential. The overpotential is the distance between the thermodynamically reduction potential and the potential at which the reaction is experimentally observed. It depends from 3 different contributions:

- Activation overpotential due to the activation energy required from the electrochemical reaction;
- Concentration overpotential due to the difference among the concentration of charge-carriers between the bulk solution and the electrode surface;
- Resistance overpotential generally due to junction between different component present in the electrochemical devices.

The half-wave potential is a potential for which the current is equal to one half of limit diffusion current i_L. The evaluation of the half-wave potential is very important since it is determined graphically from the real polarization curve and not through a mathematical correction such in the case of the kinetic current. A higher half-wave potential corresponds to higher ORR activity (for a given catalyst loading). **Figure 1.21** show the best graphical procedure useful to determine the half-wave potential from the RDE experimental polarization curve.

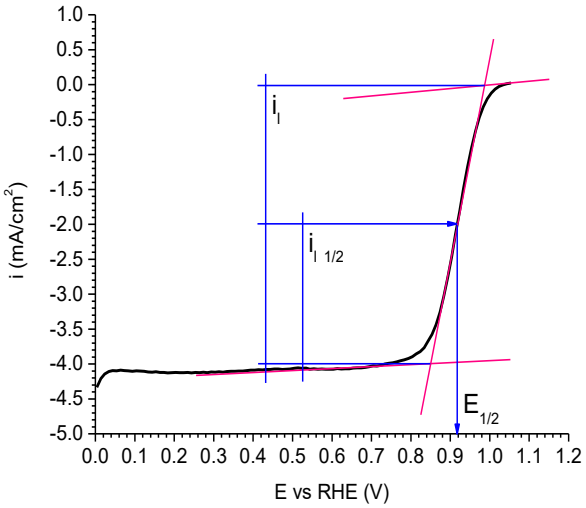

Figure 1.21. Determination of the half wave potential through graphical method

The speed of ORR is related with the exchange current density (**Equation 1.33**) since it is directly connected with the standard rate constant k^0 [150,159] which is a kinetic measure of a redox couple considering the assumption that the electrode reaction is one step and one electron process reaction (**Equation 1.34**):

$$i_0 = FAk^0C \qquad \text{Equation 1.33}$$

$$O + e^- \leftrightarrow R \qquad \text{Equation 1.34}$$

where i_0 is the kinetic current density, F is the Faraday constant, k^0 is the kinetic constant and C is the concentration of the reagent at the catalyst surface.

For the general **Equation 1.34**, the two reactions can take place in both the direction of the products and the reagents. When the reaction is at the equilibrium, the current density of the forward reactions is the same of the backward reaction and the net current density is zero. This value is called exchange current density and its magnitude determines the rapidity of the electrochemical reaction. For every type of electrochemical reaction, the exchange current density depends on the reaction, on the type of catalyst on the electrode surface.

About what was said above, is it possible relate the ORR current density with the overpotential through the Butler-Volmer equation (**Equation 1.35**):

$$I_c = i^0{}_{O_2}\left(e^{\frac{-\alpha_0 F\eta_c}{RT}} - e^{\frac{(1-\alpha_0)F\eta_c}{RT}}\right)$$ Equation 1.35

Where I_c is the current density of the reaction, i^0 is the exchange current density, α is the transfer coefficient, η_c is the overpotential of the electrochemical reaction, F is the Faraday constant, R the universal gas constant ad T the temperature in Kelvin. The transfer coefficient is the change fraction of overpotential that leads to a change in the rate constant of the exchange current density.

The exchange current density could be determined from the Tafel equation (**Equation 1.36 A-B**), which is an approximation of the Butler Volmer equation at large overpotential (with η > 118 mV). In fact, at large negative overpotentials

$$e^{\frac{-\alpha_0 F\eta_c}{RT}} > e^{\frac{(1-\alpha_0)F\eta_c}{RT}}$$

From **Equation 1.35** is possible to write:

$$i = i_0 e^{-\alpha\frac{F}{RT}\eta}$$ Equation 1.36-A

$$\eta = \frac{RT}{\alpha F} ln\, i_0 - \frac{RT}{\alpha F} ln\, i$$ Equation 1.36-B

Where

$$\text{Slope} = -2.3\frac{RT}{\alpha F}$$

$$\text{Intercept} = 2.3\frac{RT}{\alpha F} log i_0$$

From ORR polarization curve (**Figure 1.20**) is possible to draw the Tafel plot and determine its slope and the exchange current density from the intercept which

are useful for making assumptions about the reaction mechanism. **Figure 1.22** shows an example of the Tafel plot determined plotting log i_k versus E.

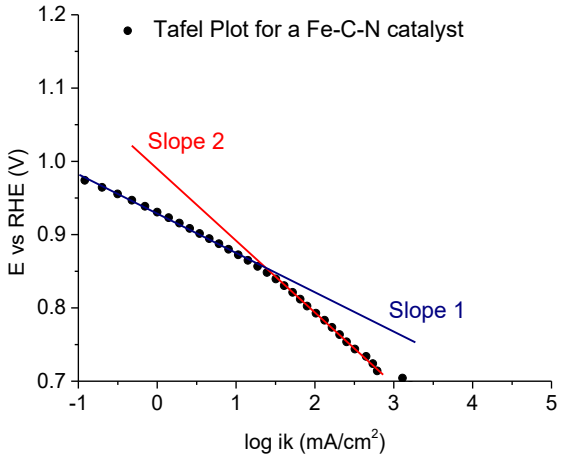

Figure 1.22. Tafel plot for a non noble metal catalyst.

All the electrocatalytic reaction should be analysed based on the kinetics evaluated by the Tafel slope. Tafel slope is kinetically always applicable, but its intercept may not always be equal to the exchange current because the Butler Volmer was derived considering an equilibrium steady state at the electrode interface. Consequently, for a simple reaction like **Equation 1.34**, it is assumed that the oxidized and the reduced species have always the same concentration ($C_O = C_R$) and the rate constant of the forward reaction equals the rate constant of the backward reaction. In reality this behavior is noticeable only in limited case. For example, even for the hydrogen oxidation reaction (HOR), which is one of the simplest reaction, the Butler Volmer is not always applicable. Definitively, the evaluation of the exchange current with a complicated reaction such as the ORR, must be done carefully.

Regarding Non-Noble Metal electrocatalysts, several Tafel slopes are reported in literature: some oxides such as Mg-MnO_x/C, Ni-MnO_x/C and MnO_x/C show Tafel slopes comprised between 47 and 57 mA/dec [162]. Pyrolyzed polypyrrole supported on mesoporous carbon show 68 and 166 mV/dec as Tafel slope 1 and Tafel slope 2 respectively [91]. To identify a possible rate determining step, a comparison with a theoretical Tafel slope is required. The ORR mechanism is difficult to determine and actually continues to be discussed [137,163,164]. Adzic et al. [165] has also proposed in recent years the formation of a superoxide anion as intermediate in ORR. Through the microkinetic analysis that includes coverage terms, Shinagawa et al. [136] have elaborate a theoretical relationship between the Tafel slope and the different steps involved of the ORR associative mechanism [166–168]. The results of the Tafel analysis on the ORR elementary steps are shown below in **Table 1.7**:

Table 1.7. ORR elementary reaction steps associated with their Tafel slope determined through microkinetic analysis. M denotes an empty site. Steps 1-4 take places in alkaline condition; step 5 is introduced instead of steps 2 and 3 in acidic conditions.

N°	Reaction steps	Tafel slope 1 (mV dec^{-1})	Tafel slope 2 (mV dec^{-1})
1	$M + O_2 \leftrightarrow MO_2$	-	-
2	$MO_2 + e^- \leftrightarrow MO_2^-$	120	-
3	$MO_2^- + H_2O \leftrightarrow MO_2H + OH^-$	60	-
4	$MO_2H + e^- \leftrightarrow MO + OH^-$ or $MO_2H + e^- \leftrightarrow MOOH^-$	40	120
5	$MO_2 + H_3O^+ + e^- \leftrightarrow MO_2H + H_2O$	120	-

Table 1.8 shows some exchange current density values taken from the literature for Pt and FeC catalysts families.

Table 1.8. ORR exchange current density for Pt/C family and non noble iron-based catalysts

Catalyst	ORR i_0 (A/cm^2)	Measure conditions	Ref.
Pt	2.8×10^{-7}	At Pt/Nafion interface at 30 °C	[169]
PtO/Pt	1.7×10^{-10}	At Pt/nafion interface at 30 °C	[169]
FePc	1.3×10^{-7}	In pH 1.2 solution	[159]
PtFe/C	2.15×10^{-7}	In 0.5 M H_2SO_4 at 60 °C	[170]

1.5.5 Polarization and power density curve

For a full interpretation of the performance relative to a general cell or battery (like a fuel cell, metal-air battery, etc.) is fundamental the basic knowledge of the polarization curve (**Figure 1.23**) obtained during the device testing phase. Starting from thermodynamic basics concepts, the Gibbs (ΔG) free energy of an electrochemical conversion system is given as showed in **Equation 1.37**:

$$\Delta G = \Delta H - T\Delta S \qquad \text{Equation 1.37}$$

Where ΔH is the energy released from the reaction (enthalpy), ΔS is the entropy and T the absolute temperature. The maximum achievable electrical work (W) is described by **Equation 1.38**:

$$W = -n\,F\,E \qquad \text{Equation 1.38}$$

Where n is the number of electrons involved in the reaction, F is the Faraday constant (96485 C mol^{-1}) and E is the cell or battery potential. The electrical work corresponds to the variation of the Gibbs free energy relative to the global electrochemical reaction that takes place inside the device. The theoretical potential of an electrochemical conversion system (evaluated at a certain temperature, pressure and reagent concentration) is thus determined through **Equation 1.39**:

$$E = -\frac{\Delta G}{n\,F} \qquad \text{Equation 1.39}$$

At the open circuit potential condition (E_{ocv}), in which no external current flows, the maximum starting potential is always lower respect the theoretical one due to the overpotential effect [171]. The potential, start to decrease as soon as the current flows through the circuit. The efficiency (ε) in every moment is given from the ratio between the measured potential and the theoretical potential (**Equation 1.40**) [172]:

$$\epsilon_{Cell} = \frac{E_{Actual}}{E_{theoretical}} \qquad \text{Equation 1.40}$$

The final polarization η is given by **Equation 1.41**:

$$\eta = E_{OCV} - E_T \qquad \text{Equation 1.41}$$

Where E_T is the final cell potential with a specific current (I) flowing. The voltage drop due to polarization phenomena result from three kinetic limitations of the reactions. In a polarization curve different polarization regions can be recognized due to three different overvoltage phenomena. As indicate in **Figure 1.23** they are called activation polarization, ohmic polarization and concentration polarization [35].

The activation polarization is located at low current density and is related to the electronic transfer process that takes place from the electrodes to the electrolyte and vice versa. It is the overpotential necessary for the activation energy of the electrochemical reaction. The kinetic of this process is well describe

with the Tafel Equation derived from Butler Volmer equation for reaction with high overpotential (see **Equation 1.35** and **Equation 1.36**).

The ohmic polarization is the electrical resistance of the device equipment. Is due to resistance and nature of the electrolyte, the type of materials used for the battery construction, the current collectors and the surface resistive films on the electrodes. There is a linear relationship between η and I. This second polarization region is described by the first Ohm law (**Equation 1.42**):

$$\eta = RI \qquad \text{Equation 1.42}$$

The concentration overpotential at higher density current is due to mass transport limitation. This phenomenon occurs in presence of limited diffusion of the active reagent or slow removal of the product at the electrodes surfaces. The polarization is described by **Equation 1.43**:

$$\eta = \left(\frac{RT}{n}\right) ln \frac{C}{C_0} \qquad \text{Equation 1.43}$$

Where C is the concentration of the species at the electrode surface and C_0 is the concentration of the same species in the bulk of the solution.

The overall voltage drop is determined through the sum of the three overpotential mentioned above. Is fundamental to recognize the similarity between the potential drop behavior of a battery polarization curve and the polarization curve obtained through ORR analysis with RDE described previously in **Paragraph 1.5.4.** In fact in that case, the potential and current axes are rotate but the RDE polarization curve shape is the same.

The power density curve (**Figure 1.24**) is directly determined from the polarization curve through the **Equation 1.44**. It is used to understand the powers generated by the device as a function of the current.

$$P = VI \qquad \text{Equation 1.44}$$

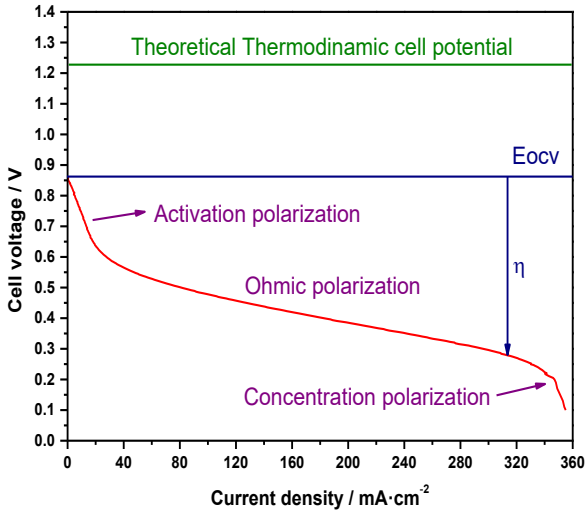

Figure 1.23. Cell polarization curve

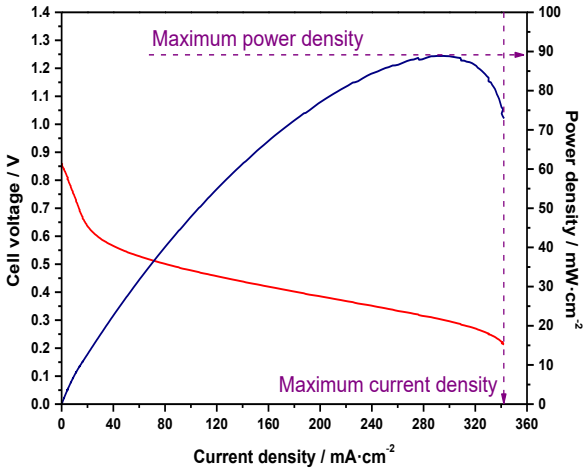

Figure 1.24. Cell power density curve

The polarization curve should to be seen as the identity card of the catalyst combined with the electrochemical device. The real power output of the device has finally decided by the electrical demand of the external circuit. Furthermore, regarding the fuel cell device fundamental is the design of the correct fuel supply systems.

1.6 Fundamental of design of experiment

In this thesis, different tools coming from the theory of the design of experiment (DOE) were used. Specifically, cube plots, Pareto charts, main effect plots, and interaction plots were analyzed in some optimizations.

The DOE is a statistical technique that allows the identification and quantification about the causes of an effect through a series of experimental test. In an experimental design, one or more variables (denoted as factors *k*), are manipulated at different levels (low, high, medium, etc) to measure their effect on another variable of interest (denoted as result *y*) [173]. The experimental design describes a series of relative guidelines (which variables? In what way? How many times? etc) with a predefined degree of confidence for a presumed cause-effect relationship. This technique finds applications in industry, agriculture, marketing, medicine, ecology, engineer, chemistry, etc., and it is an essential phase in the development of an experimental study. The goal is to understand how to change a process in the desired direction avoiding the *one factor at a time* approach (OFAT), which, in general, is time-consuming and expensive [174].

The experimental analysis can be carried out following a full factorial approach or through different types of fractional factorial DOE. A complete full factorial experiment allows evaluating, with a limited number of tests, the effect on the output of all the input variables examined covering all the possible combinations. Moreover, it allows acquiring detailed information on the behavior of the main factors and interactions between the factors examined. The full factorial approach has several advantages:

- It is easy to analyze and organize;
- The minimum number of tests is given by the number of all possible combinations of factor levels;
- If all the factors *k* have two levels of analysis, the full factorial required 2^k experiments;
- It can be used for both qualitative (color, shape, etc.) and quantitative factors (temperature, pressure, etc.);
- It can be used to quantify interactions [175]

The experiments are then organized in a standard order, however, when possible, it is recommended to perform the analysis in a randomized order to ensure the following advantages:

- Each event has the same opportunity to happen;
- Reduce the effect of the non-tested variables (the noise).

Table 1.9 and **Figure 1.25** show an organization of the experiments for a 2^3 full factorial analysis, which is used two times in the following chapter. To save space, the points in a two-level factorial experiment are often abbreviated with the – and + symbols. Sequences have as many symbols as factors, and their values

dictate the level of each factor: – for the first (or low) level, and + for the second (or high) level.

Table 1.9. DOE full factorial for 2^3 experiments

A	B	C	AB	AC	BC	ABC
–	–	–	+	+	+	–
+	–	–	–	–	+	+
–	+	–	–	+	–	+
+	+	–	+	–	–	–
–	–	+	+	–	–	+
+	–	+	–	+	–	–
–	+	+	–	–	+	–
+	+	+	+	+	+	+

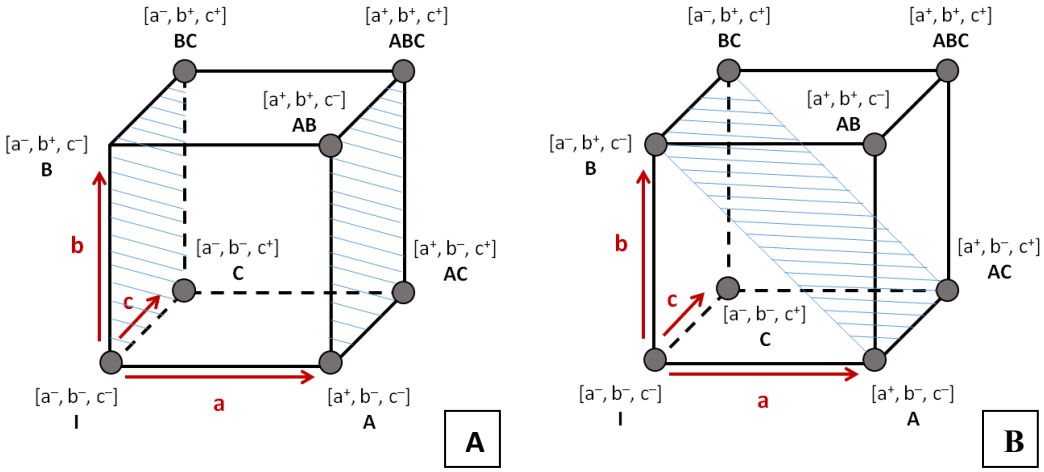

Figure 1.25. DOE full factorial for 2^3 experiments. A) faces used for the calculation of the main effect value Ma (see **Equation 1.45**). B) One of the face used for the calculation of the interaction value Mab. The other face, symmetrical to the one already represented, is voluntarily omitted for picture simplification (see **Equation 1.46**)

Instead, a fractional factorial experiment is used as an alternative to the full factorial design, excluding some experiments, when the process requires a huge screening on many factors (more than 4 variables, i.e., 2^5 number of experiments). This procedure allows analyzing a large number of factors with a small number of tests. However, it requires a further phase of experimentation. Since this specific procedure is not used in this thesis, the fractional factorial will not be further examined.

In the full factorial design, the influence of each factor on the final result could be evaluated considering the main effect and their interactions. Both are evaluated with the support of specific plots.

The *main effect* of a single factor is the difference between the average value of the results present at the vertices of the face relatives to the high level of that factor and the average value of the results present at the lower level. Thus, considering the factor a (**Figure 1.25 – A**), the main effect Ma is described by **Equation 1.45**:

$$M_a = \frac{y_A + y_{AB} + y_{AC} + y_{ABC}}{4} - \frac{y_I + y_B + y_C + y_{BC}}{4} \quad \text{Equation 1.45}$$

Similar equations are valid for the determination of the main effects of factors b (Mb) and c (Mc). The *interaction* between two or more factors is the difference between the mean cross value (**Figure 1.25 – B**) of the response results y between the upper and lower level of those factors (**Equation 1.46**) [176].

$$M_{ab} = \frac{y_I + y_C + y_{AB} + y_{ABC}}{4} - \frac{y_A + y_{AC} + y_B + y_{BC}}{4} \quad \text{Equation 1.46}$$

Considering the case of a two levels of analysis, the main effect plot (**Figure 1.26**) is represented by a straight segment. The horizontal axis shows the value of the factor while the vertical axis shows the corresponding output result. The greater is the segment slope, the greater is the influence of the factor. If the segment tends to be horizontal, the influence of that factor is null or not very significant. The straight is described by **Equation 1.47**:

$$y = m * factor \quad \text{Equation 1.47}$$

Where '*y'* is the output result and '*m'* the angular coefficient

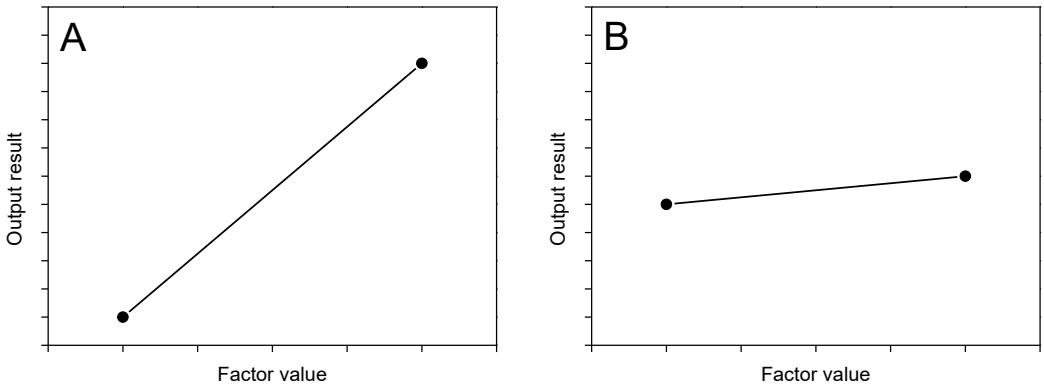

Figure 1.26. Example of main effect plot: A) high influence B) low influence

The interactions between the parameters were evaluated considering the slope of the segment in the interaction plots (**Figure 1.27**). Two parameters interact when their slopes are different: the greater the difference, the greater is the possibility that the parameters interact with each other, especially when the segment intersect. In this case, the interaction plots should drive the analysis (and not the main effects plot).

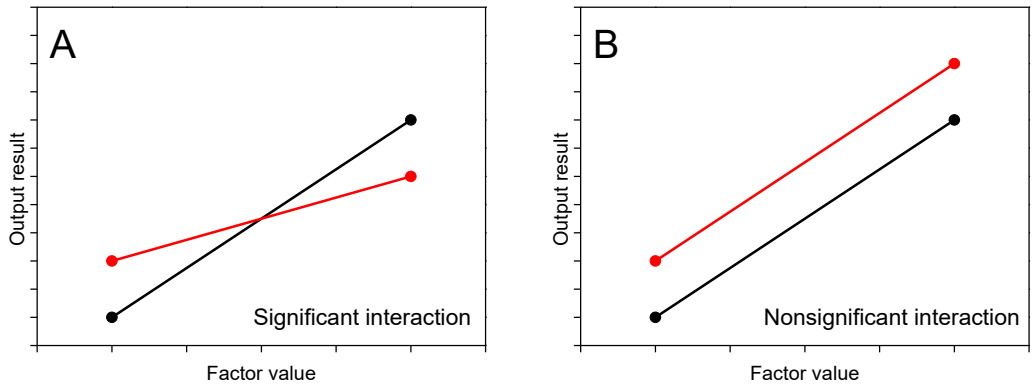

Figure 1.27. Example of interaction plot: A) high interaction B) Non-significant interaction

Cube plots are used to see immediately which process variables combination has provided the best performance showing the relationship between the factors and a response (**Figure 1.28**). Each cube plots is made up by three factors otherwise, in the case of two factors, it is a square plot. Specifically, cube plots can show the combinations of factors or the "data mean", or "fitted mean", for each combination. Cube plots could also made up with the combinations of factors without any response mean. "*Data means* are the *raw response variable*

means for each factor level combination, while *fitted means* use the least-squares method to provide the *mean response values* of a balanced design" (same level of the factors) [177]. In any case, data-mean method and fitted-mean method are identical for balanced design but can be different for unbalanced design, in which the levels of the factors are different (not in this context).

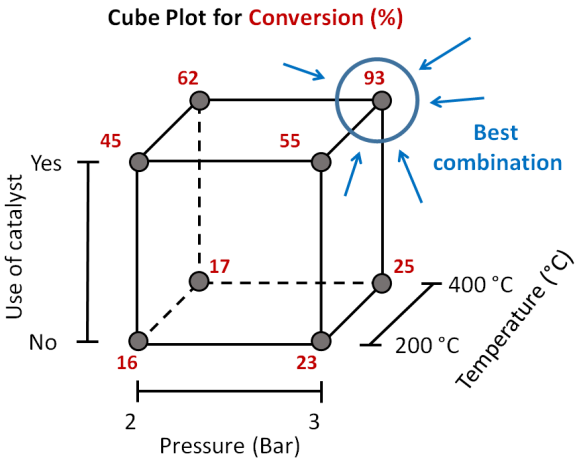

Figure 1.28. Example of cube plot applied to a chemical process in which conversion is the investigated result and pressure, temperature and the presence of the catalyst are the factors.

An additional useful tool for assessing the influence of factors is the *Pareto chart* (**Figure 1.29**). The scope of the Pareto chart is to highlight/suggest the most important among a set of factors. Generally, 20% of the input creates 80% of the result. The larger is the set of factors, the higher is the probability to discriminate fundamental parameters from useless variables. The red line indicates the threshold beyond which the parameter affects the analyzed response. It is evaluated as 1-α/2 quantile of a t-distribution where α is the significance level and the degrees of freedom equal to the degrees of freedom of the error. The results that do not cross the red line are not significant and can be removed from the model. The horizontal axis is defined by an inner calculation of statistical coefficients.

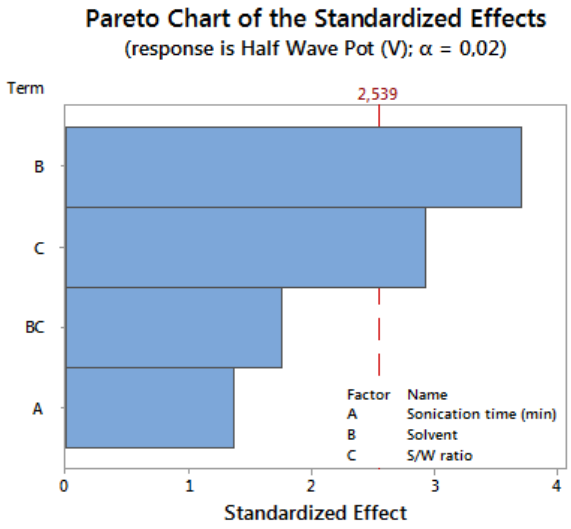

Figure 1.29. Example of Pareto chart. Results took from Chapter 5

Chapter 2

Materials and methods

2.1 Chemicals

Iron(III) phthalocyanine chloride (Fe(III)-Pc), Iron(II) phthalocyanine, Basolite® Z1200 (ZIF-8), sulfur ≥99.998 wt% (S), potassium hydroxide, ethanol ≥99%, isopropanol 99.5 wt, hexane anhydrous 95%, hydrochloric acid 37 wt. %. Sulphuric acid 97 wt. %, Nafion® solution containing 5 wt. %, Nochromix® were purchased from Sigma-Aldrich (Italy).

Pt/C 20% and PtRu/C catalyst (Pt 30% Ru 15%) Alfa Aesar was purchased from Johnson Matthey (United Kingdom).

MnO_2 Cathode as metal-air battery reference was purchased from Gaskatel (Germany)

Vulcan XC 72 carbon was purchased from Cabot (USA).

Fumapem FAA-3-50 anion membrane was purchased from Fuel Cell Store (USA).

Fumion® FAA-3 anion exchange ionomer was purchased from Fumatech (Germany).

PBI Dopozol membrane was purchased from Danish Power System (Denmark).

Neodymium magnet (NdFeB 2x1 mm N42) was purchased from Amazon.

Nitrogen, hydrogen, and oxygen gases (99.999% purity) were supplied in cylinders by SIAD (Italy).

All aqueous solutions were prepared using ultrapure water obtained from a Millipore Milli-Q system with resistivity > 18 MΩ cm.

2.2 Experimental analysis

2.2.1 Chemical-physical characterization of the electrocatalysts

Nitrogen adsorption-desorption isotherms were measured at liquid nitrogen temperature, using a Quantachrome Autosorb-1 volumetric adsorption analyzer. Physisorption Measurement were performed at relative pressure p/p_0 from 1E–6 to 1 and 60 sampling points. Samples were degassed under turbo-molecular vacuum at 150 °C for 2h followed by 275 °C for 4h before sorption measurements. Nitrogen gases with super high purity (99.999%) was used for the physisorption measurements. The Brunauer–Emmett–Teller (BET) equation was used to calculate the apparent surface area from adsorption data obtained at p/p_0 between 0.07 and 0.15. External surface and micropores area were obtained by t-method based on the statistical thickness method (STSA) for carbon black using p/p_0 between 0.3 and 0.55. Pore size distributions and cumulative pore volumes were determined by using quenched solid-state density functional theory (QSDFT) methods and slit-like pores as a pore model [178–180]. These choices for DFT and t-method were made as the best fitting against the experimental N_2 sorption isotherms and best correlation coefficient respectively was observed.

X-ray photoelectron spectroscopy (XPS) was performed to determine the elemental surface composition of the catalysts. The analysis was carried out using a Physical Electronics PHI 5000 Versa Probe electron spectrometer system with monochromated Al Ka X-ray source (1486.60 eV) run at 15 kV and 1 mA anode current. The survey spectra were collected from 0 to 1200 eV. The narrow N_{1s} spectra were collected from 396 to 405 eV, the narrow Fe 2p spectra from 700 to 740 eV, and the narrow C_{1s} spectra from 280 to 293 eV. All of the spectra were calibrated against a value of the C_{1s} binding energy of 284.5 eV. Casa XPS software was used for obtaining semi-quantitative atomic percentage compositions, using Gauss–Lorentz equations with the Shirley-type background. A 70%/30% Gaussian/Lorentzian line shape was used to evaluate peaks position and areas of the high-resolution N_{1s} spectra.

The XRD patterns were recorded on a Panalytical X'Pert PRO diffractometer with a PIXcel detector, using Cu (K radiation = 0.15418 nm), under the operating conditions of $2\theta = 20 - 90^\circ$ and 2θ step size = 0.03, in order to examine the different polymorphs. The markers were located using the Philips X'Pert HighScore Software (ICDD database).

An Hitachi S3000N scanning electron microscope (SEM) and a JEOL Ltd JEM 2010 transmission electron microscope (TEM) were used to determine the catalyst's morphology.

2.2.2 Electrochemical characterization of the electrocatalysts

The electrochemical evaluation of the electrocatalysts prepared was carried out in a conventional three-compartment electrochemical cell using a potentiostat (Bio-Logic SP150), and a rotating ring disk electrode instrument (RRDE-3A ALS Model 2323). The samples were tested in 0.1M KOH saturated with either N_2 or O_2. Before any test, glassware was clean using Nochromix® dissolved in concentrated sulfuric acid, leave it overnight at 40 C. Then glasswares were cleaned with ultrapure water until the boiling, this procedure was repeated 3 times.

For RDE measurements, the cell was equipped with a glassy carbon (GC) disk working electrode (0.1256 cm^2 geometric area), a gold wire used as a counter electrode, and a saturated Ag/AgCl used as reference electrode. All electrode potentials were referred to the reversible hydrogen electrode (RHE) using the Nernst equation previously checking the electrolyte pH by a HACH® Sension$^+$ instrument. Different GC electrodes were prepared by ink drop-casting using an ionomer-to-catalyst ITC mass ratio (mg of Nafion® over mg of catalyst) equal to 0.14 [181] and the catalyst loading was 0.400 mg cm^{-2}. At the beginning of all tests, the electrolyte was purged with N_2 for about 15 minutes with the aim of remove any active species. To obtain an electrochemical clean catalyst surface, the potential was swept between 0.0 and 1.2 V vs RHE with a sweep rate of 100 mV s^{-1}, (12 cycles), 20 mV s^{-1} (6 cycles) and 10 mV s^{-1} (3 cycles); these scans were enough to obtain stable voltammograms [182]. After this procedure a final voltammetry was recorded at 10 mV s^{-1}. After saturation with O_2 (15-20 minutes), stair case voltammetry (SCV) were performed by rotating the electrode at 900 rpm and using a step size of 10 mV at the time period of 10 s $step^{-1}$. The samples were tested thrice. Before any test, the working electrode was polished with 1 and 0.06 mm alumina powders.

The determination of the selectivity through H_2O_2 production during ORR was evaluated with the rotating ring disk electrode technique (RRDE). The ring and disk potentials were controlled with an AutoLab bipotentiostat. The experiment was carried out performing a linear sweep voltammetry (LSV) at a scan rate of 5 mV s^{-1} from 1.0 to 0.05 V vs. RHE on the disk, while the ring potential was kept constant at 1.2 V vs. RHE to ensure the oxidation of the peroxide species at the Pt ring to be under diffusion control [183]. The rotation speed was set at 900 rpm and the electrode disk current was corrected removing the background current measured under N_2 atmosphere saturation [154].

The tolerance of the catalysts to the presence of ethanol was examined by performing LSV using a step size of 10 mV with time increments of 10s $step^{-1}$ by

rotating the electrode at 900 rpm in O_2-saturated 0.1 M KOH solution with varying ethanol concentration from 0.01 to 2 M.

The stability of the best catalyst was evaluated with a "slightly modified" load cycle durability test proposed by the fuel cell commercialization conference held in Japan (2011) [184]. The solution was saturated with O_2 instead of N_2 and the measure was stopped after 2000 cycles. Each cycle was performed waiting 3 s at the potential values of 0.6 and 1.0 V vs RHE (6 s the average cycle period) using a sweep rate of 500 mV s^{-1}. The polarization curves were acquired through stair case voltammetry by rotating the electrode at 900 rpm. The activity was evaluated at the beginning of the experiment and after 250, 500, 1000, and 2000 cycles.

2.2.3 Testing on Fuel Cell

Membrane preparation

Two different alkaline membranes were activated and used in these experiments. The FAA-3-50 membrane (Fumatech) and the PBI Dopozol membrane (Danish Power System). The membranes were delivered in bromide form (Br^-) and dry form. For alkaline fuel cell applications, the membrane must be converted into OH-form (**Figure 2.1**). The FAA-3-50 membrane was converted into hydroxyl form by treating it with 0.5 – 1.0 M NaOH or KOH solution for at least 24 h. The PBI membrane required to be activated in a solution of 6 M KOH for 5 days. The different activation process is defined by the producer since the chemical composition of the two membranes is different. The FAA-3 family consists of a polyaromate (benzilic based structure) with quaternary ammonium group, while PBI consist of a polybenzimidazole structure. After this treatment, both the membranes were rinsed with demineralised water and immediately used. At the beginning of the experiment, the membrane conductivity was evaluated measuring the resistance obtained from electrochemical impedance spectroscopy (EIS) at different temperature. The analysis was carried out setting the frequency scan of a Metrohm Autolab instrument from 1E+6 to 1 Hz with a number of frequencies equals to 50 and a logarithmic frequency step.

Figure 2.1 A) FAA-3-50 membrane in dry form. B) PBI Dopozol membrane during the activation in KOH 6 M solution.

GDL preparation

The GDL preparation starts with the development of an ink containing the catalyst dispersed in a Iso-propanol and water 2:1 v:v solution. The dispersion was made through the use of an ultrasonic processor (UP50H genesys instrumentacion). The anode ink was prepared using a commercial PtRu/C catalyst (Pt 30% Ru 15%) considering a final loading of 1.33 mg_{Pt} cm^{-2} and a Nafion content of 4% in the overall amount of catalyst on the dry electrode [31,185]. The cathode ink was prepared considering a final Non Noble Metal catalyst loading of 3 mg cm^{-2}. The amount of Nafion was varied in base of the type of experiment between 15 % and 50 %. One experiment was carried out using Fumion as alkaline ionomer instead of Nafion. In this case, the amount of Fumion respect the F-N-C catalyst, was set as the 50 % of the overall weight.

The Pt reference cathode was prepared using a commercial 40% Pt/C catalyst considering a final loading of 1 mg_{Pt} cm^{-2} and a Nafion content of 4% in the overall amount of catalyst on the dry electrode [31,185]. All the cathodes and the Pt-Ru anodes were prepared by spraying the respective catalyst inks through an airbrush (**Figure 2.2**) onto a carbon cloth gas diffusion layer (ELAT LT 1400W). The GDL preparation was carried out by alternating deposition steps of a small amount of catalyst (100-200 µl) with drying steps on a heating plate until the overall amount of the catalysts was in accordance with the quantity desired. A GDL area of 16 cm^2 has required 600 ml of H_2O and 1520 ml of isopropanol for the ink preparation.

Figure 2.2. Airbrush used for the air-spraying

Testing

The DEFC tests were carried out through a fuel cell test bench Mits pro-FCTS - Arbin Instruments (**Figure 2.3 – A**). The fuel cell device construction was made following the well recognized procedures. The membrane electrode assembly (MEA), which is the combination of the membrane in contact with the sprayed GDL, was assembled without hot pressing in the cell device by direct sandwiching at room temperature of all the components. For these type of alkaline membranes it is preferable to avoid the hot pressing process since it damages the structure of the membrane, resulting in a breakage during the fuel cell testing at higher pressure. Starting from the first terminal plate supported by the working desk, the following components were added in this mandatory order: cathodic bipolar plate, first gasket, cathodic GDL (with catalyst surface in contact with the membrane), membrane, anodic GDL (with catalyst surface in contact with the membrane), second gasket, anodic bipolar plate and second terminal plate. The devices was locked using 8 screws (**Figure 2.3 – B**) closed with a torque of 3.5 N·m.

The anodic compartment was fed with a preheated 2 M ethanol / 2 M KOH solution with a flow rate of 1 ml min^{-1}. The cathodic compartment was fed with 200 NmL/min of humidified and preheated pure O_2. The polarization curves were recorded from open circuit potential E_{ocv} down to 0.01 V [31]. The experimental tests were carried at different temperature (25 – 60 – 80 – 90 °C), at different O_2 backpressure (0.5 – 1 – 2 – 3 bar) using in some case two different Nafion loading (15 and 50 %). The short durability test was carried out through a chronoamperometric test at 0.6 V for 8h recording a polarization curves every 30 min as previously described [12][186]. The temperature of the feed inside the anodic compartment and the pressure of the O_2 at the cathodic compartment were varied according to the type of the research performed.

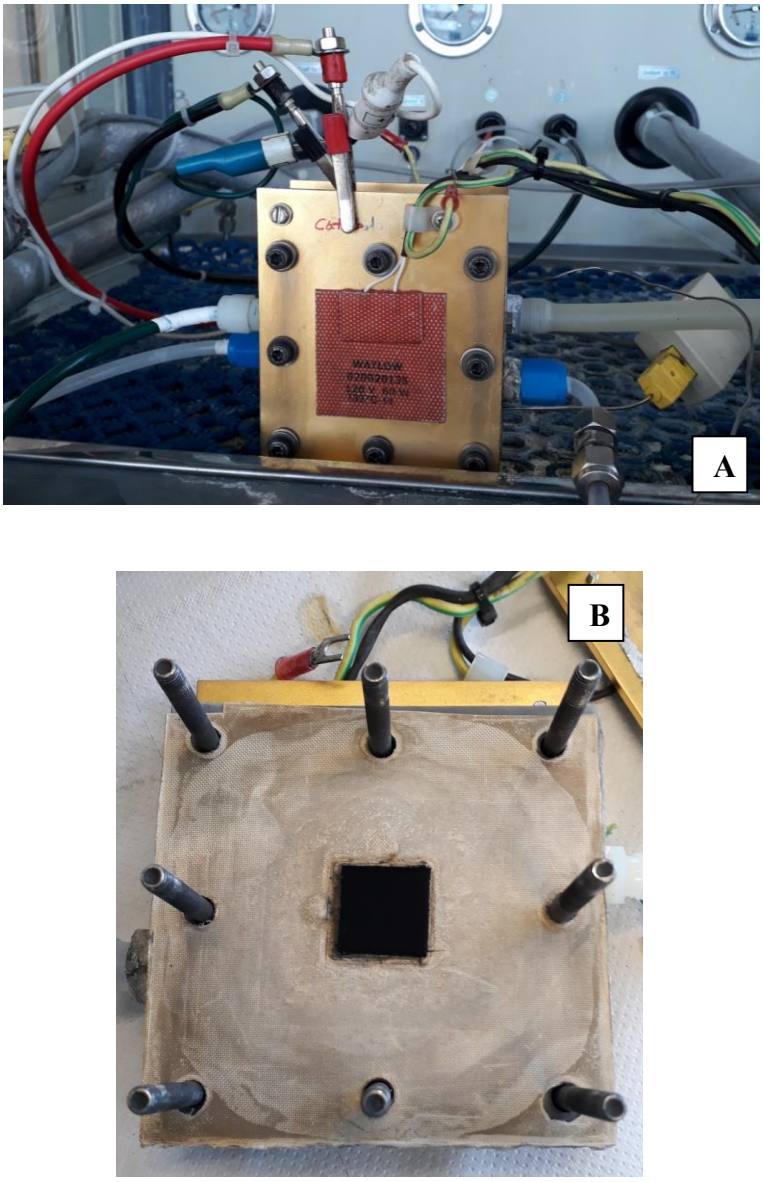

Figure 2.3. A) Fuel cell connected to the Mits pro-FCTS - Arbin Instruments. B) Cross-section of the fuel cell used in all the experiments.

2.2.4 Testing on Metal air battery

Gel preparation

The electrolyte was prepared combining an alkaline salt solution with a gelling solution. The alkaline salt solution was made adding 0.4 g of ZnO in a 10 M KOH alkaline solution (12 g of KOH 0.85% in 18 ml H_2O). ZnO was added as corrosion inhibitor of the aluminium to decrease its self corrosion rate in alkaline solution [38]. The gelling solution was made adding 0.3 g of N,N methylenebis (acrylamide) in 2 g of acrylic acid. The salt solution was combined with the gelling solution. The mixture was stirred at 700-800 rpm for 10 minutes and subsequently filtered on a plastic petri dish. Less than 1 ml (about 30 drops) of

$K_2S_2O_8$ saturated solution was added by dropping into the mixture to activate the gel polymerization process. The polymerization required almost two hours to reach completion.

Assembly of the metal-air battery

The metal-air battery used for the experimental analysis consist of 3 Teflon supports that can hold the anode and the cathode joined together. The electrolyte gel is placed between the electrodes and two copper sheet in contact with them allow the measures acquisition. The anode consist of an aluminium alloy (Al 7475) with specific area of 2 cm^2. This area corresponds to the active surface area of the battery. The cathode is made up with different material layers: a Teflon film with a carbon clothe and a nickel mesh joined together. The O_2 permeable Teflon cloth prevent liquid electrolyte leakage while it allows oxygen to flow inside the battery. The nickel grid is attached to the carbon layer on which the specific catalyst was deposited through the use of an airbrush sprayer. The nickel grid helps in the current conduction between the copper sheet and the catalyst layer. **Figure 2.4** shows all the steps required to prepare the metal-air battery.

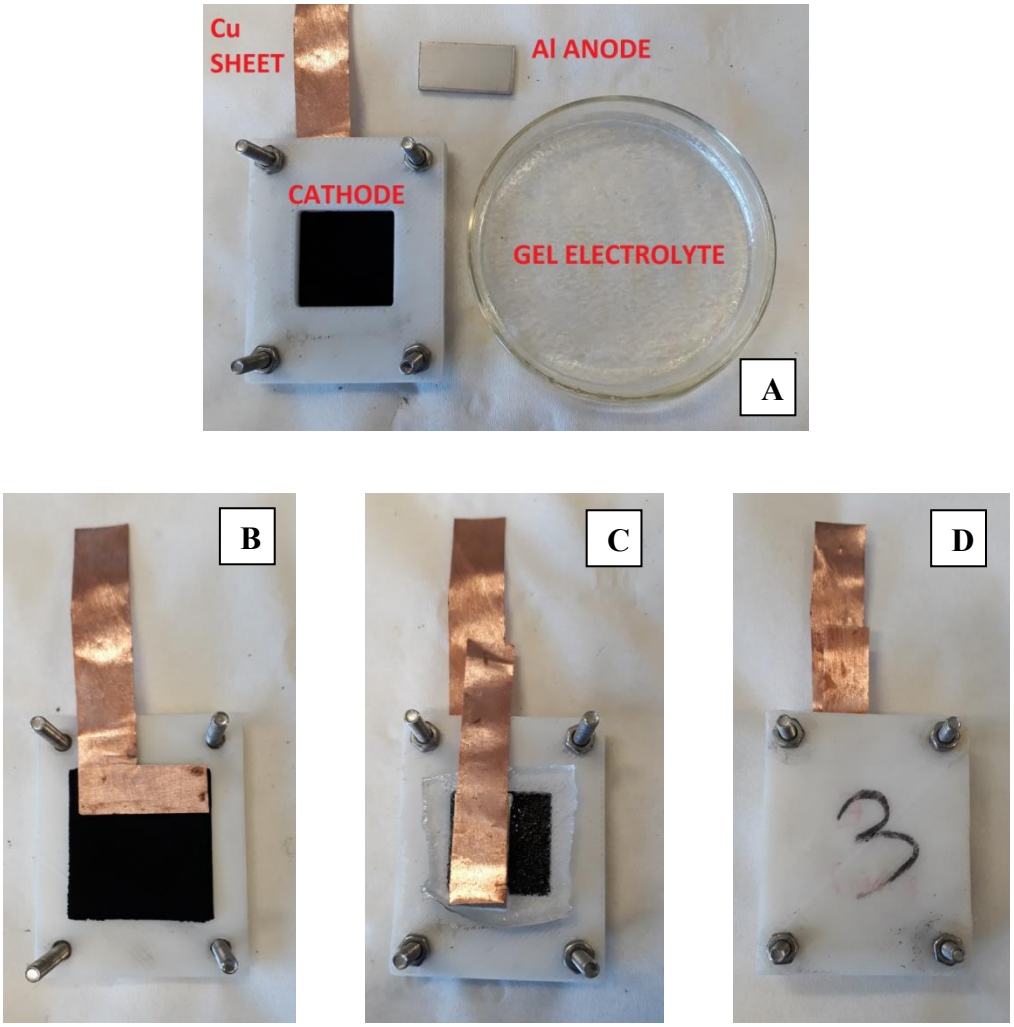

Figure 2.4. a) Metal air battery components. b) Cathode placement c) Gel and anode placement d) Battery closure.

Testing

The metal-air battery electrochemical tests were carried out using a 12-channel Arbin Instruments BT2143 workstation at room temperature (25 °C). Constant current discharges of 1.6 and 3.2 mA cm^{-2} was carried out after leaving for 5 min the battery at open circuit to allow good contact between the electrodes and the electrolyte and to stabilize the OCP. The cut-off potential for all cases was set at 0 V. Furthermore a dynamic galvanostatic measurements from 0 up to 12 mA/cm^2 with a swept of 0.4 mA cm^{-2} every 10 min was carried out to explore the maximum current density of the cells.

Chapter 3

Synthesis and Process Optimization

3.1 Basic Electrochemical characterization of the raw materials

All the raw materials were characterized in terms of activity towards ORR through SCV analysis. **Table 3.1** and **Figure 3.1** show the results. Since the activity of these materials toward ORR is not high and the shape of their curves is not fully defined, it was not possible determine all the electrochemical parameters. For sake of simplification, in this preliminary test only the onset potential and the half-wave potential (when possible) were analyzed. The analysis has demonstrated that Iron(III)phthalocyanine chloride shows the best performance in terms of onset potential (0.81 V vs RHE) and half-wave potential (0.89 V vs RHE). Moreover, this raw material has the best well-defined ORR curve (**Figure 3.1**). The electrochemical performance remains in any case far from that ideal for this type of application. From next chapter, different combinations of these reagents will be taken into account during the synthesis formulations and the process optimization of catalysts active toward the ORR in alkaline conditions.

Table 3.1. Summary of the experiment results in terms of onset and half-wave potential

Raw materials	Onset potential (V)	Half Wave potential (V)
Zif-8	0.68	n.d
Vulcan xc 72	0.87	0.72
Fe(II)-Pc	0.87	n.d
Fe(III)-Pc	0.89	0.81
Pt-C 20%	1.01	0.90

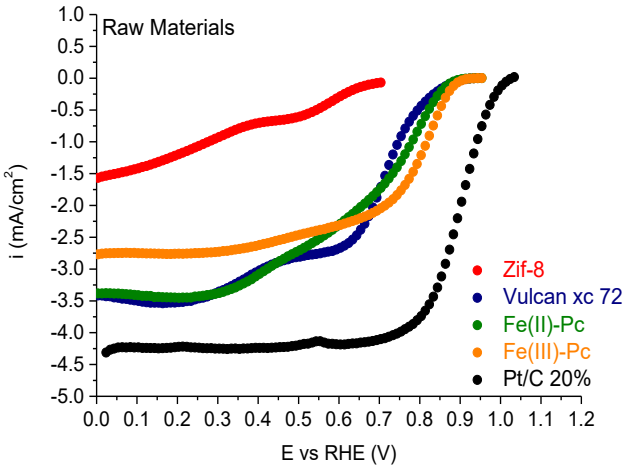

Figure 3.1. SSV recorded in O_2-saturated electrolyte in alkaline condition relatively to the raw materials analysis.

3.2 1st Catalyst: Fe(III)-Pc with Basolite Z 1200

3.2.1 Introduction to the catalyst synthesis

The first catalyst was synthesized through the following general procedure. Iron(III)-phthalocyanine chloride $C_{32}H_{16}ClFeN_8$ (Fe(III)-Pc) was dispersed into 50 ml of ethanol. Then Basolite Z 1200 $C_8H_{12}N_4Zn$ (Zif-8) was added followed from sulphur (Fe(III)-Pc : S molar ratio 1:1) and the mixture was left under stirring for 1 h at room temperature. Afterward the mixture was transferred in autoclave for 16 hours at 160 °C. After, the suspension was filtered under vacuum using a Buchner flask (provided with Whatman filter 6) and washed with deionised water. The Zif-8/Fe(III)-Pc powder was dried under N_2 atmosphere in dry box at room temperature for at least a night and finally pounded in a mortar.

The first heat treatment was performed in a pyrolysis oven under N_2 flow after 30 min of atmosphere purification. At the end of this process, the sample was treated for 3 hours with a 0.5 M sulphuric acid solution. Finally, this suspension was filtered under vacuum using a Buchner flask provided with Whatman filter 6 and washed with deionized water. The second heat treatment was performed under

forming gas flow (50% N_2/H_2) following the same procedure of the first treatment. **Figure 3.2** show a summary of the chemical process used to produce these catalysts. The synthesis optimization was carried out dividing the experiments in three steps. In the first step the optimization was mainly focused on the pyrolysis processes. A 2^3 full factorial design of experiment was used to evaluate the effect that the Zif-8 MOF support (A), the dwell time (B) and the temperature (C) have on the final activity. The aim was to investigate whether pyrolysis treatment increase activity as reported in literature [102,187].

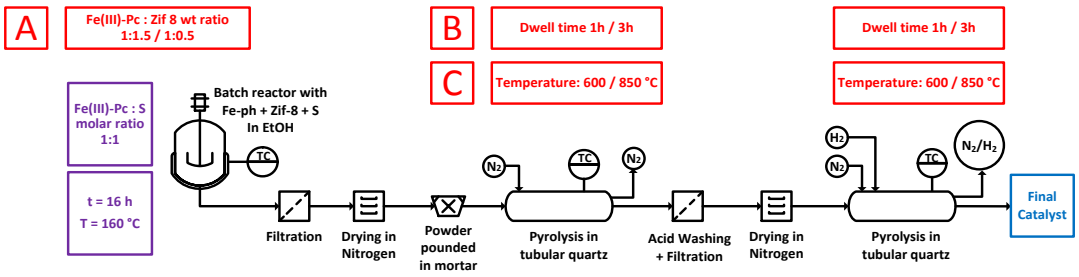

Figure 3.2. Chemical process at laboratory scale. Constant parameters in violet, variable parameters in red.

The exposure to air between the different phases of synthesis leads to the formation of inactive iron oxide that were removed by acid leaching [138,188] after the first heat treatment. The second heat treatment was carried out under forming gas flow (50% N_2/H_2) to further decrease the final amount of oxides and reduce the inorganic metal particles formation during pyrolysis [189]. Afterward a series of synthesis with different Zif-8 amount were carried out to evaluate the influence of the MOF precursor since it tends to sublimate [86] at high temperature with a subsequent increase in the catalyst surface area. For the relevant class of non-noble metal catalyst, heat treatments between 600 and 1000 °C under inert atmosphere have good benefits in ORR activity and stability [100]. Moreover, execute more than one pyrolysis step seems to affect the final performance positively [101,102]. However, to evaluate the possibility to reduce the number of the steps involved in the chemical process, further final studies were carried out considering the removal of one pyrolysis step and the acid leaching.

The second synthesis step was focused on the study related to the autoclave processes. A series of synthesis with different sulphur amount were carried out. According to the literature, the presence of sulphur produces iron monosulphide (FeS) instead of iron carbide (FexC) during the heat treatment. The absence of FexC slows the graphitization of the pyrolysis products and as a result, the catalytic active centres are preserved. Additionally, FeS can be removed during the acid leaching step [190]. Further studies were carried out on the solvent used inside the autoclave. The heterogeneous catalyst-solvent mixture is subject to reaction under heat in a closed container in the autoclave. In such cases, molecules with sufficient kinetic energy to break the intermolecular forces will

leave the liquid phase to occupy the vapour phase space above. An equilibrium state will then ensue whereby gaseous molecule-wall collisions result in these molecules exerting a force onto the liquid surface. Under these conditions, a kind of sintering takes places between the raw materials present inside the autoclave. At the beginning ethanol was chosen as non-toxic slurry solvent with the task of dispersing the reagents. 160 °C was selected as the autoclave temperature because is almost the twice of the ethanol boiling point (78.4 °C). Afterward, n-hexane was used instead of ethanol as slurry solvent in which to disperse the raw materials mixture. The temperature of the oven was set at 140 °C because also in this case is almost the twice of its boiling point (69.0 °C). Compared with ethanol, n-hexane has higher oxygen solubility, lower vapour pressure and above all is a non-polar solvent. The question to be posed is whether the oxygen solubility rather than the chemical nature of solvents (polar or non-polar) influence the protection of active centres rather than the formation of iron oxides. In any case, it is not easy to analyse the physicochemical process that take place inside the autoclave. As the temperature increase, the gases dissolved in solution (such as oxygen and nitrogen) tend to escape in vapour phase but at this point the high pressure forces their return into the solution. To equate the two solvents with the same vapour pressure inside the autoclave, a third synthesis was carried out in ethanol at 133 °C. In fact, working at 133 °C with ethanol provides the same conditions as for working at 140 °C with hexane in terms of vapour pressure (622 kPa) determined through the Antoine equation [191] (**Equation 3.1**), which is a semi-empirical correlations between saturated vapour pressure and temperature for pure solvents :

$$p^{sat} = 10^{A - \frac{B}{C+T}} \qquad \text{Equation 3.1}$$

where p is the vapour pressure, T is the temperature and A, B and C are constant terms

In the last step, the best synthesis was repeated changing the autoclave steps with a mechanical mixing at the solid-state level with ball mill process. The goal was to evaluate the repeatability of the result decreasing the overall cost of the process. **Figure 3.3** shows the summary of the 3 steps previously described. To facilitate the interpretation of the results, the Zif-8/Fe-phthalocyanine weight ratios and the sulphur/Fe-phthalocyanine molar ratios analysed during the optimization were labelled as Z/F and S/F, respectively.

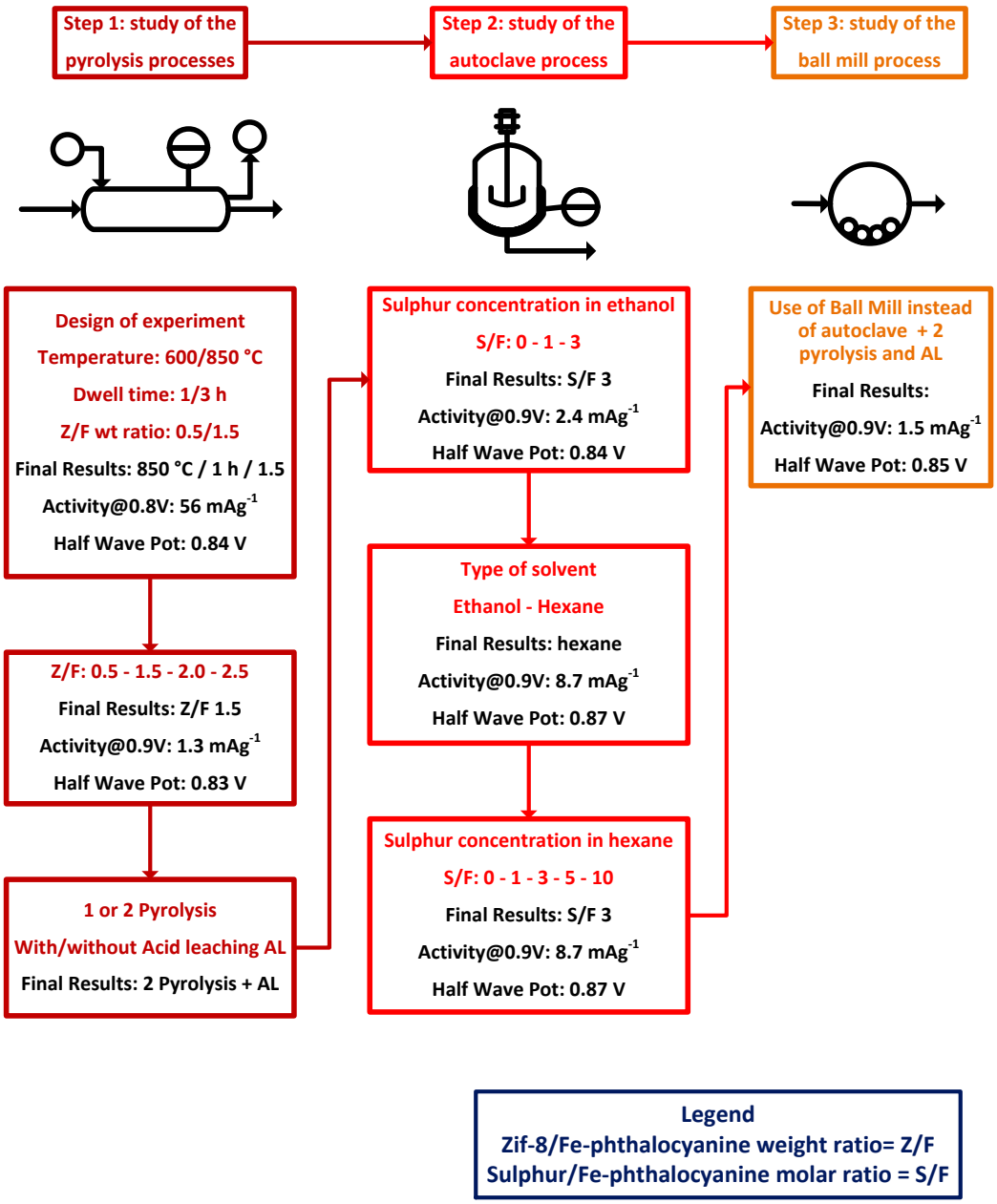

Figure 3.3. Summary of the chemical process steps relative to the first synthesis

3.2.2 Preliminary test

At the beginning of the synthesis optimization, a preliminary test was carried out to evaluate the effect of the heat treatments on this class of materials. The Zif-8/Fe(III)-Pc wt ratio was set to 1.5, the maximum temperature of the pyrolysis oven was set at 850 °C and the residence time at the maximum temperature was set to 1 h. The heating rate for the experiment was set at 10 °C min^{-1}.

The activity toward the ORR was evaluated through SCV analysis in O_2-saturated electrolyte. The catalyst was tested in three steps: after the autoclave process, after the acid leaching (subsequently the first pyrolysis) and at the end of

the process, after the second pyrolysis. The results are summarized in **Figure 3.4** and **Table 3.2.**

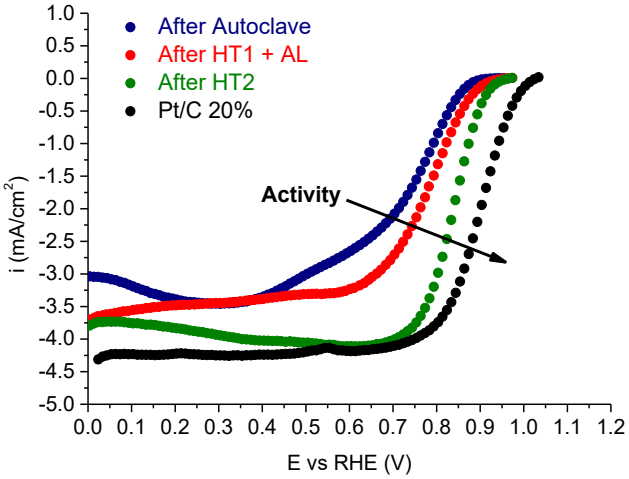

Figure 3.4. SCV recorded in O_2-saturated electrolyte in alkaline condition relative to the first catalyst after different step process.

Table 3.2. Summary of the experiment results in terms of onset and half-wave potential

Step process	Onset potential (V)	Half Wave potential (V)
After autoclave	0.87	0.74
After acid leaching (HT1+AL)	0.91	0.78
After 2nd Pyrolysis (HT2)	0.93	0.84
Pt-C 20%	1.01	0.90

The results shown in **Table 3.2** confirm the positive influence of the heats treatments. After two pyrolysis steps with intermediary acid leaching the half-wave potential of the catalyst has shifted of 100 mV indicating an increase of the activity toward the ORR. Since this result reflected what is reported in the literature, all the next synthesis consisted of a combination between Zif-8 and Fe(III)-Pc, and were carried out following two pyrolysis steps under inert atmosphere.

3.2.3 1st optimization step - Design of experiment

To investigate the effect that the main variables and their interaction have on the catalyst activity and half-wave potential, a full factorial design was used in this experiment. Following the results of the preliminary test, three parameters were tested at two levels in this work, high and low:

(A) Zif-8/Fe(III)-Pc wt ratio:	0.5 and 1.5
(B) Dwell time at maximum temperature:	1 and 3 h
(C) Maximum temperature during the pyrolysis:	600 and 850 °C

For every experiment, a mass load of 0.6 g in the first pyrolysis, and 0.3 g in the second pyrolysis were used. The 2^3 design of experiment is graphically represented in **Figure 3.5** while **Table 3.3** lists the experiments matrix useful to evaluate the three variables.

One way to increase the number of data points in a DOE is to use replicates. However, replicating an entire DOE can be expensive and time-consuming, especially in this application where the number of pyrolysis affects the total time required to complete the set of experiments. Using replicates is a way to increase the reliability. An alternative way to increase reliability of the results is to use centre points (CP). At the same time, the centre points give the possibility to determine statistically if the relationship between variables and response is linear or not. Furthermore, in this study, the central point for the temperature (725 °C) represents a value at which in theory, the formation of iron carbides (Fe_xC) does not happen anymore [192]. For the central point the process parameters were set as shown below:

(A) Zif-8/Fe(III)-Pc wt ratio:	1.0
(B) Dwell time at maximum temperature:	2
(C) Maximum temperature during the pyrolysis:	725 °C

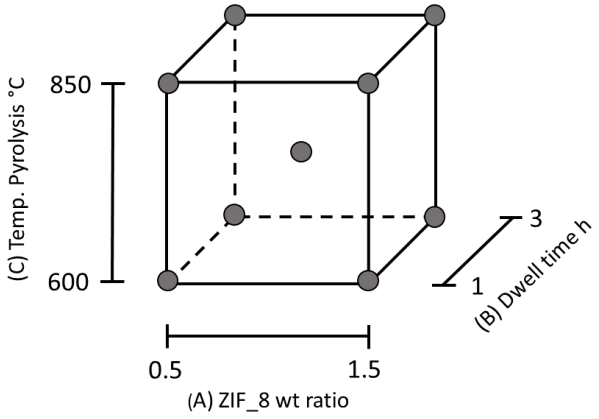

Figure 3.5. Design of experiment

Table 3.3. Experiments matrix. Coded values for each variable are reported in brackets

Experiment	Z/F wt ratio	Dwell time (h)	Temp. pyrolysis (°C)
1	0.5 (-1)	1 (-1)	850 (+1)
2	0.5 (-1)	1 (-1)	600 (-1)
3	0.5 (-1)	3 (+1)	850 (+1)
4	0.5 (-1)	3 (+1)	600 (-1)
5	1.5 (+1)	1 (-1)	850 (+1)
6	1.5 (+1)	1 (-1)	600 (-1)
7	1.5 (+1)	3 (+1)	850 (+1)
8	1.5 (+1)	3 (+1)	600 (-1)
9	1.0 (0)	2 (0)	725 (0)
10	1.0 (0)	2 (0)	725 (0)

The software Minitab was used to evaluate the effect of the parameters on the synthesis of the catalysts: the *half wave potential* ($E_{1/2}$) and *activity* (A g^{-1}), which is related with the *mass transport-corrected current density (i_k).* For this analysis, the confidence was set at 95%. Cube plots, main effect plots and interaction plots were analyzed.

Results and discussions from the DOE analysis

The results obtained after the first series of experiment are reported in **Figure 3.6** and **Table 3.4**. The electrochemical parameters were obtained from the stair case voltammetry showed in **Figure 3.7**. Since some of these experiments did not show activity at high potential (0.9 V), the research of the catalyst's performance was carried out at lower potential (0.8 V). Considering that mass transport losses cannot be completely excluded at higher current densities below E = 0.8V [193] and in some cases the diffusion limit current is not well defined (i.e., experiment 2

and 6), it was decided to take into account an average value of the electrochemical parameters. The analysis provided a first trend relative to the process parameters. The cube plot (**Figure 3.6**) shows the best results with the combination of the highest amount of Zif-8 treated at 850 °C for 1 h. Moreover, also the central point conditions (Zif-8/Fe(III)-Pc wt 1.0), treated at 725 °C for 2 h, provide good results, both as activity and half-wave potential.

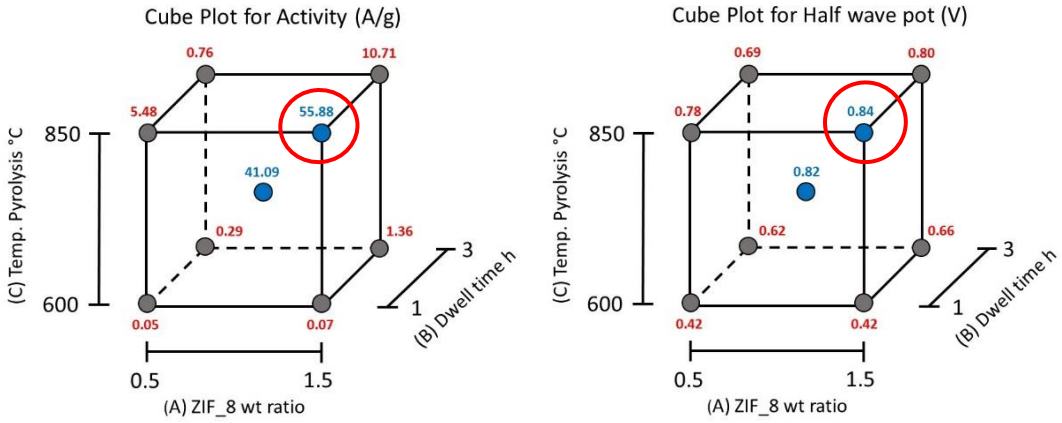

Figure 3.6. Cube plot "data means" of the variables analyzed.

Table 3.4. Summary of the experiment result in terms of activity and half wave potential.

Experiment	Z/F wt ratio	Dwell time (h)	Temp. pyrolysis (°C)	I_k ($mAcm^{-2}$)	Activity @ 0.8V ($A\ g^{-1}$)	Half Wave potential (V)
1	0.5	1	850	2.19	5.48	0.78
2	0.5	1	600	0.02	0.05	0.42
3	0.5	3	850	0.30	0.76	0.69
4	0.5	3	600	0.12	0.29	0.62
5	1.5	1	850	22.3	55.9	0.84
6	1.5	1	600	0.03	0.07	0.42
7	1.5	3	850	4.28	10.7	0.80
8	1.5	3	600	0.54	1.36	0.66
9	1.0	2	725	16.53	41.3	0.83
10	1.0	2	725	16.34	40.9	0.82

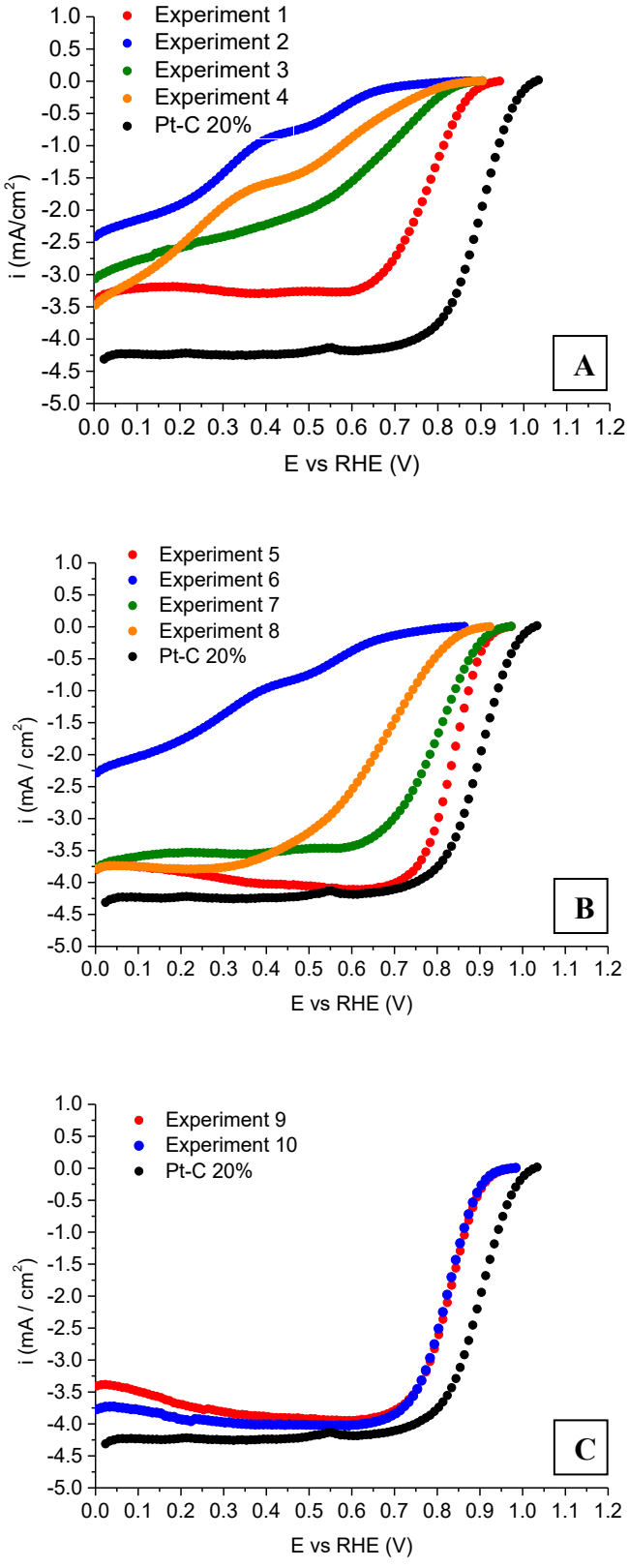

Figure 3.7. SSV recorded in O_2-saturated electrolyte in alkaline condition relative to the first run of experiments. Z/F 0.5 (A), Z/F 1.5 (B), Central point obtained with Z/F 1.0 725 °C in 2 h (C).

The main effect plots in **Figure 3.8** show the influence of the parameters taken in consideration for the activity and half-wave potential, evaluated as response of these experiments. Concerning the activity, all the variables influence the final result: high temperatures and concentrations provide better results, while extended residence time affects this response negatively. Regarding the half-wave potential, at a first glance, temperature is the only parameter that affects the result. As in the previous case, samples treated at 850 °C provide better results.

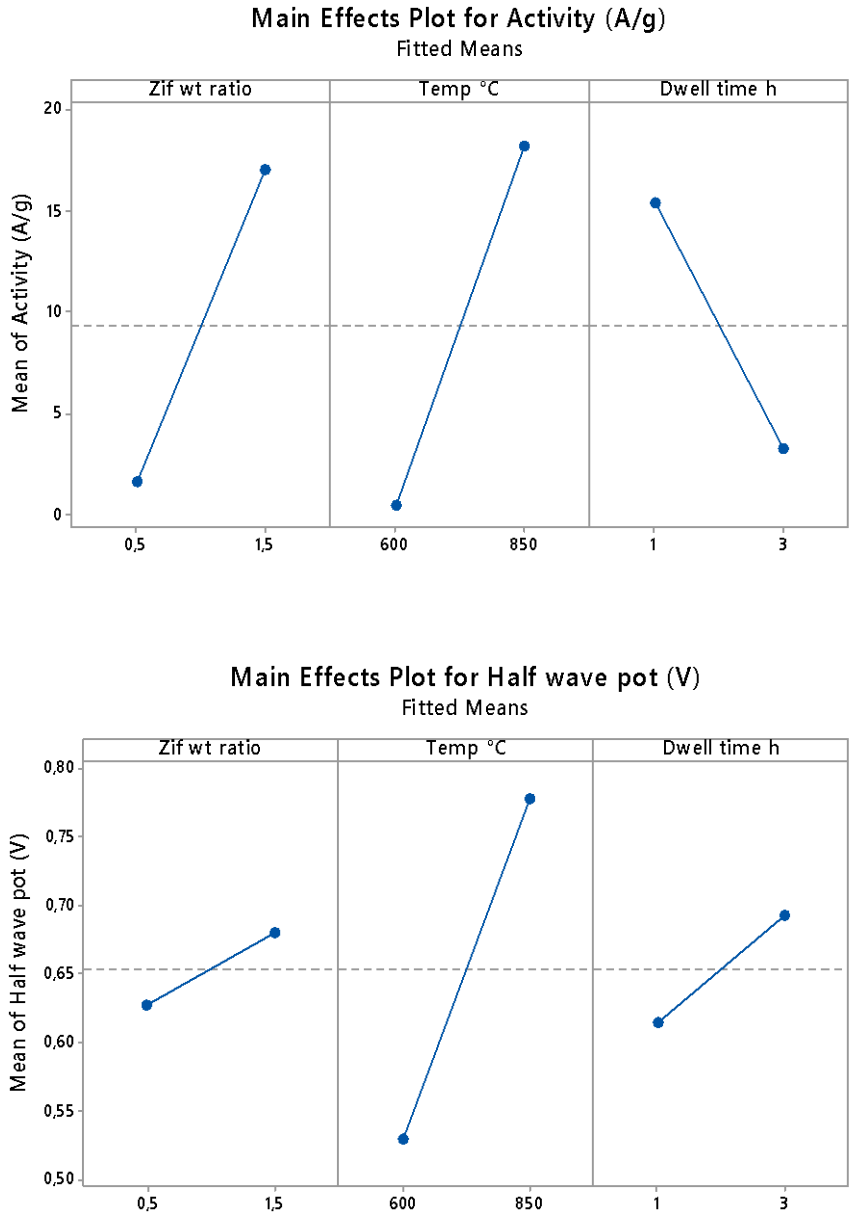

Figure 3.8. Main effect plots of the variables analyzed.

Interaction plots in **Figure 3.9** show a sort of interaction between the Zif wt ratio and the temperature in the case of activity and a strong interaction, especially between temperature and dwell time in the case of half-wave potential.

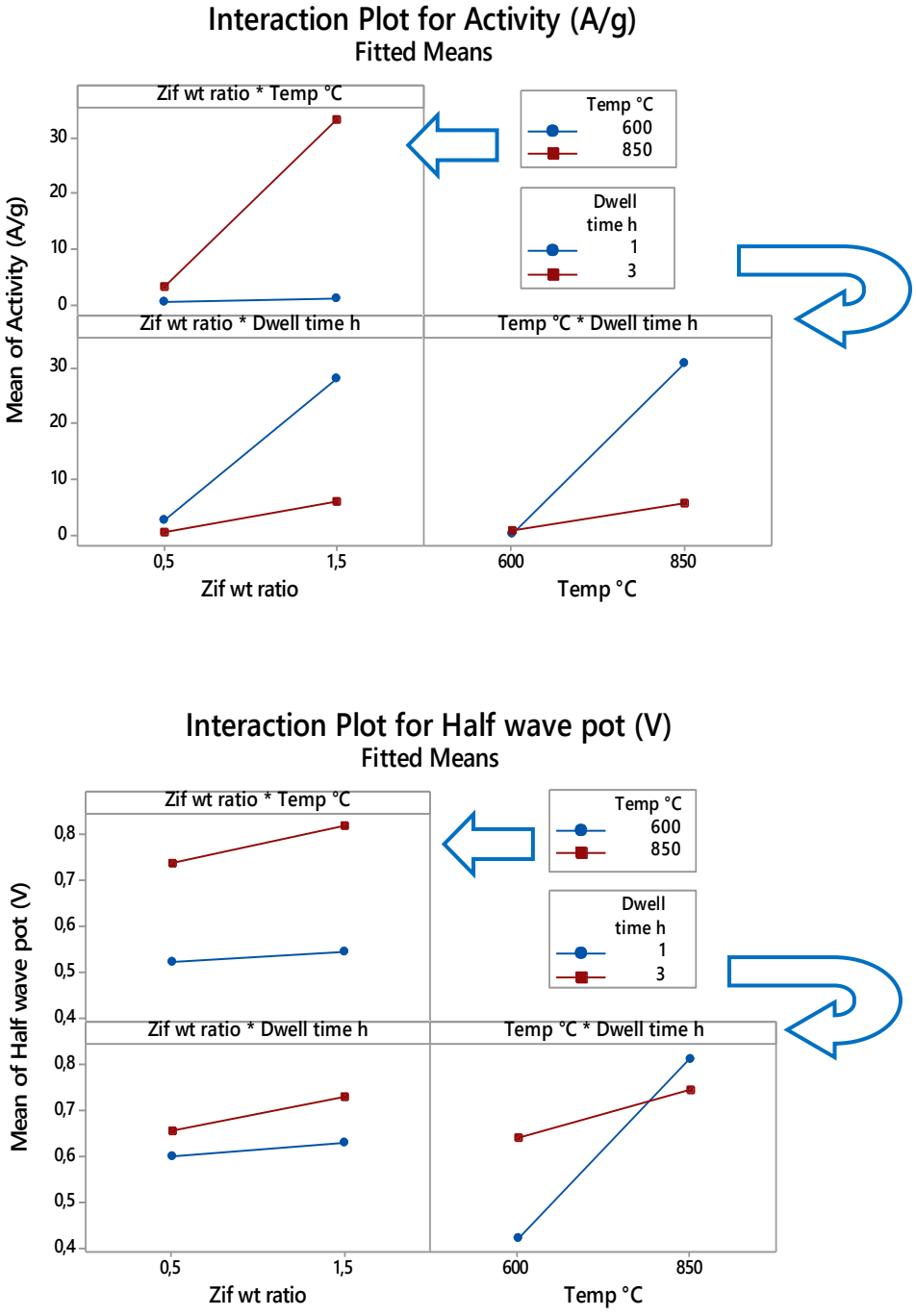

Figure 3.9. Interaction plot of the variables analyzed.

3.2.4 Zif-8/Fe(III)-Pc wt ratio (Z/F) optimization

The synthesis regarding the optimization of the Z/F was conducted following the DOE results. To increase activity, the idea was to increase the temperature of both the 1st and 2nd pyrolysis, while reducing the dwell time. Thus, additional samples with different Zif-8 weight ratio (from 0.5 to 2.5) were prepared increasing the temperature over 850 °C in only 1 h of dwell time.

During the pyrolysis steps all the samples were treated increasing the temperature from 25 to 800 °C at 10 °C min^{-1}, and then from 800 to 880 at 1.3 °C min^{-1}, followed by a natural cooling. This temperature ramp reflects in a dwell time of 1 h in which the temperature increases to reach the max value of 880 °C, whether in the previous set of experiments the temperature was maintained constant at 850 °C for 3 h, before the natural cooling. Then, the 2nd pyrolysis was conducted in the same way, but varying the atmosphere from an inert one (N_2 flow) to a reducing one (N_2/H_2 50%).

Table 3.5 shows the results of all the samples prepared with different Zif-8 weight ratio. In these analyses, the performances of the catalysts were good enough to allow the evaluation of the activity at 0.9 V, to allow for a direct comparison with platinum-based catalysts [193]. The column regarding the "mass loss" observed during the pyrolysis steps was introduced to consider the material loss caused by carbon matrix degradation and Zif-8 sublimation at high temperature. These values were obtained measuring the weight of the catalysts powder before and after the pyrolysis process (without prior drying treatment). **Figure 3.10 (A)** shows the results obtained from the stair case voltammetry recorded in O_2-saturated electrolyte in alkaline condition. **Figure 3.10 (B – C)** shows the relationship between the amounts of Zif-8 used in the synthesis and the electrochemical parameters, such as activity and onset/half-wave potential. As the Zif-8 wt ratio increases, activity mostly and electrochemical potentials improve. Unfortunately, considering the material lost during the 1st pyrolysis, these results show that the higher is the amount of Zif-8 respect the amount of Fe(III)-Pc, the higher is the mass lost during the pyrolysis. As a further matter, considering the similar onset potential and half-wave potential values of the samples Zif-8/Fe(III)-Pc = 1.5, 2, and 2.5 (**Table 3.5**), and the increasing loss of material during the pyrolysis, the sample Zif-8/Fe(III)-Pc = 1.5 has been taken as reference for further optimization, as a compromise between good activity and amount of catalyst remaining after the pyrolysis.

As a preliminary conclusion, further investigations are required to understand how to limit the material loss and how to optimize the pyrolysis process in a more effective way to keep good activity values without excessive material loss.

Table 3.5 Summary of the experiment result in terms of activity, onset and half-wave potential.

Pyrolysis parameters	Sample name	Mass Loss during pyrolysis (%)	Activity @0.9 V (A g^{-1})	Onset potential (V)	Half Wave potential (V)
Dwell time:1 h Max Temp: 880 °C	Z/F 0.5	≈ 65	0.2 ± 0.1	0.89 ± 0.01	0.79 ± 0.01
	Z/F 1.5	≈ 75	1.3 ± 0.3	0.92 ± 0.01	0.83 ± 0.02
	Z/F 2.0	≈ 80	1.7 ± 0.3	0.93 ± 0.01	0.83 ±< 0.01
	Z/F 2.5	> 85	2.1 ± 0.4	0.94 ± 0.01	0.84 ± 0.01

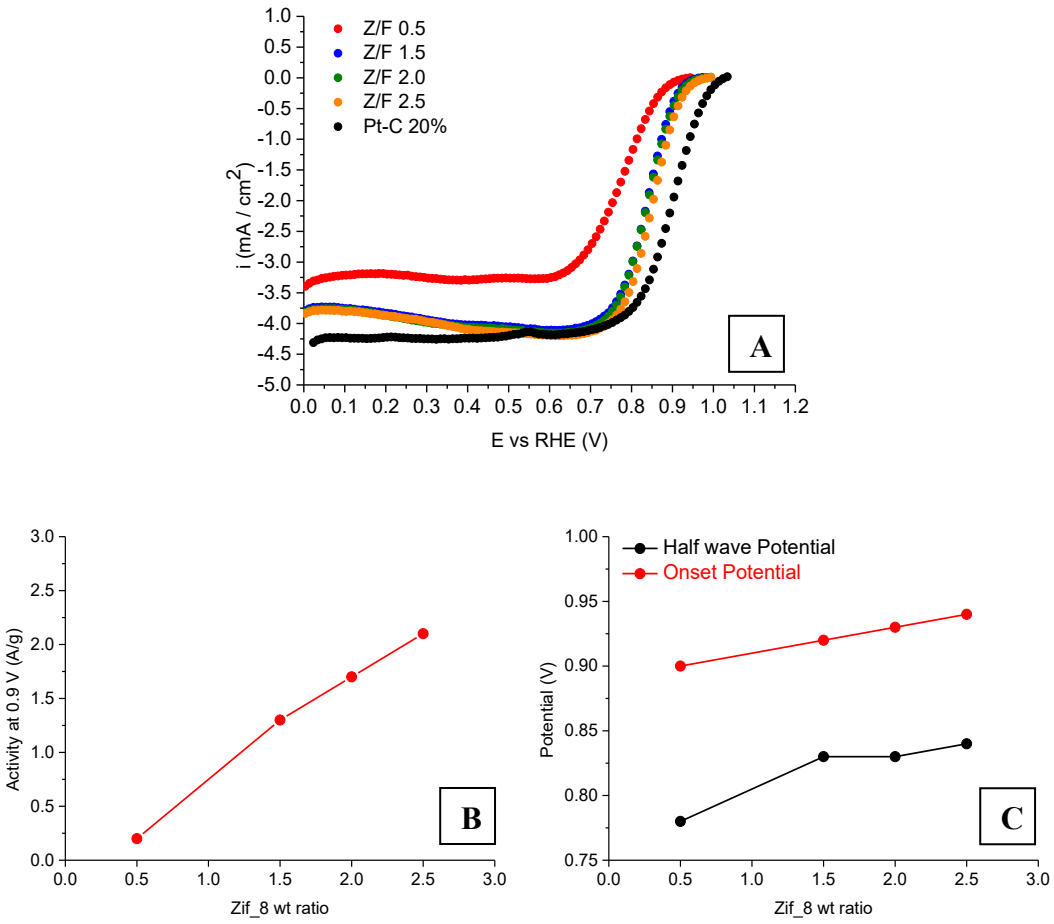

Figure 3.10. Result in terms of Stair case voltammetry (A), activity at 0.9 V (B) and onset/half-wave potential (C)

3.2.5 BET analysis

The BET analysis shows the specific surface area and the micropores properties of the four samples synthesized at different Zif-8 wt ratio (**Figure 3.11** and **Table 3.6**). The results show that increasing the amount of Zif-8 in each catalyst does not always lead to an increase in the specific surface area. In fact, sample Z/F 2.0 has less specific surface area than Z/F 1.5. The same behaviour is present considering the total micropore surface area and the total micropore surface volume. This deviation from the linearity of one sample has no significant valence since the Zif-8 sublimation process that take place during the pyrolysis involves several variables. In fact, the overall trend shows an increase of the specific surface area in function of the amount of Zif-8.

Data calculated by the DFT model show a microporous fraction comprised between 69 and 87% of the total BET specific surface area. Considering these results, a linear correlation can be observed among activity and the percentage of micropores.

Isotherms shows hysteresis loops closing at around 0.4 P/P_0. This is an indication of bottlenecks with diameter smaller than a critical size (estimated to be ca. 5–6 nm for nitrogen at 77 K) and cavitation-controlled evaporation [194,195]. Due to this effect, no quantitative information about the size and size distribution of necks can be deduced in the case of cavitation, consequently the peak located around 33 Å in the pore volume and surface DFT distributions is an artifact that corresponds to a cumulative volume and surface of mesopores hindered by bottlenecks with diameter smaller of the critical size [194,195].

A small difference in volume adsorbed and desorbed is observed in the isotherms. This difference can be ascribed to material swelling during adsorption and/or to non-reaching the equilibration time needed during the adsorption branch due to diffusion limit of nitrogen, especially for highly microporous materials as in this case.

Table 3.6. Results of nitrogen physisorption analysis

Sample name	BET specific surface area [$m^2 g^{-1}$]	Micropores surface area by DFT [$m^2 g^{-1}$]	% of microporosity	Micropores volume by DFT [$cm^3 g^{-1}$]
Z/F 0.5	224.2	155.8	69.5	0.074
Z/F 1.5	521.4	442.4	84.9	0.188
Z/F 2.0	494.5	421.4	85.2	0.171
Z/F 2.5	554.9	483.3	87.1	0.193

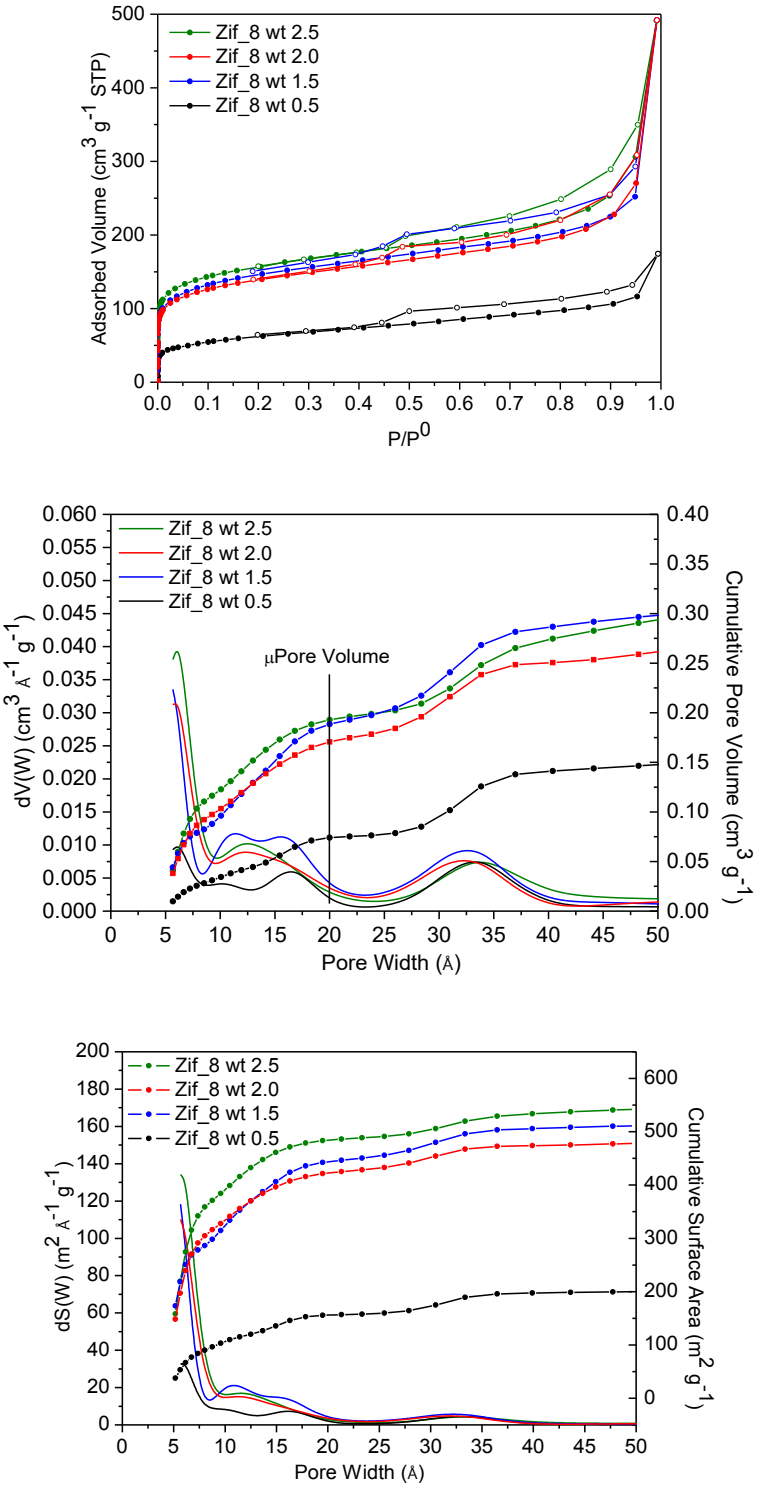

Figure 3.11. (A) Nitrogen adsorption/desorption Isotherms; (B) Cumulative total pore volume vs pore size by DFT model (N_2 on Carbon QSDFT, slit pores); (C) Cumulative total surface area vs pore size by DFT model (N_2 on Carbon QSDFT, slit pores)

3.2.6 Further considerations on the synthesis: number of pyrolysis and acid leaching investigation

This work aimed to evaluate the real influence of two pyrolysis steps and the role of the intermediary acid leaching. With the goal of have a better evaluation of the results, catalysts with higher activity were used. Z/F 2.0 S/F 1 was synthesized through two pyrolysis, respectively under N_2 atmosphere and forming gas (N_2/H_2 50%), but without intermediary acid leaching. This catalyst was then compared with the same synthesized considering the acid leaching in **Paragraph 3.2.5..** Z/F 2.5 S/F 1 was further synthesized by keeping it 2 h at the maximum temperature in a single pyrolysis instead of being subjected to two pyrolysis of 1 h at maximum temperature. This procedure provides the same amount of energy above 800 °C, but saves time and energy during the warm-up phase of the furnace. The powder obtained after this process was divided in two samples. The first one was analyzed after a final acid leaching treatment whilst the second one was directly analyzed without final acid leaching. This catalyst was then compared with the same synthesized through two pyrolysis processes described in **Paragraph 3.2.5**..

Figure 3.12 and **Table 3.7** show the results obtained after these two alternative ways. The sample Z/F 2.5 pyrolyzed twice showed higher activity at 0.9 V compared to the sample Z/F 2.5 pyrolyzed only one time. The acid leaching does not seem to affect the overall performance. After two heat treatments, sample Z/F 2.0 untreated with intermediary acid leaching shows an increase of only 0.1 A g^{-1} as activity and 0.01 V in half-wave potential (mean value). In any case the elimination of the acid leaching steps is beneficial in terms of preserved time and costs at industrial level.

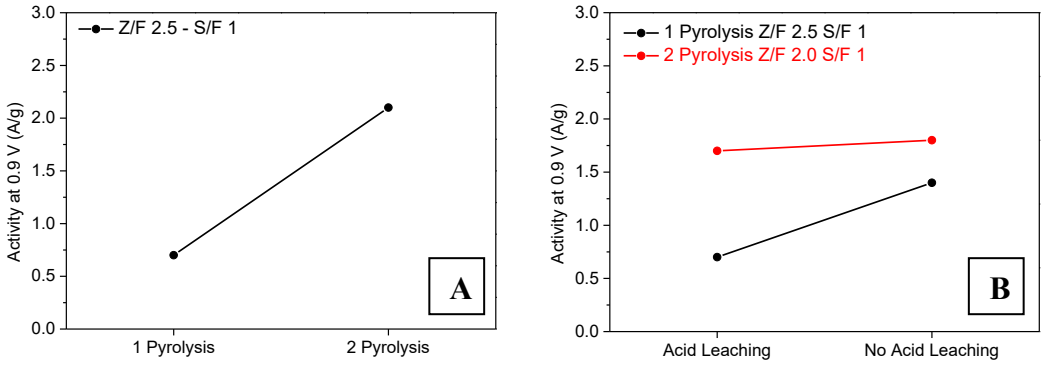

Figure 3.12. Influence of the number of pyrolysis steps (A) on the activity and evaluation of the contribution coming from the acid leaching (B).

Table 3.7. Summary of the electrochemical experiment result after 1 and 2 pyrolysis steps with/without acid leaching.

Pyrolysis parameters	Process	Activity @0.9 V (A g^{-1})	Onset pot (V)	Half Wave pot (V)
Temp 880 °C Z/F 2.0	2 pyrolysis 1 h + AL	1.7 ± 0.3	0.93 ± 0.01	0.83 ± <0.01
	2 pyrolysis 1 h	1.8 ± 0.6	0.94 ± 0.01	0.84 ± 0.01
Temp 880 °C Z/F 2.5	1 pyrolysis 2 h + AL	0.7 ± <0.1	0.92 ± <0.01	0.82 ± <0.01
	1 pyrolysis 2 h	1.4 ± <0.1	0.93 ± <0.01	0.83 ± <0.01
	2 pyrolysis 1 h + AL	2.1 ± 0.4	0.94 ± 0.01	0.84 ± 0.01

3.2.7 2nd optimization step

The process optimization continued through the study of a series of parameters concerning the synthesis in autoclave. In this step, the influence of the sulphur concentration, type of solvent and synthesis temperature (which is related with the internal vapour pressure) were studied. **Figure 3.13** summarized all the parameters studied in this section.

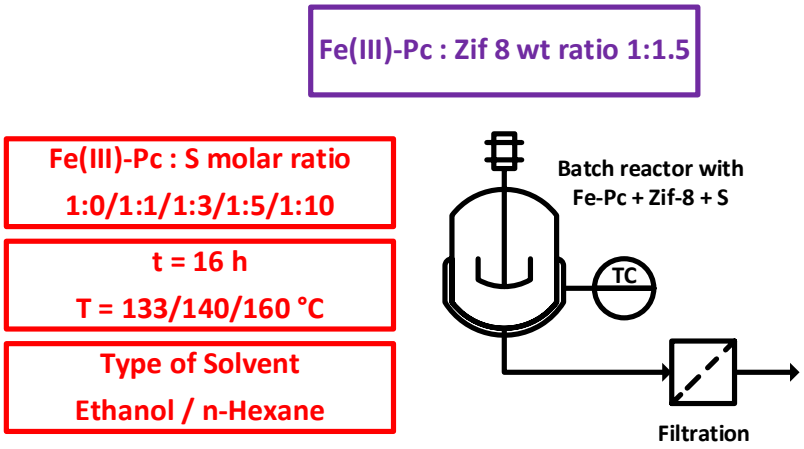

Figure 3.13. Optimization of the synthesis in autoclave. Constant parameters in violet, variable parameters in red.

First sulphur concentration evaluation in ethanol

To further increase the protection of the active centre, an addition of sulphur to the precursor mixture before the heat treatments was made. The sulphur molar concentration was varied in base of the mol of Fe(III)-Pc present in the precursor mixture keeping the Zif-8/Fe(III)-Pc wt ratio constant at 1.5. Three samples were prepared: the first without sulphur, the second with the same molar concentration

of sulphur compared to Fe(III)-Pc and the third with a triple molar concentration. The catalysts are labelled as S/F 0, S/F 1, S/F 3 respectively. **Table 3.8** and **Figure 3.14** show the electrochemical results. The catalyst with the highest concentration of sulphur (S/F 3M) has the best performance in terms of activity at 0.9 V. Using a triple sulphur molar concentration respect to the iron phthalocyanine results in an increase of activity from 1.1 to 2.4 A g^{-1}.

Table 3.8. Summary of the electrochemical experiment result for different sulfur concentrations.

Synthesis parameters	Sample name	Activity @0.9 V (A g^{-1})	Onset pot (V)	Half. wave. pot (V)
Dwell time: 1h Temp: 880 °C Z/F 1.5	S/F 0	0.1 ± 0.1	0.88 ± 0.01	0.74 ± 0.01
	S/F 1	1.1 ± 0.2	0.93 ± 0.01	0.82 ± 0.02
	S/F 3	2.4 ± 0.0	0.95 ±< 0.01	0.84 ± 0.01

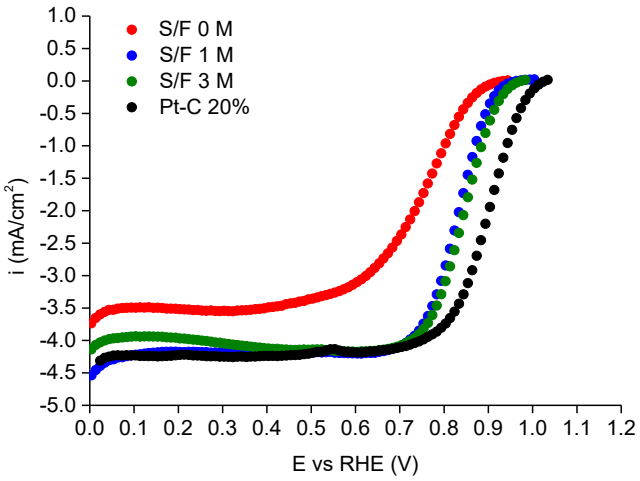

Figure 3.14. SSV recorded in O_2-saturated electrolyte in alkaline condition relating catalysts obtained with different sulphur concentration.

Role of the type of solvent inside the autoclave

Two more experiments were carried out varying the solvent used inside the autoclave. The first experiment was carried out by placing hexane at 140 °C for 16h. 140 °C was chosen as process temperature since 69 °C is the boiling temperature (140°C = 2xBoiling temp.). All the synthesis carried out previously in ethanol where performed at 160 °C since 78.4 °C is the ethanol boiling temperature. With the aim to equate the two solvents with the same vapour

pressure inside the autoclave, a second experiment was carried out in ethanol at 133 °C. In fact, working at 133 °C with ethanol provides the same conditions obtained working at 140 °C with hexane in terms of vapour pressure (622 kPa). The two catalysts were synthesised varying only the solvent or the autoclave temperature keeping constant the composition Z/F 1.5 S/F 3. The aim was to compare the results with the best catalyst described previously Paragraph. **Table 3.9** gives a summary of all the physicochemical parameters regarding the oxygen solubility (at 101325 Pa and 298.15K) and the vapour pressure constants for both the solvents: ethanol and hexane.

Table 3.9. Summary of physicochemical parameters regarding the oxygen solubility and the vapour pressure constants for ethanol and hexane.

Solvent	**O_2 Henry constant (MPa)**	**Solubility O_2 mol fraction** [196]	**T (°C)**	**A (mmHg)**	**B (mmHg)**	**C (mmHg)**	***p* *(kPa)***
Ethanol	154.2 [197]	0.57	160	7.7	1332.0	199.2	1252.3
			133	7.7	1332.0	199.2	625.6
Hexane	51.0 [198]	2.25	140	7.0	1246.3	233.0	622.2

Figure 3.15 (A-B) shows the comparison of the catalysts prepared with different solvents in terms of stair case voltammetry recorded in O_2-saturated electrolyte in alkaline condition. Specifically, **Figure 3.15 A** shows the results obtained heating the different solvents (inside the autoclave) two times their boiling temperature, while **Figure 3.15 B** shows the results obtained heating the solvents at different temperature corresponding to the same vapour pressure as suggested by the Antoine equation.

Table 3.10 lists all the results and the comparison obtained from the experiments described above. Synthesizing the sample in ethanol at different temperatures in the range of 130 - 160 °C does not change the results: activity and half-wave potential remain the same. The use of hexane instead of ethanol, significantly increases the activity of the catalyst, from 2.4 to 8.7 A/g and the half-wave potential from 0.84 to 0.87V. This result is comparable than the best current results present in literature for this class of catalysts obtained from Strickland et al.[18].

Table 3.10. Summary of the experiment result in terms of activity, onset and half-wave potential.

Synthesis parameters	Solvent	T (°C)	P (kPa)	Activity @0.9 V (A g^{-1})	Onset potential (V)	Half Wave potential (V)
Dwell time: 1h Temp: 880 °C Zif wt ratio: 1.5 S Molar ratio: 3	Ethanol	160	1252	2.4 ±< 0.1	0.95 ±< 0.01	0.84 ± 0.01
		133	626	2.4 ± 0.2	0.95 ± 0.01	0.84 ± 0.01
	Hexane	140	622	8.7 ± 0.4	0.98 ±< 0.01	0.87 ± 0.01

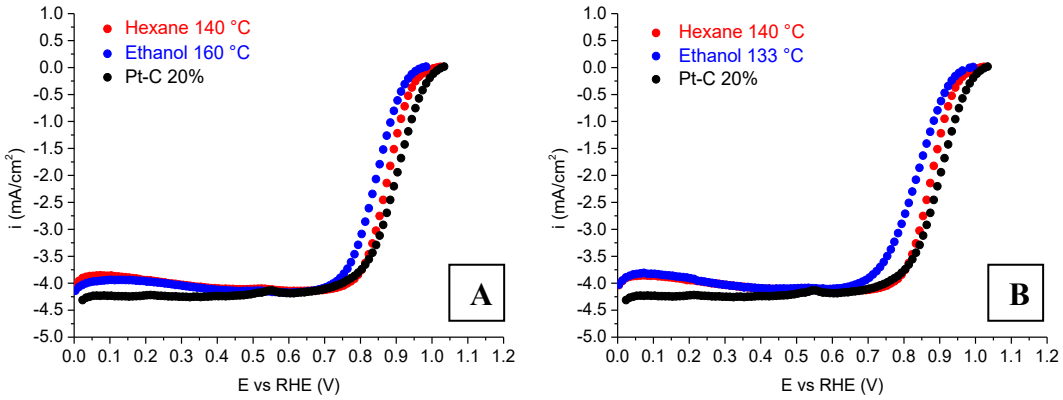

Figure 3.15. SSV recorded in O_2-saturated electrolyte in alkaline condition relating catalysts obtained heating the solvents inside the autoclave two times their boiling temperature (A) heating the solvents at different temperature corresponding to the same vapour pressure (B).

Under the previously described process condition, operating with hexane at 140 °C or with ethanol at 133 °C provides the same partial pressure, but physical parameters such as oxygen solubility and polarity are different. In order to evaluate the surface elemental composition of the catalysts obtained respectively through synthesis in ethanol or hexane, XPS analysis were made. **Figure 3.16** and **Table 3.11** show the results obtained. The chemistry of nitrogen and carbon was analyzed evaluating the different contributions of chemical groups [199,200]. At first glance, it seems that treating the raw materials with the same vapour pressure in the autoclave, produces the same final chemical composition in terms of carbon, nitrogen and oxygen %. More in detail, **Figure 3.16 (A-B)** shows C_{1s} spectra curves fitted using multiple peaks due to the presence of graphitic carbon (284.4), carbon coordinated to carbon oxides C*-C_xO_y (285.3 eV) and a combination of general carbon oxides O-C=O (288.5 eV), C-O/C-O-C (286 eV), C=O (289 eV), and COOH (289.4 eV). Metal carbides are not present (283 eV). The sample synthesized in hexane has lower amount of graphitic carbon and higher amount of CxOy and C*-C_xO_y.

Figure 3.16 (C-D) shows N_{1s} spectra curves where pyridinic-N occurs at ~398 eV, pyrrolic or hydrogenated N at 400.9-401.4 eV, N-graphite species at 403.3 eV, and Nx-Fe at 399.0-399.8 eV. The sample synthesized in hexane shows the highest amount of metal centers (N_x-Fe), typically recognized as active sites for ORR [74,93]. This behaviour seems to affect the final activity of the catalyst positively.

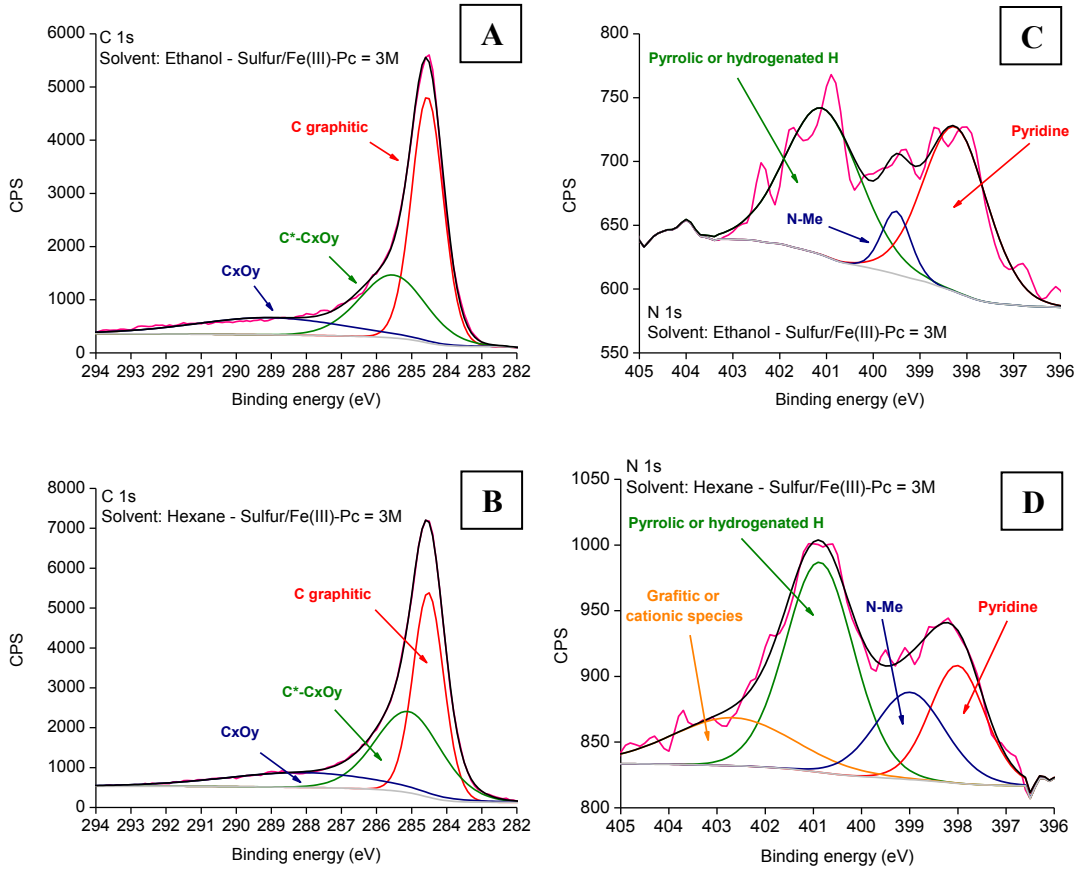

Figure 3.16. XPS spectra of C_{1s} and N_{1s} for sample synthesized in ethanol or hexane at the same vapour pressure inside the autoclave. The red and the black lines are the raw and the fitted spectra, respectively. A) XPS spectra of C_{1s}, sample prepared in ethanol. B) XPS spectra of C_{1s}, sample prepared in hexane. C) XPS spectra of N_{1s}, sample prepared in ethanol, D) XPS spectra of N_{1s}, sample prepared in hexane.

Table 3.11. Elemental composition of samples synthesized in ethanol and Hexane at the same vapour pressure (622 KPa)

Solvent		*Composition of C (Rel %)*			
	C (at%)	**Graphitic**	C_xO_y	C^*-C_xO_y	*O (at%)*
Ethanol 133 °C	90.5	53.70	17.50	28.80	6.3
Hexane 140 °C	90.6	44.96	16.40	38.65	6.2

Solvent		*Composition of N (Rel %)*			
	N (at%)	*Pyrrolic or hydrogenated H*	*Pyridinic*	*N-Me*	*Grafitic or cationic species*
Ethanol 133 °C	3.2	47.05	45.18	7.77	-
Hexane 140 °C	3.1	43.65	19.87	18.56	17.92

Second sulphur concentration evaluation in Hexane

A second study was performed to evaluate in deep the role of the sulphur when the synthesis is carried out in hexane. In this case five different molar sulphur concentration were evaluated (S/F 0, S/F 1, S/F 3, S/F 5, S/F 10) keeping the Zif-8/Fe(III)-Pc wt ratio constant at 1.5. The result showed in **Table 3.12** and in **Figure 3.17** demonstrated that also in this experiment the catalyst with molar sulphur concentration three times higher than the concentration of the phthalocyanine (S/F 3) has the best performance with 8.7 A g^{-1} in terms of activity at 0.9 V and 0.87 as half-wave potential.

Table 3.12. Summary of the electrochemical experiment result for different sulphur concentrations.

Synthesis parameters	**Sample name**	**Activity @0.9 V (A g^{-1})**	**Onset pot (V)**	**Half. Wave. pot (V)**
Dwell time: 1h Temp: 880 °C Z/F wt ratio: 1.5	S/F 0	0.7 ± 0.1	0.92 ±< 0.01	0.80 ± 0.01
	S/F 1	2.2 ± 0.2	0.92 ±< 0.01	0.84 ± 0.01
	S/F 3	8.7 ± 0.4	0.98 ±< 0.01	0.87 ± 0.01
	S/F 5	2 ± 1	0.94 ± 0.01	0.82 ± 0.02
	S/F 10	1.1 ± 0.2	0.93 ± 0.01	0.82 ± 0.01

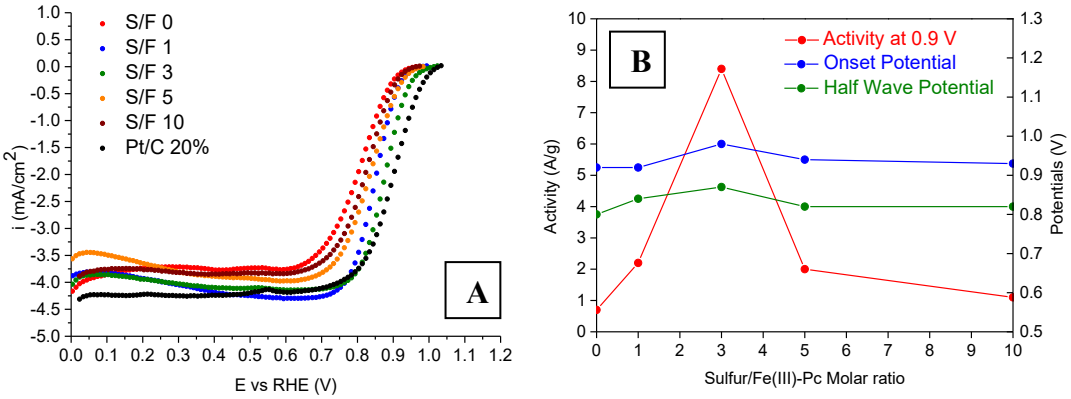

Figure 3.17. SSV recorded in O_2-saturated electrolyte in alkaline condition relating catalysts obtained with different sulphur concentration (A) and Electrochemical parameters as a function of sulphur concentration (B).

Figure 3.18 and **Table 3.13** show the XPS analysis relative to the catalyst prepared in presence and in absence of sulphur. The chemistry of nitrogen and carbon was analyzed evaluating the different contributions of chemical groups [A,B]. **Figure 3.18 (A-B)** shows C_{1s} spectra curve fitted using multiple peaks due to graphitic carbon (284.4 eV), carbon coordinated to carbon oxides C*-C_xO_y (285.3 eV), and a combination of general carbon oxides O-C=O (288.5 eV), C-O/C-O-C (286 eV), C=O (289 eV) and COOH (289.4 eV). The catalyst not treated with sulphur shows a well-defined peak in the reference zone of the metal carbides (283 eV), confirming the results reported in literature [138]. In fact, the presence of Sulphur produces iron monosulphide (FeS) instead of iron carbide (FexC) during the heat treatment [C]. Additionally, FeS can be removed during the acid leaching step.

Figure 3.18 (C-D) shows N_{1s} spectra curves where pyridinic-N occurs at ~398 eV, pyrrolic or hydrogenated N at 400.9-401.4 eV, N-graphite species at 403.3 eV, and Nx-Fe at 399.0-399.8 eV. The sample synthesized in presence of sulfur shows the highest amount of metal centers (N_x-Fe). The absence of FexC slows the graphitization of the pyrolysis products and as a result, the catalytic active centres are preserved [138].

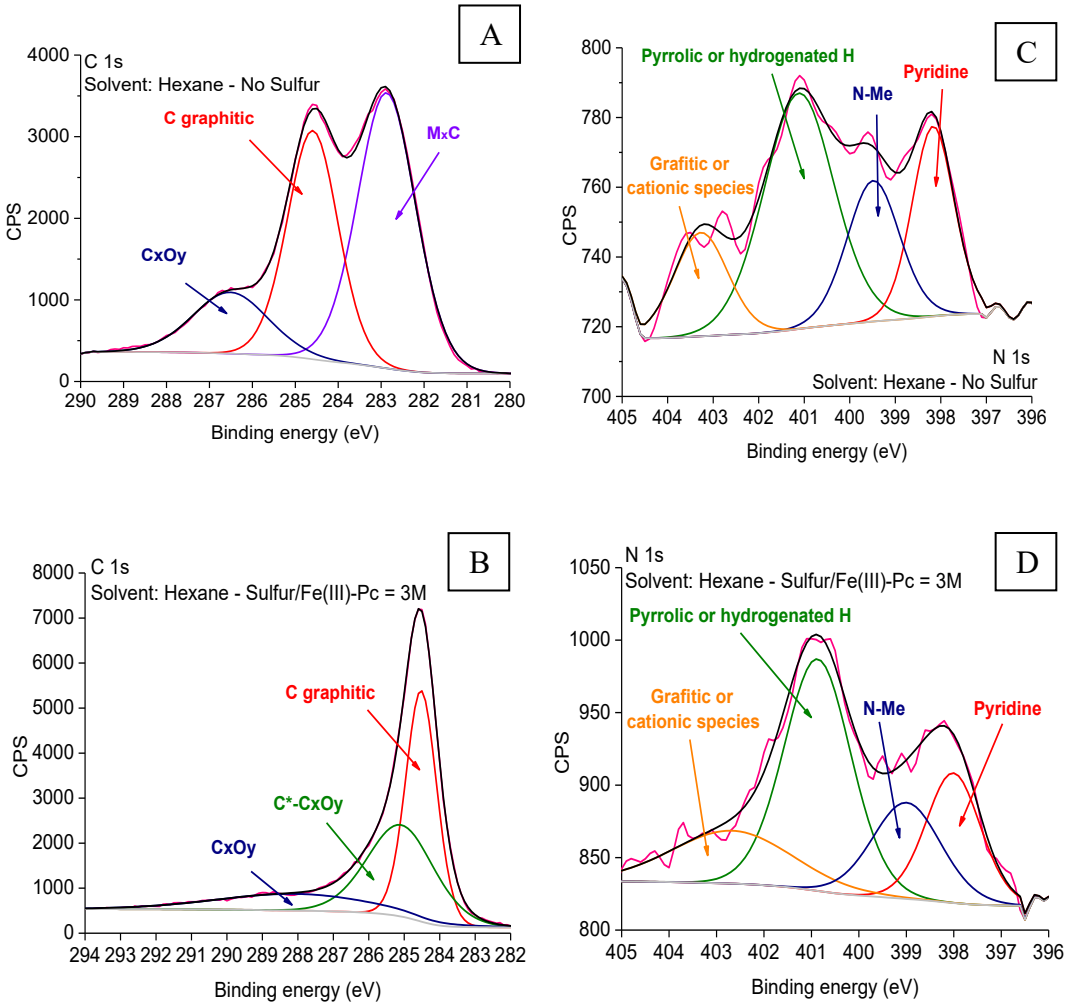

Figure 3.18. XPS spectra of C_{1s} and N_{1s} for sample synthesized in hexane in the presence or absence of sulfur. The red and the black lines are the raw and the fitted spectra, respectively. A) XPS spectra of C_{1s}, Sample without sulphur. B) XPS spectra of C_{1s}, sample in presence of sulphur. C) XPS spectra of N_{1s}, Sample without sulphur. D) XPS spectra of C_{1s}, sample in presence of sulphur.

Table 3.13. Elemental composition of samples synthesized in Hexane at 140 °C with different sulfur concentrations

S/F		*Composition of C (Rel %)*				
	C (at%)	*Graphitic*	*C_xO_y*	*C*-C_xO_y*	*FexC*	*O (at%)*
0	79.8	35.98	14.22	-	49.79	19.2
3	90.6	44.96	16.40	38.64	-	6.2

S/F		*Composition of N (Rel %)*			
	N (at%)	*Pyrrolic or hydrogenated H*	*Pyridinic*	*N-Me*	*Grafitic or cationic species*
0	1.0	45.72	24.17	15.28	14.83
3	3.1	43.65	19.87	18.56	17.92

3.2.8 Further considerations on the synthesis: use of the ball milling as alternative to the hydrothermal synthesis

The Zif-8 based catalyst was also synthesized by replacing the hydrothermal process with a mechanochemical synthesis, through the use of the ball milling technique (jar volume 25 ml, 3 balls 10 mm of diameter, frequency 20 Hz, time 15 min). This experiment had the goal to eliminate the solvents used in the autoclave, to obtain a catalyst with a comparable, or better performance (Z/F 1.5 – S/F 3). **Figure 3.19** and **Table 3.14** show the results in terms of ORR curve and electrochemical activity. **Figure 3.19** shows the difference between the ORR polarization curve of the catalyst obtained after the ball milling operation with and without the two heat treatments with intermediary acid leaching. **Table 3.14** shows only ORR parameters of the pyrolyzed catalyst because the polarization curve of the catalyst without heat treatment is not well defined and shows low activity. For this class of materials, the results confirm that heat treatments increase the performances by affecting the nature of the catalyst through the active site formation, the activation of existing sites, and the carbon graphitization, as also demonstrated in the literature [83,201].

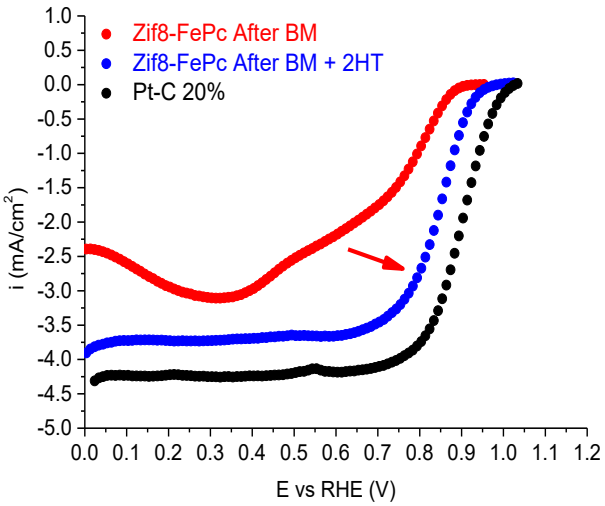

Figure 3.19. SSV recorded in O_2-saturated electrolyte in alkaline condition comparing catalysts obtained through ball milling with and without heat treatment. Pt/C catalyst performance added for comparison.

Table 3.14. Summary of the electrochemical experiment of the Zif8-FePc catalyst obtained through ball mill process after two heat treatment.

Catalyst	Activity 0.9 V (A g^{-1})	Onset pot (V)	H. W. pot (V)
Z/F 1.5 – S/F 3	1.5 ± 0.6	0.95 ± < 0.01	0.85 ± < 0.01

Although this type of process is cheaper, the catalyst show lower performance respect to the same produced by hydrothermal synthesis. The order of magnitude is the same but the half-wave potential is 20 mV lower respect the previously best catalyst (Z/F 1.5 – S/F 3 autoclave + 2 heat treatment – **Table 3.12**). In any case, these catalysts are not able to reach the performance of the reference Pt/C catalyst.

3.2.9 Fe(III)-Pc with Basolite Z 1200 catalyst conclusions

At the end of the synthesis optimization, the best catalyst has proven to be the one synthesized in hexane with a sulfur concentration three times higher respect the molar concentration of iron phthalocyanine and Zif-8/Fe-Pc weight ratio equal to 1.5. The maximum temperature reached during the pyrolysis step was 880 °C and the dwell time at high temperatures between 800 and 880 °C was 1 h. For this class of materials, the number of pyrolysis seems to affect the performance more than the acid leaching. Moreover, the hydrothermal synthesis proved to be more effective in producing active catalysts respect to the mechanochemical ball milling method. The final catalyst, obtained with the combination of the best parameters and two heat treatments, was then named **"**Z/F 2HT" catalyst and was studied more in detailed in terms of kinetics, durability, and physical-chemical properties in **Chapter 4**.

3.3 2nd Catalyst: Fe(II)-Pc with Vulcan Carbon XC 72

3.3.1 Introduction to the catalyst synthesis

In the first part of this work, Iron(II) phthalocyanine $C_{32}H_{16}FeN_8$ (Fe(II)-Pc) was mixed with Vulcan XC 72 (Vulcan) as conductive carbonaceous support [22]. The synthesis consists of only a single mechanical mixing as described by *S. Zhang et al* [133] with the modification of the type of Vulcan and the evaluation of the best weight ratio. The first weight ratio between Vulcan and the Fe(II)-Pc was set at 1.5, taken as a reference value from the optimal catalyst synthesised previously. 450 mg of Vulcan were added to 300 mg of Fe(II)Pc and the mixture was transferred in a stainless steel jar (volume 25 ml) with 3 stainless steel balls (diameter 10 mm). **Figure 3.20** shows the chemical process scheme. The jar was placed in a ball mill with translational movement (**Figure 3.21**) and subjected at a frequency of 20 Hz for 15 min. Although the combination of phthalocyanines with Vulcan is well known [203], the application of this mechanochemical process to this mixture is quite recently. Since the evaluation of the right Vulcan/Fe(II)-Pc weight ratio was not carried out and is not still present in literature [133,134], a series of different ratio were studied to understand which was the best combination in terms of RDE-ORR performances. The goal of this process was to evaluate and demonstrate the performance of the catalyst only with the use of a ball mill and without expensive thermal treatments.

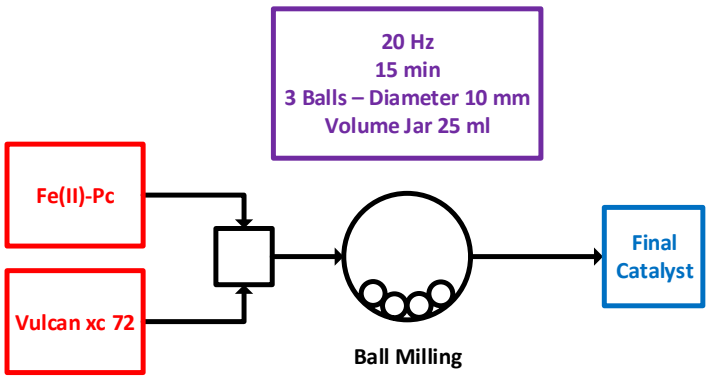

Figure 3.20. Scheme of the synthesis process - 1st step.

Afterward, the catalyst obtained from the first step, have been subjected to three different synthesis processes. These experiments aimed to evaluate if specific heat treatments positively or negatively affect the final activity and durability of the Vulcan/Fe(II)-Pc based catalysts in alkaline conditions. In the first process variation, the Vulcan was pyrolyzed before the ball milling process. This preliminary heat treatment aimed to increase the conductivity of the support improving the graphitization of the carbonaceous matrix.

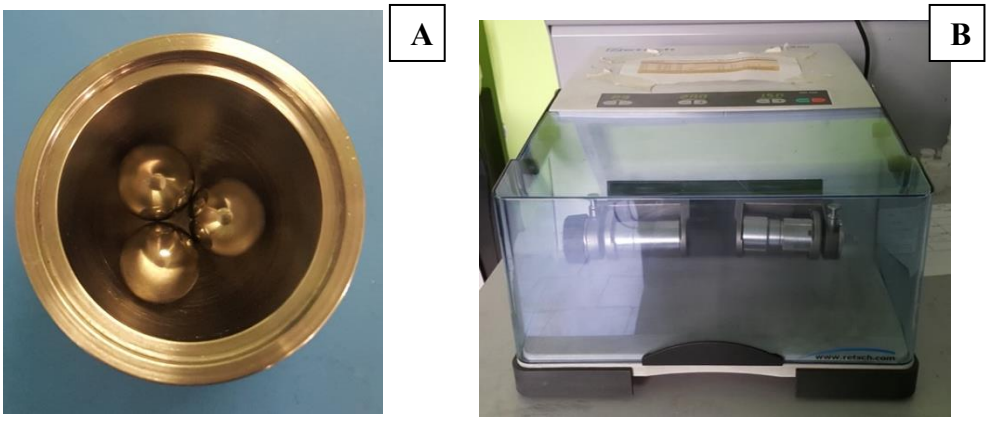

Figure 3.21. A) Stainless steel jar with balls. B) Translational ball mill.

In the second process variation, the catalyst obtained from the ball milling process was heat-treated at 400 °C for 2 h under nitrogen and hydrogen atmosphere flow. The purpose of this treatment was to carry out a sort of annealing at low temperature under hydrogen reductive atmosphere.

The last process is the most complicated. The two starting reagents are first ball milled together, then pyrolyzed, acid leached, pyrolyzed a second time, and the resulting powder ball milled again. In contrast to the previous synthesis, this experiment would like to see if for this mixture combination, an heat treatments between 600 and 1000 °C under inert atmosphere have good benefits in ORR activity and stability as describe in literature [100]. At these high temperatures the Vulcan is subjected at two different graphitization process [204,205]. The acid leaching was carried out to remove the iron oxide not incorporated in the catalyst matrix. These particles are formed during the exposure to the air after being taken out from the inert atmosphere present in the pyrolysis furnace [138,188]. **Figure 3.22** shows the summary of the 3 steps previously described. To facilitate the interpretation of the results, the Vulcan / Fe(II)-Pc weight ratios was labelled as V/F.

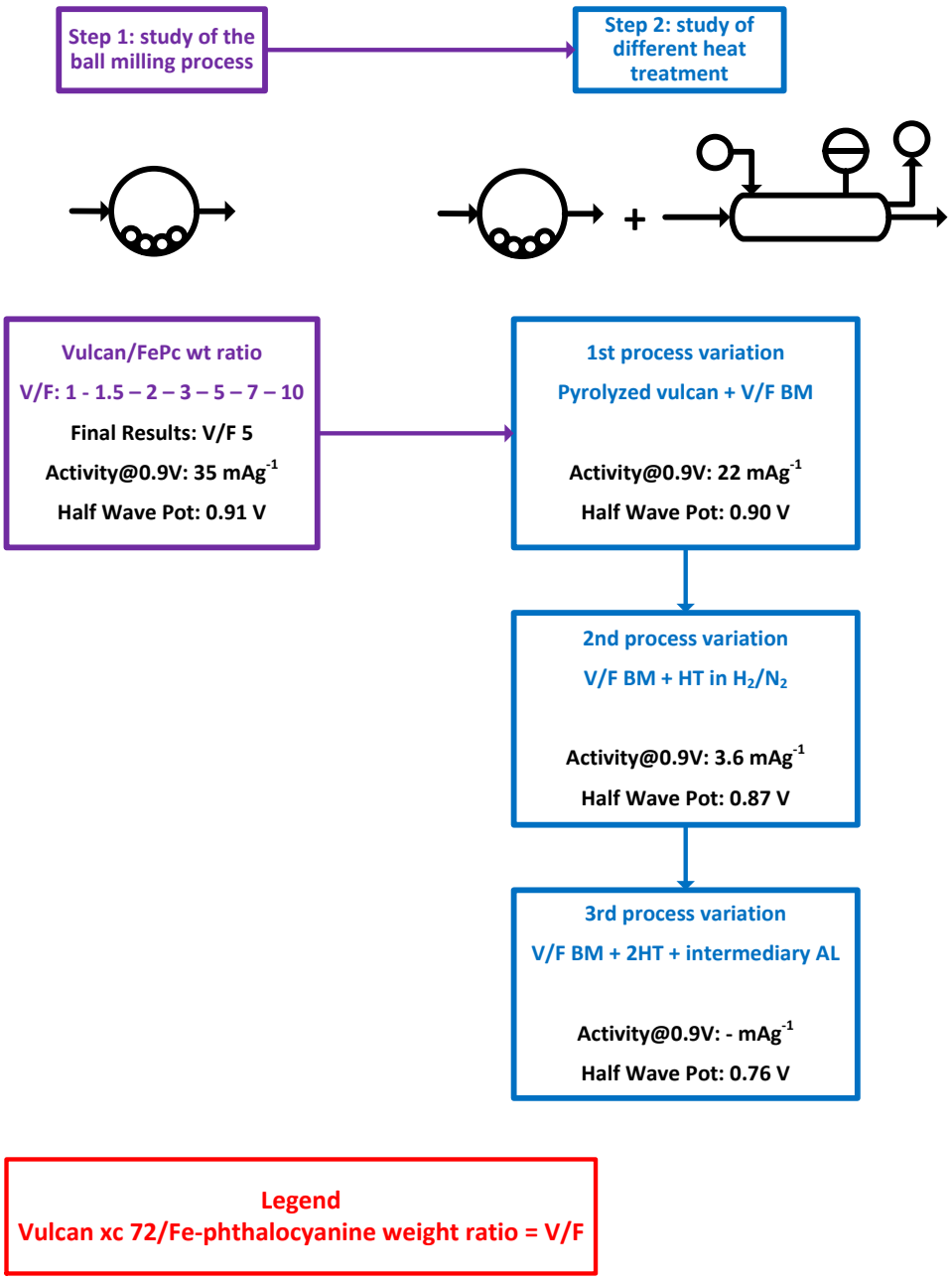

Figure 3.22. Summary of the chemical process steps relative to the second synthesis

3.3.2 1st process: Vulcan/Fe(II)-Pc wt ratio (V/F) optimization

The ratios V/F 1.0, V/F 2.0, V/F 3.0, V/F 5.0, V/F 7.0 and V/F 10 were synthesised in addition to the first reference ratio of V/F 1.5 to evaluate V/F combination. **Figure 3.23 – 3.24** and **Table 3.15** show the electrochemical results, which prove that the quality of the catalyst increases until the V/F ratio reach the value of 5. With V/F = 5, the catalyst shows an half-wave potential of 0.91 V and 35 A g^{-1} as activity at 0.90 V, which is better of the Pt/C reference (0.91 V and 23.6 A g^{-1}, respectively). Instead, in term of onset potential, the Pt/C reference is

slightly better, with a value of 1.01 V compared to 0.96 V of the non noble catalyst.

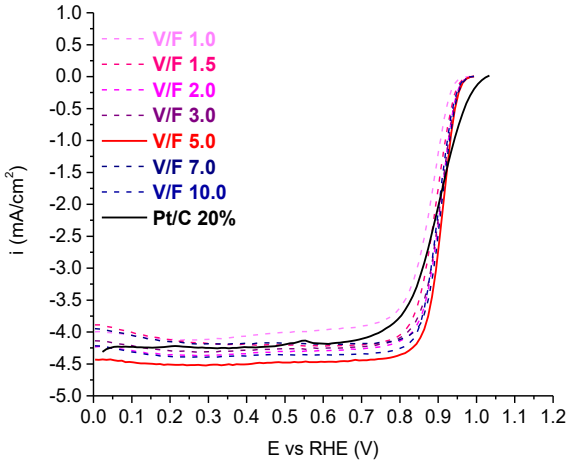

Figure 3.23: SSV recorded in O_2-saturated electrolyte in alkaline condition related to V/F catalysts obtained through ball milling. The black and red solid line indicate respectively the Pt/C 20% and the V/F 5.

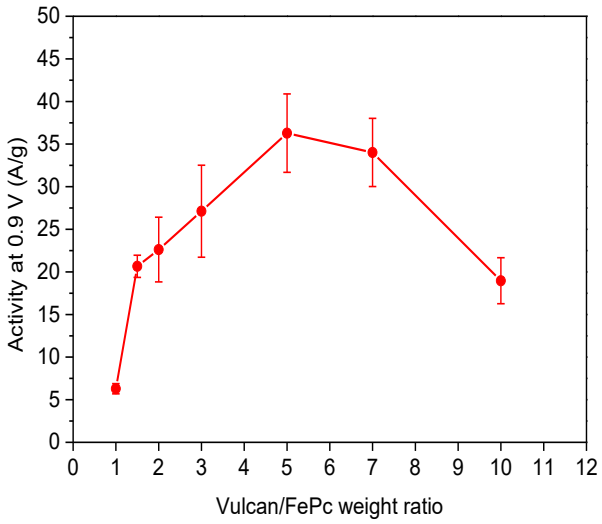

Figure 3.24: Activity at 0.9V of V/F catalysts obtained through ball milling with different weight ratios. Measurements repeated three times.

Table 3.15. Summary of the electrochemical results of V/F catalysts prepared by ball milling.

Sample name	Activity 0.9 V (A g^{-1})	Onset pot (V)	H. W. pot (V)
V/F 1.0	6.3 ± 0.6	0.94 ± < 0.01	0.88 ± < 0.01
V/F 1.5	21 ± 1	0.96 ± < 0.01	0.89 ± 0.01
V/F 2.0	23 ± 4	0.96 ± 0.01	0.90 ± < 0.01
V/F 3.0	27 ± 6	0.96 ± 0.01	0.90 ± 0.01
V/F 5.0	35 ± 4	0.96 ± < 0.01	0.91 ± 0.01
V/F 7.0	34 ± 4	0.96 ± < 0.01	0.91 ± < 0.01
V/F 10.0	19 ± 3	0.96 ± < 0.01	0.90 ± 0.01
Pt/C 20%	23.6 ± 0.2	1.01 ± < 0.01	0.91 ± 0.01

3.3.3 Application of different thermal treatment: fundamental.

The catalyst with the best wt ratio obtained from the previous analysis (V/F = 5) was used for all these type of experiments. The electrochemistry activity was analyzed through the evaluation of the kinetic current, the mass activity, the onset potential and the half-wave potential. The analysis was performed on all the catalysts except for those with bad performances or with a diffusion limit current not well defined due to low performance in this region. In this case, the calculation of the kinetic current and the activity was omitted and only the evaluation of the half-wave potential was considered.

2nd Process – Vulcan/FePc wt ratio 5:1 synthesized through ball milling after Vulcan Pyrolysis

The second process adds a pyrolysis step before the ball milling. The pyrolysis step was conducted only to the Vulcan XC 72, at 850 °C for 1 h under nitrogen atmosphere flow (N_2 flux: 50 ml/min). The heating rate was set at 10 °C/min. The Fe(II)-PC was added in the following ball milling step. **Figure 3.25** shows the process scheme. **Figure 3.26** and **Table 3.16** Showed the results. The performance are quite lower respect to the not thermally treated catalyst, with 22 A g^{-1} as mass activity and 0.90 V as half-wave potential. Since the results are not satisfactory and the process is more expensive compared to the previous one, this procedure was not considered anymore.

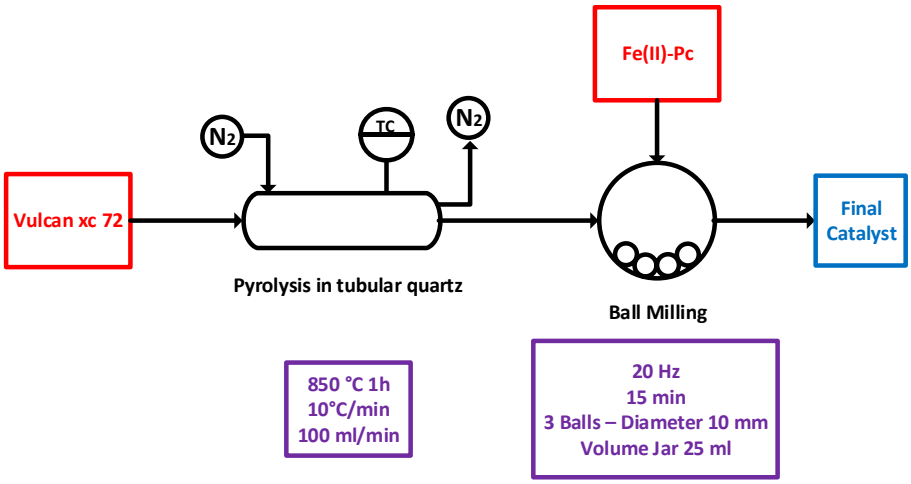

Figure 3.25. Scheme of the synthesis process – 2nd step

Table 3.16. Summary of the experiment result in terms of activity, onset and half-wave potential.

OnSet pot (V)	HW pot (V)	I_k (mA/cm^2)	Activity 0.9 V (A/g)
0.96 ± 0.01	0.90 ± 0.01	9 ± 4	22 ± 11

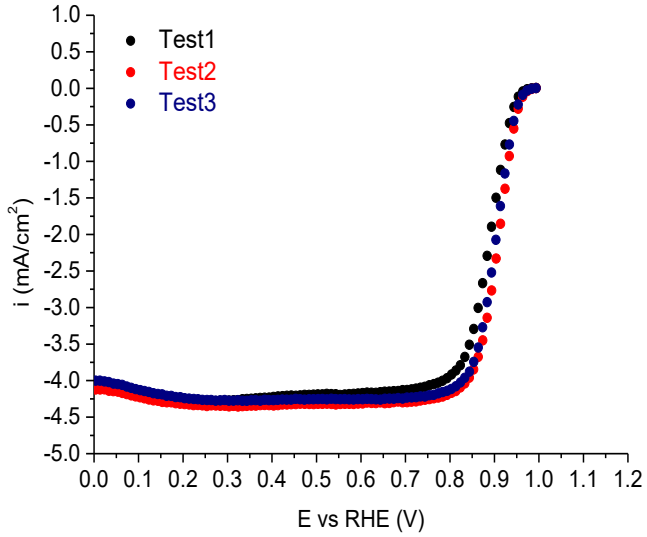

Figure 3.26. SCV recorded in O_2-saturated electrolyte in 0.1 M KOH alkaline solution. Measurements repeated three times.

3rd Process – Vulcan/FePc wt ratio 5:1 synthesized through ball mill followed by Annealing in N_2/H_2

In the third process, the two starting reagents, Vulcan and FePc, were first mixed with a ball milling step, then heat-treated at 400 °C for 2 h under nitrogen and hydrogen atmosphere flow (N_2 flux: 75 ml min^{-1}, H_2 flux: 25 ml min^{-1}). The

heating rate was set at 10 °C min^{-1}. **Figure 3.27** shows the process scheme. The relative low temperature of 400 °C is to preserve the phthalocyanine from the total thermal degradation [206]. The presence of hydrogen during the thermal process is useful to reduce the amount of the inorganic metal particles which partly decrease the final activity of the catalyst [189]. **Figure 3.28** and **Table 3.17** show the results obtained. The catalyst produced in this way has a low activity, especially if compared to the catalysts produced with the other processes. In fact, the mass activity was almost 4 A g^{-1} and half-wave potential 0.87 V.

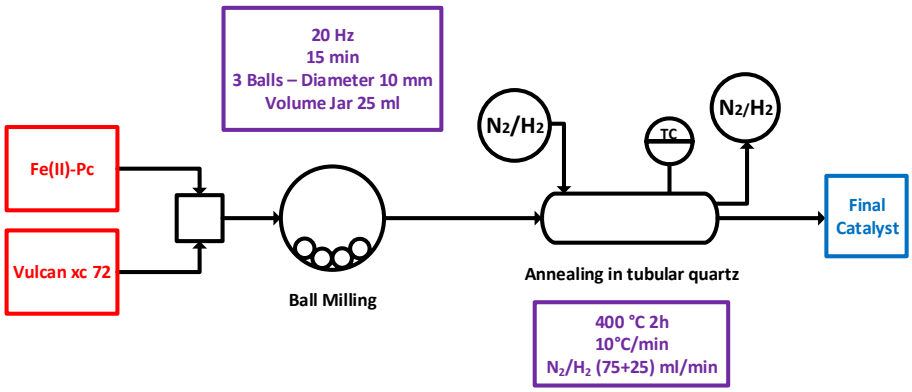

Figure 3.27. Scheme of the synthesis process – 3rd step.

Table 3.17. Summary of the experiment result in terms of activity, onset and half-wave potential.

OnSet pot (V)	HW pot (V)	Ik (mA/cm^2)	Activity 0.9 V (A/g)
0.93 ± < 0.01	0.87 ± 0.01	1.4 ± 0.2	3.6 ± 0.6

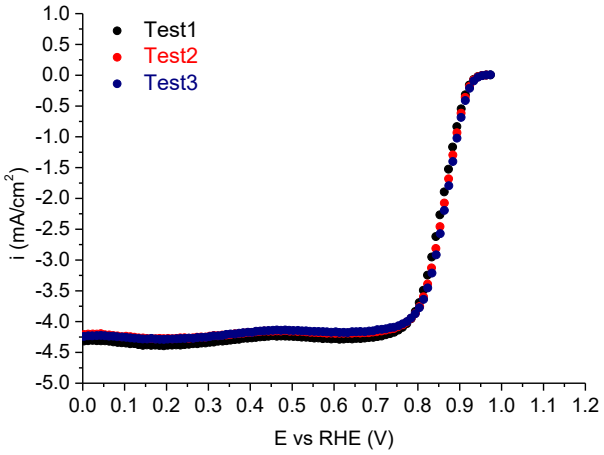

Figure 3.28. SCV recorded in O_2-saturated electrolyte in 0.1M KOH alkaline solution. Measurements repeated three times.

4th Process – Vulcan/FePc wt ratio 5:1 synthesized through ball mill with 2 heat treatment and intermediary acid leaching

The last process scheme is summarized in **Figure 3.29**. In detail, the heat treatments were carried out at 900 °C for 1.5h with a heating rate set at 10 °C min^{-1}. The inert inner atmosphere was kept under nitrogen flow (N_2 flux: 100 ml min^{-1}). The intermediary acid leaching was performed with HCl 6 M. The first ball milling helped maximizing the mixing of the raw materials, while the second ball milling homogenised the resulting catalyst. A second catalyst was also synthesised according to this procedure, by adding urea to the resulting powder after the acid leaching, before the second heat treatment. Urea was added to powder by ball milling, with a catalyst/urea weight ratio of 2:1. The aim was to increase the local nitrogen amount during the second pyrolysis for preserving, or even increasing the FeN active centres. It is known from the literature, in fact, that urea decomposition at 140-240 °C releases CO and NH_3, the latter favouring Fe-N bonding [207].

Figure 3.30 and **Table 3.18** show the results obtained. For both catalysts, with and without urea, the diffusion limit current was not well defined and, as a consequence, it was not possible to calculate the specific mass activity. The half-wave potential values were very similar, 0.74-0.76 V.

Although the literature is reporting that more than one pyrolysis step should affect the performance of non noble metal catalysts [27] positively, in this case the resulting catalyst from the balling of Vulcan/Fe(II)-Pc pyrolyzed twice had the worse ORR catalytic activity compared to the other V/F-based catalysts produced according the other processes. The addition of urea did not provide any effect.

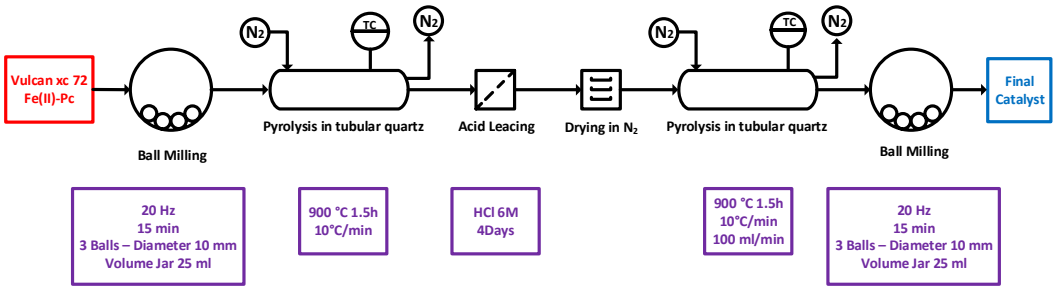

Figure 3.29. Scheme of the synthesis process – 4th step.

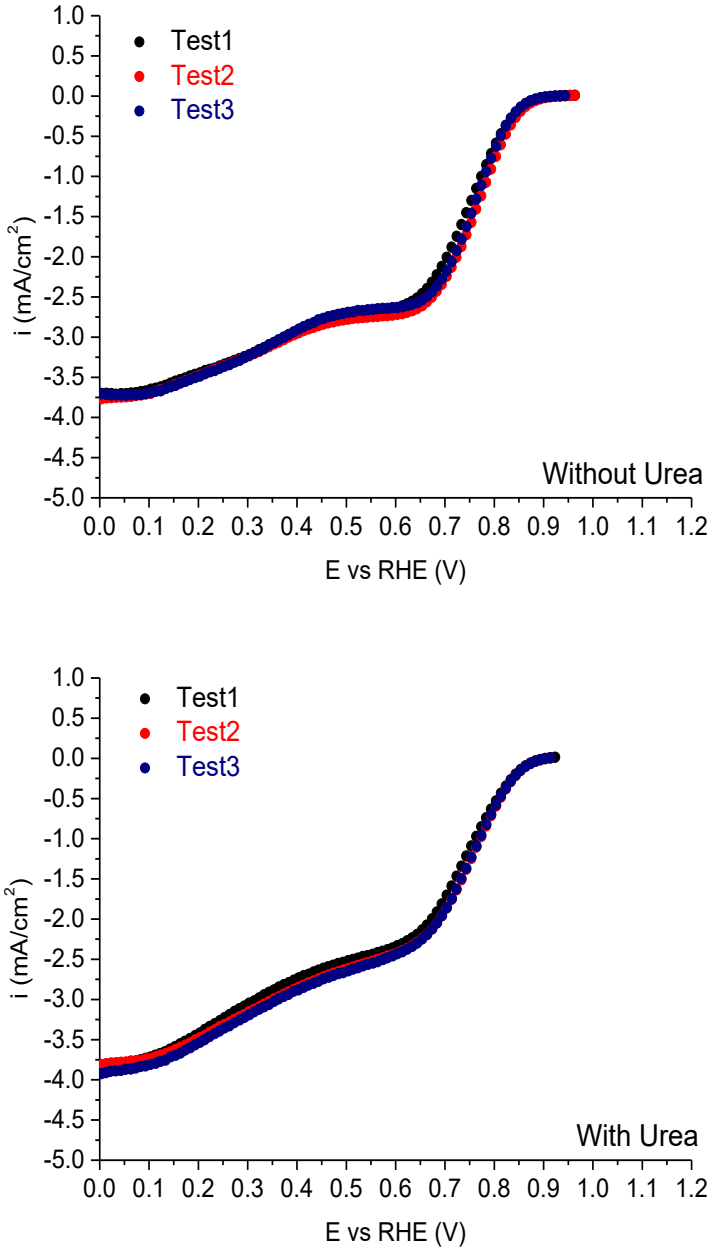

Figure 3.30. SCV recorded in O_2-saturated electrolyte in 0.1M KOH alkaline solution. Measurements repeated three times.

Table 3.18. Summary of the experiment result in terms of onset and half wave potential.

	OnSet pot (V)	**HW pot (V)**
Without Urea	0.86 ± 0.01	0.76 ± 0.01
With Urea	0.86 ± <0.01	0.74 ± 0.01

To understand more in depth this complex process, the onset potential, half-wave potential and average mass activity in the current diffusion limit region, were calculated after each single step of the 4th process, and compared with the

values of the reference Pt/C. **Figure 3.31** and **Table 3.19** show the results obtained.

With the 1st ball milling, the activity is very high, 35 A g^{-1} and 0.91 V, better than Pt/C (23.5 A/g and 0.91 V also considering the carbon present in the catalyst loading). The 1st heat treatment have drastically reduced the ORR activity (2 A g^{-1} and 0.85 V), sign that the ORR active sites are in some way destroyed by the high temperature. Similar behaviours have been found in the literature for these types of catalysts [133,208]. The acid leaching step further decreases the ORR activity (0.7 A g^{-1} and 0.83 V). The 2nd heat treatment kills the ORR activity (0.2 A g^{-1} and 0.77 V), as a further confirmation that, in this case, the temperature does not play a positive role.

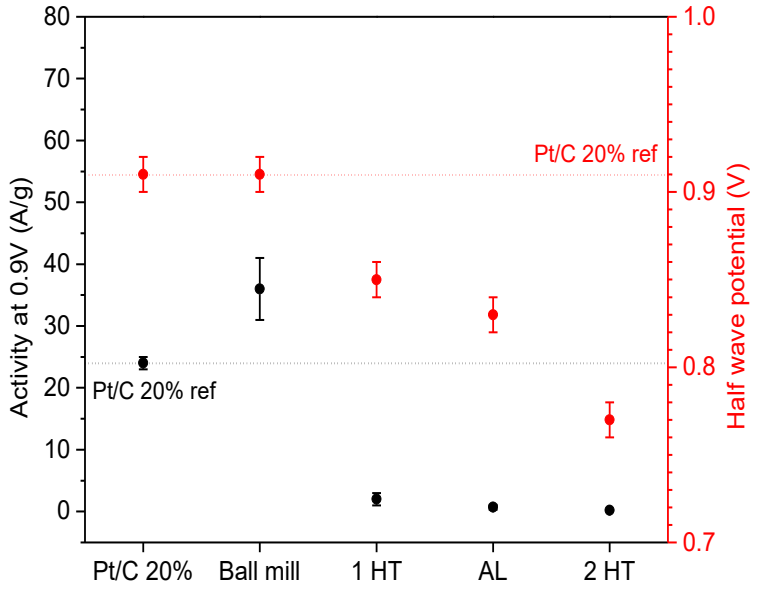

Figure 3.31. Comparison of the mass activity at 0.9V and half-wave potential after the different process steps.

Table 3.19. Summary of the experiment result in terms of activity, onset and half-wave potential.

Process step	OnSet pot (V)	HW pot (V)	Ik (mA cm^{-2})	Activity 0.9 V (A g^{-1})
Ball mill	0.96 ± < 0.01	0.91 ± 0.01	14 ± 2	35 ± 4
1st pyrolysis	0.93 ± 0.01	0.85 ± 0.01	0.8 ± 0.4	2 ± 1
After acid leaching	0.92 ± 0.01	0.83 ± 0.01	0.3 ± 0.1	0.7 ± 0.4
2nd pyrolysis	0.89 ± 0.01	0.77 ± 0.01	0.08 ± 0.02	0.19 ± 0.05
Pt/C 20%	1.01 ± <0.01	0.91 ± 0.01	9.4 ± 0.2	23.5 ± 0.3

3.3.4 Fe(II)-PC with Vulcan Carbon XC 72 catalyst conclusions

From the analysis of four different processes used to synthesise V/F-based catalysts, **Figure 3.32** clearly highlights that the ball milling step is sufficient for producing a very active catalyst. Adding further synthesis steps, such as heat treatments or acid leaching, negatively affect the ORR activity of the catalysts. Notably, during the mechanochemical synthesis the kinetic energy generated by the impact of the balls with the reagents not only favours the mixing, but also generates a local increase of the temperature, which could be sufficient to favour Fe-N-C binding, and the consequent formation of FeN active sites [110,209,210]. Thus, the best catalyst emerged from this series of investigations, V/F BM, was further investigated in terms of kinetics, durability, and physical-chemical properties in **Chapter 4**.

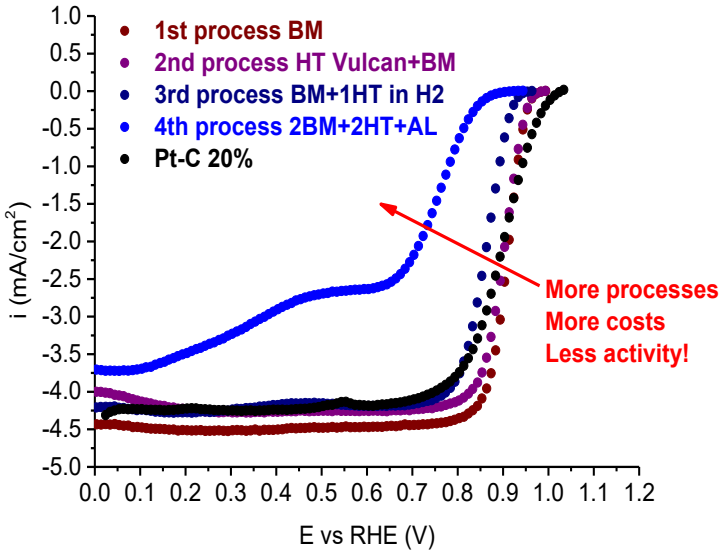

Figure 3.32. Final comparison of the 4 processes studied with the Vulcan/FePc catalysts.

Chapter 4

Electrochemical and chemical-physical characterization

4.1 Introduction

Different electrochemical chemical and surface analysis were carried out to investigate the properties and the difference between the two best catalysts obtained after their synthesis processes. Specifically, the two catalysts were analysed in terms of stair case voltammetry, cyclic voltammetry, Tafel analysis, short load cycle durability test, Koutecky Levich analysis, and H_2O_2 production as electrochemical evaluation, and BET, SEM, XPS, and %Fe with ICP analysis as physical chemical analysis. The BET and XPS analysis related to the Z/F 2HT catalyst are reported into **Chapter 3.2**, since their results were fundamental for the choice of the synthesis optimization. The V/F BM was also evaluated in terms of ethanol tolerance, because this catalyst was the only enough active to justify an experiment in Direct Ethanol Fuel Cell (DEFC). This analysis was fundamental for the understanding of the results obtained in DEFC, to evaluate the activity drop due to fuel cross over.

4.2 Electrochemical characterization of the Pt/C 20% used as a reference for Oxygen Reduction Reaction (ORR)

For this type of study, Platinum nominally 20% on carbon black (Pt/C 20% Alfa Aesar) was chosen as a reference. All the electrochemical analyses were carried out using the same methodology used for all the Non-Noble Metal catalyst (previously reported in **Chapter 2.2**), with the implementation of some modifications. The cyclic voltammetries were recorded between 0.1 V and 1.2 V vs RHE. The starting point was set at 0.1 V to avoid hydrogen evolution at lower

potential [211]. These experiments were performed in order to determine the Pt electrochemical surface area ($ECSA_{pt,cat}$) in 0.1 M KOH alkaline solution [212]. A platinum counter was used in the electrochemical cell instead of gold wire counter [193]. The experiments were repeated thrice for assuring a good repeatability.

4.2.1 Stair case voltammetry and Tafel analysis on Pt/C 20% catalyst

Figures 4.1 show the Pt/C reference SCV followed by its Tafel plot obtained in alkaline condition (KOH 0.1 M). Generally, Pt/C based catalysts exhibit two-step Tafel slope: about 60 mV dec^{-1} at lower overpotential and 120 mV dec^{-1} at higher overpotential [136]. The value of the slope may vary slightly, depending on the crystal Pt facet, uncompensated resistance correction, the purity of the electrolyte, and the chosen boundaries for linear fitting of the curve. Perchloric acid and alkaline solution are non-adsorbing electrolyte because they do not inhibit the adsorption of the intermediate. As reported in the literature, there are several measures of Tafel slope in the 50-80 mV dec^{-1} range at lower overpotential and 100-130 mV dec^{-1} range at higher overpotential [166]. In the presence of O_2, the Pt electrode surface changes according to the potential. Thus, at potential higher than 0.8 V, the electrode surface is a mixture of Pt and PtO, while at lower potentials, the Pt surface is pure Pt [159]. The two different values obtained from the Tafel analysis are associated with the two types of surface area described above and indicate a change in the reaction mechanism. Tafel slope of 120 mV dec^{-1} at higher overpotential indicates that the first electron transfer is the rate-determining step while Tafel slope of 60 mV dec^{-1} indicates a limitation of the rate reaction due to the desorption/absorption of the species involves in the reactions (**See Chapter 1.5** for more details in the ORR mechanism).

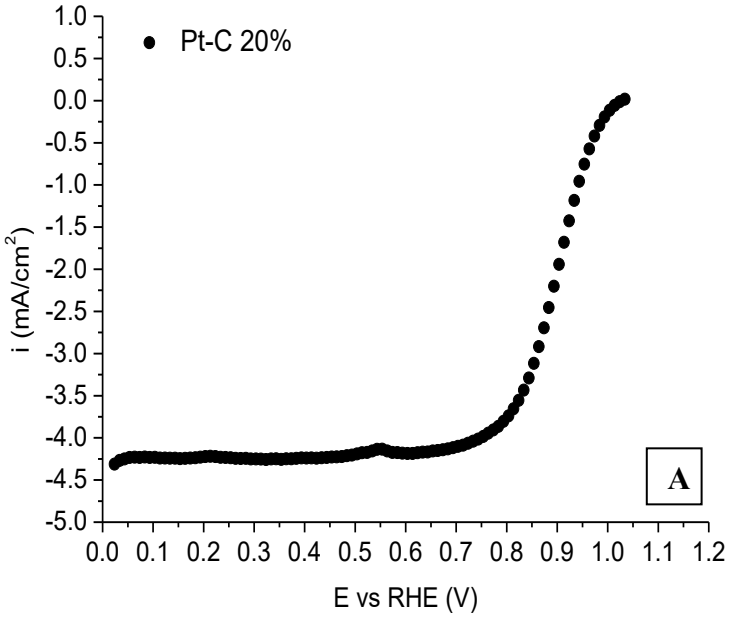

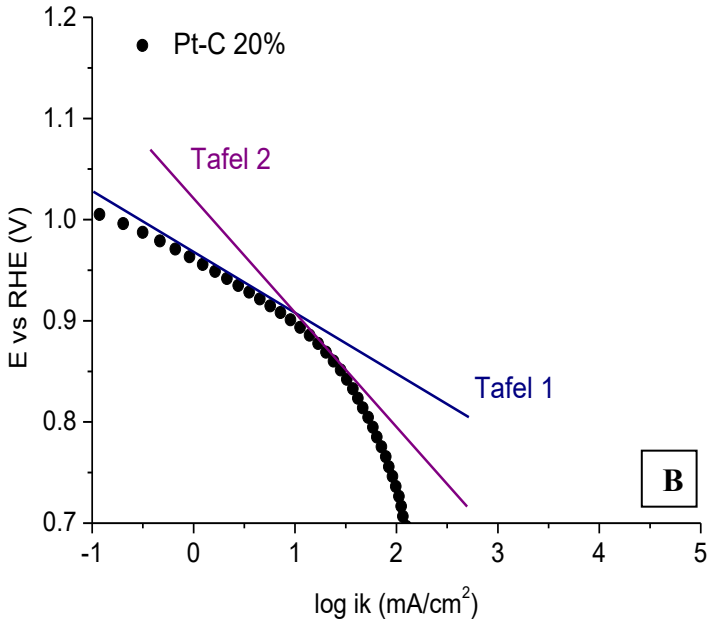

Figure 4.1. SCV recorded in O_2-saturated electrolyte in alkaline condition (A) and respectively Tafel plot (B) obtained from a reference sample of Pt-C 20% Alfa Aesar.

Figure 4.2 shows the Pt/C CV recorded with a sweep rate of 10 mV s^{-1} in N_2-saturated electrolyte in alkaline conditions. The ECSA in m^2 g_{Pt}^{-1} was determined integrating the hydrogen desorption charge in the positive-going potential scan (from 0.15 to 0.4 V vs RHE) [212] and calculating the value through the **Equation 4.1**:

$$ECSA_{Pt_{cat}}\left(m^2 {g_{P_t}}^{-1}\right) = \left[\frac{Q_{H-adsorption}(C)}{390\ \mu C\ cm_{Pt}^{-2} L_{Pt}(mg_{Pt}cm^{-2}) A_g(cm^2)}\right] 10^5 \qquad \text{Equation 4.1}$$

The charge of full coverage for clean polycrystalline Pt is QH = 390 µC cm^{-2} instead of 210 µC cm^{-2} since the measure was carried out in alkaline media rather than acidic media [213]. This value is used as the conversion factor [193]. L_{pt} is the working electrode Pt loading (0.08 mg_{Pt} cm^{-2}) and A_g is the surface area of the glassy carbon electrode (0.1256 cm^2).

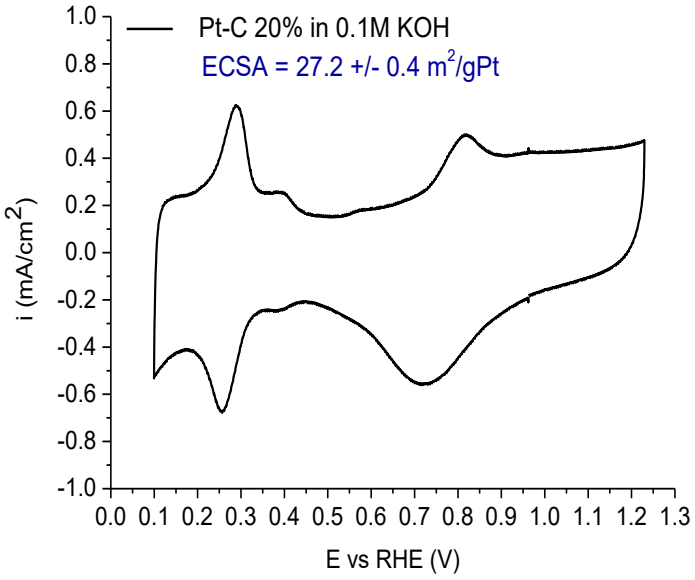

Figure 4.2. CV recorded at 10 mV/s in N_2-saturated electrolyte in alkaline conditions.

Table 4.1 summarizes the electrochemical parameters obtained from the electrochemical analysis. All the analyses show small standard deviations. Considering that the experiments have been repeated on different days and different samples, it can be affirmed that the results obtained on the Pt/C reference are constant and repeatable in this laboratory. The half-wave potential and the activity are slightly higher respect to some examples present in literature (catalyst loading 0.1 mg cm^{-2} instead of 0.4 mg cm^{-2}) [114,126,133], whereas the ECSA is slightly lower compared to similar analysis made in KOH 1 M (36.1 m^2 g_{Pt}^{-1}) instead of KOH 0.1 M (27.2 m^2 g_{Pt}^{-1}) [212]. In any case, the values remain in the typical range of this catalyst. The Tafel behavior is the same as reported in electrochemical books and literature [166].

Table 4.1. Summary of the experiment result in terms of activity, onset and half-wave potential and ECSA for the Pt-based catalysts used as reference in KOH 0.1M. The activity was calculated considering both the total amount of catalyst (first value) and only the Pt loading (second value).

Electrochemical Parameter	Value
Onset potential (V)	1.01 ± <0.01
Half wave potential (V)	0.91 ± 0.01
Ik catalyst (mA cm^{-2})	9.4 ± 0.2
Activity Catalyst at 0.9 V (A g^{-1})	23.5 ± 0.3
Activity Pt at 0.9 V (A g^{-1})	118 ± 2
ECSA (m^2 g_{Pt}^{-1})	27.2 ± 0.4
Tafel slope 1 (mV dec^{-1})	58 ± 2
Tafel slope 2 (mV dec^{-1})	122 ± 8
$I_0$1 (mA cm^{-2})	(2.4 ± 0.9) E-05
$I_0$2 (mA cm^{-2})	(2.1 ± 0.7) E-02

4.2.2 Durability test under O_2 stress condition in alkaline condition

Figures 4.3 – 4.4 shows the SCV and the activity loss of the Pt/C obtained after the durability tests under O_2-saturated solution, subjected to stress conditions through a series of repeated CV with a sweep rate of 500 mV s^{-1} and holding time of 3 s at the potential values of 0.6 and 1.0 V vs RHE (6 s the average cycle period: inset of **Figure 4.4**). **Table 4.2** summarizes the main electrochemical parameters achieved from the durability experiments described above. The results show a reduction of the catalyst performance. After 2000 cycles, the half-wave potential has shifted by 30 mV and the activity evaluated at 0.9 V showed a loss of about 65%. This behavior is in accordance with the literature; other studies has demonstrated huge instability of Pt/C catalyst in alkaline medium through the study of the ECSA loss after several CV cycles [211].

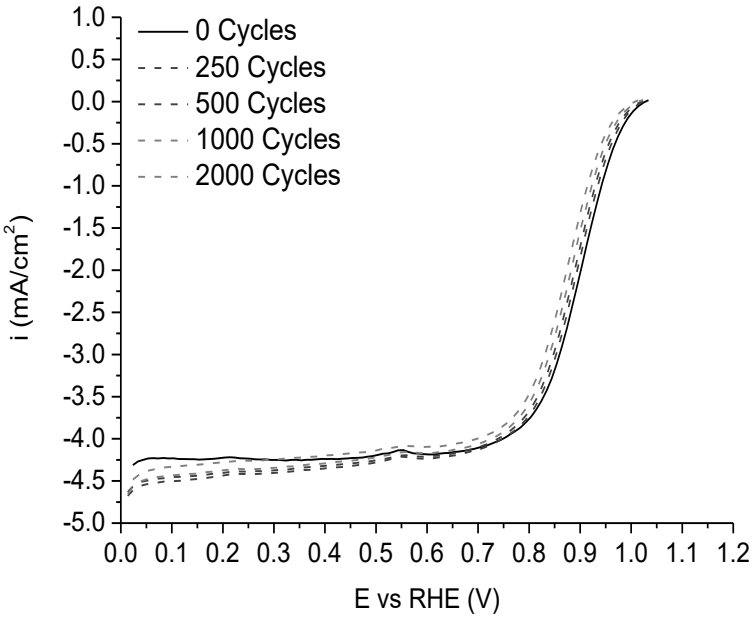

Figure 4.3. SSV of Pt/C recorded in O_2-saturated electrolyte in alkaline condition after different cycles under O_2 stress conditions acquired at 500 mV/s from 0.6 to 1.0 V vs RHE, 6 s each cycle.

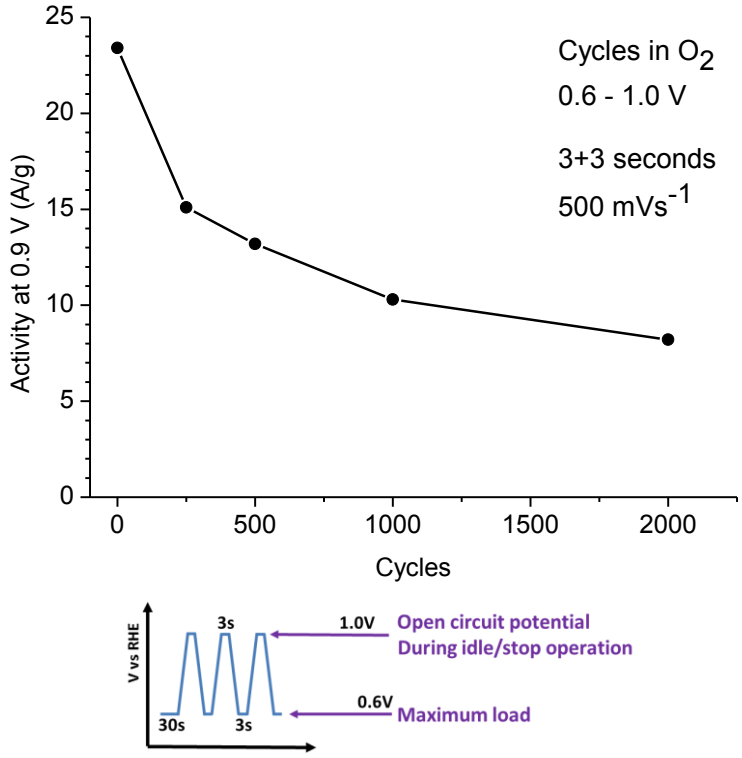

Figure 4.4. Pt/C 20 % activity loss at 0.9 in alkaline condition after different cycles under O_2 stress conditions with a sweep rate of 500 mV/s from 0.6 to 1.0 V vs RHE, 6 s each cycle.

Table 4.2. Summary of the experiment result in terms of activity, onset and half-wave potential and exchange current density for the Pt-based catalyst after different CV cycles.

Cycles	Onset pot (V)	Half Wave pot (V)	I_k (mA cm^{-2})	Activity 0.9 V (A g^{-1})
0	1.01	0.90	9.34	23.4
250	1.00	0.89	6.06	15.1
500	1.00	0.89	5.30	13.2
1000	0.99	0.88	4.13	10.3
2000	0.98	0.87	3.29	8.23

4.3 1st Catalyst: Z/F 2HT

4.3.1 Stair case voltammetry (SCV) and Tafel analysis

Figure 4.5 – 4.6 show the SCV and the Tafel plots of the corrected kinetic current density in alkaline conditions (KOH 0.1M) for the catalyst Z/F 2HT. **Table 4.3** summarizes all the electrochemical results. The first Tafel slope at lower overpotential, was calculated starting from a potential lower than the onset potential (0.98 V vs RHE) because it should be calculated considering a faradic kinetic current. As previously described, the onset potential is the potential at which a current density of 0.1 mA cm^{-2} is measured in the polarization curve [214] and after this value, the ORR faradic current start to be predominant. The second Tafel slope, at higher overpotential, was calculated starting from the point of variation of the first slope until the beginning of the diffusional control region (0.75 – 0.70 V).

Table 4.3. Summary of the experiment result in terms of activity, onset and half-wave potential Tafel slope and exchange current density

OnSet pot (V)	0.98 ± < 0.01
HW pot (V)	0.87 ±< 0.01
I_k (mA cm^{-2})	3.5 ± 2
Activity 0.9 V (A g^{-1})	8.7 ± 0.4
Tafel slope 1 (mV dec^{-1})	53 ± 1
$I_0$1 (mA cm^{-2})	(1.9 ± 0.3) E-06
Tafel slope 2 (mV dec^{-1})	100 ± 25

As evident from the results reported in **Table 4.3**, the catalyst shows repeatable results in terms of electrochemical results, activity at 0.9 V, and the first Tafel slope. Only the second Tafel slope is not constant and this can be associated with a not constant transition between the kinetic ↔ diffusion current control regions. From the first Tafel plot, it was possible determine the values of the exchange current i_{01}. These values, with lower order of magnitude respect to the Pt/C reference (E-06 instead of E-05 mA cm^{-2}) are in any case questionable since

the Tafel equation arise from Butler-Volmer equation, as preannounced in the introductory chapter. The Buttler-Volmer equation is valid only if a series of limitations are respected and cannot be applied to any reversible electrochemical reaction, especially in the case of ORR. If it is imposed as a condition, the equivalence between the ORR mechanism of Z/F 2HT and the mechanism described in **Chapter 1.5**, it could be argued that the experimental Tafel slope 1 of 53 mV dec^{-1} indicates that the migration of a proton from a water molecule to the superoxide group (OO–) has become the rate-limiting step of the reaction. This result is almost the same showed in the previous paragraph relating to the Pt/C benchmark. Since the real ORR mechanism of the synthetized catalyst is not known, it is not possible to confirm with certainty. The change of gradient in Tafel slope at higher overpotential (100 mV dec^{-1}) denotes a modification in the reaction mechanism [159].

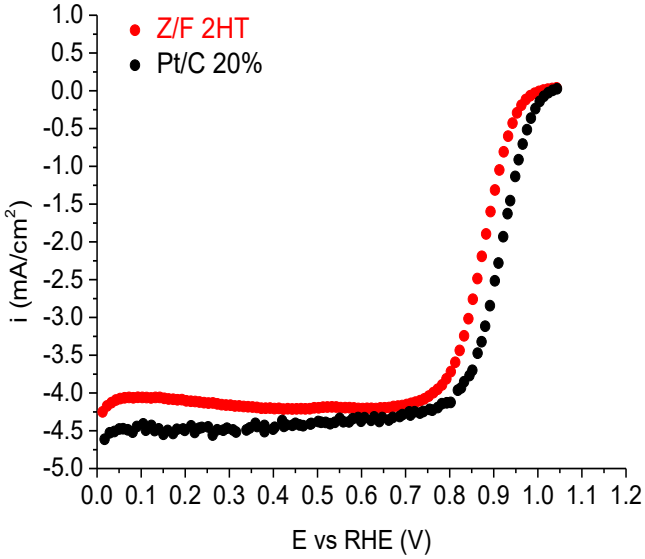

Figure 4.5. SCV recorded in O_2-saturated electrolyte in alkaline condition.

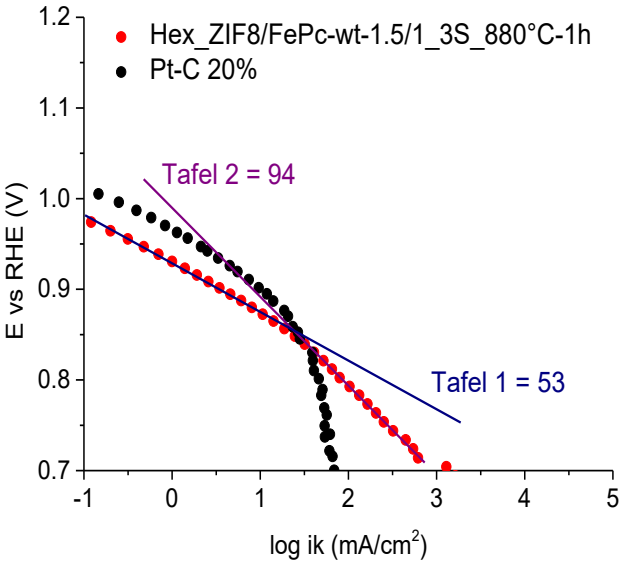

Figure 4.6. Tafel plot obtained from Figure 4.5.

4.3.2 Cyclic voltammetry (CV)

Figure 4.7 shows the CV recorded in N_2-saturated KOH 0.1 M alkaline electrolyte at 10 mV s^{-1}. The CV shows the typical capacitive current shape that arises from the presence of many oxidized functional groups on its surface. These groups, indicated as C_xO_y and C*-C_xO_y, are visible from the XPS analysis described in **Chapter 3.2**. The presence of oxygenated groups increases the specific pseudo-capacitance of carbonaceous and heteroatom-doped carbon materials. In fact, the total capacitive current is caused both by the electrostatic charge and the fast faradic charge transfer reactions that occur at the double layer [156]. **Table 4.4** summarizes the specific and mass capacitances. Since the results are not competitive for supercapacitor applications [215], and the increment of the capacitive current is not the aim of this work, further studies in other common electrolytes have not been made.

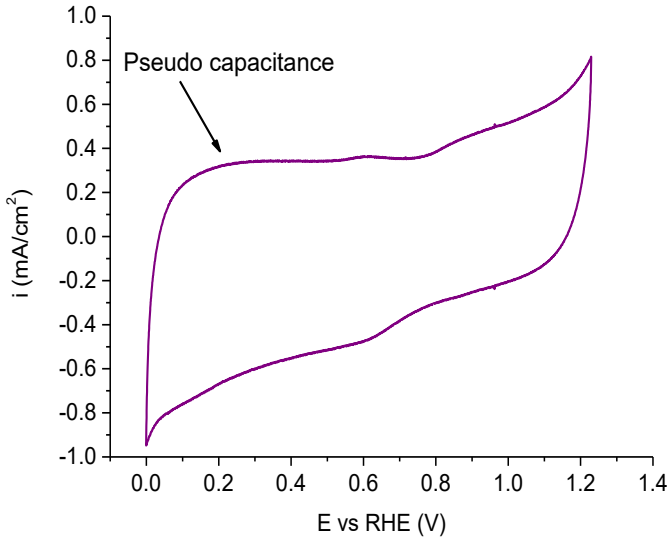

Figure 4.7. CV recorded in N_2-saturated electrolyte in alkaline condition at 10 mV s^{-1}.

Table 4.4. Summary of the experiment result in terms of specific capacitance and mass specific capacitance determined from CV recorded in N_2-saturated electrolyte in 0.1 M KOH. Area of the electrode: 0.1256 cm^2, catalyst loading: 400 µg cm^{-2}.

Electrolyte	Voltage range (V)	Scan rate mV s^{-1}	Specific capacitance (mF cm^{-2})	Mass specific capacitance (F g^{-1})
0.1 M KOH	0.0 – 1.2	10	38 ± 3	95 ± 8

4.3.3 Load cycle durability test

The stability of the catalyst was evaluated with a "slightly modified" durability test proposed during the FC Commercialization Conference held in Japan (2011) [184], and described in detail previously in **Chapter 2.2**. **Table 4.5** and **Figure 4.8** show the results obtained. After 2000 cycles, the half-wave potential has slightly decreased with a shift of 10 mV. The activity evaluated at 0.9 V has showed a reduction of about 25%. This loss is lower compared to the Pt/C used as a reference (loss of about 65%, see **Paragraph 4.2.2**), but the overall activity of this Fe-N-C catalyst remains below to the required standards.

Table 4.5. Variation of electrochemical parameters at different durability cycles.

Cycles	0	250	500	1000	2000
Half wave potential (V)	0.87	0.86	0.86	0.86	0.86
Onset Potential (V)	0.97	0.97	0.97	0.96	0.96
I_k (mA cm^{-2})	3.4	3.1	2.9	2.7	2.5
Activity at 0.9 V (A g^{-1})	8.4	7.8	7.2	6.7	6.2

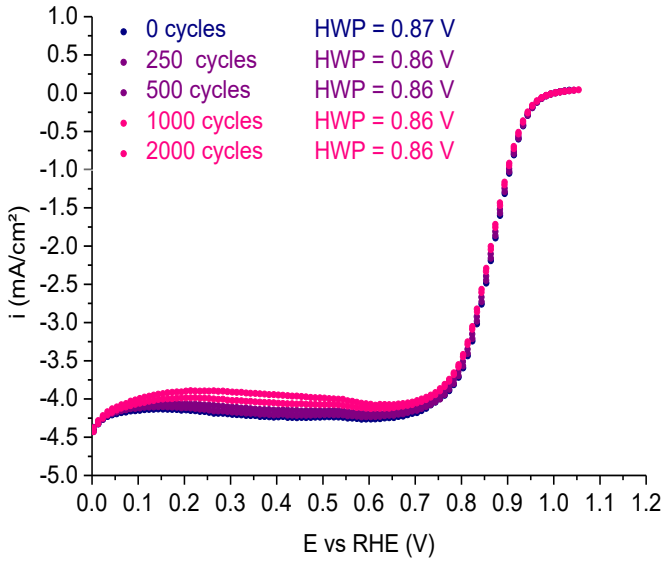

Figure 4.8. SSV recorded in O_2-saturated electrolyte in alkaline condition after different cycles under O_2 stress conditions acquired at 500 mV/s from 0.6 to 1.0 V vs RHE, 6 s each cycle.

4.3.4 Koutecky Levich analysis

To evaluate the overall theoretical number of the electrons transferred in the reaction, a Koutecky Levich (K-L) analysis was performed. **Figure 4.9** shows the different SCV curves obtained respectively at 300, 500, 700, 900 rpm, and the corresponding Koutecky-Levich plots calculated at 0.2, 0.3, 0.4 and 0.5 V. The experiments were not carried out at electrode rotation rate higher than 900 rpm due to laboratory limitation with the aim to preserve the deterioration of the internal RRDE graphite brush. In any case, the rotation rate affect only the limit current i_L values and the range comprised between 300 rpm and 900 rpm is enough to perform the koutecky levich analysis. The half-wave potential and the onset potential are not affected from the rotation rate variation. **Table 4.6** lists the number of electrons determined from the slopes of the Koutecky-Levich plots. The parallel plots showed in **Figure 4.9 – B** indicate a first-order kinetics concerning oxygen [216].

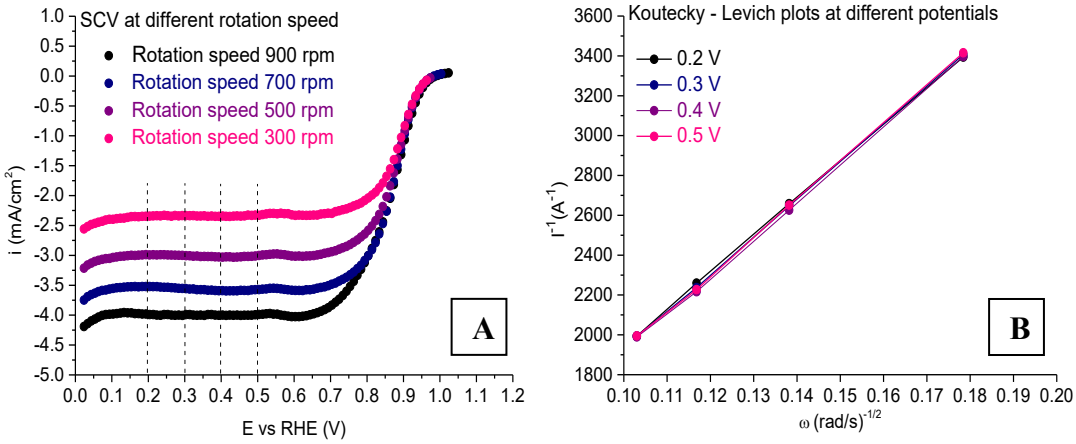

Figure 4.9. SCV curves at different rotation speed recorded using a step size of 10 mV at the time period of 10 s step^{-1} in O_2-saturated KOH 0.1 M solution (A). Corresponding Koutecky-Levich plots at different potentials (B).

Table 4.6. Overall number of electrons involved in the ORR for the Z/F 2HT catalyst.

V vs RHE	n e^-
0.2	4.0
0.3	3.9
0.4	3.9
0.5	3.9

The number of electrons determined through the **Equation 1.22** (**Chapter 1.5**) at different potentials (0.2 V – 0.5 V) exhibits values very close to the theoretical value of 4 electrons, suggesting the expected reaction pathway with low formation of H_2O_2. Since the analysis is only a theoretical approach, it is appropriate to confirm the results through the H_2O_2 evaluation via RRDE experiment.

4.3.5 Hydrogen peroxide analysis

A RRDE analysis was performed to evaluate the hydrogen peroxide generation. The experiment and the calculations were carried out as described previously in **Chapter 1.5.1. Figure 4.10** shows the H_2O_2 molar concentration and the ORR pathway through the real overall number of electrons involved in the reaction during the cathodic potential scan from 1.00 to 0.05 V. **Table 4.7** summarizes all the numerical results obtained in RRDE.

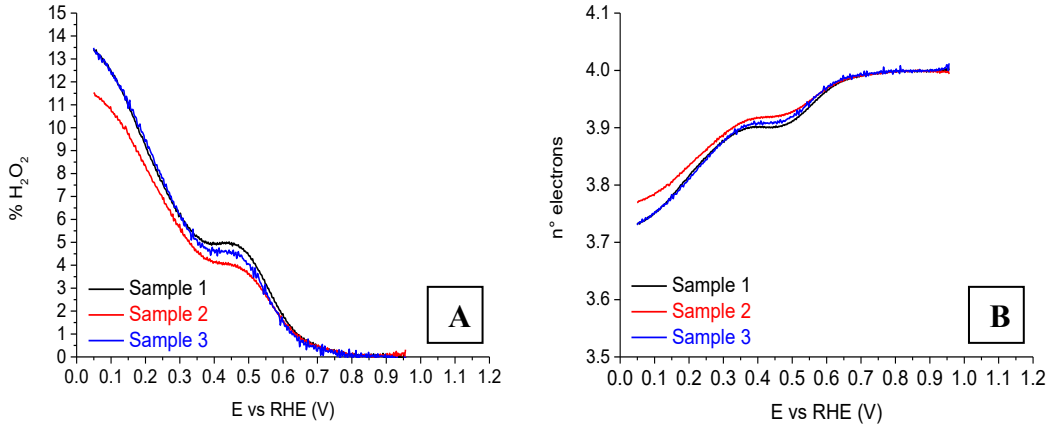

Figure 4.10. A) H_2O_2 molar percent generation in function of the disk electrode potential measured at 900 rpm in O_2 saturated 0.1M KOH solution. B) N° of electrons involved in the ORR in function of the disk electrode potential.

Table 4.7. H_2O_2 molar percent and N° of electrons involved in the ORR at 0.1, 0.5, and 0.9 V.

Sample	Potential	% H_2O_2	N° electrons
Sample 1	0.1	12.4	3.75
	0.5	4.45	3.91
	0.9	0.00	4.00
Sample 2	0.1	10.7	3.78
	0.5	3.63	3.92
	0.9	0.00	4.00
Sample 3	0.1	12.4	3.75
	0.5	4.04	3.92
	0.9	0.00	4.00

The catalyst shows different molars H_2O_2 generation depending on the electrode potential. Up to 0.4 V the molar % is lower than 6%. This value increases until 14 % at lower potential, where the diffusion current resistance is dominant. This behavior is reflected in the decrease of the electrons involved in the ORR from 4 to 3.75, since some oxygen molecules have followed the 2-electron reduction pathway. The H_2O_2 % is slightly higher respect to the 20% Pt/C reference, as reported in the literature and analyzed in the same conditions [217]. At 0.1 V the Pt/C reference shows only 10% of H_2O_2 production.

4.3.6 Morphological analysis – HRTEM

The morphological analysis of the Z/F 2HT catalyst was performed through the acquisition of HRTEM images at different magnifications. At lower magnifications (**Figure 4.11-A**) the sample shows a typical amorphous carbon agglomeration. More in depth, in **Figure 4.11-B** it is possible to recognize a distorted rhombic shape of Zif-8 crystal embedded inside the carbon matrix [218]. In some cases, due to the graphitization processes that occurs during the pyrolysis, a carbonization of some Zif-8 crystal took place into the nitrogen-doped graphitic porous carbons, leading to a residual carbonized capsule embedded into the matrix (**Figure 4.11-C** at larger magnification).

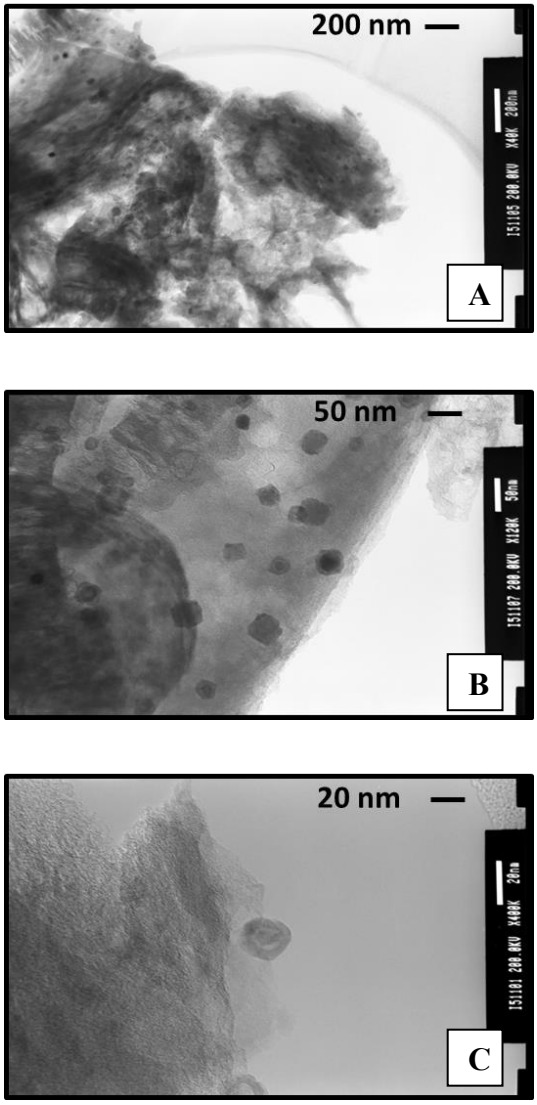

Figure 4.11. HRTEM images of Z/F 2HT catalyst at different magnifications. 40k (A), 120k (B), 400k (C).

4.3.7 ICP analysis

The total iron amount was determined through ICP-MS analysis after dissolution of the sample in 12 M HCl solution. This analysis has been useful to compare the activity with the real amount of metal inside the catalyst. **Table 4.8** shows the results of this experiment. The average amount of iron present in the catalyst after two pyrolysis and an intermediary acid leaching is about 1.1 % by weight. Considering the chemical composition of the not treated catalyst (Z/F 1.5) starting from the raw materials, the Fe % should be 3.7 % by weight while the Fe % contained in the Fe(III)-Pc is not more than 9.2% by weight.

Table 4.8. ICP analysis of the Z/F 2HT catalyst

Sample	Concentration (ppm)	Concentration %
1	0.36	1.33
2	0.21	0.77
3	0.33	1.21
Average value	0.30 ± 0.08	1.1 ± 0.3

4.4 2nd Catalyst: V/F BM

The best catalyst obtained from the previous process optimization (V/F BM) was further synthesised to evaluate the reproducibility of the experiment. **Table 4.9** shows the ORR performance of both the synthesis. The second batch confirmed the results obtained with the first experiment then it was further analyzed.

Table 4.9. Summary of the experiment result in terms of activity, onset and half-wave potential.

	OnSet pot (V)	HW pot (V)	Ik (mA cm^{-2})	Activity 0.9 V (A g^{-1})
Batch 1	0.96 ± <0.01	0.91 ± 0.01	14 ± 1	35 ± 4
Batch 2	0.96 ± <0.01	0.91 ± 0.01	14 ± 2	36 ± 5

4.4.1 Stair case voltammetry (SCV) and Tafel analysis

Figure 4.12 – 4.13 show the SCV and Tafel plots of the corrected kinetic current density in alkaline conditions (KOH 0.1 M) for the catalyst V/F BM. **Table 4.10** lists all the electrochemical results obtained. This catalyst shows low standard deviations and repeatable results. The half-wave potential is comparable with the Pt/C reference and the activity is slightly higher. The Tafel slopes were

calculated following the same procedure described in the previously Paragraph (4.3). At lower overpotential (0.95 - 0.90 V) the Tafel slope shows a result of 35 mV dec^{-1}, whereas the second Tafel slope, at higher overpotential (0.86 - 0.80 V) is 108 mV dec^{-1}. Both the slopes are lower respect to the Pt/C reference, but are in accordance with the typical results for carbonaceous materials reported in the literature [203,219]. Also the exchange current density, as a consequence of the lower Tafel slope, shows a value of 5.0 E-09 mA cm^{-2}, which is 4 orders of magnitude lower respect to the platinum even if the activity is higher.

Table 4.10. Summary of the experiment result in terms of activity, onset and half-wave potential Tafel slope and exchange current density

OnSet potential (V)	0.96 ± <0.01
HalfWave potential (V)	0.91 ± 0.01
Ik (mA cm^{-2})	14 ± 2
Activity @0.9 V (A g^{-1})	36 ± 5
Tafel slope 1 (mV dec^{-1})	35 ± 1
$I_0$1 (mA cm^{-2})	(5.0 ± 1.8) · 10^{-9}
Tafel slope 2 (mV dec^{-1})	108 ± 9

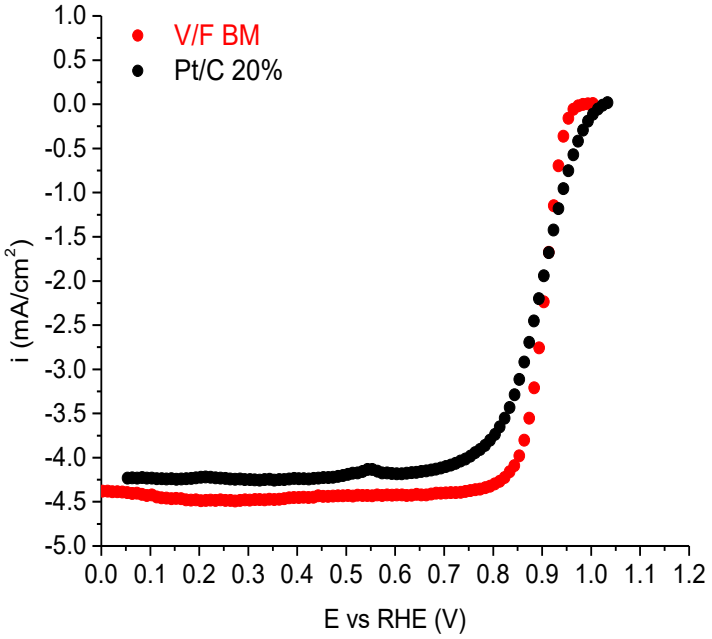

Figure 4.12. SCV recorded in O_2-saturated electrolyte in alkaline condition.

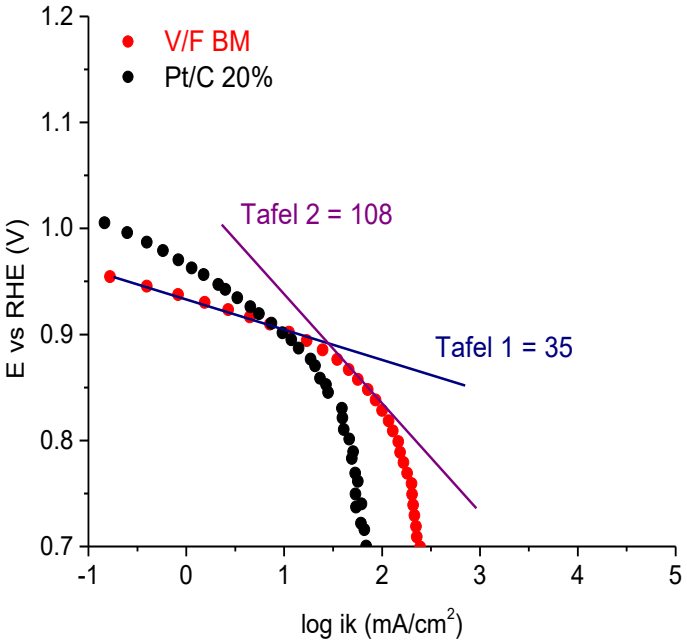

Figure 4.13. Tafel plot obtained from Figure 4.12.

4.4.2 Load cycle durability test

The durability test was carried out as previously described in **Chapter 2.2.. Table 4.11** and **Figure 4.14** shows the results obtained. After 2000 cycles, the half-wave potential has slightly decreased with a shift of 10 mV. The activity evaluated at 0.9 V has showed a reduction of about 40%. The activity loss in terms of % is lower compared to the reference Pt/C. Furthermore, the absolute activity value is higher and the half-wave potential, which is more important, remains more stable respect to the same number of cycles of the Pt/C 20% catalyst. Even if the standard requirements are not reached [75], this good performance invites to further test the catalyst in fuel cell .

Table 4.11. Variation of electrochemical parameters at different durability cycles.

Cycles	0	250	500	1000	2000
Half wave potential (V)	0.91	0.91	0.90	0.90	0.90
Onset Potential (V)	0.96	0.96	0.96	0.96	0.96
I_k (mA cm^{-2})	14.2	11.1	10.6	9.8	8.2
Activity at 0.9 V (A g^{-1})	35.7	27.7	26.6	24.6	20.4

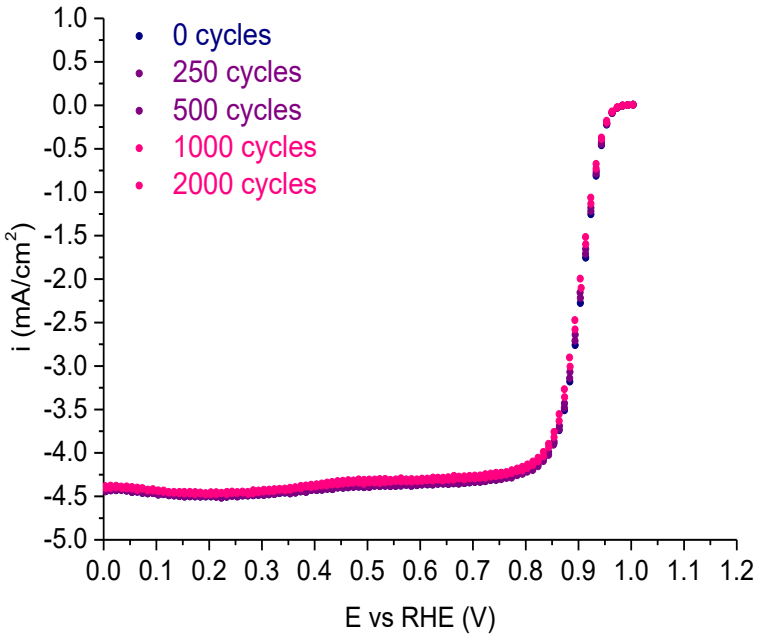

Figure 4.14. SSV recorded in O_2-saturated electrolyte in alkaline condition after different cycles under O_2 stress conditions acquired at 500 mV s^{-1} from 0.6 to 1.0 V vs RHE, 6 s each cycle.

4.4.3 Cyclic voltammetry (CV)

Figure 4.15 shows the CV recorded in N_2-saturated KOH 0.1 M alkaline solution at 10 mV s^{-1}. The CV shows two pairs of peaks related to two different redox processes. From the graph it was possible to determine the anodic (E_{pa}) and the cathodic (E_{pc}) potentials. Afterward, the formal potential (E'_0) was calculated through the use of **Equation 4.2**:

$$E_0' = \frac{E_{pa}+E_{pc}}{2} \qquad \text{Equation 4.2}$$

The first formal potential is equivalent to 0.815 V, while the second one is 0.245 V. These two values refer to the phthalocyanine iron redox processes since 0.80 V corresponds to the $Fe^{2+/3+}$ redox couple, while 0.25 V is related to the $Fe^{1+/2+}$ redox couple [208,220,221]. In this catalyst, the iron redox peaks are clearly visible because the material was not pyrolyzed. **Table 4.12** lists the results obtained.

Table 4.12. Anodic, cathodic and formal potential of the redox couples showed from Vulcan/Fe(II)Pc CV

Redox 1	E_{pa} [V vs RHE]	0.82 ± < 0.01
	E_{pc} [V vs RHE]	0.81 ± < 0.01
	E'_0 [V vs RHE]	0.82 ± < 0.01
Redox 2	E_{pa} [V vs RHE]	0.26 ± < 0.01
	E_{pc} [V vs RHE]	0.23 ± 0.01
	E'_0 [V vs RHE]	0.24 ± 0.01

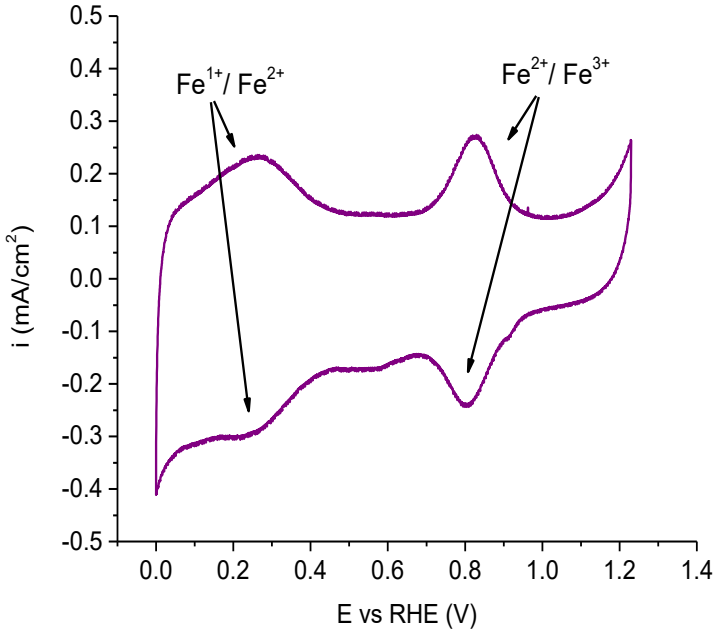

Figure 4.15. CV recorded in N_2-saturated electrolyte in alkaline condition at 10 mV s^{-1}.

4.4.4 Koutecky Levich analysis

Figure 4.16 and Table 4.13 show the results obtained from the Koutecky Levich analysis. **Figure 4.16** shows the different SCV curves obtained respectively at 300, 500, 700, 900 rpm and the corresponding Koutecky-Levich plots calculated at 0.2, 0.3, 0.4, and 0.5 V. **Table 4.13** lists the number of the electrons determined from the slopes of the Koutecky-Levich plots. The parallel plots showed in **Figure 16 – B** indicate a first-order kinetics concerning the oxygen.

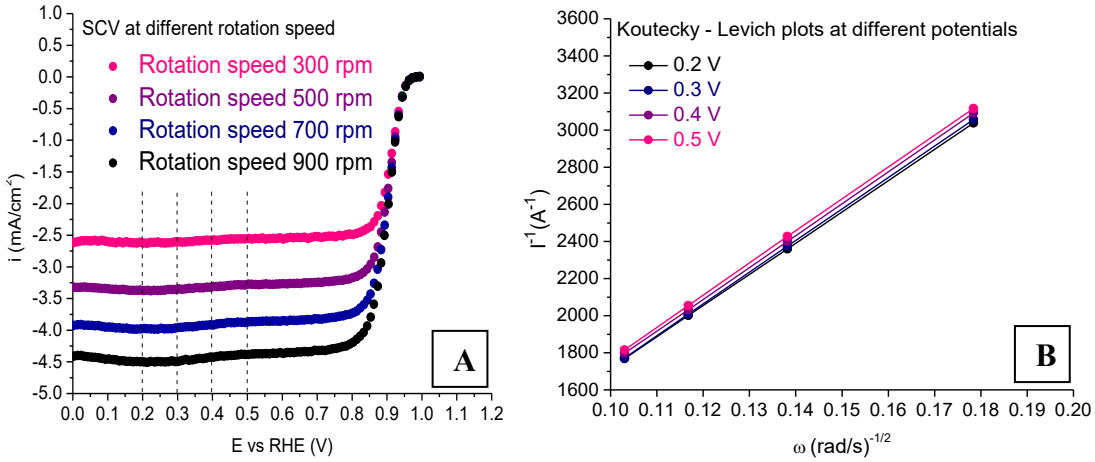

Figure 4.16. SCV curves at different rotation speed recorded using a step size of 10 mV at the time period of 10 s step^{-1} in O_2-saturated KOH 0.1 M solution (A). Corresponding Koutecky-Levich plots at different potentials (B).

Table 4.13. Overall number of electrons involved in the ORR for the V/F BM.

V vs RHE	n e$^-$
0.2	4.4
0.3	4.3
0.4	4.3
0.5	4.2

For this class of catalyst, the number of electrons obtained at different potentials is slightly higher respect to 4. As previously reported, the K-L analysis is a theoretical approach applicable to noble catalyst, in fact Pt/C in 0.1 M NaOH solution shows 4 e$^-$ for the reduction of oxygen [216]. However, the theory is wide used also for non noble catalysts [91]. An electrons number higher than 4 is attributable to the imperfect validity of the theory.

4.4.5 Hydrogen peroxide analysis

Figure 4.17 shows the H_2O_2 molar concentration and the overall number of electrons involved in the ORR during the cathodic potential scan from 1.00 to 0.05 V of the V/F BM catalyst conducted in RRDE. **Table 4.14** lists all the numerical results obtained.

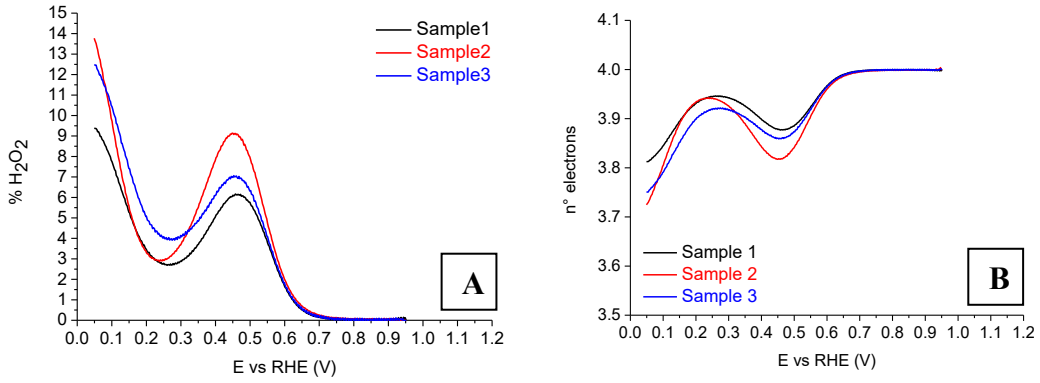

Figure 4.17. A) H_2O_2 molar percent generation in function of the disk electrode potential measured at 900 rpm in O_2 saturated 0.1 M KOH solution. B) N° of electrons involved in the ORR in function of the disk electrode potential.

Table 4.14 H_2O_2 molar percent and N° of electrons involved in the ORR at 0.1, 0.5, and 0.9 V.

Sample	Potential	% H_2O_2	N° electrons
Sample 1	0.1	7.82	3.84
	0.5	5.67	3.88
	0.9	0.00	4.00
Sample 2	0.1	9.87	3.80
	0.5	7.90	3.84
	0.9	0.00	4.00
Sample 3	0.1	10.5	3.79
	0.5	6.31	3.87
	0.9	0.00	4.00

The behavior of this second catalyst is similar to the Z/F 2HT, with a maximum H_2O_2 molar % lower than 14%. The overall production of hydrogen peroxide in slightly higher respect to the first catalyst, especially after a potential of 0.5 V when the molar H_2O_2 % increases until 7-10 %. The increase of hydrogen peroxide is not linear, in fact the curves show a maximum at around 0.45 V, just at the beginning of the well-defined diffusion limit current region, as also reported in the literature for similar non-noble catalysts [91,217]. In any case, like for the other Z/F catalyst, the number of electrons never drops below 3.75 and the results are very close to the 20% Pt/C reference analyzed in the literature at the same experiment conditions (which shows a 10% of maximum H_2O_2 production at 0.1 V [217]).

4.4.6 Ethanol tolerance test

The tolerance of the catalyst toward ethanol was tested by measuring the ORR activity in alkaline solution in the presence of different concentrations of ethanol. **Figure 4.18** and **Table 4.15** show the results obtained. This Fe-N-C catalyst is

highly tolerant at low ethanol concentration. Below an ethanol concentration of 0.10 M, the half-wave potential of the ORR polarization curve remains constant at the value of 0.91 V vs RHE. As the ethanol concentration increases from 0.5 to 2 M, the ORR activity decreases and the half-wave potential shifts from 0.91 to 0.89 V vs RHE. This high concentration is in any case almost impossible to be found at the cathode due to the crossover phenomena, since 2 M is the concentration of ethanol typically fed to the anode of the DEFC [185]. High concentrations of ethanol at the cathode indicate a broken or malfunctioning of the MEA or other components of the device. The decrease of the activity can also be attributed to the reduction of electrical conductivity and O_2 solubility in the electrolyte solution. Furthermore, a diminution of the oxygen solution concentration results in a slight reduction of the diffusion limit current, as described from Levich equation [31]. Although this class of catalysts remain selective with regard to the ORR and is inert toward the oxidation of alcohols [30], the solubility effects of ethanol on phthalocyanine should not be ignored.

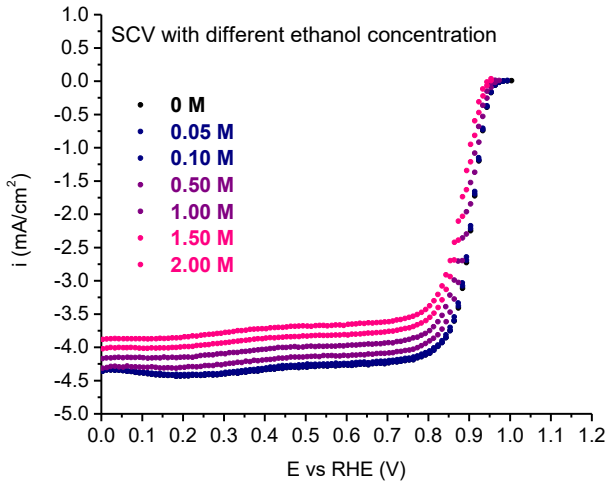

Figure 4.18. SCV measured in O_2-saturated KOH 0.1 M at different ethanol concentrations ranging from 0.05 M to 2.0 M.

Table 4.15. Variation of electrochemical parameters at different ethanol concentration.

Ethanol Concentration (M)	0	0.05	0.10	0.50	1.00	1.50	2.00
Half wave potential (V)	0.91	0.91	0.91	0.90	0.89	0.89	0.89
Onset Potential (V)	0.96	0.96	0.96	0.95	0.95	0.94	0.94
I_k (mA cm^{-2})	12.7	11.4	10.7	7.4	5.4	3.9	2.8
Activity at 0.9 V	31.8	28.6	26.7	18.6	13.5	9.8	7.0

Instead, considering the ethanol tolerance of the reference catalyst, the performance of Pt/C 20% in diluted ethanol solution is poor, as already published [31]. In fact, the activity starts to decrease already with an ethanol concentration lower than 0.01 M. At higher ethanol concentrations, the Pt/C catalyst shows low

selectivity toward ORR and this behaviour could be well noticed through the presence of high electro-oxidation peaks [31]. From this point of view, the V/F BM is more promising respect to the Pt/C commercial catalyst. [222–224].

4.4.7 BET analysis

Table 4.16 and **Figure 4.19** show the BET results relative to the specific surface area and pore size distribution of the V/F BM catalyst. Respect to the Z/F 2HT catalyst, the V/F BM catalyst shows a higher cumulative volume value derived from mesopores. The micropore area is more than an order of magnitude lower respect to the other catalyst. Moreover, even if a more precisely DFT analysis was not carried out, it is clear that the specific surface area of V/F BM is lower than the Zif-8 thermally treated catalyst (**Chapter 3.2**), and above all, it is also lower than the Vulcan XC 72 raw material [225]. While the high surface porosity of Z/F 2HT resulted from the heat treatment and sublimation of the Zif-8 at high temperatures, here, the decrease of the specific surface area is certainly due to the mechanical process in which the raw materials are subjected to high impacts and local compression phenomena. Furthermore, the difference in volume adsorbed and desorbed observed in the isotherms plotted in **Figure 4.19** is lower compared to the Z/F 2HT catalyst. This behaviour confirms the low microporosity level, since significant differences in volume are typically for highly microporous materials. In fact, phenomena like material swelling or nonequilibrium problems take place due to diffusion adsorption limit of nitrogen.

Table 4.16. Results of nitrogen physisorption analysis of V/F BM catalyst.

Analysis	Physical property	Value	Unit
BET	Surface area	130.5	$m^2\ g^{-1}$
t-Plot report	External surface area	117.7	$m^2\ g^{-1}$
	Micropore area	12.8	$m^2\ g^{-1}$
	Micropore volume	0.623 E-02	$cm^3\ g^{-1}$
BJH Adsorption	Cumulative surface area of pores (0,1 – 300 nm)	227.5	$m^2\ g^{-1}$
	Cumulative volume of pores (0,1 – 300 nm)	0.522	$cm^3\ g^{-1}$
BJH Desorption	Cumulative surface area of pores (0,1 – 300 nm)	130.3	$m^2\ g^{-1}$
	Cumulative volume of pores (0,1 – 300 nm)	0.491	$cm^3\ g^{-1}$

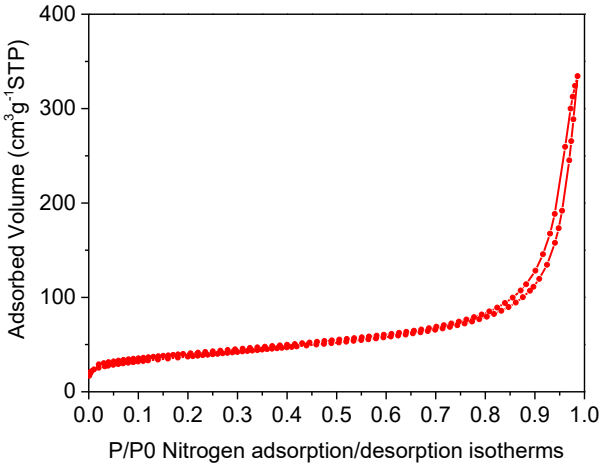

Figure 4.19. Nitrogen adsorption/desorption Isotherms for the V/F BM catalyst.

4.4.8 XPS analysis

Figure 4.20 and **Tables 4.17 – 4.19** show the surface elemental composition obtained through XPS analysis. The catalyst shows an higher concentration of carbon, around 97%, and a nitrogen content less than 1%. The amount of surface oxygen is around 2 % and a low quantity of sulphur (0.18%) is present due to the use of Vulcan XC 72, which contains a small percentage of this element.

The chemistry of carbon was analyzed through C_{1s} spectra (**Figure 4.20 A**). The catalyst shows the predominant graphitic carbon peak (284.4 eV) followed by multiple peaks due to carbon coordinated to nitrogen at 284 eV, and a series of general carbon oxides C*-CxO_y at 285.3 eV, O-C=O at 288.5 eV, C-O/C-O-C at 286 eV, C=O at 289 eV, and COOH at 289.4 eV. The chemistry of N_{1s} nitrogen is quite more complicated (**Figure 4.20 B**). The spectra show different absorption peaks: pyridinic-N occurs at ~398.3 eV, N-ammine at 399.5 eV, pyrrolic at 400.9 eV, graphitic or cationic N at 402.1 eV, N-Ox species at energy higher than 403 eV, and Nx-Fe at 399.0-399.8 eV [200]. The XPS analysis was not able to detect the presence of Fe.

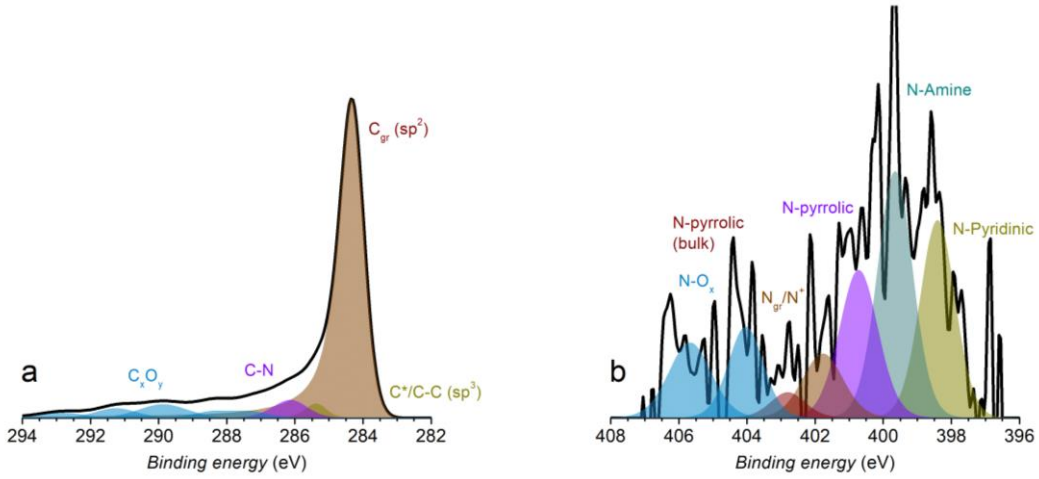

Figure 4.20. C_{1s} (A) and N_{1s} (B) high-resolution X-ray photoelectron patterns for V/F BM catalyst.

Table 4.17. Atomic surface composition of V/F BM catalyst.

Element	Atomic %
O (at. %)	2.20 ± 0.07
C (at. %)	97.00 ± 0.12
N (at. %)	0.62 ± 0.19
S (at. %)	0.18 ± 0.01

Table 4.18. C1s speciation of the different electrocatalysts.

Group	Atomic %
C_{gr}	71.17 ± 0.58
C*	2.83 ± 1.04
C-N	5.64 ± 0.93
C-O	4.39 ± 1.56
C=O	4.50 ± 0.02
COOH	5.90 ± 0.29
C_xO_y	3.54 ± 0.23
C_xO_y	2.05 ± 0.08

Table 4.19. N1s speciation of the different electrocatalysts.

Group	Atomic %
N-pyridinic	20.89 ± 2.02
N-amine	34.92 ± 10.10
N-pyrrolic	16.66 ± 2.30
N4 N_{gr}/N^{+}	9.26 ± 1.22
Bulk N-H	4.92 ± 2.95
N-O	8.24 ± 2.72
N-O	5.10 ± 7.21

4.4.9 Morphological analysis – SEM

The morphological analysis of the V/F BM catalyst was carried out by scanning electron microscope (SEM) at different magnifications (**Figures 4.21 A – B**). The pictures show a sort of agglomerated dark carbon black particles with size lower than 50 μm. The distribution of the particle size is not uniform. This catalyst's morphology is typical for materials mainly consisting of carbonaceous support [133,226]. **Figure 4.21 – A**, acquired at lower magnitude, showed different iron oxide particles confirmed by EDX analysis made on the particle displayed in **Figure 4.21 – B**. Considering their size, is it possible to affirm that they do not participate to ORR activity since iron needs to be coordinated with nitrogen in a carbon matrix at atomic level. Their formation could be due to the loss of the inner phthalocyanine iron during the high energy collisions of the ball milling process.

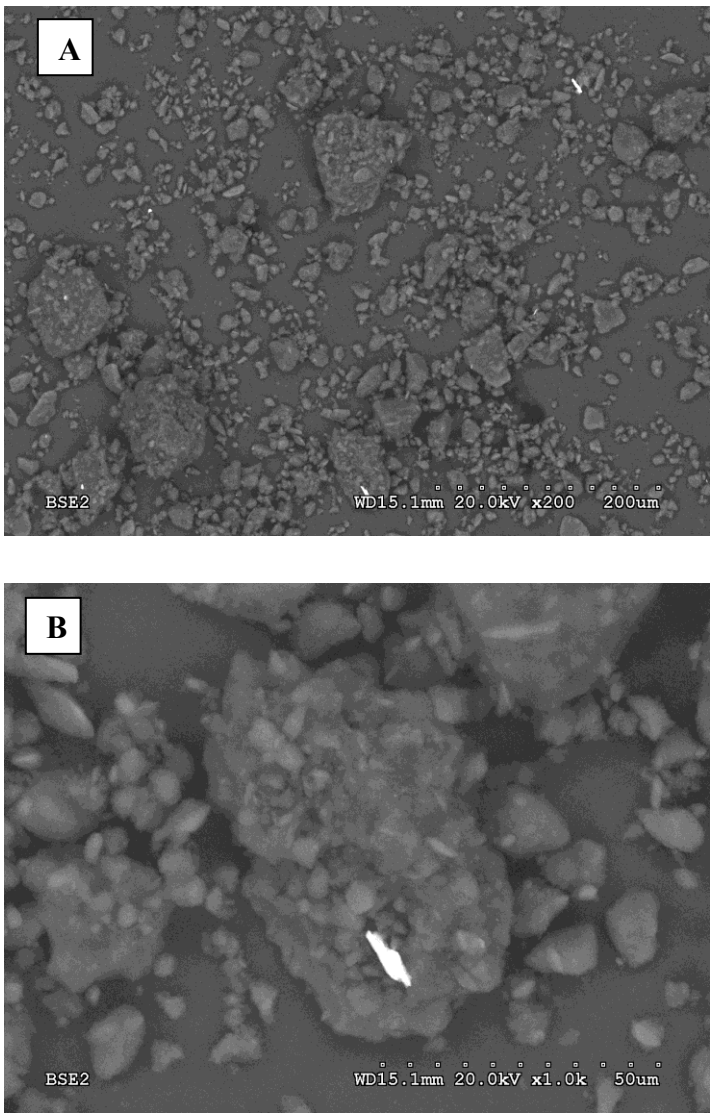

Figure 4.21. SEM images of V/F BM at different magnifications: 0.2K(A), 1K (B)

4.4.10 ICP analysis

The Fe % content was determined through ICP-MS analysis after dissolution of the sample in 12 M HCl solution. This analysis has been useful to compare the activity with the real amount of metal inside the catalyst. **Table 4.20** shows the results of this measurement. The average amount of iron present in the catalyst after the ball milling process is less than 0.5 % by weight. The analysis confirms that almost all the catalyst consists of carbonaceous materials. This result is also in accordance with the XPS and SEM analysis. Considering the chemical composition of the not treated catalyst (Z/F 1.5) starting from the raw materials, the Fe % should be 1.6 % by weight while the Fe % contained in the Fe(II)-Pc is not more than 9.8% by weight.

Table 4.20. ICP analysis of the V/F BM catalyst

Sample	Concentration (ppm)	Concentration wt %
1	0.30	0.41
2	0.22	0.30
3	0.36	0.48
Average value	0.29 ± 0.07	0.40 ± 0.09

4.5 Conclusions

The two best catalysts selected from the optimization of the synthesis processes, Z/F 2HT and V/F BM, showed good results, in line with the best materials of these non noble metal class of catalysts present in the literature [86,126,133]. Furthermore, it is appropriate to remember that the advantages of these catalysts arise from the full optimization and deep evaluation of their synthesis processes. Although the Z/F 2HT shows higher specific surface area and its Tafel plot is more similar to the Pt/C reference, the V/F BM catalyst obtained by simple mixing raw materials in ball mill shows better performance in terms of mass activity, half-wave potential, and durability. The H_2O_2 % production results for both catalysts are in accordance, and in some case better, respect to the literature [91,217,227]. The short RRDE durability of V/F BM catalyst compared to Pt/C 20% in alkaline condition is very promising. The V/F BM catalyst was studied for both fuel cell and metal-air battery applications since it has showed better performance respect to the Z/F 2HT catalyst in terms of activity. The Z/F 2HT material was tested only in metal-air batteries. All the results and performances relative to the application in electrochemical devices are described extensively in **Chapter 6**. As a reminder, **Figure 4.22** shows the ORR activity obtained in RDE of both the catalysts.

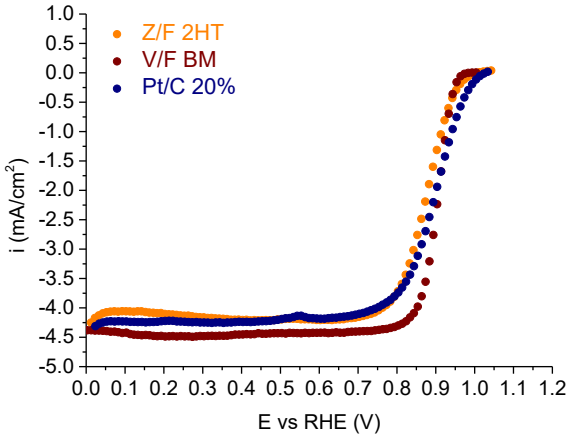

Figure 4.22. Comparison of SCV recorded in O_2-saturated electrolyte in alkaline condition between Z/F 2HT catalyst, V/F BM catalyst and Pt/C reference catalyst.

Chapter 5

Improvement of the ink for RDE with the Design of Experiment

5.1 Introduction

Among the several steps involved between the synthesis of a new catalyst and its testing in a fuel cell, the role of the ink in terms of composition and dispersion for the preparation of the electrodes is sometimes overlooked. Recently, different studies have evaluated the fundamental role of the optimization of the ink containing the catalysts for the preparation of electrodes, either at RDE or MEA level [193,228]. These works show the importance of the catalyst dispersion obtained with ultrasonic bath before the deposition on an electrode. The electrochemical performance and rheology of on ink are affected by a countless number of variables. Many parameters come from the ultrasonic equipment, such as frequency, power, duration and the bath temperature. Other variables arise from the catalyst ink vessel, as for example, if it is kept close to increase the pressure or if mixed at high rotation speed [229].

In the last two decades, different studies have demonstrated the importance of ultrasonic and sonochemical methods in the preparation of metallic nanoparticles/carbon-supported electrocatalysts ink. All the advantages arise from enhanced mass transport phenomena, ultrasound cavitation and water sonolysis [230]. The ultrasound are sound wave with a frequency comprised between 16 kHz - 5 MHz in the case of gases and between 16 kHz - 500 MHz in the case of liquids and solids. The use of ultrasonic wave is very common for improving both synthesis and

catalytic processes in the chemical industry. This specific research field is called sonochemistry and is focused in the use of liquids to enhance reaction rates, product, yields, and erosion of surfaces [231]. In reality, these events are directly connected with a well-known secondary effect called cavitation, which takes place when an ultrasonic wave passes through a liquid medium. When this phenomenon occurs, microbubbles form and violently collapse through implosion resulting in the formation of high-energy jets of liquid that interact with the surfaces/substances of whatever is present in the liquid.

In this work, a detailed study of the ink formulation was carried out using the design of the experiment (DOE). A full factorial design approach was taken into account through the evaluation of three variables: the sonication time, the type of solvent and solvent/water volume ratio. The electroactivity toward oxygen reduction reaction (ORR) was considered as the output effect and was analyzed with a rotating disk electrode (RDE) apparatus. The results were analyzed through cube plots, main effect and interaction plots, and Pareto charts. The goal of this study was to demonstrate the importance of the DOE methodology in the study of the parameters that most affect the final performance of an electrocatalyst in terms of activity and repeatability of the tests. The experiment was carried out on the previously best V/F BM catalyst (mass activity: 36 A g^{-1} - half-wave potential: 0.91 V) obtained from a mechano-chemical synthesis through ball milling process (**Chapter 3.3**).

5.2 Design of experiment

A full factorial design approach was used in this experiment to investigate the effect of some parameters and their interaction on the preparation of the ink for testing the catalyst's performance at RDE level. Based on the instrument present in our laboratory, three parameters were tested at two levels, high and low:

(A) Sonication time	20 and 40 min
(B) Type of solvent	ethanol and 2-propanol
(C) Solvent/water volume ratio (S/W)	2 and 3

All the tests were performed on the V/F catalyst, prepared in a single batch. The sonication frequency was kept constant at 40 ± 5 kHz and the bath temperature was kept at 35 ± 5 °C. The ink was always prepared inside the same vial geometry.

The 2^3 design of experiment is graphically represented in **Figure 5.1**, while **Table 5.1** shows the experiments matrix useful to evaluate the three variables. The experimental set was repeated thrice (24 analysis in total).

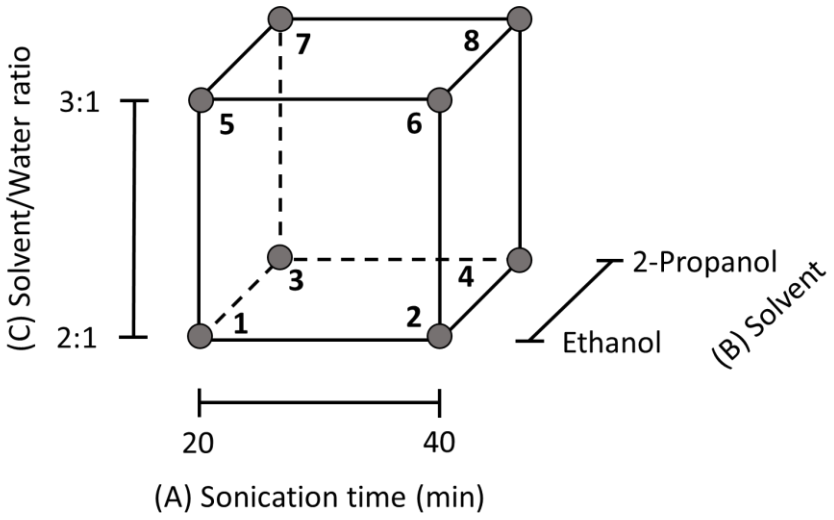

Figure 5.1. Design of experiment for the optimization of the ink containing the V/F catalyst.

Table 5.1. Experiments matrix. Code values for each variable are reported in brackets

Experiment	Sonication time (min)	Solvent	Solvent/water ratio (S/W)
1	20 (-1)	Eth (-1)	2:1 (-1)
2	40 (+1)	Eth (-1)	2:1 (-1)
3	20 (-1)	Prop (+1)	2:1 (-1)
4	40 (+1)	Prop (+1)	2:1 (-1)
5	20 (-1)	Eth (-1)	3:1 (+1)
6	40 (+1)	Eth (-1)	3:1 (+1)
7	20 (-1)	Prop (+1)	3:1 (+1)
8	40 (+1)	Prop (+1)	3:1 (+1)

The software Minitab was used to evaluate the effect of the parameters on the ORR performance in alkaline media: *half-wave potential* ($E_{1/2}$) and activity (A g^{-1}), which is related with the *mass transport-corrected current density (i_k)* but it is a more comprehensible physical parameter. The ORR kinetic current I_k was calculated taking into account the mass transport by using the Koutecky–Levich (K–L) theory [151,193]. (see **Chapter 1.5**).

The software has showed the results in terms of Cube plots, main effect/interaction plots, and Pareto chart. The p-value was determined through the analysis of variance (ANOVA) with the confidence level set at 98%. If the p-value is less than 0.02 (2%), is it possible to reject the null hypothesis that there is no difference between the "means". Thus, it is possible to conclude that a significant difference does exist.

Cube plots were used to see immediately which combination of variables has provided the best performance in activity and half-wave potential through the calculation of the "fitted means". "Fitted means" uses least squares to predict the mean response values of a balanced design and are useful for assessing response differences due to changes in factor levels.

The main effect plots were useful to understand the influence of each parameter: the greater the slope, the greater the influence. The interactions between the parameters were evaluated considering the slope of the line in the interaction plots. Two parameters interact when their slopes are different: the greater the difference, the greater the possibility that the parameters considered interact with each other, especially when the lines intersect.

Pareto Chart is another way to see the relevance of each parameter on the analyzed phenomenon. The purpose of this chart is to highlight the most important factor among a set of factors.

5.3 Electrochemical and statistical results

Tables 5.2 – 5.7 list the electrochemical results obtained from all the SCV analysis, including their respective averages and standard deviation values. The results are expressed in terms of kinetic current density (mA cm^{-2}), mass activity (A g^{-1}), onset potential (V), and half-wave potential (V). The sample with the best performance (highlighted in red) was found to be the one sonicated for 40 min and treated with ethanol in a solvent/water ratio of 3:1. This result is also supported from the cube plot shown in **Figure 5.2**. The difference in terms of mass activity is more pronounced than the half-wave potential because the first one is determined from a mass-transport correction for thin-film RDEs (**Equation 5.1**), which is valid under a faradic process. The catalyst electroactivity toward ORR is quantified at E = 0.90 V because at higher current densities (below E = 0.90 V) the interference from mass-transport losses cannot be completely excluded [193]. In case of catalyst with an activity comparable to that of the Pt/C reference at 0.90 V, it is not possible to guarantee a total faradic process at this potential. This fact leads to further variability in the results. Thus, with the idea of approaching the faradic behaviour at higher potential, was decided to analyze the kinetic properties also at 0.92 V.

In any case, the consideration of the half-wave potential has remained fundamental since it derives from a polarization curve acquired experimentally. An increase of only 0.1 volts involves significant improvements in terms of electro-catalytic performance.

The results collected in **Table 5.7** have shown that the best catalyst's inks have a half-wave potential close to 0.91 V, and, indeed, the results are reproducible.

Table 5.2. I_k at 0.90 V (mA cm^{-2})

Experiment	Sonication time (min)	Solvent	S/W ratio	Sample 1	Sample 2	Sample 3	Average	St. Dev.
1	20 (-1)	Eth (-1)	2:1 (-1)	7	8	6	7	± 1
2	40 (+1)	Eth (-1)	2:1 (-1)	9	10	7	9	± 2
3	20 (-1)	Prop (+1)	2:1 (-1)	3	3	1	2	± 1
4	40 (+1)	Prop (+1)	2:1 (-1)	5	3	3	4	± 1
5	20 (-1)	Eth (-1)	3:1 (+1)	10	10	6	9	± 3
6	**40 (+1)**	**Eth (-1)**	**3:1 (+1)**	**16**	**17**	**18**	**17**	**± 1**
7	20 (-1)	Prop (+1)	3:1 (+1)	6	8	4	6	± 2
8	40 (+1)	Prop (+1)	3:1 (+1)	8	6	6	7	± 1

Table 5.3. Activity at 0.90 V (A g^{-1})

Experiment	Sonication time (min)	Solvent	S/W ratio	Sample 1	Sample 2	Sample 3	Average	St. Dev.
1	20 (-1)	Eth (-1)	2:1 (-1)	17	20	14	17	± 3
2	40 (+1)	Eth (-1)	2:1 (-1)	23	24	17	21	± 4
3	20 (-1)	Prop (+1)	2:1 (-1)	8	8	2	6	± 3
4	40 (+1)	Prop (+1)	2:1 (-1)	14	7	7	9	± 4
5	20 (-1)	Eth (-1)	3:1 (+1)	24	25	14	21	± 6
6	**40 (+1)**	**Eth (-1)**	**3:1 (+1)**	**41**	**42**	**45**	**43**	**± 2**
7	20 (-1)	Prop (+1)	3:1 (+1)	14	19	10	15	± 4
8	40 (+1)	Prop (+1)	3:1 (+1)	21	15	15	17	± 3

Table 5.4. I_k at 0.92 V (mA cm^{-2})

Experiment	Sonication time (min)	Solvent	S/W ratio	Sample 1	Sample 2	Sample 3	Average	St. Dev.
1	20 (-1)	Eth (-1)	2:1 (-1)	1.9	1.4	1.5	1.6	± 0.3
2	40 (+1)	Eth (-1)	2:1 (-1)	2.1	1.8	2.5	2.1	± 0.3
3	20 (-1)	Prop (+1)	2:1 (-1)	0.9	1.0	0.4	0.8	± 0.3
4	40 (+1)	Prop (+1)	2:1 (-1)	1.4	1.0	0.9	1.1	± 0.3
5	20 (-1)	Eth (-1)	3:1 (+1)	1.9	2.6	2.8	2.4	± 0.5
6	**40 (+1)**	**Eth (-1)**	**3:1 (+1)**	**3.6**	**4.3**	**4.8**	**4.2**	**± 0.6**
7	20 (-1)	Prop (+1)	3:1 (+1)	1.6	1.9	1.1	1.6	± 0.4
8	40 (+1)	Prop (+1)	3:1 (+1)	2.0	1.4	1.5	1.6	± 0.4

Table 5.5. Activity at 0.92 V (A g^{-1})

Experiment	Sonication time (min)	Solvent	S/W ratio	Sample 1	Sample 2	Sample 3	Average	St. Dev.
1	20 (-1)	Eth (-1)	2:1 (-1)	5	4	4	4	± 1
2	40 (+1)	Eth (-1)	2:1 (-1)	5	4	6	5	± 1
3	20 (-1)	Prop (+1)	2:1 (-1)	2	2	1	2	± 1
4	40 (+1)	Prop (+1)	2:1 (-1)	4	3	2	3	± 1
5	20 (-1)	Eth (-1)	3:1 (+1)	5	6	7	6	± 1
6	**40 (+1)**	**Eth (-1)**	**3:1 (+1)**	**9**	**11**	**12**	**11**	**± 2**
7	20 (-1)	Prop (+1)	3:1 (+1)	4	5	3	4	± 1
8	40 (+1)	Prop (+1)	3:1 (+1)	5	3	4	4	± 1

Table 5.6. Onset potential (V)

Experiment	Sonication time (min)	Solvent	S/W ratio	Sample 1	Sample 2	Sample 3	Average	St. Dev.
1	20 (-1)	Eth (-1)	2:1 (-1)	0.95	0.95	0.95	0.95	± <0.01
2	40 (+1)	Eth (-1)	2:1 (-1)	0.95	0.96	0.96	0.96	± 0.01
3	20 (-1)	Prop (+1)	2:1 (-1)	0.95	0.95	0.94	0.95	± 0.01
4	40 (+1)	Prop (+1)	2:1 (-1)	0.95	0.95	0.95	0.95	± <0.01
5	20 (-1)	Eth (-1)	3:1 (+1)	0.96	0.96	0.96	0.96	± <0.01
6	**40 (+1)**	**Eth (-1)**	**3:1 (+1)**	**0.96**	**0.96**	**0.96**	**0.96**	**± <0.01**
7	20 (-1)	Prop (+1)	3:1 (+1)	0.95	0.95	0.94	0.95	± 0.01
8	40 (+1)	Prop (+1)	3:1 (+1)	0.95	0.95	0.95	0.95	± <0.01

Table 5.7. Half wave potential (V)

Experiment	Sonication ime (min)	Solvent	S/W ratio	Sample 1	Sample 2	Sample 3	Average	St. Dev.
1	20 (-1)	Eth (-1)	2:1 (-1)	0.90	0.90	0.89	0.90	± 0.01
2	40 (+1)	Eth (-1)	2:1 (-1)	0.90	0.89	0.90	0.90	± 0.01
3	20 (-1)	Prop (+1)	2:1 (-1)	0.88	0.88	0.84	0.87	± 0.02
4	40 (+1)	Prop (+1)	2:1 (-1)	0.89	0.87	0.88	0.88	± 0.01
5	20 (-1)	Eth (-1)	3:1 (+1)	0.89	0.90	0.90	0.90	± 0.01
6	**40 (+1)**	**Eth (-1)**	**3:1 (+1)**	**0.90**	**0.91**	**0.91**	**0.91**	**± 0.01**
7	20 (-1)	Prop (+1)	3:1 (+1)	0.90	0.90	0.88	0.89	± 0.01
8	40 (+1)	Prop (+1)	3:1 (+1)	0.90	0.89	0.89	0.89	± 0.01

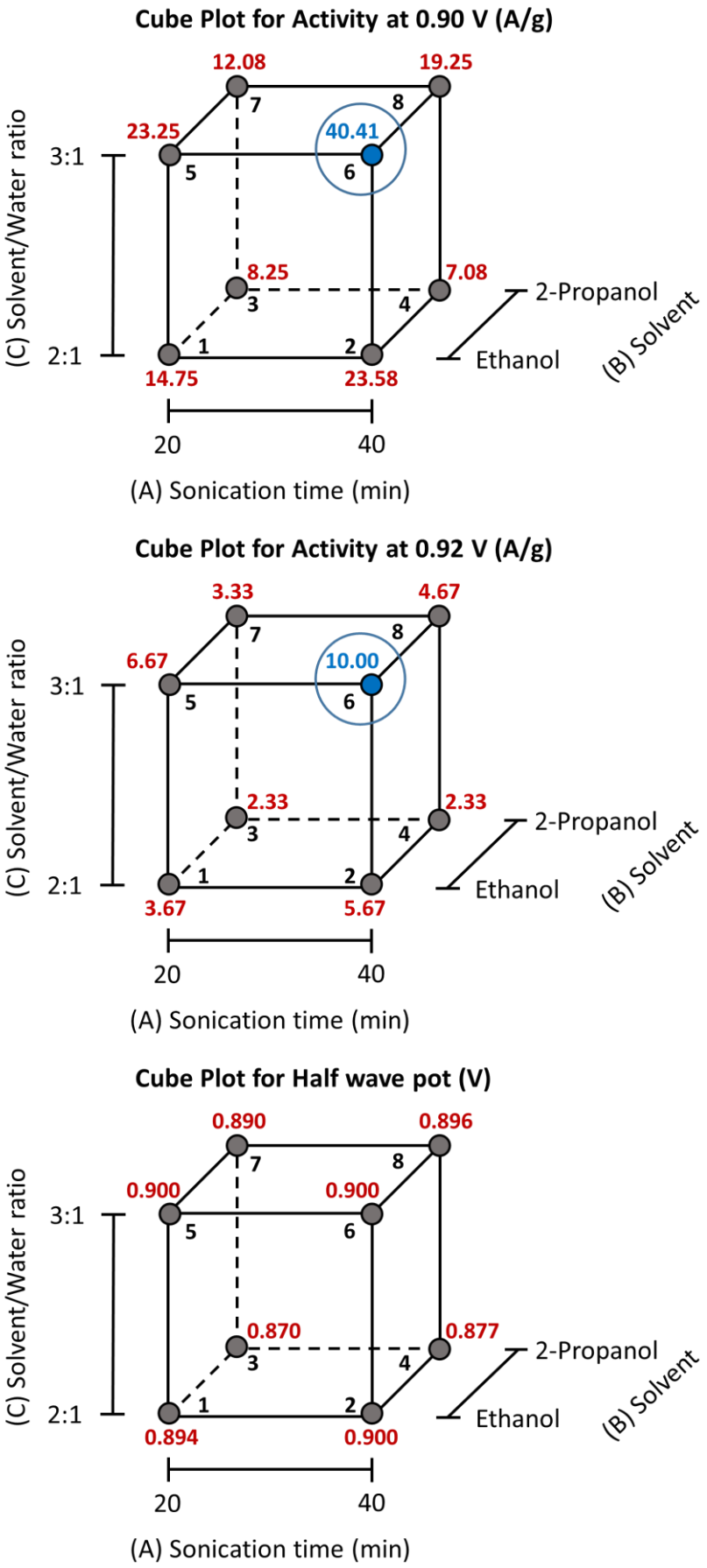

Figure 5.2. Cube plot "fitted means" of the variables analyzed. A) Activity at 0.90 V (A g^{-1}), B) Activity at 0.92 V (A g^{-1}) C) Half wave potential (V).

The main effect plots shown in **Figure 5.3** are useful if different levels of a factor affect the response differently. The chart is represented from a line: if it is not horizontal, then there is a main effect. The greater the slope, the greater the influence of that level.

In these results, the trend is clearly the same for all the responses. In fact, 40 minutes as sonication time, ethanol as solvent type, and 3 as solvent/water volume ratio always provide the best results.

Figure 5.4 shows the interaction plots between all the combinations of the factors. The non-parallel lines on the interaction plot indicate interaction effects between the parameters (for instance sonicated time combined with the type of solvent showed in the first section of each figure). If the non-parallelism is more pronounced, the interactions are more intense, especially when the lines are intersected.

It this study, the three variables do not interact with each other since the lines are almost parallel and never intersect. This means that the factors can be considered individually. Also in this case the trend of the results is the same for all the responses.

The parameters and the interaction that most affect the final responses can be viewed more intuitively through the Pareto Chart shown in **Figure 5.5.**

Although these interaction plots are helpful to display the effects, it is also useful to evaluate statistical significance by looking at the effects in an analysis of variance (**Table 5.8 – 5.10**) in terms of p-value, which is the most frequently used tools for deciding if a result is statistically significant.

In this analysis, the confidence level was set at 98% and a p-value of 0.02 was used as the cut-off for significance. If the p-value is below 0.02 the factor (or the combination of more factor) is significant, over 0.02 is not significant. Considering both the activity and half-wave potential, the combination of all the results has shown that only the factors “type of solvent” and “solvent/water vol ratio” have p-value under 0.02. The half-wave potential is the limiting factor. If the activities are evaluated individually, then also the sonication time has a fundamental role (**Figure 5 α – β**).

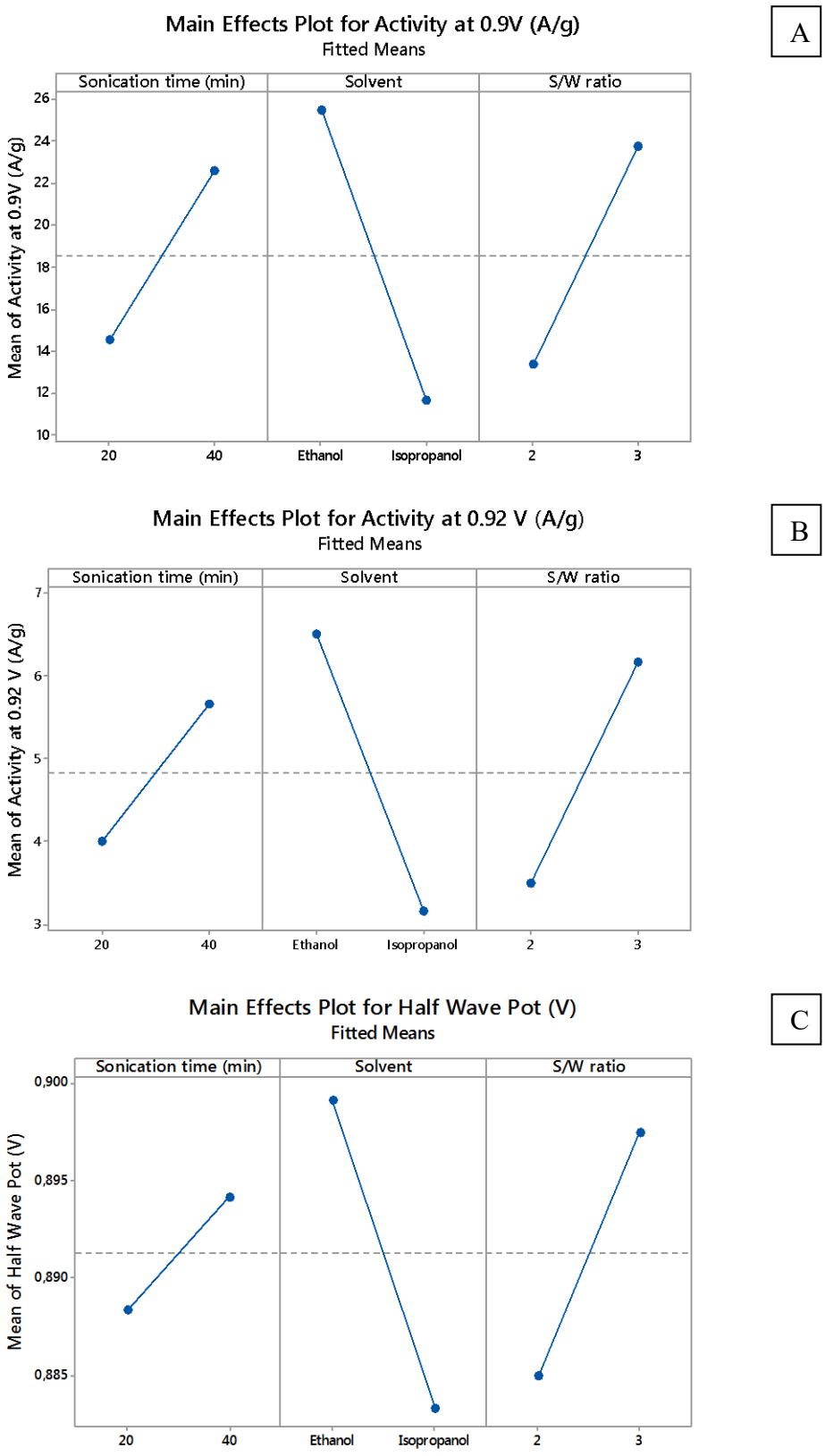

Figure 5.3. Main effect plot of the variables analyzed. A) Activity at 0.90 V (A g^{-1}), B) Activity at 0.92 V (Ag^{-1}), C) Half wave potential (V).

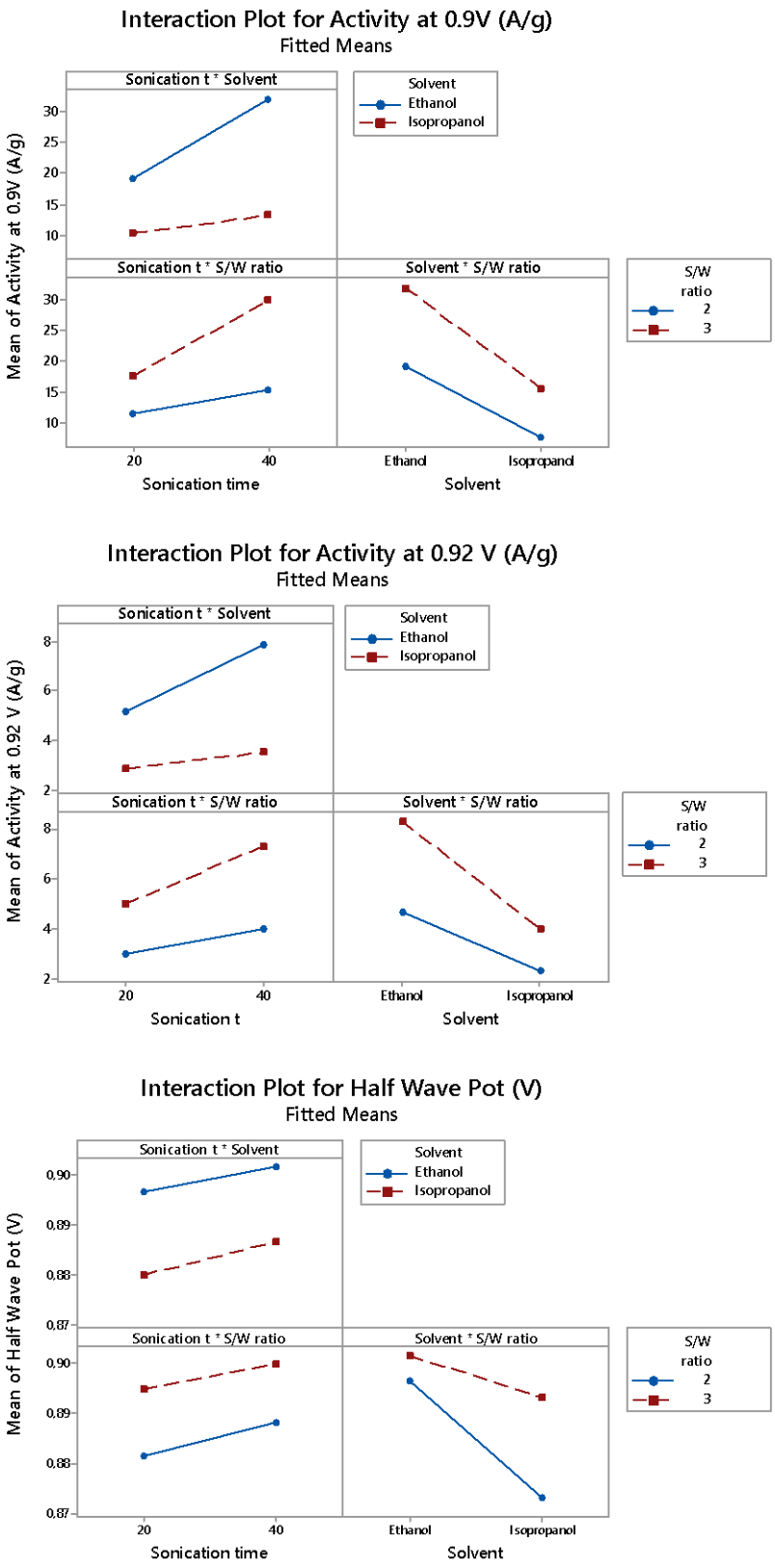

Figure 5.4. Interaction plot of the variables analyzed. A) Activity at 0.90 V (A g^{-1}) as response, B) Activity at 0.92 V (A g^{-1}) as response C) Half wave potential (V) as response.

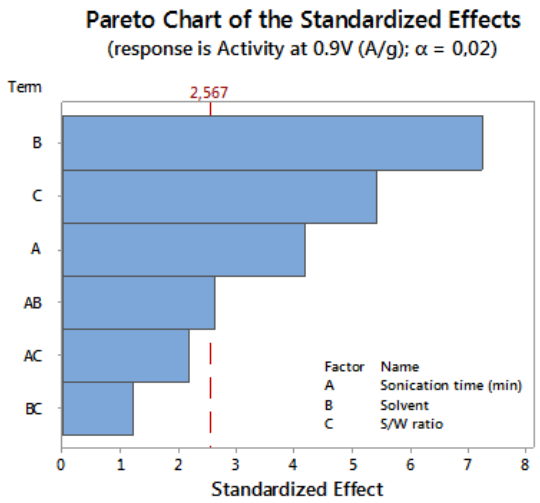

α

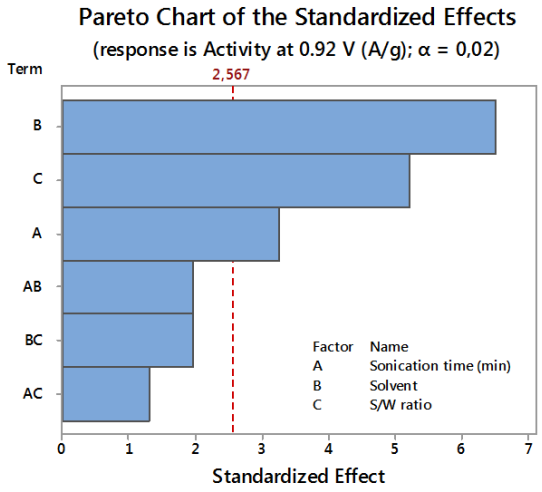

β

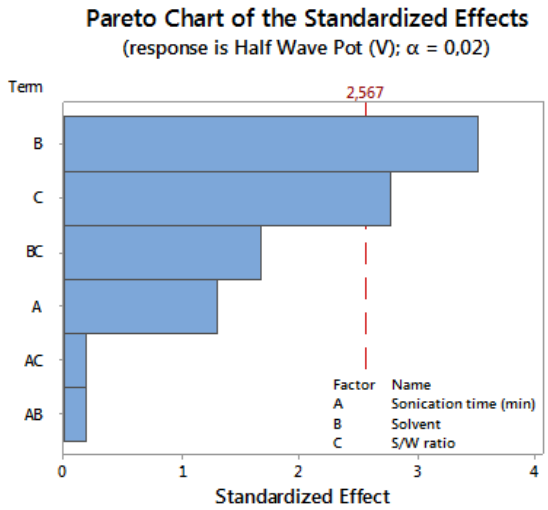

γ

Figure 5.5 Pareto Chart of the standardized effect. α)Activity at 0.90 V (A g^{-1}), β) Activity at 0.92 V (A g^{-1}), γ) Half wave potential (V). Factor: A-Sonication time, B-Solvent, C-S/W ratio.

Table 5.8. p-value related to the evaluation of the activity in A g^{-1} at 0.90 V for the parameters analyzed experimentally.

Model	Parameters	p-Value
Linear	Sonication time	0.001
	Solvent	0.000
	Solvent/water ratio	0.000
2-Way interaction	Sonication time*Solvent	0.018
	Sonication time*S/W ratio	0.043
	Solvent*S/W ratio	0.239

Table 5.9. p-value related to the evaluation of the activity in A g^{-1} at 0.92 V for the parameters analyzed experimentally.

Model	Parameters	p-Value
Linear	Sonication time	0.005
	Solvent	0.000
	Solvent/water ratio	0.000
2-Way interaction	Sonication time*Solvent	0.067
	Sonication time*S/W ratio	0.210
	Solvent*S/W ratio	0.067

Table 5.10. p-value related to the evaluation of the halfwave potential in V for the parameters analyzed experimentally.

Model	Parameters	p-Value
Linear	Sonication time	0.213
	Solvent	0.003
	Solvent/water ratio	0.013
2-Way interaction	Sonication time*Solvent	0.855
	Sonication time*S/W ratio	0.855
	Solvent*S/W ratio	0.114

The statistical analysis was repeated removing the non-significant Sonication time*Solvent (AB) + Sonication time*S/W ratio (AC) from the half-wave potential evaluation. This procedure was useful to increase the number of degrees of freedom and to improve the quality of the results. **Figure 5.6** and **Table 5.11** show the new results in terms of Pareto Chart and p-Value, respectively. After all, the elimination of the non-significant interaction has not shown significant differences from previous results leaving the Solvent (B) and the Solvent/Water ratio (C) as the two most influential parameters for the half-wave potential.

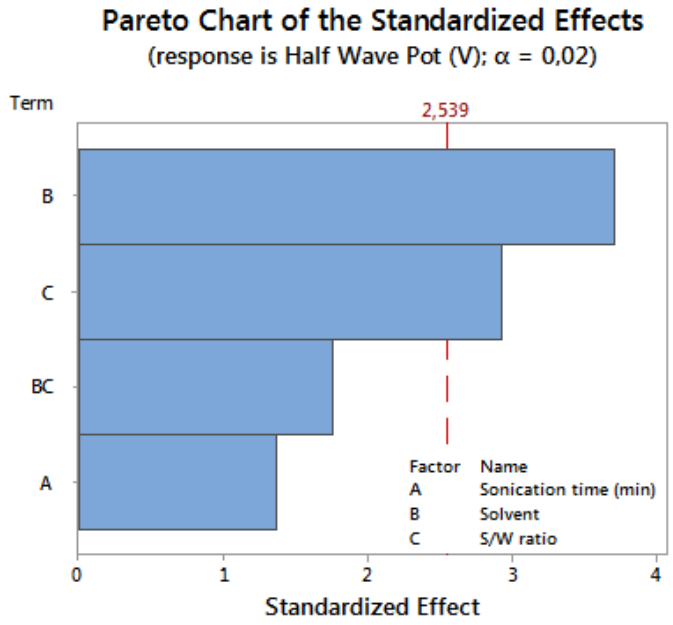

Figure 5.6. Pareto Chart of the standardized effect with halfwave potential (V) as response after the removal of the non-significant interaction Sonication time*Solvent (AB) + Sonication time*S/W ratio (AC). Factor: A-Sonication time, B-Solvent, C-Solvent/water ratio.

Table 5.11. p-value related to the evaluation of the halfwave potential in V after the removal of the non-significant interaction Sonication time*Solvent (AB) + Sonication time*S/W ratio (AC).

Model	Parameters	p-Value
Linear	Sonication time	0.188
	Solvent	0.001
	Solvent/water ratio	0.009
2-Way interaction	Solvent*S/W ratio	0.095

At the end of the DOE analysis, the results have showed that ethanol is better than iso-propanol. Furthermore, a higher sonication time and a higher solvent/water (S/W) ratio positively influence the electrochemical performance of the ink, when tested at RDE level. To investigate more in depth these two parameters, further analyses were made using a solvent/water volume ratio equals to 4:1 and a sonication time of 40 minutes. **Table 5.12** and **Figure 5.7** show the results of these experiments and demonstrate that a volume ratio higher than 3 does not increase the electrochemical performance. Respect to the best samples obtained working with an S/W volume ratio equal to 3, the analyses performed using a S/W volume ratio equal to 4 showed lower average values both in terms of activity and half-wave potential. The wide standard deviation also proves a non-constant dispersion of the catalyst in the solution. Considering this latter information, a further analysis was carried out to investigate the ink behavior by increasing the sonication time until 60 minutes, keeping constant the S/W volume ratio at 3. The results in **Table 5.13** and **Figure 5.8** do not show an improvement

of the performance, both in terms of activity and half-wave potential. The only remarkable information is a decrease in the standard deviation of the half-wave potential. All this information indicated that after 40 minutes of sonication the ink has reached its ideal performance and further sonication processes could lead to small improvements compared to the time and energy involved.

Table 5.12. Electrochemical parameters for the three inks prepared with the following specifications: 40 min as sonication time, ethanol as solvent, 4:1 as solvent/water volume ratio.

	Sample 1	Sample 2	Sample 3	Average	St. Dev.
I_k (mA cm^{-2}) at 0.90 V	6	14	12	11	4
Activity at 0.90 V (A g^{-1})	14	36	30	27	11
I_k (mA cm^{-2}) at 0.92 V	1	4	3	3	1
Activity at 0.92 V (A g^{-1})	4	10	7	7	3
Onset Potential (V)	0.95	0.96	0.96	0.96	± 0.01
Half wave potential (V)	0.89	0.91	0.90	0.90	± 0.01

Table 5.13. Electrochemical parameters for the three inks prepared with the following specifications: 60 min as sonication time, ethanol as solvent, 3:1 as solvent/water volume ratio.

	Sample 1	Sample 2	Sample 3	Average	St. Dev.
I_k (mA cm^{-2}) at 0.92 V	14	16	15	15	1
Activity at 0.90 V (A g^{-1})	35	41	38	38	3
I_k (mA cm^{-2}) at 0.92 V	4.0	4.2	4.2	4.1	0.1
Activity at 0.92 V (A g^{-1})	9.9	10.6	10.4	10.3	0.3
Onset Potential (V)	0.96	0.96	0.96	0.96	± <0.01
Half wave potential (V)	0.91	0.91	0.91	0.91	± <0.01

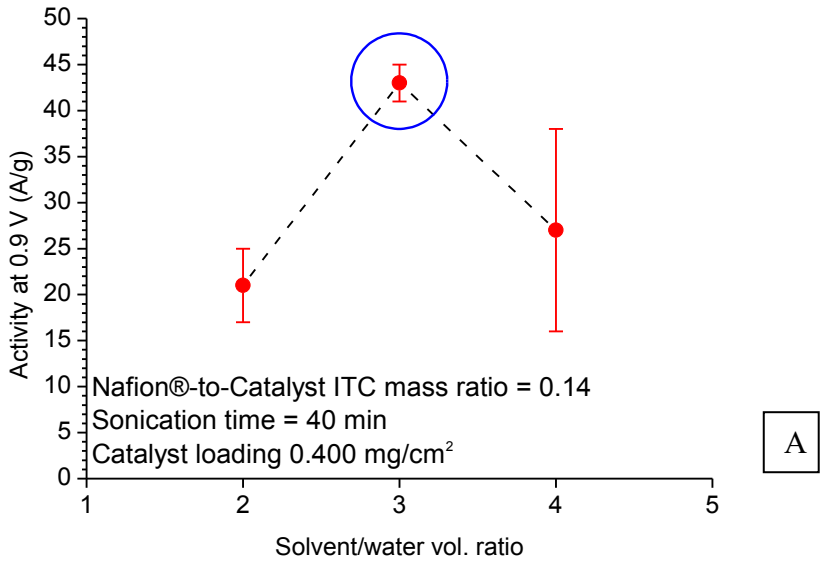

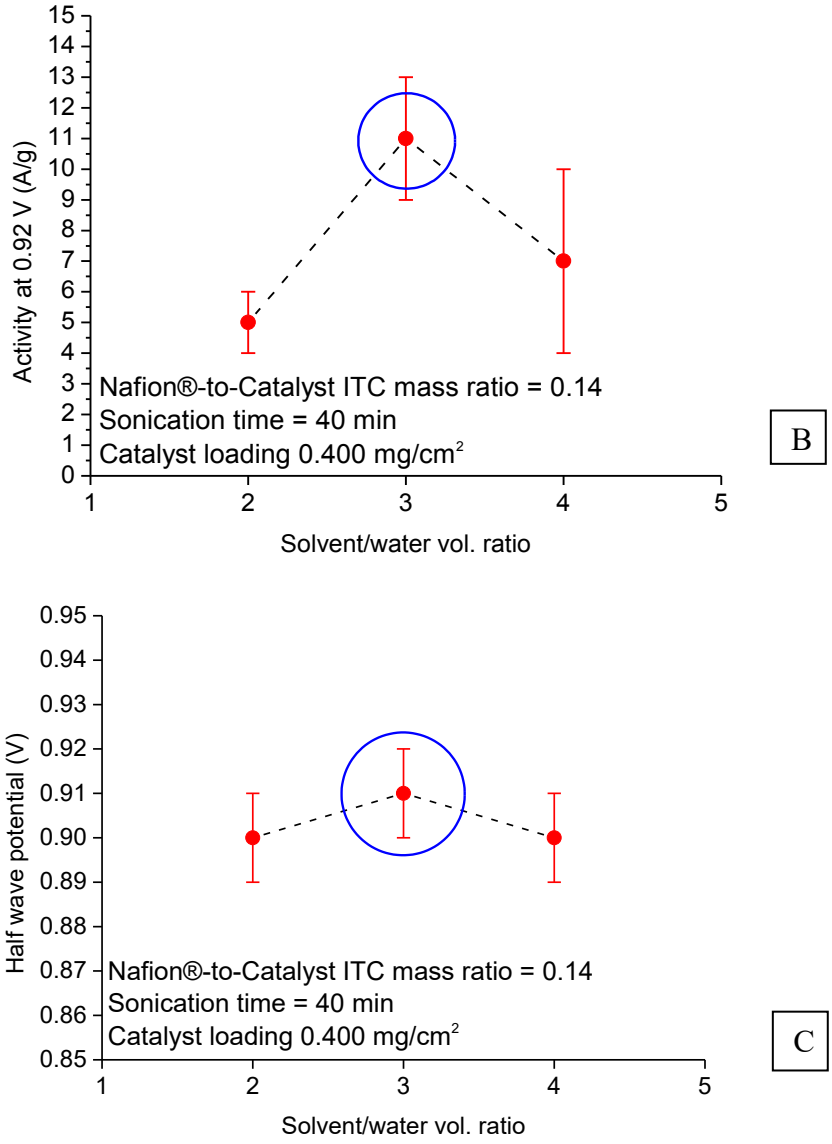

Figure 5.7. Results in terms of activity and half wave potential in ethanol varying the S/W ratio and keeping the sonication time constant. A) Activity at 0.9 V vs RHE, B) Activity at 0.2 V vs RHE, C) Half wave potential.

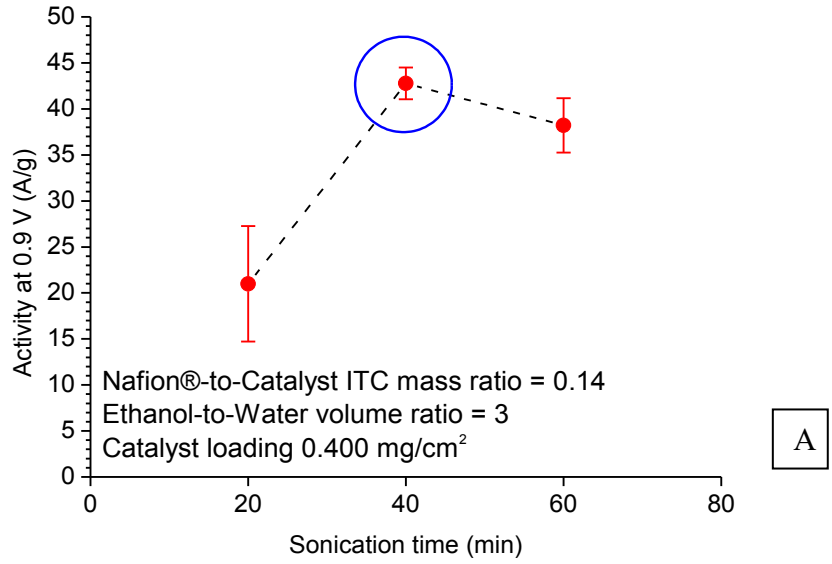

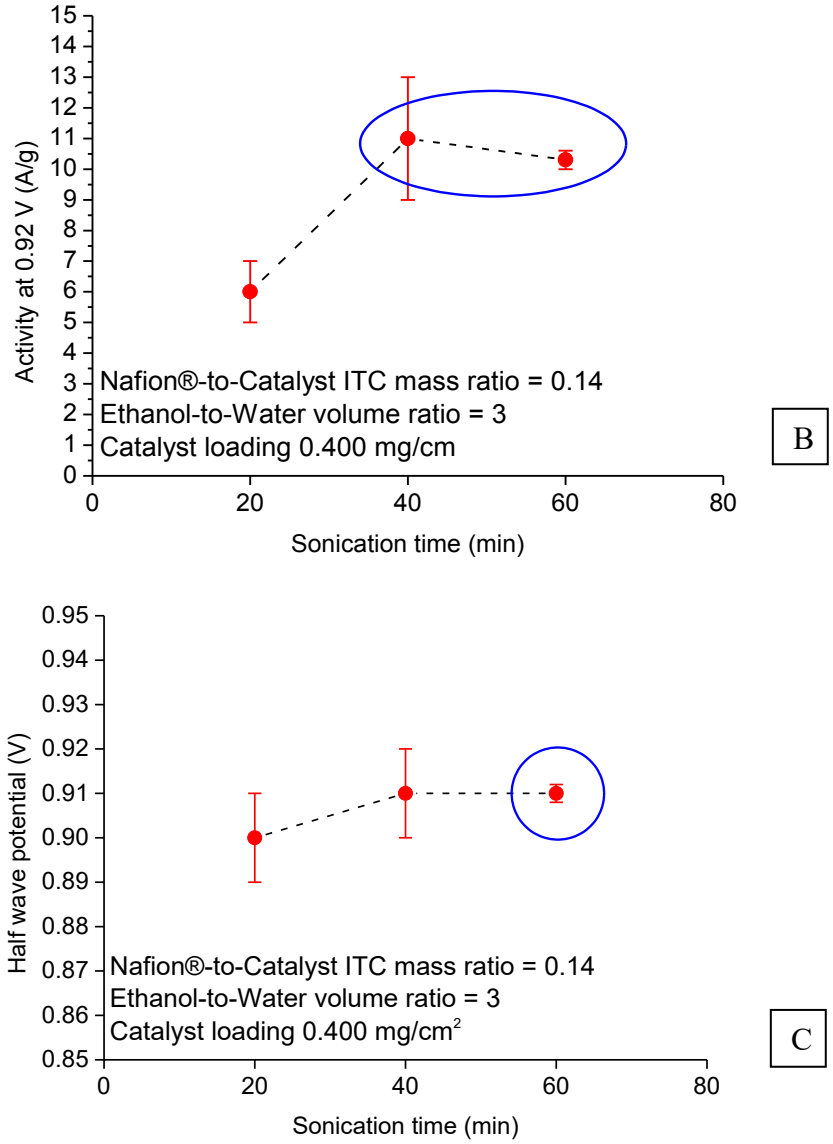

Figure 5.8. Results in terms of activity and half-wave potential in ethanol varying the sonication time and keeping the S/W ratio constant. A) Activity at 0.9 V vs RHE, B) Activity at 0.2 V vs RHE, C) Half wave potential.

Figure 5.9 A – B show the most representative results coming from the statistical analysis made above. The pictures represent the polarization curves obtained from the analysis of the ink after 40 and 60 minutes of sonication in ethanol with a solvent/water ratio of 3. These are the parameters that increase more the final performance, and decrease the dispersion, as clearly visible in **Figure 5.9** in the range from the half-wave potential to higher potential where the reaction in under faradic control.

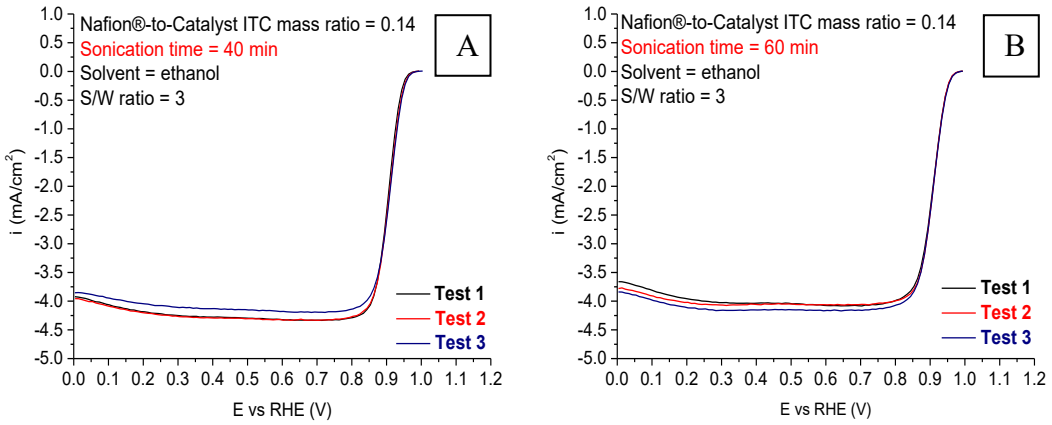

Figure 5.9. SCV recorded in O_2-saturated KOH 0.1 M alkaline solution. Results obtained through the analysis of a triple set of ink prepared in ethanol with a S/W ratio of 3 and sonicated for 40 min (A) and 60 min (B).

5.4 Conclusions

The experimental data set analyzed in this work has demonstrated that the best conditions to prepare an ink for RDE electrodes, with the V/F BM catalyst, are:

- Sonicate at least 40 minutes,
- Use ethanol as organic
- Keep the solvent/water volume ratio equals to 3.

Considering both the responses (activity and half-wave potential), the Pareto charts, and the p-values have showed that the type of solvent and its volume ratio affect the final performance more than the sonication time. The sonication time, however, remains fundamental to increase the performance of the results especially after 20 minutes. In terms of half-wave potentials, the longer is the sonication time, the lower is the final standard deviation of the half-wave potential.

This work wanted to prove the importance of the use of multivariate statistics to optimize the ink composition before its deposition on the electrode surface.

The possibility to increase the number of variables involved in the statistical analysis (for instance bath temperature, sonication frequency, etc.) would imply the use of a more time expensive “fractional” design of experiment but it would certainly lead to further improvement in terms of ink formulation.

With a focus on future improvements, it would be also appropriate to combine the electrochemical results with the dispersion particles distribution inside the ink. This type of study approach could also be used to evaluate the behavior of the ink

in case of the use of an automated robotics as spray system, for preparing electrodes of bigger size (e.g., gas diffusion layers, MEAs, etc.). Considering the repeatability of its operation, is it possible to find the best conditions that provide the best dispersion and the highest activity performance. It is not possible to apply the DOE evaluation if the deposition is made through the use of a manual sprayer. The variability during the spray deposition is very high respect to the simple deposition on a rotating disk and depends on different variables, such as the ability of the operator, the pressure of the air, the gun condition, etc.

Chapter 6

Testing in electrochemical devices

6.1 Introduction

Two different catalyst previously described were tested in electrochemical devices. The V/F BM was tested both in Direct Ethanol Fuel Cell (DEFC) and in Metal-Air Battery (MAB), since it showed a promising ORR performance at the RDE scale in alkaline conditions (in terms of activity, selectivity, and durability, see **Chapter 4**). The Z/F 2HT was tested only in MAB due to its lower activity. **Figure 6.1** shows their performance at RDE laboratory scale in terms of ORR polarization curves.

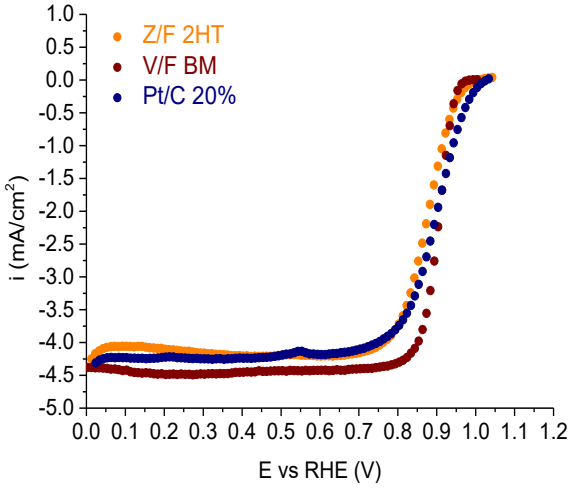

Figure 6.1. Comparison of SCV recorded in O_2-saturated electrolyte in alkaline condition between Z/F 2HT catalyst, V/F BM catalyst and Pt/C reference catalyst.

6.2 Testing of V/F BM in DEFC

The V/F BM cathode catalyst was tested in DEFC as described in the materials and methods chapter (**Chapter 2.2**). Briefly, the non noble cathode behaviour was originally evaluated at different temperatures and O_2 backpressures. Afterward, the catalyst was studied considering two different Nafion loading. The tests were mainly performed realizing MEAs with an alkaline membrane (Danish PBI). The maximum performance obtained in terms of polarization and power curves were compared with the performance of the commercial Pt/C catalyst, tested at the same test conditions. A final short durability test was carried out to evaluate the performance loss during 8 h of working time. A second set of experiments was also carried out using another type of commercial alkaline membrane, Fumapem FAA-3-50 (Germany). A comparison between the two commercial membranes was made. The experimental details and all the results are showed and described below. As a brief reminder, PtRu/C (Pt 30% Ru 15%) was always used as anodic catalyst with a final Pt loading of 1.33 mg Pt cm^{-2} and a Nafion content equal to 4% (see **Chapter 2.2** for all the details). The DEFC was always fed with 2 M EtOH/KOH solution. The potassium hydroxide was used to increase the hydroxyl ions concentrations with strong benefits for the anodic reaction kinetics and the alkaline membrane conductivity [232].

Several MEAs were prepared for different set of experiments. The aim was to evaluate the repeatability in the preparation procedure of the MEAs and their performance.

6.2.1 Cathode analysis at different temperatures: MEA1 with PBI membrane

Figure 6.2 shows the polarization and power density curves obtained increasing the temperature of the DEFC from 25 to 80 °C. As expected, the results clearly demonstrated that the temperature positively affects the maximum performance of the cell: In fact, the temperature improves the diffusion coefficient of oxygen and membrane conductivity. Furthermore, the raise of the temperature results in a reduction of the activation energy of the system [233,234].

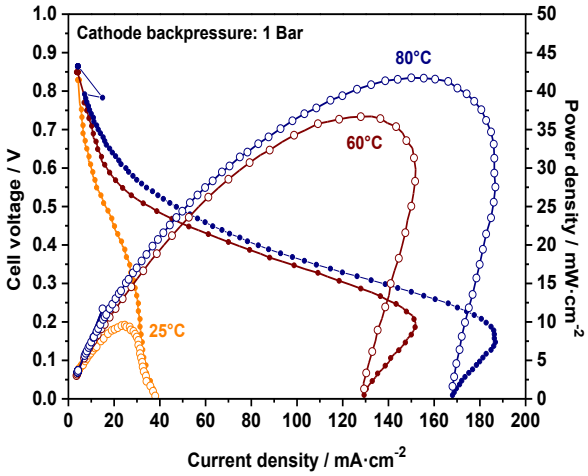

Figure 6.2. Polarization curves (filled symbols) and power density curves (open symbols) for alkaline DEFC MEA 1 prepared using V/F BM as a cathodic catalyst. The experiments were carried out at 25, 60 and 80 °C, 1 bar of O_2 backpressure, and 15% of Nafion content. Cathode catalyst loading: 3 mg/cm^2. Anode: Pt loading 1.33 mg/cm^2 and 4% of Nafion content.

6.2.2 Cathode analysis at different O_2 back pressure: MEA2 with PBI Membrane

Figure 6.3 shows the polarization and the power density curves obtained at different relative O_2 pressure (1 – 2 – 3 bar). The experiments were performed keeping constant the DEFC temperature at 90 °C. The results have showed that an increase of the O_2 back pressure results in a diminution of the overall performance in terms of maximum power and current density. This behaviour is totally in contrast respect to the performance of Fe-N-C catalysts produced from phthalocyanine and thermal treatments [31]. This result could be due to the different BET specific surface area, since phthalocyanine-based Fe-N-C catalysts had approx 1500 m^2g^{-1}, much higher that V/F BM, only 130 m^2 g^{-1} (see **Chapter 4.4**). Generally, materials with high specific surface and with high micropores require higher pressure to force oxygen diffusion to the active sites. The anodic pressure was kept constant at ambient pressure. In all experiments, the polarization curves rapidly decay beyond 200 mA cm^{-2}, with a drastic decrease of the power density. This rapidly variation could be ascribed to mass transport limitation of oxygen into the cathode catalyst layer, because of its porosity structure [232], or flooding phenomena [235,236].

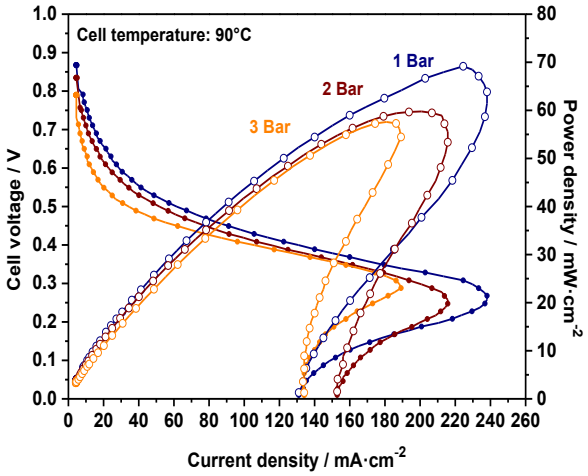

Figure 6.3. Polarization curves (filled symbols) and power density curves (open symbols) for alkaline DEFC MEA 2 prepared using V/F BM as a cathodic catalyst. The experiment was carried out at 1, 2 and 3 bar of O_2 backpressure, 90 °C as fuel cell temperature and 15% of Nafion content. Cathode catalyst loading: 3 mg/cm^2. Anode: Pt loading 1.33 mg/cm^2 and 4% of Nafion content.

6.2.3 Cathode analysis with different Nafion loading: MEA3 and MEA2 with PBI membrane

Figure 6.4 – 6.5 show the result obtained testing the V/F catalyst with different Nafion content. The presence of Nafion inside the catalyst ink is supposed to act as a binder and not as a polymer electrolyte, since the alkaline environment of DEFC. **Figure 6.4** shows the results obtained with a Nafion loading equal to 50% respect to the catalyst weight. The graph demonstrates again that an increase in pressure results in a diminution of the performance, even in the case of higher Nafion amount. This behaviour confirms what has just been described in the previous paragraph. **Figure 6.5** compares two MEAs, with 50% and 15% of Nafion at the cathode. The 15% MEA shows the best performance with 70 mW cm^{-2} as max power density at 220 mA cm^{-2} of current density, higher values compared to the 50% MEA (that is, +12% more as max power density).

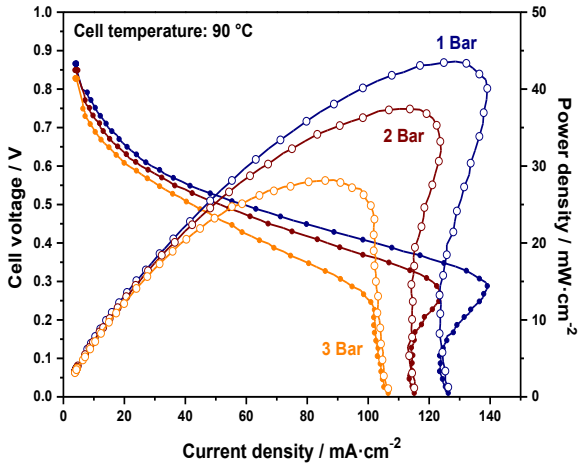

Figure 6.4. Polarization curves (filled symbols) and power density curves (open symbols) for alkaline DEFC MEA 3: prepared using V/F BM as a cathodic catalyst. The experiment was carried out at 1, 2 and 3 bar of O_2 backpressure, 90 °C as fuel cell temperature and 50% of Nafion content. Cathode catalyst loading: 3 mg cm^{-2}. Anode: Pt loading 1.33 mg cm^{-2} and 4% of Nafion content.

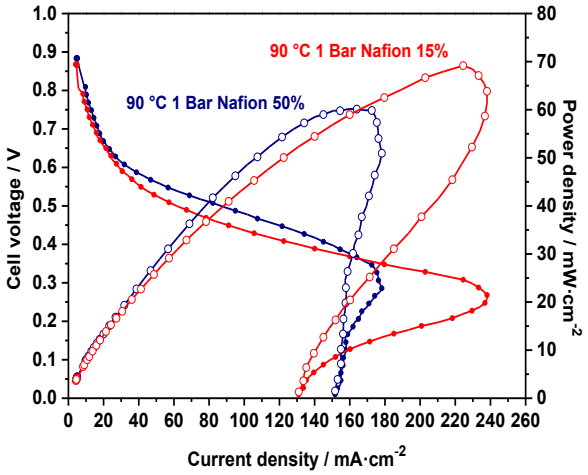

Figure 6.5. Polarization curves (filled symbols) and power density curves (open symbols) for alkaline DEFC prepared using V/F BM as a cathodic catalyst. Comparison between cathodes loaded respectively with 15% and 50% of Nafion (MEA 2 vs MEA 3). The experiment was carried out at 1 bar of O_2 backpressure at 90 °C as fuel cell temperature. Cathode catalyst loading: 3 mg cm^{-2}. Anode: Pt loading 1.33 mg cm^{-2} and 4% of Nafion content.

6.2.4 Comparison between V/F BM and Pt/C reference

Figure 6.6 shows the comparison between the best results obtained from the V/F BM (MEA 2) catalyst and the Pt/C reference working in alkaline DEFC with Danish PBI membrane. The Pt/C MEA was also tested at 3 bar as O_2 backpressure, because its performance increases with this physical parameter. As evident from the charts, respect to the Pt/C reference catalyst, the V/F BM catalyst shows better performance as power density only at 1 bar (**Figure 6.6 A**), while it remains less powerful if compared at higher

pressure (**Figure 6.6 B**). At low current density, below 40 mA cm^{-2}, the polarization curves of V/F BM and Pt/C catalysts (MEAs) are almost coincident, with the same E_{ocv} values. Either at 1 and 3 bar, the V/F BM catalyst reaches the maximum power density at lower current density values compared to Pt/C.

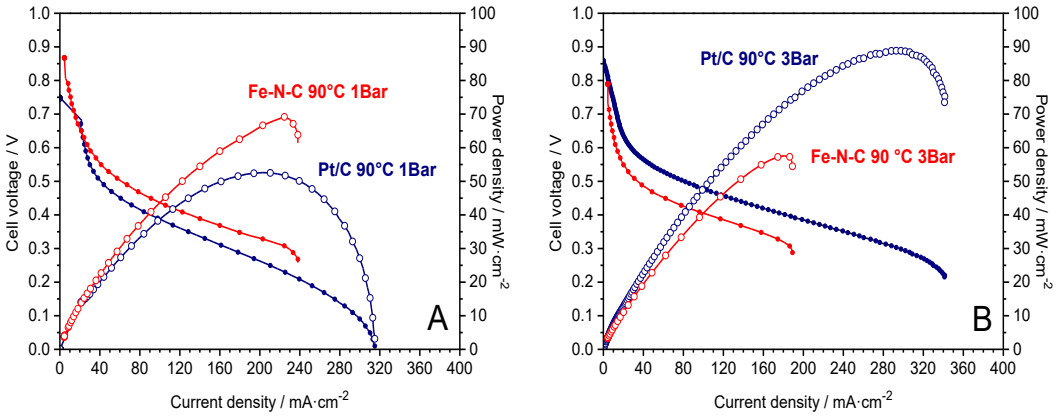

Figure 6.6 Comparison of the Polarization curves (filled symbols) and power density curves (open symbols) for alkaline DEFC between V/F BM MEA 2 and Pt/C 40% cathodic catalyst at 1 bar (A) and 3 bar (B) Non noble Cathode catalyst loading: 3 mg cm^{-2} with 15% of Nafion. Pt/C cathode catalyst loading: 1mg Pt cm^{-2} with 4% of Nafion. Anode: Pt loading 1.33 mg cm^{-2} and 4% of Nafion content.

Table 6.1 summarizes all the most important results. The mass specific power density take into account the overall amount of Pt present in the fuel cell also considering the anode. It is a sort of representation used from who is involved in this research field to demonstrate the enhancement of the results if the amount of the noble catalyst (and consequently the price) is considered. Moreover, working with Pt at 3 bar of pressure requires to spend more energy for the fuel cell operation.

Table 6.1. Comparison between V/F BM and Pt/C catalysts in terms of electrodes preparation and DEFC results. See **Table 1.2** in **Chapter 1** for details.

Catalyst type	**Anode Pt/Pd load ($mgcm^{-2}$)**	**Cathode Pt load ($mgcm^{-2}$)**	**Nafion amount (%)**	**Operating conditions**	**Power density ($mW\ cm^{-2}$)**	**Mass Pt power ($mWmg_{Pt}^{-1}$)**	**Ref**
V/C BM	1.33	3.0	15	1 bar 90°C	70	53	-
Pt/C	1.33	1.0	4	3 bar 90°C	90	39	-
Hypermec TM K14	15	3.5	n.a.	60 °C	101	n.a.	[27]
Hypermec TM K14	Pd 1 $mg_{Pd}Cm^{-2}$	n.a.	n.a.	80 °C	73	73	[28]
Fe-N-C	45% PtRu/C: 1.33 $mg_{Pt}Cm^{-2}$	2.5	50	90 °C 3 bar	73	55	[30]

Although the overall performance does not exceed that of the Pt/C catalyst, the results are promising and show the same order of magnitude of the best non noble metal catalysts reported in literature for DEFC, as shown in **Table 6.1**. Furthermore, they demonstrate the validity of the economic feasibility of the synthesis process of this V/F BM catalyst.

6.2.5 Short term durability test applied to V/F BM cathode catalyst – MEA4 with PBI membrane

In the literature, there is no specific protocol available for testing the durability for MEAs in DEFC. For this type of studies, it is fundamental guaranteeing a very stable membrane containing fixed OH−conducing groups (such as quaternary ammonium groups) that could facilitate the movement of OH−ions [237,238]. Actually, a commercial membrane with these characteristics is not still available on the market, notwithstanding the many efforts made by the scientific community.

Thus, the PBI membrane used in this experiment is doped with hydroxyl ions, but it does not contains fixed OH groups. A short durability test was conducted on a new MEA, MEA4, through a chronoamperometric test at 0.6 V for 8 h, recording a polarization curve every 30 min, as previously described in the materials and methods chapter (**Chapter 2.2**). **Figures 6.7 – 6.8** and **Table 6.2** summarize the best results obtained every hour. The working potential was fixed as 0.6 V, since it is a potential in which the current density is still far from the mass diffusion limit region (**Figure 6.7**), and the power density is approx. the 70% of the maximum initial value (**Figure 6.8**).

Table 6.2. Resume of maximum current density, maximum power density and Open circuit potential at different working time obtained after short durability test.

Time (h)	E_{OCV} (V)	Max Power density ($mWcm^{-2}$)	Power density loss (%)
0	0.87	50.6	100%
1	0.81	20.2	- 60.0%
2	0.80	24.9	- 50.8 %
3	0.77	19.7	- 61.1 %
4	0.77	23.3	- 54.0 %
Rest 30 min	0.83	36.4	- 28.1(+56.2%)
5	0.76	29.3	- 42.1 %
6	0.74	26.1	- 48.4 %
7	0.75	27.8	- 45.1 %
8(end)	0.74	25.8	- 49.0 %

The values listed in **Table 6.2** show a gradual decrease of the maximum power density and open circuit potential with the time. At the end of the test, after

8 hours of work, the maximum power density has lost the 50% of its performance. It is fundamental to notice that it is possible to recover the value of the open circuit potential and part of the maximum power density by shutting-off the DEFC for 30 minutes (DEFC at open circuit voltage without interrupting the fluxes of reagents). Shutting-off the cell after 4 h has led to a good recovery of the E_{ocv}, and a recovery of the max power density from 23 to 36 mW cm^{-2} (+56%). This behavior is promising because the increment caused by the rest suggests that the power density reduction could be due to flooding problems in the catalyst's pores, and not to a deactivation of the catalyst's active sites. In fact, the literature reports that flooding is more relevant at intermediate values of currents density, at which experiments are carried out, where usually most of the resistance is due to ohmic phenomena, and not to mass transport issues [10].

This means that the decrease of the performance is not only caused by the degradation of the catalyst, but it depends on the system itself (MEA fabrication, cell assembly, etc.). In fact, in support to this assumption, the durability results obtained with RDE were very positives, with a minimum performance decay (**Chapter 4.4**). In a DEFC, even if water is consumed as a reactant at the cathode and the electro-osmotic drag moves water from cathode to anode, studies regarding cathode flooding are well described in literature [10,239]. If the flooding affects the performance of this device, further experiments are mandatory in order to confirm this effect and evaluate catalyst hydrophilic/hydrophobic properties and contact angle, membrane conductivity, and dimensional change caused by swelling. Last but not least, also the type of membrane, fuel cell size and fluid dynamic into the bipolar plate channels affect the flooding and must be taken into account [240].

The low durability performance in DEFC may also be associated to incompatibility between the membrane materials (PBI alkaline membrane) with the ionomer adopted for the ink preparation (Nafion acid ionomer), instability of the membrane [241], lose of the close contact between the electrodes and the membrane surface, since the MEA was not prepared by hot pressing procedures [30].

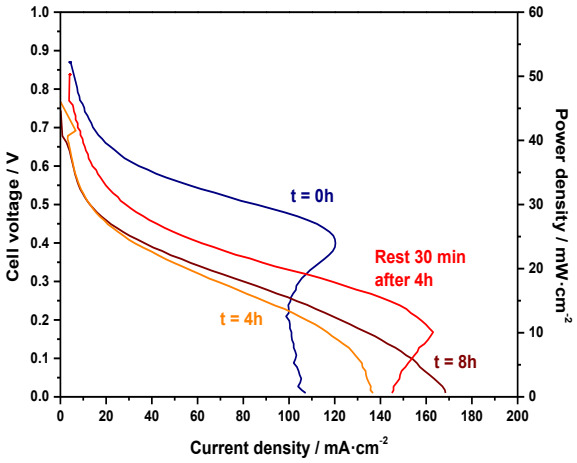

Figure 6.7. Short-term durability test in DEFC at 1 bar and 90 °C. Polarization curves acquired at different time ranges. MEA4

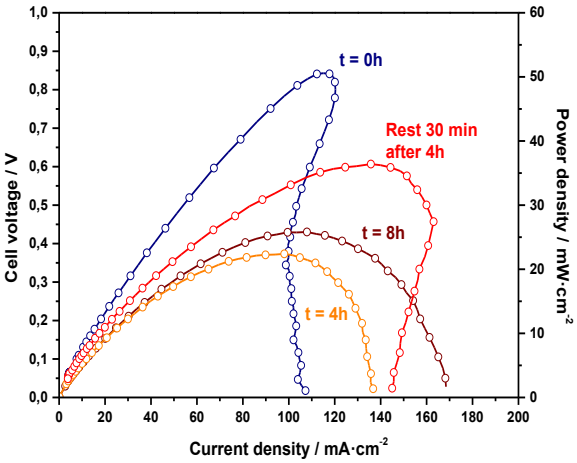

Figure 6.8. Short-term durability test in DEFC at 1 bar and 90 °C. Power density curves acquired at different time ranges. MEA4

6.2.6 Comparison between Danish PBI MEA 3 and Fumapem FAA-3-50 (MEA 5 and MEA6) alkaline membranes

The V/F BM cathode catalyst was also tested through the use of a second alkaline membrane provided by Fumapem, the FAA-3-50. Two different experiments (two different MEAs) were carried out. The first experiment was performed testing the MEA5 with the FAA-3-50 membrane following the same procedure adopted in the previous analysis conducted with the PBI membrane. The test was performed starting from low temperature and low O_2 back pressure followed by their gradually increment until the MEA reached the maximum performance. The second experiment was carried out preparing a new MEA,

MEA6, using an alkaline ionomer (Fumion 50%, see method **Chapter 2.2**) solubilized in the V/F BM catalyst ink instead of the Nafion as a binder. In fact, the idea was to combine an alkaline membrane with its specifically –OH conductive ionomer provided by the same manufacturer, since it is preferable to use a ionomer strongly compatible with the material of the membrane [242]. However, the cathode GDL preparation through manual airbrush was difficult due the high viscosity of the ink loaded with high amount of Fumion –OH ionomer. **Figure 6.9** shows different aggregations as flakes on the surface of the GDL, which appeared at the end of the spray/dry operations. These flakes did not appear when Nafion was used as binders, instead of Fumion. This problem could be solved as well suggested in the literature [243,244], through a further electrode preparation and ink optimization.

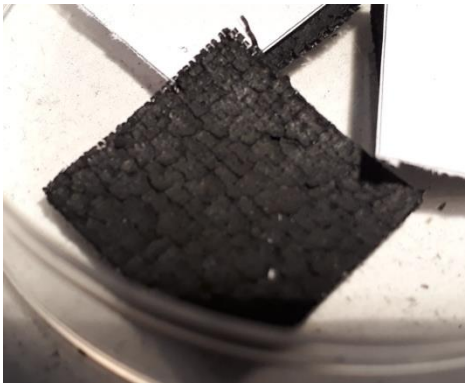

Figure 6.9. Cathodic GDL prepared using Fumion ionomer. Flake aggregations are present on the GDL surface after airbrush spray/dry operation.

Furthermore, with the Fumapem alkaline membrane it was not possible to increase the O_2 backpressure, because of a rapid O_2 crossover (**Figure 6.10**) resulting in a decrease of the open circuit and power density. Due to this technical problem, it was not possible a direct comparison between the PBI and Fumapem membranes at same operative conditions.

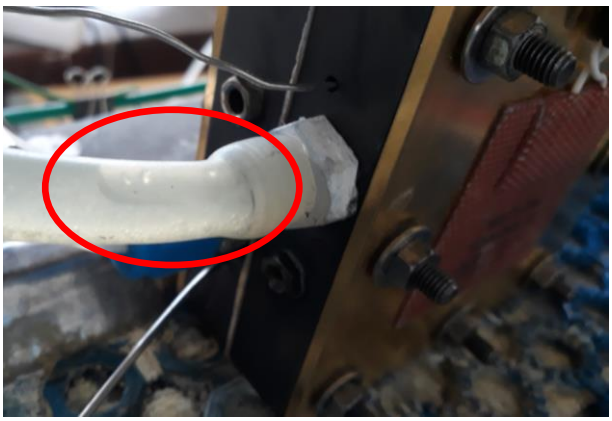

Figure 6.10. Crossover effect (red circle) produce by O_2 backpressure increment from 0.5 to 1bar.

Table 6.3 summarises the MEA composition, the operative condition and the maximum power density obtained from the experiments while **Figure 6.11** shows the best results obtained.

Table 6.3. Comparison between Danish PBI MEA 3 and Fumapem FAA-3-50. Operative conditions.

Sample name	Membrane	Ionomer	Operative conditions	Max power density ($mWcm^{-2}$)
MEA3	PBI Dopozol Danish Power System	Nafion 50%	90 °C 1 bar	53.6
MEA5	FAA-3-50 Fumapem	Nafion 15%	80 °C 0.5 bar	47.4
MEA6	FAA-3-50 Fumapem	Fumion 50%	90 °C 0.5 bar	20.0

Although the polarization curves of the two different configurations start with the same open circuit potential, the V/F BM based catalyst tested with the 50 % of Nafion in contact with the PBI membrane shows the best performance as power density compared to the FAA-3-50 membrane in contact with the same amount of Fumion (red line). The FAA-3-50 membrane showed relatively good performance with MEA5 working at 0.5 bar as O_2 backpressure. The best result showed in **Figure 6.11**, was unique and achieved after a series of unsuccessful tests. The polarization curve was close to the average performance of the curves obtained with the PBI membrane but this behaviour was not replicable. Furthermore, with the FAA-3-50 membranes it was not possible to increase the pressure more than 0.5 bar to avoid cross over effects and membrane rupture. The comparison between the PBI and FAA-3-50 membranes (**Figure 6.12 A – B**) after their most arduous working condition shows a FAA-3-50 membrane more worn even if has worked at only 80 °C under 0.5 bar of O_2 backpressure. In fact, the FAA-3-50

membrane suffered the testing in DEFC: the membrane showed signs of degradation, and appeared more worn than the PBI membrane, notwithstanding milder conditions of testing (see **Table 6.3**).

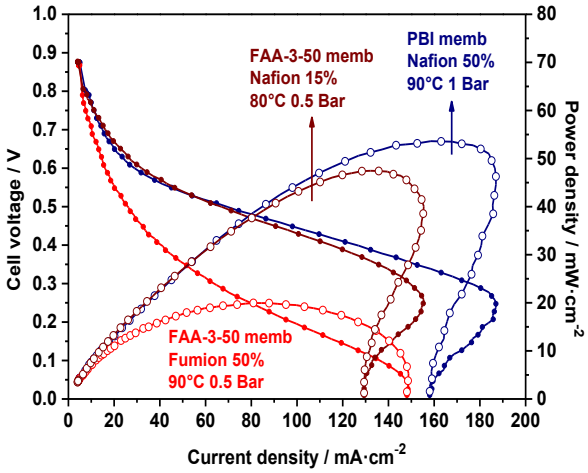

Figure 6.11. Comparison of the Polarization curves (filled symbols) and power density curves (open symbols) for alkaline DEFC equipped with PBI membrane (MEA3 blue) and FAA-3-50 membrane (MEA6 red). The best FAA-3-50 performance are coloured in brown (MEA5). Non noble Vulcan/FePc cathode loading: 3 mg cm^{-2}. PtRu/C anode loading: 1.33mg Pt cm^{-2} with 4% of Nafion.

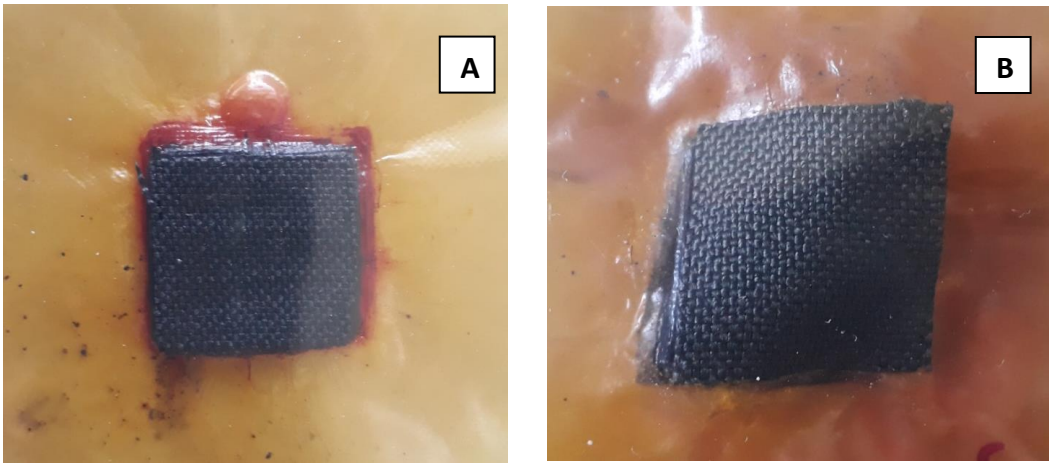

Figure 6.12. Comparison between FAA-3-50 membrane after working test at 80°C 0.5bar (A) and Danish PBI membrane after working test at 90 °C 3 bar (B).

The difference in terms of membrane performance was studied more in depth through conductivity analysis (**Figure 6.13**). The conductivity values were calculated from the resistance values obtained at different temperature through EIS experiments using the **Equation 6.1**:

$$\sigma = \frac{S}{A*R}$$ **Equation 6.1**

Where σ is the conductivity in S cm^{-1}, S is the membrane thickness in cm, A is the membrane area in cm^2 and R is the membrane resistance in ohm.

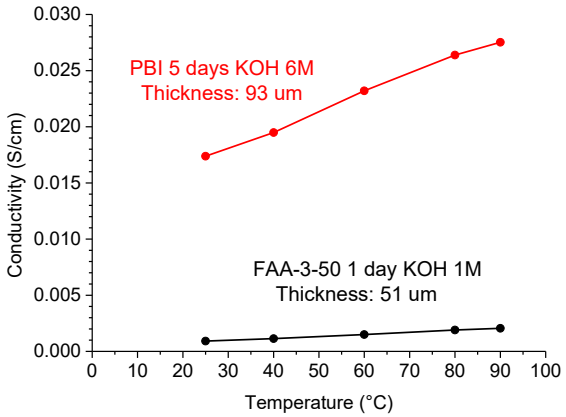

Figure 6.13. Membrane conductivity at different temperature. PBI membrane after activation in KOH 6 M 5 days (red line). FAA-3-50 after activation in KOH 1 M 1 day (black line).

The log(σ) was then plotted in function of 1000/T in an Arrhenius plot (**Figure 6.14 A – B**) to estimate the activation energy as the slope of **Equation 6.2**:

$$\ln \sigma = lnk - \frac{E_a}{RT}$$ **Equation 6.2**

In which k is a membrane constant, R is the universal gas constant, T is the temperature in K and Ea is the activation energy that activates the H^+ or OH^- motion, based on the membrane type mechanism.

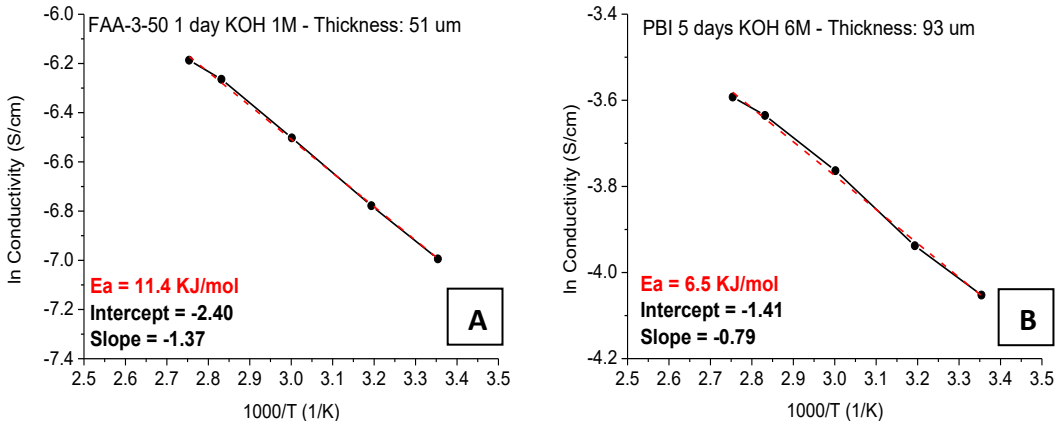

Figure 6.14. Comparison between the FAA-3-50 (A) and Danish PBI (B) Arrhenius Plot

The results obtained from this study demonstrate that a higher membrane conductivity is related to the lower energy activation. This is the case of the PBI membrane, which shows higher conductivity even if the higher thickness (93 µm) respect to the FAA-3-50 membrane (51 µm). In general, higher thickness is related to better mechanical properties. In fact, PBI membrane has showed lower O_2 crossover during the DEFC experiments.

6.3 Testing of V/F BM and Z/F 2HT in Metal-Air Battery (MAB)

The V/F BM and Z/F 2HT cathodes catalysts were also tested in alkaline MAB devices. At the beginning, the V/F BM catalyst was tested at different current density to evaluate the current working range for this class of materials. The V/F BM has been chosen since was the most promising catalyst resulted from the RDE analysis. After the selection of the most appropriate currents, the experiments were repeated with a Vulcan catalyst with double amount of iron dispersed in the carbon matrix. Z/F 2HT catalyst and MnO_2 reference were subsequently tested at the same condition, and all the catalyst were analysed through a series of dynamic galvanostatic measurements from 0 to 12 mA cm^{-2}. The cell setup and the electrode preparation are described in **Chapter 2.2**.

The data analysis of the MAB was carried out considering that are different electrochemical devices respect the fuel cells battery. For instance, the MABs tested in this work are realized with an alkaline gel electrolyte instead of a polymer alkaline membrane. Furthermore, as fundamental consideration, the MABs are primary batteries, which works with air instead of oxygen as cathodic fuel, with no backpressure to help the contact between the gas and the catalyst.

6.3.1 Preliminary tests at different discharge current density

As first set of experiment, constant discharge currents of 1.6, 3.2, 5 and 7 mA cm^{-2}, respectively, were applied to 4 different MAB with V/F BM cathode catalyst. The discharge currents were applied after 5 min of rest at open circuit potential to stabilize the E_{ocv} and allow a good contact between the electrodes and the electrolyte [38]. **Figure 6.15 A** shows the results with the evolution of the cell potential, which immediately demonstrates that the higher is the current density applied to the battery, the lower is its life time. As expect, a linear correlation between these two variables was demonstrated plotting the results in **Figure 6.15 B**. As a final result, considering the short life time of the battery at higher current density (4 h at 5 $mAcm^{-2}$ and 11 h at 7 $mAcm^{-2}$), 1.6 and 3.2 $mAcm^{-2}$ were chosen as current density for all the following experiments. The lower results at higher current density could be attributed to the low amount of iron at the cathode, and a general low activity of this class of material towards ORR in MAB fed with air at atmospheric pressure.

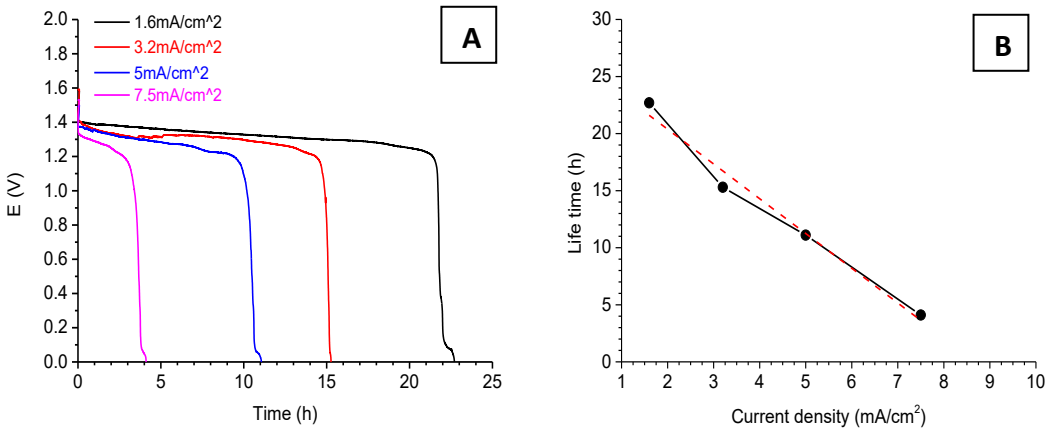

Figure 6.15. A) MAB V/F BM discharge curves at different current density. B) Relationship between current density and life time. Non noble V/F BM cathode loading: 3 mg/cm^2. Anode Al 2 cm^2. Alkaline gel electrolyte.

6.3.2 Tests with V/F BM at different Fe(II)Pc ratio

The second V/F BM with wt ratio of 2:1 was prepared and tested to compare two different iron amounts dispersed into the Vulcan carbon matrix. In fact, it is reasonable to expect an improvement in the battery lifetime increasing the amount of the active metal involved in the reaction process. As expected, the results shown in **Figure 6.16 A – B** demonstrate an increment in the lifetime of the MAB by doubling the amount of iron (V/F BM catalyst with 2:1 as weight ratio). Unfortunately, the increment in durability is not linearly connected with the

increase of iron amount. In fact, considering for example 100 g of catalyst, V/F BM 2:1 contains a double amount of iron respect to V/F BM 5:1, but it has not shown a double increment of the MAB durability.

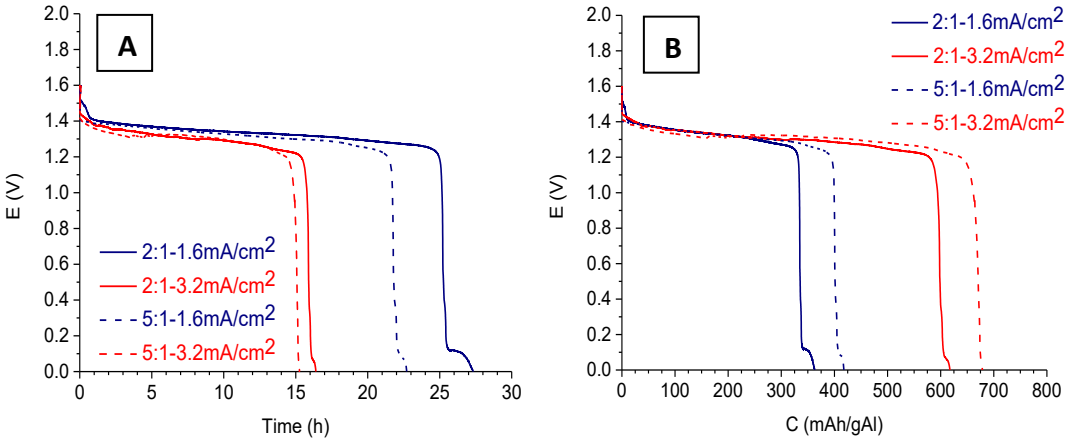

Figure 6.16. A) MAB V/F BM discharge curves at different current density (1.6 – 3.2 $mAcm^{-2}$) for different V/F BM wt ratio (5:1, 2:1) B) Mass specific capacitance of the same catalysts referred to the amount of aluminum lost during the battery discharge. Non noble V/F BM cathode loading: 3 mg cm^{-2}. Anode Al 2 cm^2. Alkaline gel electrolyte.

The mass specific capacity has followed the opposite trend: V/F BM 2:1 had lower mass capacity because more aluminum has react during the discharge process due to the higher content of Fe. A further explanation could be due to the generation of aluminates via self-corrosion, which produce $Al(OH)_3$ on the Al surface through blackening (see **Chapter 1.4**). In fact, the results is a black and porous aspect of the anode, due to the formation of an aluminate layer located on the surface of the electrode [245]. The higher is the accumulation of $Al(OH)_3$ between the gel electrolyte and the aluminium electrode, the lower is the battery lifetime because $Al(OH)_3$ blocks the diffusion process of OH^- ions to the electrode surface [38]. In conclusion, increasing the amount of iron slightly increases the battery performance. However, the use of phthalocyanine as a precursor is not a real advantage since it is the most expensive raw material in the synthesis process of the V/F BM catalyst. In particular, a double amount of iron phthalocyanine is far to be related with a double increment of the battery lifetime. Using alternative iron precursors, cheaper then phthalocyanine, like iron acetate, to the catalyst formulation could be a possible solution to this problem.

6.3.3 Comparison between V/F BM, Z/F 2HT and MnO_2/C catalysts

The synthesized catalysts were compared to a commercial MnO_2/C catalyst pasted on a Ni mesh and pressed together on a film of O_2-permeable Teflon capable to avoid liquid electrolyte leakage and water inlets. **Figure 6.17 A-D** shows the results. The initial E_{ocv} value resulted to be always comprised between 1.5-1.6 V.

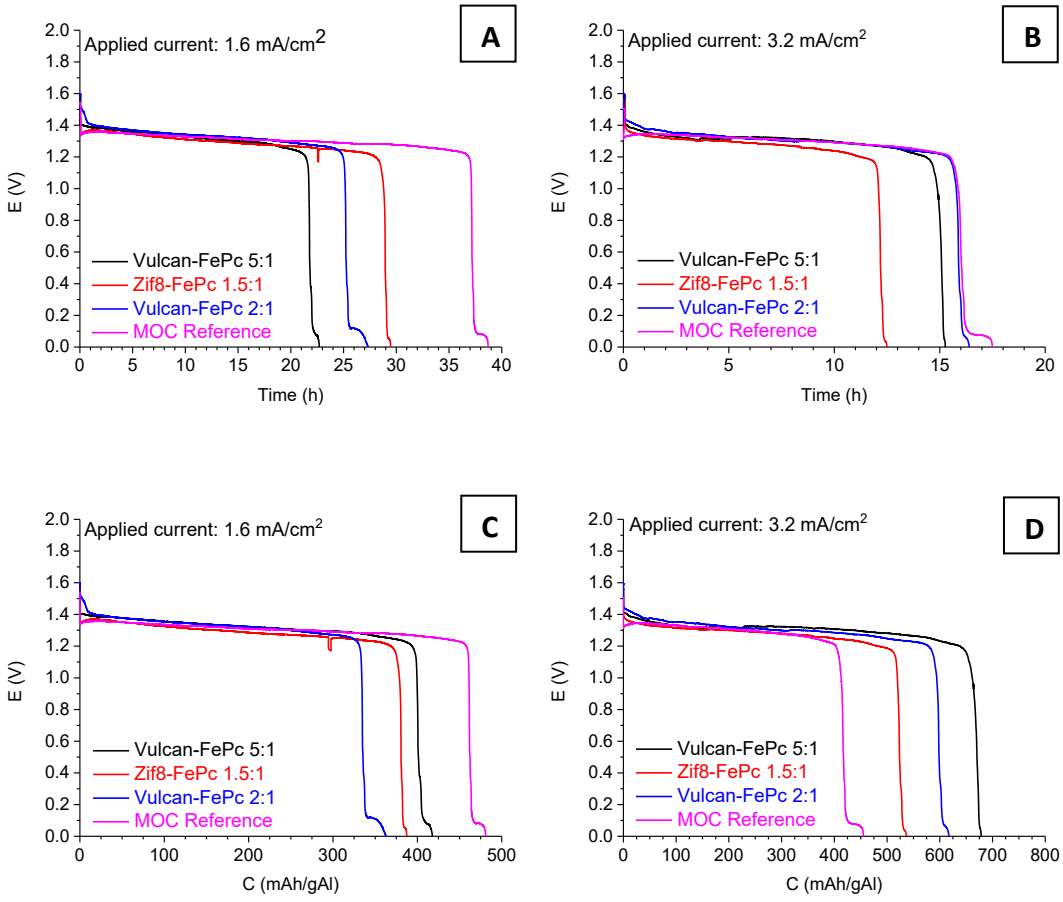

Figure 6.17. A-B) Discharge plot of the different catalysts at 1.6 and 3.2 mA cm^{-2}. Mass specific capacitance referred to the amount of aluminium lost during the battery discharge. Tests with V/F BM at different FePc ratio. Non noble V/F cathode loading: 3 mg cm^{-2}. Anode Al 2 cm^2. Alkaline gel electrolyte.

These values have immediately dropped at 1.3-1.4 V after the 5 minutes of rest time used to stabilize the open circuit potential. All the catalysts have showed a plateau in the potential curve starting from the E_{ocv} and finishing at their specific lifetime drop. At a current density of 3.2 mA cm^{-2}, the V/F BM catalysts have shown more durability respect to the Z/F 2HT catalyst, which has shown better performance at 1.6 mA cm^{-2}. In any case, regarding the durability, the MnO_2/C reference has shown better performance at both current densities.

The mass specific capacitance of this family of catalysts was difficult to understand because it has not followed a logical path. The interpretation of the maximum capacitance instead of the mass capacitance (**Table 6.4**) resulted in this case easier since it was not possible to discriminate the reasons regarding the aluminium weight loss of one catalyst compared to another (real amount of sprayed catalyst, cell assembly, $Al(OH)_3$ formation, etc.). In terms of mass capacitance, the MnO_2 reference has shown again the best performance with 124 at 1.6 mA cm^{-2} and 112 at 3.2 mA cm^{-2}.

Table 6.4. Resume of MAB results for all the catalysts analyzed in this experiment. Area electrode: 2 cm^2. Cathode catalyst loading: 3 mg cm^{-2}

	Current density (mA cm^{-2})	ΔAl (gr)	Time (h)	Capacitance (mAh)	Capacitance (mAh gr_{Al}^{-1})
Vulcan/FePc 5:1	1.6	0.174	22.7	73	417
	3.2	0.144	15.3	98	680
Vulcan/FePc 2:1	1.6	0.241	27.3	87	363
	3.2	0.170	16.4	105	617
ZIF8/FePc 1.5:1	1.6	0.243	29.4	94	387
	3.2	0.148	12.5	79	537
MnO_2/C reference	1.6	0.257	38.7	124	481
	3.2	0.246	17.5	112	455

Figures 6.18 A-D show the dynamic galvanostatic of each catalyst. The measurements were made from 0 to 12 mA cm^{-2} with a shift of 0.4 mA cm^{-2} every 10 min. The V/F BM and Z/F 2HT non noble catalysts start at higher E_{ocv}, 1.6-1.5 V, respect to the MnO_2/C, 1.4 V. However the MnO_2/C showed a constant plateau from the beginning of the test up to the end at almost 9 mA cm^{-2}, while the other synthesized catalysts exhibited a faster initial decay of the potential. All the materials showed a rapid decrease of the battery potential once reached 8.5-10 mA cm^{-2} as applied current density. In this type of experiment, Vulcan/Fe 5:1 catalyst showed the best performance in terms of maximum durability (4.5 h).

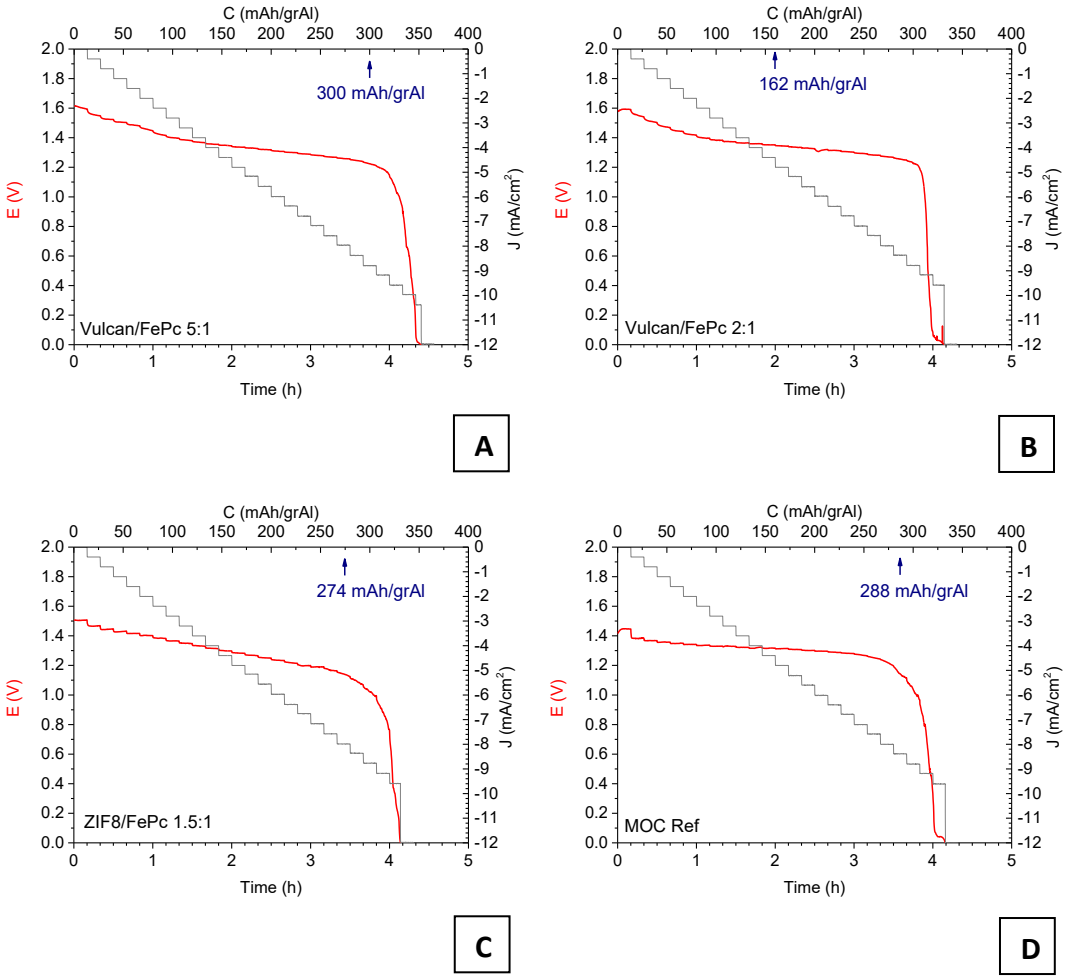

Figure 6.18. Dynamic galvanostatic measurements from 0 up to 12 mA cm^{-2} with a shift of 0.4 mA cm^{-2} every 10 min for A) Vulcan/FePc 5:1 B) V/F BM 2:1 C) Z/F 2HT 1.5:1 D) MnO_2/C reference alkaline MAB. Non noble V/F BM cathode loading: 3 mg cm^{-2}. Anode Al size: 2 cm^2. Alkaline gel electrolyte.

The small differences between the catalyst are more visible plotting the polarization and density power curves showed in **Figure 6.19 A-D** and compared in **Figure 6.20 A-B**. The polarization curves were obtained from the galvanostatic measurement. In fact, the mean value of the potential in every current step, could be considered as a potential value in function of the applied current. The results placed in a plot E (V) vs i (mA cm^{-2}) generate the typical polarization curve a general battery device [35]. The power density curve was then calculated directly through the usual P=VI equation. From **Figure 6.20 B** it is clear that V/F BM 5:1 showed the best performance in terms of maximum current and power density, but the differences with the other material are very low. This could be related to the not fully reproducible manual preparation of the cathode layer with the airbrush gun, or in the cell assembly phase.

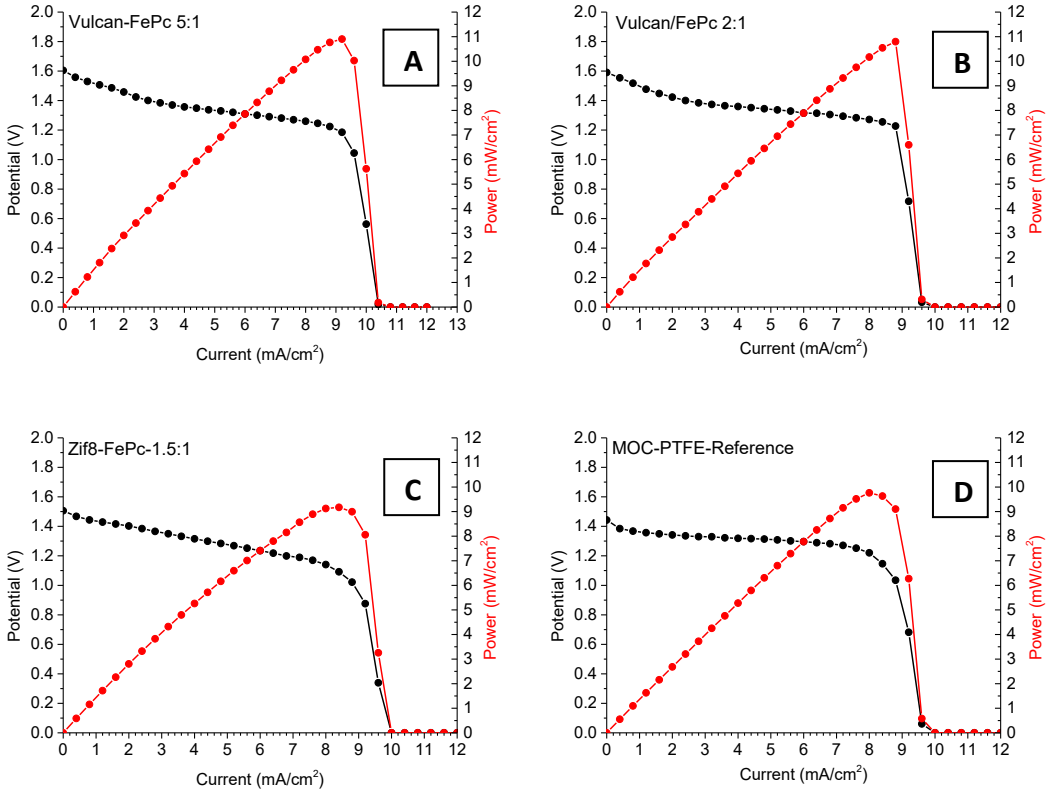

Figure 6.19. Polarization curves (filled symbols) and power density curves (open symbols) for A) V/F BM 5:1 B) V/F BM 2:1 C) Z/F 2HT 1.5:1 D) MnO_2/C reference alkaline MAB. Non noble V/F BM cathode loading: 3 mg cm^{-2}. Anode Al 2 cm^2. Alkaline gel electrolyte.

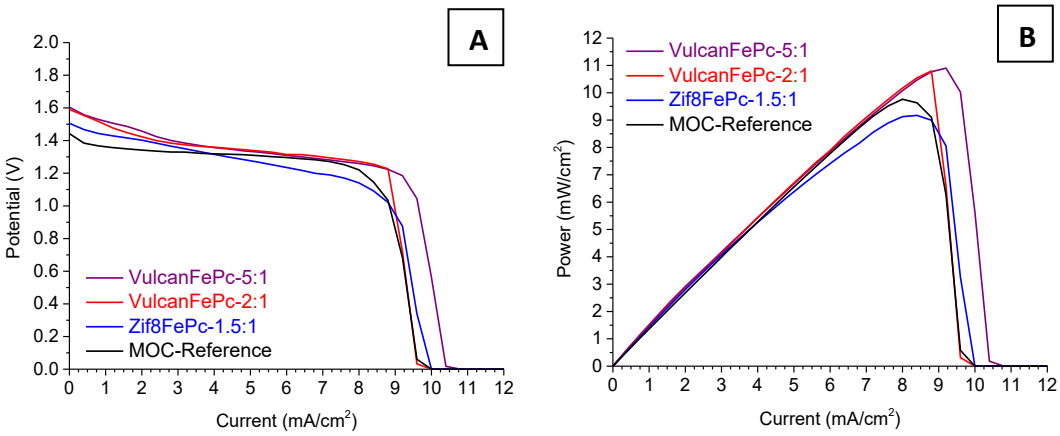

Figure 6.20. Final comparison in terms of Polarization curves (A) and power density curves (B) of all the catalysts analyzed in MAB.

Figures 6.21 A-B show final resume histograms regarding the comparison at different current density of the aluminium weight loss and the battery lifetime for

all the catalysts analyzed. From **Figure 6.21 A**, the aluminium weight loss was related with the current density and the battery lifetime: lower was the current density, more durable was the battery and higher was the final anode weight loss. Only the MnO_2 reference showed a similar Al weight loss for both the current density tested, even if even its durability at 1.6 mA cm^{-2} was double respect to that at 3.2 mA cm^{-2}. Unfortunately, part of the aluminium was lost due to the anode self-corrosion process in alkaline media, which starts immediately when the battery was closed. This secondary reaction generates H_2 and $Al(OH)_4^-$ and it is not possible to discriminate the amount of aluminium involved in the primary reaction respect to the amount involved in the second undesired reaction. In this experiment, at the end of the current discharge, the Al anode was always not totally consumed because the production and accumulation of $Al(OH)_3$ at the interface between the gel and the Al anode was the reason for the death of the battery. The lifetime behaviour showed in **Figure 6.21-B** demonstrates that the higher is the applied current density, the lower is the battery lifetime. In theory, the use of a double current density should halve the lifetime and this phenomena was observed especially with the Z/F 2HT catalyst, and even more in the case of MnO_2/C reference catalyst. At 1.6 mA cm^{-2} the durability lifetime of the non noble catalysts increased with the iron catalyst content, while at 3.2 mA cm^{-2} the histograms did not show great differences. The aim of a primary metal-air battery catalyst is to work as long as possible time with the highest consumption rate of materials, to exploit as much as possible (till to the end of life) the aluminium anode. From this point of view, Z/F 2HT catalyst was the best at 1.6 mA cm^{-2} of current density and V/F BM 2:1 was the most performing at 3.2 mA cm^{-2}.

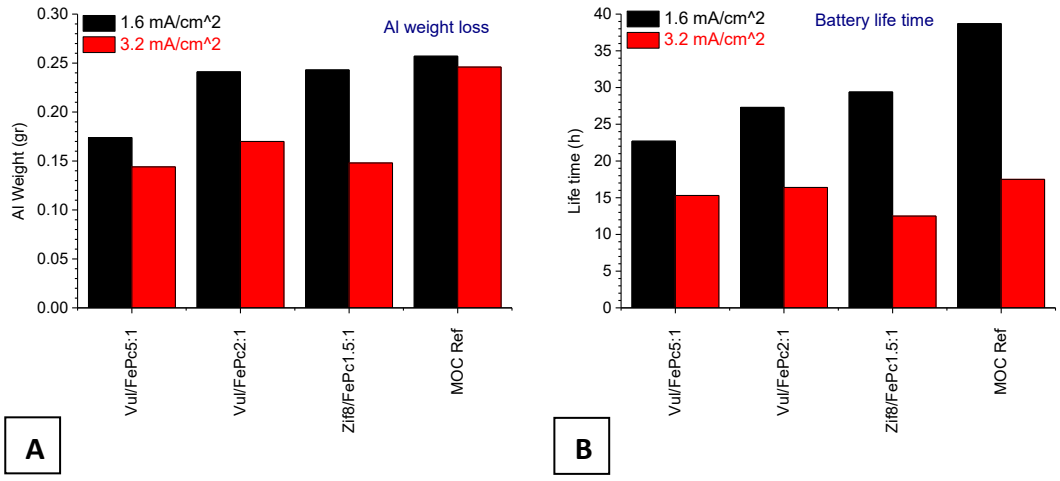

Figure 6.21. Final resume histograms of aluminium weight loss (A) and battery lifetime (B) of all the catalysts analyzed in MAB.

Chapter 7

Main conclusions and scale up evaluation

7.1 Conclusions

In this work of thesis, two non noble metal catalysts active toward ORR, were synthesized, optimized, characterized and tested in DEFC and MAB.

The Z/F 2HT synthesis optimization, has demonstrated that the best conditions are obtained working in hexane with a sulphur concentration three times higher respect the molar concentration of iron phthalocyanine and Z/F 2HT weight ratio equal to 1.5. Sulphur has demonstrated to preserve the Fe-N_4 ensembles during the pyrolysis phase. Thus, the value of 1.5 was chosen as optimal Z/F 2HT weight ratio since it was the best compromise between catalyst activity in RDE and mass loss during the synthesis, due to the Zif-8 evaporation at high temperature. The maximum temperature reached during the pyrolysis step was 880 °C and the dwell time at high temperatures between 800 and 880 °C was 1 h. For this class of materials, two pyrolysis steps seem to affect the performance more than only one heat treatment. Moreover, the hydrothermal synthesis proved to be a more effective synthesis in producing active catalysts respect to the mechano-chemical ball milling method. The final catalyst, named **"**Z/F 2HT", was able to reach 8.7 A g^{-1} as mass specific activity and 0.87 V as half-wave potential at RDE level. This result is comparable to the best current results present in the literature for this class of catalysts obtained from Strickland et al. [86,126] at higher temperature (1000 °C under NH_3 atmosphere vs 800-880 °C under N_2/H_2 atmosphere).

The V/F BM synthesis optimization has demonstrated that the best conditions are obtained mixing these two raw materials with a weight ratio of 5:1. The ball milling step without further thermal treatments was sufficient for producing a very active catalyst. In fact, the optimization process demonstrated that adding further synthesis steps, such as heat treatments or acid leaching, negatively affected the

ORR activity of the catalysts. The reproducibility of the synthesis, the production of almost one gram of catalyst (750 mg) and the testing in DEFC have also been demonstrated. The final catalyst, named "V/F BM", was able to reach 35 A g^{-1} as mass specific activity and 0.91 V as half-wave potential at RDE level. This result was comparable with the Pt/C reference tested in the same conditions.

In terms of electrochemical performance, although the Z/F 2HT shows higher specific surface area and its Tafel plot is more similar to the Pt/C reference, the V/F BM catalyst obtained by simple mixing raw materials in ball mill shows better performance in terms of mass activity, half-wave potential, and durability. The H_2O_2 % production results for both catalysts are in accordance, and in some case better, respect to the literature [91,217,227]. The short RRDE durability of V/F BM catalyst compared to Pt/C 20% in alkaline condition is very promising. The V/F BM catalyst was studied both for fuel cell and metal-air battery applications since it showed better performance respect to the Z/F 2HT catalyst in terms of activity.

The optimization carried out on the ink formulation using the design of experiment has demonstrated the best conditions useful to maximize the activity and the reproducibility of the results in terms of mass specific activity and half wave potential. Sonication for at least 40 minutes using ethanol as organic solvent with a solvent/water volume ratio equals to 3 was identified as the best condition to improve the V/F BM catalyst ink formulation. Moreover, this work proved the importance of the use of multivariate statistics with the aim of optimize the ink composition before its deposition on the electrode surface

The experiments carried out in DEFC have demonstrated that the best operative condition in terms of activity, are obtained working with the Danish PBI alkaline membrane at 90 °C as cell temperature, with 1 bar as O_2 back pressure and 15% as Nafion cathode content. Although the overall performance does not exceed that of the Pt/C catalyst, the results are promising since have reached 70 mW cm^{-2} as maximum power density and 53 mW mg_{Pt}^{-1} as mass specific power density. These values have the same order of magnitude of the best non noble metal catalysts reported in literature for DEFC [27,28,30,31,33].

Concerning the durability, after 8 hours of work, the cell has lost 0.1 V as E_{ocv} and the 50% of its performance in terms of maximum power density. By shutting-off the DEFC for 30 minutes after 4 h of work (DEFC at open circuit voltage without interrupting the fluxes of reagents), has led to a partial recovery of the E_{ocv} and a recovery of the maximum power density from 23 to 36 mW cm^{-2} (+56%). This behaviour was promising because the increment caused by the refresh suggested that the power density reduction could be due to flooding problems in the catalyst's pores, and not to a deactivation of the catalyst's active sites.

The application of the two catalysts in MAB have demonstrated a different behaviour from the RDE analysis. At lower discharge current density (1.6 mA

cm^{-2}) the Z/F 2HT showed better results in both terms of durability and capacitance (29.4 h, 94 mAh). At higher discharge current density (3.2 mA cm^{-2}) V/F BM catalyst showed the best performance (15.3 h, 98 mAh). Moreover, by doubling the amount of Fe(II)Pc in the V/F BM catalyst formulation, the performance at 3.2 mA cm^{-2} further increased (16.4 h, 105 mAh). This behaviour is opposed to the results obtained at RDE level, in which the V/F 5 activity was higher than the V/F 2 activity (see **Chapter 3**.). The explanation lies in the difference between the devices since the MAB is a primary battery fed with air at atmospheric pressure and the polymer membrane is replaced by an electrolytic gel. Compared to the commercial MnO_2/C reference catalyst (38.7 h and 124 mAh at 1.6 mA cm^{-2}, 17.5 h and 112 mAh at 3.2 mA cm^{-2}), the Z/F 2HT and V/F BM catalysts showed lower durability and lower capacitance (see **Table 6.4**). The power density of the V/F BM catalyst (both V/F 5 and V/F 2), is the only most performing feature compared to the MnO_2/C reference. In any case, further improvements are required.

In conclusion, it is also fundamental to make a consideration regarding the possible scale-up development of these two catalysts. Regarding the hydrogen PEMFC, the American Department of Energy (DOE) have deeply analyzed the minimum requirements in terms of cost and performance mandatory for a sustainable application in the automotive sector [75,76]. In the case of AEMFC and DAFC, there are no current guidelines.

While the Pt/C catalysts are already in a production phase, the non noble metal catalyst are still in a scale-up/validation/MEA testing phase. Few companies are evaluating the commercialization of non noble metal catalysts [246]. These materials, in some applications, are showing promising results in terms of activity and durability. E.g., Lo Vecchio et al. [247], have demonstrated high activity (70 mW cm^{-2}) and good durability (loss of the 60% of the initial performance after 100 h of work) of the PMF-011904 commercial catalyst purchased from Pajarito Powder, LLC tested in DMFC (90 °C, 5 M CH_3OH, 45 % of Nafion amount, 6 mg cm^{-2} FeNC catalyst loading). According to Banham and Ye from Ballard Power Systems [248], three basic criteria must be respected to consider an industrial development of the fuel cell catalyst: activity, durability[249], and cost. Among the two catalysts synthesised in this work, the V/F BM is the one to be considered since it showed higher performance in terms of activity and durability. The activity in DEFC, which is related to the power density requirements of the devices, has shown good performance compared to the Pt/C reference and the literature best results. The durability has not shown excellent results, but the decrease of the performance was not only caused by the degradation of the catalyst, since it also depends on the system itself (MEA fabrication, cell assembly, type of membrane, fuel cell size, flooding due to fluid dynamic into the bipolar plate, etc.[240]). Activity and durability in MAB have shown results close, but not higher, to that of the MnO_2/C reference cathode. However, improvements in synthesis can fill the gap.

In terms of costs, the reagent prices and the development/management (not only R&D costs, but also energy, equipment purchase and its amortisation, waste

management, gas and solvent recovery, etc) of the industrial process should be considered. The prices of the raw materials bought in large amount for chemical processes are very different from the prices proposed for laboratory and small research applications. However, commercial laboratory prices have been used as reference to make a sort of comparison. **Table 7.1** summarises the costs of the commercial raw materials (from Sigma Aldrich and FuelCellStore) and the hypothetical costs of Z/F 1.5, V/F 5 and Pt/C 20% catalysts obtained combining only the starting reagents in their specific wt ratios.

Table 7.1. Raw materials costs from commercial company

Category	Raw material	Producer	Prize (€/g)
Precious metal	Pt	Stock index October 2019	26
Carbon support	Vulcan xc 72	FuelCellStore	0.9
Sulfur Precursor	Sulfur 100%	Sigma Aldrich	1.9
Nitrogen/Iron Precursor	Iron(III)-phthalocyanine chloride	Sigma Aldrich	14.4
	Iron(II)-phthalocyanine	Sigma Aldrich	15.5
Organic Framework	Basolite Z1200	Sigma Aldrich	7.9
	Methyl-imidazole	Sigma Aldrich	0.3
	Zinc chloride	Sigma Aldrich	11.9
Solvent/Acid	n-Hexane 95%	Sigma Aldrich	0.2
	Ethanol 99.8%	Sigma Aldrich	0.2
	Sulfuric acid 95-97 %	Sigma Aldrich	0.02
Pt/C 20%	**Sigma Aldrich - Merk**		**113**
Raw Materials combined without process	**Z/F 1.5 2HT**	**-**	**10.5**
	V/F 5 BM	**-**	**3.3**
	Pt/C 20%	**-**	**5.9**

The Z/F 1.5 catalyst should cost at the beginning around 10.5 € g^{-1} considering the synthesis carried out from Zif-8 and phthalocyanine. Starting from their precursor (Methyl-imidazole, Zinc chloride, etc) the final cost partially decreases. However, considering the 80% of mass loss during the heat treatments the final price increases five times (at laboratory scale). Moreover, it is necessary to take into account high-pressure vessel, the use of solvent inside the autoclave, the energy required for the heat treatments at high temperature, the intermediary acid leaching process, the use of hydrogen gas during the 2nd pyrolysis with the possible formation of H_2S in the presence of sulphur, which must be recovered with Claus process. For example, it was estimated that synthesis based on carbon

wet impregnation with metal/nitrogen precursor requires about 200-300 litres of solvent for the preparation of 1 kg of M-N-C catalyst. The use of solvents and acids also introduce the problem of waste management [110]. The process could be optimized at higher scale, but all these treatments could not exclude a higher final price compared to the commercial Pt/C catalyst.

The V/F 5 shows a more suitable condition. Starting from the raw materials, the catalyst should cost around 3.3 €/g, which is lower compared to the Pt/C and the Z/F counterpart. Moreover, the main process at this stage of work is the dry ball milling step, since heat treatment and solvents are not present. Thus, the fundamental step in the scale-up phase is the understanding of the ball mill sizing. The ball milling is widely used in the manufacturing industries for size reduction, synthesis, mechanical alloying and mechanochemical treatment. In some applications, such as for the mine manufacturing industries, the ball mill operation is an energy-intensive process and every improvement in the energy efficiency results in economic benefits [250]. However, guidelines and methodologies for the optimization and the scale-up of the ball milling process are not established yet. The knowledge is mainly based on "*trial-and-error"* experience [251]. Among the different process variables, it is definitely confirmed that the impact energy of grinding balls is a controlling factor directly connected with the mechanical energy required from the ball-milling process. Moreover, it is fundamental for the determination of the final specific energy in terms of ratio between the power and throughput in the case of continuous systems (given typically in kWh t^{-1}) [250]. Several approaches have been studied in the last years to get closer to the real scale-up results. In the past, traditional energy-size reduction methods (Bond 1952) and the population balance model (PBM) (Fuerstenau and Hebst – 1980, Austin et al 1984 [252]) have mainly been used. Actually, the most powerful and promising methodology used to calculate the motion of the grinding balls is the computational modelling through discrete element method (DEM) [250,251,253].

7.1 Future perspectives

The design and optimization of the catalyst requires further investigation.

The durability of the catalyst must be evaluated more deeply. The aim is to understand if the performance loss are caused by the device (membrane conductivity, dimensional change caused by swelling, flooding, fluid dynamics of the bipolar plate channel) or by the catalyst (deactivation of active sites, hydrophilic/hydrophobic properties and contact angle, etc). Moreover, it is fundamental to test the V/F BM catalyst in AEM-FC fed with hydrogen, to evaluate its performance with this promising fuel.

Concerning the MAB, the synthesis should be re-evaluated increasing the amount of the Fe-N precursor, since they operate differently compared to the PEMFCs.

Regarding the scale-up process, it would be appropriate to evaluate the impact energy of the V/F BM soft material using traditional or computational methods.

Chapter 8

References

[1] A. J. Appleby and F.R. Foulkes, Fuel Cell Handbook, 2004. doi:10.1002/zaac.200300050.

[2] L. Osmieri, L. Pezzolato, S. Specchia, Recent trends on the application of PGM-free catalysts at the cathode of anion exchange membrane fuel cells, Curr. Opin. Electrochem. 9 (2018) 240–256. doi:10.1016/j.coelec.2018.05.011.

[3] C.A.D. Rodriguez, G. Tremiliosi-Filho, Electrochemical Deposition, 2013. doi:10.1007/978-0-387-92897-5_700.

[4] L.J.M.J. Blomen, M.N. Mugerwa, Fuel cell systems, Springer Science & Business Media, 2013.

[5] S. Rousseau, C. Coutanceau, C. Lamy, J.M. Léger, Direct ethanol fuel cell (DEFC): Electrical performances and reaction products distribution under operating conditions with different platinum-based anodes, J. Power Sources. 158 (2006) 18–24. doi:10.1016/j.jpowsour.2005.08.027.

[6] Y. Chen, M. Bellini, M. Bevilacqua, P. Fornasiero, A. Lavacchi, H.A. Miller, L. Wang, F. Vizza, Direct Alcohol Fuel Cells: Toward the Power Densities of Hydrogen-Fed Proton Exchange Membrane Fuel Cells, ChemSusChem. 8 (2015) 524–533. doi:10.1002/cssc.201402999.

[7] C. Venkateswara Rao, Y. Ishikawa, Activity, selectivity, and anion-exchange membrane fuel cell performance of virtually metal-free nitrogen-doped carbon nanotube electrodes for oxygen reduction reaction, J. Phys. Chem. C. 116 (2012) 4340–

4346. doi:10.1021/jp210840a.

[8] K.N. Grew, W.K.S. Chiu, A dusty fluid model for predicting hydroxyl anion conductivity in alkaline anion exchange membranes, ECS Trans. 13 (2008) 61–72. doi:10.1149/1.3010877.

[9] D.R. Dekel, Review of cell performance in anion exchange membrane fuel cells, J. Power Sources. 375 (2018) 158–169. doi:10.1016/j.jpowsour.2017.07.117.

[10] Y.S. Li, T.S. Zhao, R. Chen, Cathode flooding behaviour in alkaline direct ethanol fuel cells, J. Power Sources. 196 (2011) 133–139. doi:10.1016/j.jpowsour.2010.06.111.

[11] S. Sarangapani, F.J. Luczak, M. Enayetullah, T. Vitella, P. Osenar, Alkaline direct methanol fuel cell, ECS Trans. 1 (2006) 11–22. doi:10.1149/1.2209385.

[12] C. Cremers, D. Bayer, B. Kintzel, M. Joos, F. Jung, M. Krausa, J. Tübke, Oxidation of alcohols in acidic and alkaline environments, ECS Trans. 16 (2008) 1263–1273. doi:10.1149/1.2981967.

[13] C. Kunusch, P. Puleston, M. Mayosky, Sliding-Mode Control of PEM Fuel Cells (Advances in Industrial Control), Control. (2012) 197. doi:10.1007/978-1-4471-2431-3.

[14] S. Park, J. Lee, B.N. Popov, A review of gas diffusion layer in PEM fuel cells : Materials and designs, Int. J. Hydrogen Energy. 37 (2012) 5850–5865. doi:10.1016/j.ijhydene.2011.12.148.

[15] Z.F. Pan, L. An, T.S. Zhao, Z.K. Tang, Advances and challenges in alkaline anion exchange membrane fuel cells, Prog. Energy Combust. Sci. 66 (2018) 141–175. doi:10.1016/J.PECS.2018.01.001.

[16] L. Jinlong, W. Zhuqing, L. Tongxiang, S. Ken, M. Hideo, Enhancing the corrosion resistance of the 2205 duplex stainless steel bipolar plates in PEMFCs environment by surface enriched molybdenum, Results Phys. 7 (2017) 3459–3464. doi:10.1016/j.rinp.2017.09.001.

[17] Q. Li, R. Cao, J. Cho, G. Wu, Nanocarbon electrocatalysts for oxygen reduction in alkaline media for advanced energy conversion and storage, Adv. Energy Mater. 4 (2014).

doi:10.1002/aenm.201301415.

[18] V. V. Shevchenko, M.A. Gumennaya, Synthesis and properties of anion-exchange membranes for fuel cells, Theor. Exp. Chem. 46 (2010) 139–152. doi:10.1007/s11237-010-9131-4.

[19] G. Merle, M. Wessling, K. Nijmeijer, Anion exchange membranes for alkaline fuel cells: A review, J. Memb. Sci. 377 (2011) 1–35. doi:10.1016/j.memsci.2011.04.043.

[20] S. Watanabe, K. Fukuta, H. Yanagi, Determination of Carbonate Ion in MEA During the Alkaline Membrane Fuel Cell(AMFC) Operation, ECS Trans. 33 (2010) 1837–1845. doi:10.1149/1.3484674.

[21] S. Song, P. Tsiakaras, Recent progress in direct ethanol proton exchange membrane fuel cells (DE-PEMFCs), Appl. Catal. B Environ. 63 (2006) 187–193. doi:10.1016/j.apcatb.2005.09.018.

[22] S.P.S. Badwal, S. Giddey, A. Kulkarni, J. Goel, S. Basu, Direct ethanol fuel cells for transport and stationary applications - A comprehensive review, Appl. Energy. 145 (2015) 80–103. doi:10.1016/j.apenergy.2015.02.002.

[23] D.D. James, P.G. Pickup, Effects of crossover on product yields measured for direct ethanol fuel cells, Electrochim. Acta. 55 (2010) 3824–3829. doi:10.1016/J.ELECTACTA.2010.02.007.

[24] M.Z.F. Kamarudin, S.K. Kamarudin, M.S. Masdar, W.R.W. Daud, Review: Direct ethanol fuel cells, Int. J. Hydrogen Energy. 38 (2013) 9438–9453. doi:10.1016/j.ijhydene.2012.07.059.

[25] T.J. Omasta, L. Wang, X. Peng, C.A. Lewis, J.R. Varcoe, W.E. Mustain, Importance of balancing membrane and electrode water in anion exchange membrane fuel cells, J. Power Sources. 375 (2018) 205–213. doi:10.1016/j.jpowsour.2017.05.006.

[26] X. Li, I. Sabir, J. Park, A flow channel design procedure for PEM fuel cells with effective water removal, 163 (2007) 933–942. doi:10.1016/j.jpowsour.2006.10.015.

[27] M. Zhiani, H.A. Gasteiger, M. Piana, S. Catanorchi, Comparative study between platinum supported on carbon and non-noble metal cathode catalyst in alkaline direct ethanol fuel cell (ADEFC), Int. J. Hydrogen Energy. 36 (2011) 5110–5116. doi:10.1016/j.ijhydene.2011.01.079.

[28] V. Bambagioni, C. Bianchini, A. Marchionni, J. Filippi, F. Vizza, J. Teddy, P. Serp, M. Zhiani, Pd and Pt-Ru anode electrocatalysts supported on multi-walled carbon nanotubes and their use in passive and active direct alcohol fuel cells with an anion-exchange membrane (alcohol = methanol, ethanol, glycerol), J. Power Sources. 190 (2009) 241–251. doi:10.1016/j.jpowsour.2009.01.044.

[29] M. Rauf, R. Chen, Q. Wang, Y.C. Wang, Z.Y. Zhou, Nitrogen-doped carbon nanotubes with encapsulated Fe nanoparticles as efficient oxygen reduction catalyst for alkaline membrane direct ethanol fuel cells, Carbon N. Y. 125 (2017) 605–613. doi:10.1016/j.carbon.2017.09.093.

[30] L. Osmieri, R. Escudero-Cid, M. Armandi, A.H.A. Monteverde Videla, G.F. Luís, P. Ocón, S. Specchia, Fe-N/C catalysts for oxygen reduction reaction supported on different carbonaceous materials. Performance in acidic and alkaline direct alcohol fuel cells, Appl. Catal. B Environ. 205 (2017) 637–653. doi:10.1016/j.apcatb.2017.01.003.

[31] L. Osmieri, R. Escudero-Cid, A.H.A. Monteverde Videla, P. Ocón, S. Specchia, Application of a non-noble Fe-N-C catalyst for oxygen reduction reaction in an alkaline direct ethanol fuel cell, Renew. Energy. 115 (2018) 226–237. doi:10.1016/j.renene.2017.08.062.

[32] H. Peng, Z. Mo, S. Liao, H. Liang, L. Yang, F. Luo, H. Song, Y. Zhong, B. Zhang, High performance Fe- and N- Doped carbon catalyst with graphene structure for oxygen reduction, Sci. Rep. 3 (2013) 1–7. doi:10.1038/srep01765.

[33] L. Gu, L. Jiang, X. Li, J. Jin, J. Wang, G. Sun, A Fe-N-C catalyst with highly dispersed iron in carbon for oxygen reduction reaction and its application in direct methanol fuel cells, Cuihua Xuebao/Chinese J. Catal. 37 (2016) 539–548. doi:10.1016/S1872-2067(15)61049-X.

[34] S. Price, A.E. Russell, X. Li, F. Walsh, S. Gorman, R. Wills, D. Pletcher, S. Thompson, The fabrication of a bifunctional oxygen electrode without carbon components for alkaline secondary batteries, J. Power Sources. 259 (2014) 43–49. doi.org/10.1016/j.jpowsour.2014.02.058.

[35] M. Winter, R.J. Brodd, What are batteries, fuel cells, and supercapacitors?, Chem. Rev. 104 (2004) 4245–4269.

doi:10.1021/cr020730k.

[36] Y.J. Wang, B. Fang, D. Zhang, A. Li, D.P. Wilkinson, A. Ignaszak, L. Zhang, A Review of Carbon - Composited Materials as Air - Electrode Bifunctional Electrocatalysts for Metal – Air Batteries, Springer Singapore, 2018. doi:10.1007/s41918-018-0002-3.

[37] A.H. Tullo, Batteries that breathe air, Chem. Eng. News. 95 (2017).

[38] M. Pino, J. Chacón, E. Fatás, P. Ocón, Performance of commercial aluminium alloys as anodes in gelled electrolyte aluminium-air batteries, J. Power Sources. 299 (2015) 195–201. doi:10.1016/j.jpowsour.2015.08.088.

[39] F. Cheng, J. Chen, Metal-air batteries: From oxygen reduction electrochemistry to cathode catalysts, Chem. Soc. Rev. 41 (2012) 2172–2192. doi:10.1039/c1cs15228a.

[40] J. Su, X. Cao, J. Wu, C. Jin, J.H. Tian, R. Yang, One-pot synthesis of boron-doped ordered mesoporous carbons as efficient electrocatalysts for the oxygen reduction reaction, RSC Adv. 6 (2016) 24728–24737. doi:10.1039/c6ra01296e.

[41] A.J. Esswein, M.J. Mcmurdo, P.N. Ross, A.T. Bell, T.D. Tilley, Size-dependent activity of Co3O4 nanoparticle anodes for alkaline water electrolysis, J. Phys. Chem. C. 113 (2009) 15068–15072. doi:10.1021/jp904022e.

[42] Q. Li, R. Cao, J. Cho, G. Wu, Nanostructured carbon-based cathode catalysts for nonaqueous lithium-oxygen batteries, Phys. Chem. Chem. Phys. 16 (2014) 13568–13582. doi:10.1039/c4cp00225c.

[43] S. Gupta, W. Kellogg, H. Xu, X. Liu, J. Cho, G. Wu, Bifunctional Perovskite Oxide Catalysts for Oxygen Reduction and Evolution in Alkaline Media, Chem. - An Asian J. 11 (2016) 10–21. doi:10.1002/asia.201500640.

[44] M.S. Park, J. Kim, K.J. Kim, J.W. Lee, J.H. Kim, Y. Yamauchi, Porous nanoarchitectures of spinel-type transition metal oxides for electrochemical energy storage systems, Phys. Chem. Chem. Phys. 17 (2015) 30963–30977. doi:10.1039/c5cp05936d.

[45] F. Li, R. Ohnishi, Y. Yamada, J. Kubota, K. Domen, A. Yamada,

H. Zhou, Carbon supported TiN nanoparticles: An efficient bifunctional catalyst for non-aqueous Li-O2 batteries, Chem. Commun. 49 (2013) 1175–1177. doi:10.1039/c2cc37042e.

[46] L. Zhang, Z. Su, F. Jiang, L. Yang, J. Qian, Y. Zhou, W. Li, M. Hong, Highly graphitized nitrogen-doped porous carbon nanopolyhedra derived from ZIF-8 nanocrystals as efficient electrocatalysts for oxygen reduction reactions, Nanoscale. 6 (2014) 6590–6602. doi:10.1039/c4nr00348a.

[47] K. Huang, K. Bi, J.C. Xu, C. Liang, S. Lin, W.J. Wang, T.Z. Yang, Y.X. Du, R. Zhang, H.J. Yang, D.Y. Fan, Y.G. Wang, M. Lei, Novel graphite-carbon encased tungsten carbide nanocomposites by solid-state reaction and their ORR electrocatalytic performance in alkaline medium, Electrochim. Acta. 174 (2015) 172–177. doi:10.1016/j.electacta.2015.05.152.

[48] Z. Lyu, J. Zhang, L. Wang, K. Yuan, Y. Luan, P. Xiao, W. Chen, CoS 2 nanoparticles-graphene hybrid as a cathode catalyst for aprotic Li-O 2 batteries, RSC Adv. 6 (2016) 31739–31743. doi:10.1039/c6ra00723f.

[49] J. Wu, S. Dou, A. Shen, X. Wang, Z. Ma, C. Ouyang, S. Wang, One-step hydrothermal synthesis of NiCo2S4i-rGO as an efficient electrocatalyst for the oxygen reduction reaction, J. Mater. Chem. A. 2 (2014) 20990–20995. doi:10.1039/c4ta05159a.

[50] X. Zhai, W. Yang, M. Li, G. Lv, J. Liu, X. Zhang, Noncovalent hybrid of CoMn2O4 spinel nanocrystals and poly (diallyldimethylammonium chloride) functionalized carbon nanotubes as efficient electrocatalysts for oxygen reduction reaction, Carbon N. Y. 65 (2013) 277–286. doi:10.1016/j.carbon.2013.08.026.

[51] Y.C. Lu, Z. Xu, H.A. Gasteiger, S. Chen, K. Hamad-Schifferli, Y. Shao-Horn, Platinum-gold nanoparticles: A highly active bifunctional electrocatalyst for rechargeable lithium-air batteries, J. Am. Chem. Soc. 132 (2010) 12170–12171. doi:10.1021/ja1036572.

[52] D. Su, H.S. Kim, W.S. Kim, G. Wang, A study of PtxCoy alloy nanoparticles as cathode catalysts for lithium-air batteries with improved catalytic activity, J. Power Sources. 244 (2013) 488–493. doi:10.1016/j.jpowsour.2012.11.024.

[53] Y. Zhang, X. Wu, Y. Fu, W. Shen, X. Zeng, W. Ding, Carbon aerogel supported Pt-Zn catalyst and its oxygen reduction catalytic performance in magnesium-air batteries, J. Mater. Res. 29 (2014) 2863–2870. doi:10.1557/jmr.2014.343.

[54] R. Yu, W. Fan, X. Guo, S. Dong, Highly ordered and ultra-long carbon nanotube arrays as air cathodes for high-energy-efficiency Li-oxygen batteries, J. Power Sources. 306 (2016) 402–407. doi:10.1016/j.jpowsour.2015.12.042.

[55] M. Raynal, P. Ballester, A. Vidal-ferran, P.W.N.M. Van Leeuwen, Supramolecular catalysis : a rapidly expanding and fascinating research, (2015) 1–48. doi:10.1039/b000000x.

[56] W.J. Kwak, T.G. Kang, Y.K. Sun, Y.J. Lee, Iron-cobalt bimetal decorated carbon nanotubes as cost-effective cathode catalysts for Li-O2 batteries, J. Mater. Chem. A. 4 (2016) 7020–7026. doi:10.1039/c5ta10550a.

[57] X. Ren, S.S. Zhang, D.T. Tran, J. Read, Oxygen reduction reaction catalyst on lithium/air battery discharge performance, J. Mater. Chem. 21 (2011) 10118–10125. doi:10.1039/c0jm04170j.

[58] J. Huang, B. Zhang, Y.Y. Xie, W.W.K. Lye, Z.L. Xu, S. Abouali, M. Akbari Garakani, J.Q. Huang, T.Y. Zhang, B. Huang, J.K. Kim, Electrospun graphitic carbon nanofibers with in-situ encapsulated Co-Ni nanoparticles as freestanding electrodes for Li-O2 batteries, Carbon N. Y. 100 (2016) 329–336. doi:10.1016/j.carbon.2016.01.012.

[59] H. Cheng, K. Scott, Selection of oxygen reduction catalysts for rechargeable lithium-air batteries-Metal or oxide?, Appl. Catal. B Environ. 108–109 (2011) 140–151. doi:10.1016/j.apcatb.2011.08.021.

[60] L. Wang, M. Ara, K. Wadumesthrige, S. Salley, K.Y.S. Ng, Graphene nanosheet supported bifunctional catalyst for high cycle life Li-air batteries, J. Power Sources. 234 (2013) 8–15. doi:10.1016/j.jpowsour.2013.01.037.

[61] J. Yin, B. Fang, J. Luo, B. Wanjala, D. Mott, R. Loukrakpam, M.S. Ng, Z. Li, J. Hong, M.S. Whittingham, C.J. Zhong, Nanoscale alloying effect of gold-platinum nanoparticles as cathode catalysts on the performance of a rechargeable lithium-oxygen battery, Nanotechnology. 23 (2012). doi:10.1088/0957-4484/23/30/305404.

[62] J. Li, Y. Zhao, M. Zou, C. Wu, Z. Huang, L. Guan, An effective integrated design for enhanced cathodes of Ni foam-supported Pt/carbon nanotubes for Li-O2 batteries, ACS Appl. Mater. Interfaces. 6 (2014) 12479–12485. doi:10.1021/am502411y.

[63] M. Wu, Q. Tang, F. Dong, Y. Wang, D. Li, Q. Guo, Y. Liu, J. Qiao, The design of Fe, N-doped hierarchically porous carbons as highly active and durable electrocatalysts for a Zn-air battery, Phys. Chem. Chem. Phys. 18 (2016) 18665–18669. doi:10.1039/c6cp02785g.

[64] J. Li, M. Zou, L. Chen, Z. Huang, L. Guan, An efficient bifunctional catalyst of Fe/Fe3C carbon nanofibers for rechargeable Li-O2 batteries, J. Mater. Chem. A. 2 (2014) 10634–10638. doi:10.1039/c4ta01831a.

[65] D. Oh, J. Qi, B. Han, G. Zhang, T.J. Carney, J. Ohmura, Y. Zhang, Y. Shao-Horn, A.M. Belcher, M13 virus-directed synthesis of nanostructured metal oxides for lithium-oxygen batteries, Nano Lett. 14 (2014) 4837–4845. doi:10.1021/nl502078m.

[66] H.A.W. Endt, T.H. Darmstadt, H.E. V Ogt, T.F. Berlin, G.E.K. Reysa, F. Main, D.I.M.K. Olb, H.E.S. Chmieder, F. Karlsruhe, Electrochemistry, (2009).

[67] H. Wang, Z. Jusys, R.J. Behm, Ethanol Electrooxidation on a Carbon-Supported Pt Catalyst: Reaction Kinetics and Product Yields, J. Phys. Chem. B. 108 (2004) 19413–19424. doi:10.1021/jp046561k.

[68] T.S. Almeida, L.M. Palma, P.H. Leonello, C. Morais, K.B. Kokoh, A.R. De Andrade, An optimization study of PtSn / C catalysts applied to direct ethanol fuel cell : Effect of the preparation method on the electrocatalytic activity of the catalysts, J. Power Sources. 215 (2012) 53–62. doi:10.1016/j.jpowsour.2012.04.061.

[69] S.Q. Song, W.J. Zhou, Z.H. Zhou, L.H. Jiang, G.Q. Sun, Q. Xin, V. Leontidis, S. Kontou, P. Tsiakaras, Direct ethanol PEM fuel cells : The case of platinum based anodes, 30 (2005) 995–1001. doi:10.1016/j.ijhydene.2004.11.006.

[70] H. Wang, Z. Jusys, R.J. Behm, Ethanol electro-oxidation on carbon-supported Pt , PtRu and Pt 3 Sn catalysts : A quantitative DEMS study, 154 (2006) 351–359.

doi:10.1016/j.jpowsour.2005.10.034.

[71] C. Yougui, Z. Lin, L.U. Juntao, Non-Pt Anode Catalysts for Alkaline Direct Alcohol Fuel Cells, 28 (2007) 8–11.

[72] S. Yang, H. Knickle, Design and analysis of aluminum/air battery system foe electric vehicles, J. Power Sources. 112 (2002) 162–173.

[73] W. Xiong, G.T. Qi, X.P. Guo, Z.L. Lu, Anodic dissolution of Al sacrificial anodes in NaCl solution containing Ce, Corros. Sci. 53 (2011) 1298–1303. doi:10.1016/j.corsci.2011.01.001.

[74] U. Kramm, J. Herranz, N. Larouche, T. Arruda, M. Lefevre, F. Jaouen, P. Bogdanoff, S. Fiechter, I. Wurmbach, S. Mukerjee, J. Dodelet, Structure of the catalytic sites in Fe/N/C-catalysts for O2-reduction in PEM fuel cells, Phys Chem Chem Phys. 14 (2012) 11673–11688.

[75] S.T. Thompson, A.R. Wilson, P. Zelenay, D.J. Myers, K.L. More, K.C. Neyerlin, D. Papageorgopoulos, ElectroCat: DOE's approach to PGM-free catalyst and electrode R&D, Solid State Ionics. 319 (2018) 68–76. doi:10.1016/j.ssi.2018.01.030.

[76] P. Zelenay, State of the Art of PGM-free Catalyst Activity and Durability, 1808 (2011) 424–432. doi:10.1016/j.bbamem.2010.09.013.

[77] M. Lefèvre, E. Proietti, F. Jaouen, J.P. Dodelet, Iron-Based catalysts with improved oxygen reduction activity in polymer electrolyte fuel cells, Science (80-.). 324 (2009) 71–74. doi:10.1126/science.1170051.

[78] G. Wu, K.L. More, C.M. Johnston, P. Zelenay, High-performance electrocatalysts for oxygen reduction derived from polyaniline, iron, and cobalt, Science (80-.). 332 (2011) 443–447. doi:10.1126/science.1200832.

[79] G. Wu, K. More, C. Johnston, P. Zelenay, High-performance electrocatalysts for oxygen reduction derived from polyaniline, iron, and cobalt, Science (80-.). 332 (2011) 443–447.

[80] O.A. Baturina, A.E. Smirnova, Chapter 4 - Catalytic Processes Using Fuel Cells, Catalytic Batteries, and Hydrogen Storage Materials, in: S.L.B.T.-N. and F.D. in C. Suib (Ed.), Elsevier, Amsterdam, 2013: pp. 69–97. doi:https://doi.org/10.1016/B978-

0-444-53880-2.00005-3.

[81] S. Sui, X. Wang, X. Zhou, Y. Su, C. Liu, Journal of Materials Chemistry A, (n.d.). doi:10.1039/c6ta08580f.Biography.

[82] J.F. Lin, V. Kamavaram, A.M. Kannan, Synthesis and characterization of carbon nanotubes supported platinum nanocatalyst for proton exchange membrane fuel cells, 195 (2010) 466–470. doi:10.1016/j.jpowsour.2009.07.055.

[83] K. Liu, J. Masa, Electrochemistry of N4 Macrocyclic Metal Complexes, 2016. doi:10.1007/978-3-319-31172-2.

[84] E. Environ, A. Morozan, B. Jousselme, S. Palacin, Energy & Environmental Science Low-platinum and platinum-free catalysts for the oxygen reduction reaction at fuel cell cathodes, (2011) 1238–1254. doi:10.1039/c0ee00601g.

[85] R. Alipour Moghadam Esfahani, L.M. Rivera Gavidia, G. García, E. Pastor, S. Specchia, Highly active platinum supported on Mo-doped titanium nanotubes suboxide (Pt/TNTS-Mo) electrocatalyst for oxygen reduction reaction in PEMFC, Renew. Energy. 120 (2018) 209–219. doi:10.1016/j.renene.2017.12.077.

[86] H. Zhang, H. Osgood, X. Xie, Y. Shao, G. Wu, Engineering nanostructures of PGM-free oxygen-reduction catalysts using metal-organic frameworks, Nano Energy. 31 (2017) 331–350. doi:10.1016/j.nanoen.2016.11.033.

[87] G. Chen, J. Sunarso, Y. Zhu, J. Yu, Y. Zhong, W. Zhou, Z. Shao, Highly Active Carbon/α-MnO 2 Hybrid Oxygen Reduction Reaction Electrocatalysts, ChemElectroChem. 3 (2016) 1760–1767. doi:10.1002/celc.201600433.

[88] F. Jaouen, J. Herranz, M. Lefévre, J.P. Dodelet, U.I. Kramm, I. Herrmann, P. Bogdanoff, J. Maruyama, T. Nagaoka, A. Garsuch, J.R. Dahn, T. Olson, S. Pylypenko, P. Atanassov, E.A. Ustinov, Cross-laboratory experimental study of non-noble-metal electrocatalysts for the oxygen reduction reaction, ACS Appl. Mater. Interfaces. 1 (2009) 1623–1639. doi:10.1021/am900219g.

[89] P. Trogadas, T.F. Fuller, P. Strasser, Carbon as Catalyst and Support for Electrochemical Energy, Carbon N. Y. (2014). doi:10.1016/j.carbon.2014.04.005.

[90] G. Wu, Z. Chen, K. Artyushkova, F.H. Garzon, P. Zelenay,

Polyaniline-derived non-precious catalyst for the polymer electrolyte fuel cell cathode, ECS Trans. 16 (2008) 159–170. doi:10.1149/1.2981852.

[91] L. Osmieri, A.H.A. Monteverde Videla, S. Specchia, Optimization of a Fe–N–C electrocatalyst supported on mesoporous carbon functionalized with polypyrrole for oxygen reduction reaction under both alkaline and acidic conditions, Int. J. Hydrogen Energy. 41 (2016) 19610–19628. doi:10.1016/j.ijhydene.2016.05.270.

[92] C.W.B. Bezerra, L. Zhang, K. Lee, H. Liu, A.L.B. Marques, E.P. Marques, H. Wang, J. Zhang, A review of Fe-N/C and Co-N/C catalysts for the oxygen reduction reaction, Electrochim. Acta. 53 (2008) 4937–4951. doi:10.1016/j.electacta.2008.02.012.

[93] P. Matter, E. Wang, M. Arias, E. Biddinger, U. Ozkan, Oxygen reduction reaction activity and surface properties of nanostructured nitrogen-containing carbon, J Mol Catal A Chem. 264 (2007) 73–81.

[94] J. Dodelet, The controversial role of the metal in Fe- or Co-based electrocatalysts for the oxygen reduction reaction in acid medium, in: Springer (Ed.), Electrocatal. Fuel Cells a Non-Low-Platinum Approach, London, United Kingdom, 2013: pp. 271–338.

[95] L. Osmieri, Transition Metal – Nitrogen – Carbon (M – N – C) Catalysts for Oxygen Reduction Reaction . Insights on Synthesis and Performance in Polymer Electrolyte Fuel Cells, (2019) 1–32. doi:10.3390/chemengineering3010016.

[96] G. Liu, X. Li, P. Ganesan, B.N. Popov, Development of non-precious metal oxygen-reduction catalysts for PEM fuel cells based on N-doped ordered porous carbon, Appl. Catal. B Environ. 93 (2009) 156–165. doi:10.1016/j.apcatb.2009.09.025.

[97] G. Wu, B.Q. Xu, Carbon nanotube supported Pt electrodes for methanol oxidation: A comparison between multi- and single-walled carbon nanotubes, J. Power Sources. 174 (2007) 148–158. doi:10.1016/j.jpowsour.2007.08.024.

[98] F. Jaouen, F. Charreteur, J.P. Dodelet, Fe-based catalysts for oxygen reduction in PEMFCs, J. Electrochem. Soc. 153 (2006). doi:10.1149/1.2168418.

[99] E. Bayram, G. Yilmaz, S. Mukerjee, A solution-based procedure for synthesis of nitrogen doped graphene as an efficient electrocatalyst for oxygen reduction reactions in acidic and alkaline electrolytes, Appl. Catal. B Environ. 192 (2016) 26–34. doi:10.1016/j.apcatb.2016.03.043.

[100] F. Jaouen, E. Proietti, M. Lefèvre, R. Chenitz, J.-P. Dodelet, G. Wu, H.T. Chung, C.M. Johnston, P. Zelenay, Recent advances in non-precious metal catalysis for oxygen-reduction reaction in polymer electrolyte fuelcells, Energy Environ. Sci. 4 (2011) 114–130. doi:10.1039/C0EE00011F.

[101] L. Osmieri, A.H.A. Monteverde Videla, S. Specchia, Activity of Co-N multi walled carbon nanotubes electrocatalysts for oxygen reduction reaction in acid conditions, J. Power Sources. 278 (2015) 296–307. doi:10.1016/j.jpowsour.2014.12.080.

[102] M. Ferrandon, A.J. Kropf, D.J. Myers, K. Artyushkova, U. Kramm, P. Bogdanoff, G. Wu, C.M. Johnston, P. Zelenay, Multitechnique characterization of a polyaniline-iron-carbon oxygen reduction catalyst, J. Phys. Chem. C. 116 (2012) 16001–16013. doi:10.1021/jp302396g.

[103] S.R. Sulub, W. Martínez-Millán, M.A. Smit, Study of the catalytic activity for oxygen reduction of polythiophene modified with cobalt or nickel, Int. J. Electrochem. Sci. 4 (2009) 1015–1027.

[104] Q. Wang, Z.Y. Zhou, Y.J. Lai, Y. You, J.G. Liu, X.L. Wu, E. Terefe, C. Chen, L. Song, M. Rauf, N. Tian, S.G. Sun, Phenylenediamine-based FeNx/C catalyst with high activity for oxygen reduction in acid medium and its active-site probing, J. Am. Chem. Soc. 136 (2014) 10882–10885. doi:10.1021/ja505777v.

[105] Z. Chen, D. Higgins, A. Yu, L. Zhang, J. Zhang, A review on non-precious metal electrocatalysts for PEM fuel cells, Energy Environ. Sci. 4 (2011) 3167–3192. doi:10.1039/c0ee00558d.

[106] Q. Liu, S. Cao, Y. Qiu, L. Zhao, Bimetallic Fe-Co promoting one-step growth of hierarchical nitrogen-doped carbon nanotubes/nanofibers for highly efficient oxygen reduction reaction, Mater. Sci. Eng. B Solid-State Mater. Adv. Technol. 223 (2017) 159–166. doi:10.1016/j.mseb.2017.06.012.

[107] H.S. Oh, H. Kim, The role of transition metals in non-precious

nitrogen-modified carbon-based electrocatalysts for oxygen reduction reaction, J. Power Sources. 212 (2012) 220–225. doi:10.1016/j.jpowsour.2012.03.098.

[108] Performance Durability of Polyaniline-derived Non-precious Cathode Catalysts Gang Wu and Piotr Zelenay, Time. (2009) 87545–87545.

[109] J.M. Ziegelbauer, T.S. Olson, S. Pylypenko, F. Alamgir, C. Jaye, P. Atanassov, S. Mukerjee, Direct spectroscopic observation of the structural origin of peroxide generation from Co-based pyrolyzed porphyrins for ORR applications, J. Phys. Chem. C. 112 (2008) 8839–8849. doi:10.1021/jp8001564.

[110] A. Serov, K. Artyushkova, N.I. Andersen, S. Stariha, P. Atanassov, Original Mechanochemical Synthesis of Non-Platinum Group Metals Oxygen Reduction Reaction Catalysts Assisted by Sacrificial Support Method, Electrochim. Acta. 179 (2015) 154–160. doi:10.1016/j.electacta.2015.02.108.

[111] S. Shrestha, W.E. Mustain, Properties of nitrogen-functionalized ordered mesoporous carbon prepared using polypyrrole precursor, J. Electrochem. Soc. 157 (2010). doi:10.1149/1.3489412.

[112] H. Furukawa, K.E. Cordova, M. O'Keeffe, O.M. Yaghi, The chemistry and applications of metal-organic frameworks, Science (80-.). 341 (2013). doi:10.1126/science.1230444.

[113] G. Goenaga, S. Ma, S. Yuan, D.J. Liu, New approaches to non-PGM electrocatalysts using porous framework materials, ECS Trans. 33 (2010) 579–586. doi:10.1149/1.3484554.

[114] L. Grabstanowicz, D. Liu, D. Zhao, J. Shui, C. Chen, L. Grabstanowicz, D. Zhao, D. Liu, Highly efficient nonprecious metal catalyst prepared with metal – organic framework in a continuous carbon nanofibrous network, (2015). doi:10.1073/pnas.1507159112.

[115] Q. Jia, N. Ramaswamy, H. Hafiz, U. Tylus, K. Strickland, G. Wu, B. Barbiellini, A. Bansil, E.F. Holby, P. Zelenay, S. Mukerjee, Experimental Observation of Redox-Induced Fe-N Switching Behavior as a Determinant Role for Oxygen Reduction Activity, ACS Nano. 9 (2015) 12496–12505. doi:10.1021/acsnano.5b05984.

[116] S.J. Yang, T. Kim, J.H. Im, Y.S. Kim, K. Lee, H. Jung, C.R. Park, MOF-derived hierarchically porous carbon with exceptional porosity and hydrogen storage capacity, Chem. Mater. 24 (2012) 464–470. doi:10.1021/cm202554j.

[117] I. Martinaiou, A. Shahraei, F. Grimm, H. Zhang, C. Wittich, S. Klemenz, S.J. Dolique, H.J. Kleebe, R.W. Stark, U.I. Kramm, Effect of metal species on the stability of Me-N-C catalysts during accelerated stress tests mimicking the start-up and shut-down conditions, Electrochim. Acta. 243 (2017) 183–196. doi:10.1016/j.electacta.2017.04.134.

[118] P.R. Ortiz de Montellano, Cytochrome P450 Structure, Mechanism, and Biochemistry, Springer US, 2005. doi:10.1007/b139087.

[119] G. Bottari, G. De La Torre, D.M. Guldi, T. Torres, Covalent and noncovalent phthalocyanine - Carbon nanostructure systems: Synthesis, photoinduced electron transfer, and application to molecular photovoltaics, Chem. Rev. 110 (2010) 6768–6816. doi:10.1021/cr900254z.

[120] F. D'Souza, O. Ito, Supramolecular donor–acceptor hybrids of porphyrins/phthalocyanines with fullerenes/carbon nanotubes: electron transfer, sensing, switching, and catalytic applications, Chem. Commun. (2009) 4913–4928.

[121] G. De La Torre, T. Torres, M.V. Martínez-Díaz, Lighting porphyrins and phthalocyanines for molecular photovoltaics, Chem. Commun. 46 (2010) 7090–7108. doi:10.1039/C0CC02213F.

[122] G. De la Torre, T. Claessensa, Christian G. Torres, Phthalocyanines: old dyes, new materials. Putting color in nanotechnology, Chem. Commun. (2007) 2000–2015. doi:10.1039/B614234F.

[123] L. Li, X. Yuan, Z. Ma, Z.F. Ma, Properties of pyrolyzed carbon-supported cobalt-polypyrrole as electrocatalyst toward oxygen reduction reaction in alkaline media, J. Electrochem. Soc. 162 (2015) F359–F365. doi:10.1149/2.0081504jes.

[124] Y. V. Tolmachev, M.A. Vorotyntsev, Fuel cells with chemically regenerative redox cathodes (review), Russ. J. Electrochem. 50 (2014) 403–411. doi:10.1134/S1023193514020050.

[125] I. Gunasekara, M.N. Ates, S. Mukerjee, E.J. Plichta, M.A. Hendrickson, K.M. Abraham, Solid phase FePC catalysts for increased stability of oxygen reduction reaction intermediates at the cathode/electrolyte interface in lithium air batteries, J. Electrochem. Soc. 164 (2017) A760–A769. doi:10.1149/2.1221704jes.

[126] K. Strickland, E. Miner, Q. Jia, U. Tylus, N. Ramaswamy, W. Liang, M.T. Sougrati, F. Jaouen, S. Mukerjee, Highly active oxygen reduction non-platinum group metal electrocatalyst without direct metal-nitrogen coordination, Nat. Commun. 6 (2015) 1–8. doi:10.1038/ncomms8343.

[127] T. Liu, P. Zhao, X. Hua, W. Luo, S. Chen, G. Cheng, An Fe-N-C hybrid electrocatalyst derived from a bimetal-organic framework for efficient oxygen reduction, J. Mater. Chem. A. 4 (2016) 11357–11364. doi:10.1039/c6ta03265f.

[128] Y. Wu, S. Zhao, K. Zhao, T. Tu, J. Zheng, J. Chen, H. Zhou, D. Chen, S. Li, Porous Fe-Nx/C hybrid derived from bi-metal organic frameworks as high efficient electrocatalyst for oxygen reduction reaction, J. Power Sources. 311 (2016) 137–143. doi:10.1016/j.jpowsour.2016.02.020.

[129] C. Mao, A. Kong, Y. Wang, X. Bu, P. Feng, MIL-100 derived nitrogen-embodied carbon shells embedded with iron nanoparticles, Nanoscale. 7 (2015) 10817–10822. doi:10.1039/c5nr02346g.

[130] S. Zhao, H. Yin, L. Du, L. He, K. Zhao, L. Chang, G. Yin, H. Zhao, S. Liu, Z. Tang, Carbonized nanoscale metal-organic frameworks as high performance electrocatalyst for oxygen reduction reaction, ACS Nano. 8 (2014) 12660–12668. doi:10.1021/nn505582e.

[131] P. Su, H. Xiao, J. Zhao, Y. Yao, Z. Shao, C. Li, Q. Yang, Nitrogen-doped carbon nanotubes derived from Zn-Fe-ZIF nanospheres and their application as efficient oxygen reduction electrocatalysts with in situ generated iron species, Chem. Sci. 4 (2013) 2941–2946. doi:10.1039/c3sc51052b.

[132] Q. Li, P. Xu, W. Gao, S. Ma, G. Zhang, R. Cao, J. Cho, H.L. Wang, G. Wu, Graphene/graphene-tube nanocomposites templated from cage-containing metal-organic frameworks for oxygen reduction in Li-O2 batteries, Adv. Mater. 26 (2014) 1378–1386. doi:10.1002/adma.201304218.

[133] S. Zhang, H. Zhang, X. Hua, S. Chen, Tailoring molecular architectures of Fe phthalocyanine on nanocarbon supports for high oxygen reduction performance, J. Mater. Chem. A. 3 (2015) 10013–10019. doi:10.1039/c5ta01400j.

[134] H. Zhang, S. Zhang, Y. Wang, J. Si, Y. Chen, L. Zhuang, S. Chen, Boosting the Performance of Iron-Phthalocyanine as Cathode Electrocatalyst for Alkaline Polymer Fuel Cells Through Edge-Closed Conjugation, ACS Appl. Mater. Interfaces. 10 (2018) 28664–28671. doi:10.1021/acsami.8b09074.

[135] X. Ge, A. Sumboja, D. Wuu, T. An, B. Li, F.W.T. Goh, T.S.A. Hor, Y. Zong, Z. Liu, Oxygen Reduction in Alkaline Media : From Mechanisms to Recent Advances of Catalysts, (2015). doi:10.1021/acscatal.5b00524.

[136] T. Shinagawa, A.T. Garcia-Esparza, K. Takanabe, Insight on Tafel slopes from a microkinetic analysis of aqueous electrocatalysis for energy conversion, Sci. Rep. 5 (2015) 1–21. doi:10.1038/srep13801.

[137] N. Ramaswamy, S. Mukerjee, Fundamental mechanistic understanding of electrocatalysis of oxygen reduction on Pt and non-Pt surfaces: Acid versus alkaline media, Adv. Phys. Chem. 2012 (2012). doi:10.1155/2012/491604.

[138] U.I. Kramm, I. Herrmann-Geppert, S. Fiechter, G. Zehl, I. Zizak, I. Dorbandt, D. Schmeißer, P. Bogdanoff, Effect of iron-carbide formation on the number of active sites in Fe–N–C catalysts for the oxygen reduction reaction in acidic media, J. Mater. Chem. A. 2 (2014) 2663–2670. doi:10.1039/C3TA13821F.

[139] Y. Qian, P. Du, P. Wu, C. Cai, D.F. Gervasio, Chemical Nature of Catalytic Active Sites for the Oxygen Reduction Reaction on Nitrogen-Doped Carbon-Supported Non-Noble Metal Catalysts, J. Phys. Chem. C. 120 (2016) 9884–9896. doi:10.1021/acs.jpcc.6b02670.

[140] J. Herranz, F. Jaouen, M. Lefevre, K. UI, E. Proietti, J. Dodelet, P. Bogdanoff, S. Fiechter, I. Wurmbach, P. Bertrand, T. Arruda, S. Mukerjee, Unveiling N-protonation and anion-binding effects on Fe/N/C catalysts for O2 reduction in proton-exchange-membrane fuel cells, J Phys Chem C. 115 (2011) 16087–16097.

[141] U. Kramm, I. Wurmbach, H. Geppert, J. Radnik, S. Fiechter, P. Bogdanoff, Influence of the electron-density of FeN-centers

towards the catalytic activity of pyrolyzed FeTMPPCl-based ORR-electrocatalysts, J Electrochem Soc. 158 (2011) B69–B78.

[142] P. Matter, E. Wang, J. Millet, U. Ozkan, Characterization of the iron phase in CNxbased oxygen reduction reaction catalysts, J Phys Chem C. 111 (2007) 1444–1450.

[143] F. Jaouen, M. Lefevre, J. Dodelet, M. Cai, Heat-treated Fe/N/C catalysts for O2 electroreduction: Are active sites hosted in micropores?, J Phys Chem B. 110 (2006) 5553–5558.

[144] F. Jaouen, S. Marcotte, J. Dodelet, G. Lindbergh, Oxygen reduction catalysts for polymer electrolyte fuel cells from the pyrolysis of iron acetate adsorbed on various carbon supports, J Phys Chem B. 107 (2003) 1376–1386.

[145] S. Kattel, G. Wang, A density functional theory study of oxygen reduction reaction on Me-N 4 (Me = Fe, Co, or Ni) clusters between graphitic pores, J. Mater. Chem. A. 1 (2013) 10790–10797. doi:10.1039/c3ta12142a.

[146] Z. Duan, G. Wang, A first principles study of oxygen reduction reaction on a Pt(111) surface modified by a subsurface transition metal M (M = Ni, Co, or Fe), Phys. Chem. Chem. Phys. 13 (2011) 20178–20187. doi:10.1039/c1cp21687b.

[147] J. Nikolic, E. Expósito, J. Iniesta, J. González-García, V. Montiel, Theoretical Concepts and Applications of a Rotating Disk Electrode, J. Chem. Educ. 77 (2000) 1191–1194.

[148] D. Pletcher, A First Course in Electrode Processes, Hants, England, 1991.

[149] R.N. Adams, Electrochemistry at Solid Electrodes, New York, 1962. doi:doi.org/10.1002/bbpc.19690731029.

[150] A.J. Bard, L.R. Faulkner, Fundamentals and Fundamentals and Applications, 2015. doi:10.1016/B978-0-08-098353-0.00003-8.

[151] J. Masa, C. Batchelor-McAuley, W. Schuhmann, R.G. Compton, Koutecky-Levich analysis applied to nanoparticle modified rotating disk electrodes: Electrocatalysis or misinterpretation, Nano Res. 7 (2014) 71–78. doi:10.1007/s12274-013-0372-0.

[152] C.G. Zoski, Handbook of electrochemistry, 2007. doi:10.1016/B978-0-444-51958-0.X5000-9.

[153] Determination of diffusion coefficient using a rotating disc electrode, Department of Inorganic Technology, ICT Prague, n.d.

[154] A. Serov, U. Tylus, K. Artyushkova, S. Mukerjee, P. Atanassov, Mechanistic studies of oxygen reduction on Fe-PEI derived non-PGM electrocatalysts, Appl. Catal. B Environ. 150–151 (2014) 179–186. doi:10.1016/j.apcatb.2013.12.009.

[155] N. Elgrishi, K.J. Rountree, B.D. McCarthy, E.S. Rountree, T.T. Eisenhart, J.L. Dempsey, A Practical Beginner's Guide to Cyclic Voltammetry, J. Chem. Educ. 95 (2018) 197–206. doi:10.1021/acs.jchemed.7b00361.

[156] E. Frackowiak, F. Béguin, Carbon materials for the electrochemical storage of energy in capacitors, Carbon N. Y. 39 (2001) 937–950. doi:10.1016/S0008-6223(00)00183-4.

[157] G. KRISHNAN, Cyclic voltammetry slides geetha, Ceer. (2011) 1–35. doi:10.1021/ed060p702.

[158] V. Climent, J.M. Feliu, Cyclic Voltammetry, Encycl. Interfacial Chem. 2 (2018) 48–74. doi:10.1016/B978-0-12-409547-2.10764-4.

[159] C. Song, J. Zhang, Electrocatalytic Oxygen Reduction Reaction, PEM Fuel Cell Electrocatal. Catal. Layers. Fundam. Appl. (2008) 89–134. doi:10.1007/978-1-84800-936-3_2.

[160] W. Xia, A. Mahmood, Z. Liang, R. Zou, S. Guo, Earth-Abundant Nanomaterials for Oxygen Reduction Angewandte, (2016) 2650–2676. doi:10.1002/anie.201504830.

[161] A. Maljusch, E. Ventosa, R.A. Rincón, A.S. Bandarenka, W. Schuhmann, Revealing onset potentials using electrochemical microscopy to assess the catalytic activity of gas-evolving electrodes, Electrochem. Commun. 38 (2014) 142–145. doi:10.1016/j.elecom.2013.11.024.

[162] I. Roche, E. Chaînet, M. Chatenet, J. Vondrák, Carbon-supported manganese oxide nanoparticles as electrocatalysts for the Oxygen Reduction Reaction (ORR) in alkaline medium: Physical characterizations and ORR mechanism, J. Phys. Chem. C. 111 (2007) 1434–1443. doi:10.1021/jp0647986.

[163] S. Mukerjee, S. Srinivasan, A.J. Appleby, Effect of sputtered film of platinum on low platinum loading electrodes on

electrode kinetics of oxygen reduction in proton exchange membrane fuel cells, Electrochim. Acta. 38 (1993) 1661–1669. doi:10.1016/0013-4686(93)85056-5.

[164] D. Sepa, M. Vojnovic, A. Damjanovic, KINETICS AND MECHANISM OF 02 REDUCTION AT Pt IN ALKALINE SOLUTIONS, Electrochim. Acta. 25 (1980) 1491–1496.

[165] M. Shao, P. Liu, R.R. Adzic, Superoxide Anion is the Intermediate in the Oxygen Reduction Reaction on Platinum Electrodes, J. Am. Chem. Soc. 128 (2006) 7408–7409. doi:10.1021/ja061246s.

[166] A. Holewinski, S. Linic, Elementary Mechanisms in Electrocatalysis: Revisiting the ORR Tafel Slope, J. Electrochem. Soc. 159 (2012) H864–H870. doi:10.1149/2.022211jes.

[167] Y. Wang, P.B. Balbuena, Design of oxygen reduction bimetallic catalysts: Ab-initio-derived thermodynamic guidelines, J. Phys. Chem. B. 109 (2005) 18902–18906. doi:10.1021/jp0543779.

[168] N.M. Marković, T.J. Schmidt, V. Stamenković, P.N. Ross, Oxygen Reduction Reaction on Pt and Pt Bimetallic Surfaces: A Selective Review, Fuel Cells. 1 (2001) 105–116. doi:10.1002/1615-6854(200107)1:2<105::AID-FUCE105>3.3.CO;2-0.

[169] A. Parthasarathy, S. Srinivasan, A.J. Appleby, C.R. Martin, Temperature dependence of the electrode kinetics of oxygen reduction at the platinum/nafion(R)interface - a microelectrode investigation, J. Electrochem. Soc. 139 (1992) 2530–2537. doi:10.1149/1.2221258.

[170] A. Stassi, C. D'Urso, V. Baglio, A. Di Blasi, V. Antonucci, A.S. Arico, A.M. Castro Luna, A. Bonesi, W.E. Triaca, Electrocatalytic behaviour for oxygen reduction reaction of small nanostructured crystalline bimetallic Pt-M supported catalysts, J. Appl. Electrochem. 36 (2006) 1143–1149. doi:10.1007/s10800-006-9197-9.

[171] F. Barbir, PEM Fuel Cells: Theory and Practice, 2013. doi:10.1016/B978-0-12-387710-9.00003-5.

[172] College of the Desert, SunLine Transit Agency, Hydrogen Fuel Cell Engines and Related Technologies Course Manual - Module 4: Fuel Cell Technology, (2001) 1–62.

https://www1.eere.energy.gov/hydrogenandfuelcells/tech_validation/h2_manual.html.

[173] M. Peralta, Fundamental of statistics and design of experimets, Amazon Distribution, Germany, n.d.

[174] B.L. Barrentine, An introduction to Design of Experiment, ASQ Quality Press, Milwaukee, Wisconsin, 1999.

[175] C.D. Montgomery, Progettazione e analisi degli esperimenti, McGraw-Hill, Milano, 2005.

[176] S. Varetti, Design and characterization of trabecular structures of aluminium alloy produced by DMLM (Direct Metal Laser Melting) for aeronautical sandwich panels, Politecnico di Torino, 2016.

[177] Comparison of data means and fitted means, (n.d.). https://support.minitab.com/en-us/minitab/19/help-and-how-to/modeling-statistics/anova/supporting-topics/anova-statistics/data-means-vs-fitted-means/.

[178] A. V. Neimark, Y. Lin, P.I. Ravikovitch, M. Thommes, Quenched solid density functional theory and pore size analysis of micro-mesoporous carbons, Carbon N. Y. 47 (2009) 1617–1628. doi:10.1016/j.carbon.2009.01.050.

[179] G.Y. Gor, M. Thommes, K.A. Cychosz, A. V. Neimark, Quenched solid density functional theory method for characterization of mesoporous carbons by nitrogen adsorption, Carbon N. Y. 50 (2012) 1583–1590. doi:10.1016/j.carbon.2011.11.037.

[180] J. Silvestre-Albero, A. Silvestre-Albero, F. Rodríguez-Reinoso, M. Thommes, Physical characterization of activated carbons with narrow microporosity by nitrogen (77.4 K), carbon dioxide (273 K) and argon (87.3 K) adsorption in combination with immersion calorimetry, Carbon N. Y. 50 (2012) 3128–3133. doi:10.1016/j.carbon.2011.09.005.

[181] A.H.A. Monteverde Videla, S. Ban, S. Specchia, L. Zhang, J. Zhang, Non-noble Fe-NXelectrocatalysts supported on the reduced graphene oxide for oxygen reduction reaction, Carbon N. Y. 76 (2014) 386–400. doi:10.1016/j.carbon.2014.04.092.

[182] A. Muthukrishnan, Y. Nabae, T. Hayakawa, T. Okajima, T.

Ohsaka, Fe-containing polyimide-based high-performance ORR catalysts in acidic medium: A kinetic approach to study the durability of catalysts, Catal. Sci. Technol. 5 (2015) 475–483. doi:10.1039/c4cy01001a.

[183] J. Zeng, C. Francia, M.A. Dumitrescu, A.H.A. Monteverde Videla, V.S. Ijeri, S. Specchia, P. Spinelli, Electrochemical performance of Pt-based catalysts supported on different ordered mesoporous carbons (Pt/OMCs) for oxygen reduction reaction, Ind. Eng. Chem. Res. 51 (2012) 7500–7509. doi:10.1021/ie2016619.

[184] A. Ohma, K. Shinohara, A. Iiyama, T. Yoshida, A. Daimaru, Membrane and Catalyst Performance Targets for Automotive Fuel Cells by FCCJ Membrane, Catalyst, MEA WG, 41 (2011) 775–784. doi:10.1149/1.3635611.

[185] L. Osmieri, R. Escudero-Cid, M. Armandi, A.H.A. Monteverde Videla, G.F. Luís, P. Ocón, S. Specchia, Fe-N/C catalysts for oxygen reduction reaction supported on different carbonaceous materials. Performance in acidic and alkaline direct alcohol fuel cells, Appl. Catal. B Environ. 205 (2017) 637–653. doi:10.1016/j.apcatb.2017.01.003.

[186] L. Osmieri, R. Escudero-cid, A. Monteverde, P. Ocón, S. Specchia, Environmental Performance of a Fe-N-C catalyst for the oxygen reduction reaction in direct methanol fuel cell : Cathode formulation optimization and short-term durability, Appl. Catal. B, Environ. 201 (2017) 253–265.

[187] L. Osmieri, A.H.A. Monteverde Videla, S. Specchia, Activity of Co-N multi walled carbon nanotubes electrocatalysts for oxygen reduction reaction in acid conditions, J. Power Sources. 278 (2015) 296–307. doi:10.1016/j.jpowsour.2014.12.080.

[188] R. Salmimies, P. Vehmaanperä, A. Häkkinen, Acidic dissolution of magnetite in mixtures of oxalic and sulfuric acid, Hydrometallurgy. 163 (2016) 91–98. doi:10.1016/j.hydromet.2016.03.011.

[189] U.I. Kramm, I. Herrmann-Geppert, J. Behrends, K. Lips, S. Fiechter, P. Bogdanoff, On an Easy Way to Prepare Metal-Nitrogen Doped Carbon with Exclusive Presence of MeN4-type Sites Active for the ORR, J. Am. Chem. Soc. 138 (2016) 635–640. doi:10.1021/jacs.5b11015.

[190] U.I. Kramm, I. Herrmann, S. Fiechter, G. Zehl, I. Zizak, I. Abs-Wurmbach, J. Radnik, I. Dorbandt, P. Bogdanoff, On the Influence of Sulphur on the Pyrolysis Process of FeTMPP-Cl-based Electro-Catalysts with Respect to Oxygen Reduction Reaction (ORR) in Acidic Media, ECS Trans. . 25 (2009) 659–670. doi:10.1149/1.3210617.

[191] Antoine Louis Charles, Tensions des vapeurs; nouvelle relation entre les tensions et les températures [Vapor Pressure: a new relationship between pressure and temperature], Comptes Rendus Des Séances l'Académie Des Sci. 107 (1888) 681–684, 778–780, 836–837.

[192] U.I. Kramm, A. Zana, T. Vosch, S. Fiechter, M. Arenz, D. Schmeißer, On the structural composition and stability of Fe–N–C catalysts prepared by an intermediate acid leaching, J. Solid State Electrochem. 20 (2016) 969–981. doi:10.1007/s10008-015-3060-z.

[193] O.A. Baturina, K.E. Swider-lyons, Y. Garsany, S.S. Kocha, Experimental Methods for Quantifying the Activity of Platinum Electrocatalysts for the Oxygen, Anal. Chem. 82 (2010) 6321–6328.

[194] M. Thommes, K.A. Cychosz, Physical adsorption characterization of nanoporous materials: Progress and challenges, Adsorption. 20 (2014) 233–250. doi:10.1007/s10450-014-9606-z.

[195] P.A. Monson, Understanding adsorption/desorption hysteresis for fluids in mesoporous materials using simple molecular models and classical density functional theory, Microporous Mesoporous Mater. 160 (2012) 47–66. doi:10.1016/j.micromeso.2012.04.043.

[196] T. Sato, Y. Hamada, M. Sumikawa, S. Araki, H. Yamamoto, Solubility of oxygen in organic solvents and calculation of the Hansen solubility parameters of oxygen, Ind. Eng. Chem. Res. 53 (2014) 19331–19337. doi:10.1021/ie502386t.

[197] T. Schnabel, J. Vrabec, H. Hasse, Henry's law constants of methane, nitrogen, oxygen and carbon dioxide in ethanol from 273 to 498 K: Prediction from molecular simulation, Fluid Phase Equilib. 233 (2005) 134–143. doi:10.1016/j.fluid.2005.04.016.

[198] A.M.A. Dias, R.P. Bonifácio, I.M. Marrucho, A.A.H. Pádua,

M.F. Costa Gomes, Solubility of oxygen in n-hexane and in n-perfluorohexane. Experimental determination and prediction by molecular simulation, Phys. Chem. Chem. Phys. 5 (2003) 543–549. doi:10.1039/b207512c.

[199] G. Wu, C.M. Johnston, N.H. Mack, K. Artyushkova, M. Ferrandon, M. Nelson, J.S. Lezama-Pacheco, S.D. Conradson, K.L. More, D.J. Myers, P. Zelenay, Synthesis–structure–performance correlation for polyaniline–Me–C non-precious metal cathode catalysts for oxygen reduction in fuel cells, J. Mater. Chem. 21 (2011) 11392. doi:10.1039/c0jm03613g.

[200] R. Gokhale, Y. Chen, A. Serov, K. Artyushkova, P. Atanassov, Direct synthesis of platinum group metal-free Fe-N-C catalyst for oxygen reduction reaction in alkaline media, Electrochem. Commun. 72 (2016) 140–143. doi:10.1016/j.elecom.2016.09.013.

[201] Wijnoltz, A. L., Oxygen reduction catalysed by carbon supported metal chelates, Eindhoven: Technische Universiteit Eindhoven, 1995. doi:10.6100/IR430240.

[202] Q. Li, G. Wu, D.A. Cullen, K.L. More, N.H. Mack, H.T. Chung, P. Zelenay, Phosphate-tolerant oxygen reduction catalysts, ACS Catal. 4 (2014) 3193–3200.

[203] L. Osmieri, A.H.A. Monteverde Videla, M. Armandi, S. Specchia, Influence of different transition metals on the properties of Me–N–C (Me = Fe, Co, Cu, Zn) catalysts synthesized using SBA-15 as tubular nano-silica reactor for oxygen reduction reaction, Int. J. Hydrogen Energy. 41 (2016) 22570–22588. doi:10.1016/j.ijhydene.2016.05.223.

[204] P. Examiner, V. Afremova, (12) United States Patent, 2 (1995).

[205] M. Sevilla, A.B. Fuertes, Catalytic graphitization of templated mesoporous carbons, Carbon N. Y. 44 (2006) 468–474. doi:10.1016/j.carbon.2005.08.019.

[206] R.N. Tantry, K. Jathi, M.N.K. Harish, S.A.R. Angadi, K.K.T. Chinnagiri, Synthesis, Spectral and Thermal Degradation Kinetics Studies of Benzimidazole substituted Metal Phthalocyanine through oxadiazole, Res. J. Chem. Sci. 3 (2013) 36–46.

[207] P.M. Schaber, J. Colson, S. Higgins, D. Thielen, B. Anspach, J.

Brauer, Thermal decomposition (pyrolysis) of urea in an open reaction vessel, Thermochim. Acta. 424 (2004) 131–142. doi:10.1016/j.tca.2004.05.018.

[208] S.Y. Lee, D.Y. Chung, M.J. Lee, Y.S. Kang, H. Shin, M.J. Kim, C.W. Bielawski, Y.E. Sung, Charting the Outer Helmholtz Plane and the Role of Nitrogen Doping in the Oxygen Reduction Reaction Conducted in Alkaline Media Using Nonprecious Metal Catalysts, J. Phys. Chem. C. 120 (2016) 24511–24520. doi:10.1021/acs.jpcc.6b04771.

[209] F. Jaouen, V. Goellner, M. Lefèvre, J. Herranz, E. Proietti, J.P. Dodelet, Oxygen reduction activities compared in rotating-disk electrode and proton exchange membrane fuel cells for highly active FeNC catalysts, Electrochim. Acta. 87 (2013) 619–628. doi:10.1016/j.electacta.2012.09.057.

[210] E. Proietti, F. Jaouen, M. Lefèvre, N. Larouche, J. Tian, J. Herranz, J.P. Dodelet, Iron-based cathode catalyst with enhanced power density in polymer electrolyte membrane fuel cells, Nat. Commun. 2 (2011). doi:10.1038/ncomms1427.

[211] A. Zadick, L. Dubau, N. Sergent, Huge Instability of Pt / C Catalysts in Alkaline Medium, (2015). doi:10.1021/acscatal.5b01037.

[212] W. Huang, H. Wang, J. Zhou, J. Wang, P.N. Duchesne, D. Muir, P. Zhang, N. Han, F. Zhao, M. Zeng, J. Zhong, C. Jin, Y. Li, S. Lee, H. Dai, Highly active and durable methanol oxidation electrocatalyst based on the synergy of platinum-nickel hydroxide-graphene, Nat. Commun. (2015) 1–8. doi:10.1038/ncomms10035.

[213] C. Breitkopf, K. Swider-Lyons, Handbook of Electrochemical Energy, Springer, 2017.

[214] G. Wu, K.L. More, C.M. Johnston, P. Zelanay, High-performance electrocatalysts for oxygen reduction derived from polyanine, iron and cobalt., Science (80-.). 332 (2011) 443–447.

[215] L. Wang, H. Yang, G. Pan, L. Miao, S. Chen, Y. Song, Polyaniline-Carbon Nanotubes@Zeolite Imidazolate Framework-67-Carbon Cloth Hierarchical Nanostructures for Supercapacitor Electrode, Electrochim. Acta. 240 (2017) 16–23. doi:10.1016/j.electacta.2017.04.035.

[216] N.R.Ć. Elezovi, B.M.Ć. Babi, L.J.M.V.R.A.Č. Ar, N.V.Ć. Krstaji, Oxygen reduction at platinum nanoparticles supported on carbon cryogel in alkaline solution, 72 (2007) 699–708. doi:10.2298/JSC0707699E.

[217] A. Kostuch, J. Gryboś, P. Indyka, L. Osmieri, S. Specchia, Z. Sojka, K. Kruczała, Morphology and dispersion of nanostructured manganese-cobalt spinel on various carbon supports: The effect on the oxygen reduction reaction in alkaline media, Catal. Sci. Technol. 8 (2018) 642–655. doi:10.1039/c7cy02228j.

[218] H. Zhang, S. Hwang, M. Wang, Z. Feng, S. Karakalos, L. Luo, Z. Qiao, X. Xie, C. Wang, D. Su, Y. Shao, G. Wu, Single Atomic Iron Catalysts for Oxygen Reduction in Acidic Media: Particle Size Control and Thermal Activation, J. Am. Chem. Soc. 139 (2017) 14143–14149. doi:10.1021/jacs.7b06514.

[219] J. Perez, A.A. Tanaka, E.R. Gonzalez, E.A. Ticianelli, Application of the Flooded-Agglomerate Model to Study Oxygen Reduction on Thin Porous Coating Rotating Disk Electrode, 141 (1994).

[220] J. Zagal, M. Páez, A.A. Tanaka, J.R. dos Santos, C.A. Linkous, Electrocatalytic activity of metal phthalocyanines for oxygen reduction, J. Electroanal. Chem. 339 (1992) 13–30. doi:10.1016/0022-0728(92)80442-7.

[221] A. Alsudairi, J. Li, N. Ramaswamy, S. Mukerjee, K.M. Abraham, Q. Jia, Resolving the Iron Phthalocyanine Redox Transitions for ORR Catalysis in Aqueous Media, J. Phys. Chem. Lett. 8 (2017) 2881–2886. doi:10.1021/acs.jpclett.7b01126.

[222] S. Mukerjee, S. Srinivasan, Enhanced electrocatalysis of oxygen reduction on platinum alloys in proton exchange membrane fuel cells, J. Electroanal. Chem. 357 (1993) 201–224. doi:10.1016/0022-0728(93)80380-Z.

[223] A.M. Gómez-Marín, R. Rizo, J.M. Feliu, Some reflections on the understanding of the oxygen reduction reaction at Pt(111), Beilstein J. Nanotechnol. 4 (2013) 956–967. doi:10.3762/bjnano.4.108.

[224] N.M. Marković, T.J. Schmidt, B.N. Grgur, H.A. Gasteiger, R.J. Behm, P.N. Ross, Effect of Temperature on Surface Processes at the Pt(111)−Liquid Interface: Hydrogen Adsorption, Oxide

Formation, and CO Oxidation, J. Phys. Chem. B. 103 (1999) 8568–8577. doi:10.1021/jp991826u.

[225] M. Bevilacqua, C. Bianchini, A. Marchionni, J. Filippi, A. Lavacchi, H. Miller, W. Oberhauser, F. Vizza, G. Granozzi, L. Artiglia, S.P. Annen, F. Krumeich, H. Grützmacher, Improvement in the efficiency of an OrganoMetallic Fuel Cell by tuning the molecular architecture of the anode electrocatalyst and the nature of the carbon support, Energy Environ. Sci. 5 (2012) 8608–8620. doi:10.1039/c2ee22055e.

[226] C. Santoro, R. Gokhale, B. Mecheri, A. D'Epifanio, S. Licoccia, A. Serov, K. Artyushkova, P. Atanassov, Design of Iron(II) Phthalocyanine-Derived Oxygen Reduction Electrocatalysts for High-Power-Density Microbial Fuel Cells, ChemSusChem. 10 (2017) 3243–3251. doi:10.1002/cssc.201700851.

[227] L. Osmieri, R. Escudero-Cid, M. Armandi, P. Ocón, A.H.A. Monteverde Videla, S. Specchia, Effects of using two transition metals in the synthesis of non-noble electrocatalysts for oxygen reduction reaction in direct methanol fuel cell, Electrochim. Acta. 266 (2018) 220–232. doi:10.1016/j.electacta.2018.02.036.

[228] I. Takahashi, S.S. Kocha, Examination of the activity and durability of PEMFC catalysts in liquid electrolytes, J. Power Sources. 195 (2010) 6312–6322. doi:10.1016/j.jpowsour.2010.04.052.

[229] B.G. Pollet, Let's Not Ignore the Ultrasonic Effects on the Preparation of Fuel Cell Materials, Electrocatalysis. 5 (2014) 330–343. doi:10.1007/s12678-014-0211-4.

[230] B.G. Pollet, The use of ultrasound for the fabrication of fuel cell materials, Int. J. Hydrogen Energy. 35 (2010) 11986–12004.

[231] B.G. Pollet, Power Ultrasound in Electrochemistry: From Versatile Labboratory Tool to Engineering Solution, John Wiley & Sons, Ltd, Chichester, UK, 2012.

[232] Y.S. Li, T.S. Zhao, Z.X. Liang, Performance of alkaline electrolyte-membrane-based direct ethanol fuel cells, J. Power Sources. 187 (2009) 387–392. doi:10.1016/j.jpowsour.2008.10.132.

[233] H.K. Esfeh, M.K.A. Hamid, Temperature effect on proton exchange membrane fuel cell performance Part II: Parametric

study, Energy Procedia. 61 (2014) 2617–2620. doi:10.1016/j.egypro.2014.12.261.

[234] J. Zhang, J. Wu, H. Zhang, J. Zhang, The Effects of Temperature on PEM Fuel Cell Kinetics and Performance, in: Pem Fuel Cell Test. Diagnosis, 2013: pp. 121–141. doi:10.1016/B978-0-444-53688-4.00004-8.

[235] G. Zhang, R. Chenitz, M. Lefèvre, S. Sun, J.-P. Dodelet, Is iron involved in the lack of stability of Fe/N/C electrocatalysts used to reduce oxygen at the cathode of PEM fuel cells?, Nano Energy. 29 (2016) 111–125. doi:10.1016/j.nanoen.2016.02.038.

[236] N.S. Vasile, R. Doherty, A.H.A. Monteverde Videla, S. Specchia, 3D multi-physics modeling of a gas diffusion electrode for oxygen reduction reaction for electrochemical energy conversion in PEM fuel cells, Appl. Energy. 175 (2016) 435–450. doi:10.1016/j.apenergy.2016.04.030.

[237] S.D. Poynton, R.C.T. Slade, T.J. Omasta, W.E. Mustain, R. Escudero-Cid, P. Ocón, J.R. Varcoe, Preparation of radiation-grafted powders for use as anion exchange ionomers in alkaline polymer electrolyte fuel cells, J. Mater. Chem. A. 2 (2014) 5124–5130. doi:10.1039/c4ta00558a.

[238] L. Wang, E. Magliocca, E.L. Cunningham, W.E. Mustain, S.D. Poynton, R. Escudero-Cid, M.M. Nasef, J. Ponce-González, R. Bance-Souahli, R.C.T. Slade, D.K. Whelligan, J.R. Varcoe, An optimised synthesis of high performance radiation-grafted anion-exchange membranes, Green Chem. 19 (2017) 831–843. doi:10.1039/c6gc02526a.

[239] E. Antolini, E.R. Gonzalez, Alkaline direct alcohol fuel cells, J. Power Sources. 195 (2010) 3431–3450. doi:10.1016/j.jpowsour.2009.11.145.

[240] T.J. Mason, J. Millichamp, T.P. Neville, P.R. Shearing, S. Simons, D.J.L. Brett, A study of the effect of water management and electrode flooding on the dimensional change of polymer electrolyte fuel cells, J. Power Sources. 242 (2013) 70–77. doi:10.1016/j.jpowsour.2013.05.045.

[241] H. Hou, S. Wang, Q. Jiang, W. Jin, L. Jiang, G. Sun, Durability study of KOH doped polybenzimidazole membrane for air-breathing alkaline direct ethanol fuel cell, J. Power Sources. 196 (2011) 3244–3248. doi:10.1016/j.jpowsour.2010.11.104.

[242] Y.S. Li, T.S. Zhao, Z.X. Liang, Effect of polymer binders in anode catalyst layer on performance of alkaline direct ethanol fuel cells, J. Power Sources. 190 (2009) 223–229. doi:10.1016/j.jpowsour.2009.01.055.

[243] D. Sebastián, V. Baglio, A. S.Aricòa, A. Serov, P. Atanassov, Performance analysis of a non-platinum group metal catalyst based on iron-aminoantipyrine for direct methanol fuel cells, Appl. Catal. B Environ. 182 (2016) 297–305. doi:10.1016/j.apcatb.2015.09.043.

[244] L. Osmieri, R. Escudero-Cid, A.H.A.M. Videla, P. Ocón, S. Specchia, Performance of a Fe-N-C catalyst for the oxygen reduction reaction in direct methanol fuel cell: Cathode formulation optimization and short-term durability, Appl. Catal. B Environ. 201 (2017) 253–265. doi:10.1016/j.apcatb.2016.08.043.

[245] S. Gustafsson, Corrosion properties of aluminium alloys and surface treated alloys in tap water, Sapa Technol. (2011). doi:10.1007/s11126-011-9193-z.

[246] Pajarito Powder, (n.d.). https://pajaritopowder.com/.

[247] C. Lo Vecchio, A. Serov, H. Romero, A. Lubers, B. Zulevi, A.S. Aricò, V. Baglio, Commercial platinum group metal-free cathodic electrocatalysts for highly performed direct methanol fuel cell applications, J. Power Sources. 437 (2019) 226948. doi:10.1016/j.jpowsour.2019.226948.

[248] D. Banham, S. Ye, Current Status and Future Development of Catalyst Materials and Catalyst Layers for Proton Exchange Membrane Fuel Cells: An Industrial Perspective, ACS Energy Lett. 2 (2017) 629–638. doi:10.1021/acsenergylett.6b00644.

[249] A. Serov, M.J. Workman, K. Artyushkova, P. Atanassov, G. McCool, S. McKinney, H. Romero, B. Halevi, T. Stephenson, Highly stable precious metal-free cathode catalyst for fuel cell application, J. Power Sources. 327 (2016) 557–564. doi:10.1016/j.jpowsour.2016.07.087.

[250] L.M. Tavares, A review of advanced ball mill modelling, KONA Powder Part. J. 2017 (2017) 106–124. doi:10.14356/kona.2017015.

[251] T. Iwasaki, T. Yabuuchi, H. Nakagawa, S. Watano, Scale-up

methodology for tumbling ball mill based on impact energy of grinding balls using discrete element analysis, Adv. Powder Technol. 21 (2010) 623–629. doi:10.1016/j.apt.2010.04.008.

[252] L.G. Austin, H. Cho, An alternative method for programming mill models, Powder Technol. 122 (2002) 96–100. doi:10.1016/S0032-5910(01)00404-1.

[253] V.A. Rodriguez, R.M. de Carvalho, L.M. Tavares, Insights into advanced ball mill modelling through discrete element simulations, Miner. Eng. 127 (2018) 48–60. doi:10.1016/j.mineng.2018.07.018.